Titre: Title:	Nonlinear Propagation of Femtosecond Laser Pulses in Plasmonic Nano-Colloids
Auteur: Author:	Leonidas Agiotis
Date:	2022
Type:	Mémoire ou thèse / Dissertation or Thesis
Référence: Citation:	Agiotis, L. (2022). Nonlinear Propagation of Femtosecond Laser Pulses in Plasmonic Nano-Colloids [Thèse de doctorat, Polytechnique Montréal]. PolyPublie. https://publications.polymtl.ca/10264/

POLYTECHNIQUE MONTRÉAL

affiliée à l'Université de Montréal

Nonlinear propagation of femtosecond laser pulses in plasmonic nano-colloids

LEONIDAS AGIOTIS

Département de génie physique

Thèse présentée en vue de l'obtention du diplôme de *Philosophiæ Doctor*

Génie physique

Avril 2022

POLYTECHNIQUE MONTRÉAL

affiliée à l'Université de Montréal

Cette thèse intitulée :

Nonlinear propagation of femtosecond laser pulses in plasmonic nano-colloids

présentée par **Leonidas AGIOTIS**

en vue de l'obtention du diplôme de *Philosophiæ Doctor*

a été dûment acceptée par le jury d'examen constitué de :

Denis SELETSKIY, président
Michel MEUNIER, membre et directeur de recherche
Sébastien FRANCOEUR, membre
François LÉGARÉ, membre externe

DEDICATION

To my family

ACKNOWLEDGEMENTS

My deepest appreciation is extended to my supervisor at Polytechnique Montreal, Michel Meunier, who supported and encouraged me to aim for the highest standards throughout my PhD. His guidance and long experience have been invaluable to me in my research.

I would also like to thank the members of the jury who have agreed to be in my evaluation committee and for their time assessing my work.

I am grateful to a number of (current or past) members of the LP^2L group, for fruitful collaborations and for accompanying me throughout the years, making my PhD journey a great experience: Lu Wang, Cécile Darviot, Jennyfer Zapata-Farfan, Isabelle Largilliere, Morteza Kafshgari, Sergiy Patskovsky, Jie OuYang, Hassan Khalil, Antoine Uzel, Yves Drolet, Mengjiao Qi, Siyu Tu, Vi Tching de Lille, Rémi Lachaine, David Rioux, Nicolas Le Hir, Samuel Pinsonneault-Marotte, Thomas Ricard.

Finally, I would like to thank my twin brother Vassilis, my brother Spyros and my mother Youla for their love, encouragement, and firm belief in me throughout all my life, and my partner Shanny for her support and understanding during my studies.

RÉSUMÉ

Cette thèse traite de la quantification et des origines de l'auto-(dé)focalisation et de la propagation des impulsions femtosecondes à travers des suspensions aqueuses de nanoparticules métalliques avec des impulsions amplifiées et des impulsions à haut taux de répétition. Dans les deux cas, des équations de propagation non linéaires sont utilisées pour décrire physiquement les observations expérimentales, en traitant le matériau composite en se basant sur ses propriétés optiques de milieu effectif.

Il est bien connu qu'au-dessus d'une puissance seuil, les impulsions femtosecondes amplifiées subissent une auto-focalisation lorsqu'elles se propagent dans l'eau pure, ce qui entraîne les effets de la filamentation laser et de la génération de supercontinuum. Il est intéressant de noter que le renforcement et la modulation du supercontinuum ont été observés lorsque l'eau est dopée avec des nanoparticules plasmoniques. Ce phénomène a été principalement attribué à l'amélioration de la non-linéarité de Kerr de l'eau, toutefois, sans que les origines physiques de l'interaction ne soient clairement établies. En fait, les mesures z-scan dans des échantillons minces de nanocomposites métalliques donnent typiquement une faible non-linéarité de Kerr, pratiquement impossible à distinguer de leur hôte diélectrique non dopé, lorsque des impulsions femtosecondes sont utilisées. Une autre façon de quantifier le renforcement plasmonique serait d'étudier directement la puissance seuil pour l'autofocalisation à travers des échantillons épais, avec la manifestation simultanée de la filamentation laser et de la génération de supercontinuum.

À cette fin, une technique de limitation de la puissance optique a été utilisée, pour la première fois avec des impulsions femtosecondes. En premier lieu, il était important de démontrer l'applicabilité de la technique dans le cas de la transparence optique, c'est-à-dire sans dopage plasmonique. En effet, le montage a été testé sur de l'eau pure et de l'éthanol. On a montré que le signal optique de sortie ne présente pas une réponse de type 'step-function' par rapport à la puissance de l'impulsion, comme cela est généralement attendu lorsque des impulsions nanosecondes ou picosecondes sont utilisées. Cependant, le signal présente des caractéristiques de la transformation des impulsions en ondes coniques non linéaires. La réponse a été systématiquement étudiée et il a été démontré comment la non-linéarité de Kerr peut être évaluée de manière fiable.

Dans un deuxième temps, des colloïdes de nanobâtons d'or résonants de concentration variable ont été étudiés par la même technique. On a montré comment la non-linéarité de Kerr peut être entièrement déterminée en utilisant la technique proposée en combinaison avec (i) des mesures de transmittance optique, pour évaluer la partie imaginaire, (ii) une analyse spectroscopique, pour estimer les effets de déformation des particules et (iii) des simulations numériques, pour modéliser les conditions d'effondrement optique. Physiquement, il a été démontré que les échantillons présentent une saturation de l'absorption bien avant le seuil d'autofocalisation. Cependant, une déformation considérable des particules se produit près du seuil précité. En effet, la non-linéarité de Kerr "renforcée par les plasmons" du composite est fortement saturée à proximité du seuil de collapse optique. Cela s'explique par la génération ultrarapide d'une population d'électrons non thermiques près des surfaces des nanoparticules métalliques, qui détruisent la cohérence plasmonique et l'amplification du champ, en modulant la permittivité diélectrique du métal.

Au contraire, au-dessus d'un seuil de puissance, les impulsions femtosecondes à haut taux de répétition présentent une propagation phénoménologique sans diffraction (self-channeling) à travers les nanocolloïdes plasmoniques. En particulier sous une illumination cw, l'effet susmentionné a été attribué à des forces optiques de gradient exercées sur les particules, induisant une modulation locale de l'indice de réfraction par transport de masse, ou à l'absorption, donnant lieu à des gradients de température et à un effet de lentille thermique non linéaire. Nous montrons ici que dans les conditions de focalisation typiques rapportées dans la littérature, self-channeling est en fait un effet de lentille thermique non linéaire, même pour une longueur d'onde d'illumination non résonante. Notamment, sous un éclairage cw, les forces de gradient ne peuvent devenir dominantes que par le confinement thermique spatial en employant des conditions de focalisation plus fortes. Ces observations sont généralisées au cas d'impulsions femtosecondes à taux de répétition élevé. En outre, les observations résolues dans le temps de la lentille thermique à haute puissance montrent que les impulsions femtosecondes, par opposition à l'illumination cw, peuvent être utilisées pour obtenir un confinement thermique spatio-temporel. Une discussion détaillée montre comment ce dernier peut potentiellement être optimisé par le paramètre du taux de répétition avec la possibilité de favoriser self-channeling par des forces de gradient.

ABSTRACT

This thesis deals with the quantification and origins of femtosecond laser self-(de)focusing and propagation through aqueous suspensions of metallic nanoparticles with amplified pulses and with high-repetition rate pulses. In both cases, nonlinear propagation equations are employed to describe the physical picture in accordance with experimental observations, treating the composite material based on its effective medium optical properties.

It is well-known that above a threshold power, amplified femtosecond pulses undergo self-focusing when they propagate through pure water, which leads to the effects of laser filamentation and supercontinuum generation. Interestingly, enhancement and modulation of the resulted supercontinuum has been noted when water is doped with plasmonic nanoparticles. It has been principally attributed to enhancement of the Kerr nonlinearity of water, however, without clear insights on the physical origins of the interaction. In fact, z-scan measurements in thin samples of metallic nanocomposites yield typically a weak Kerr nonlinearity, hardly distinguishable from their undoped dielectric host, when femtosecond pulses are employed. An alternative approach to quantify plasmonic enhancement would be to directly investigate the threshold power for self-focusing through thick samples, under the concurrent manifestation of laser filamentation and white-light continuum generation.

Toward this objective, a power limiting technique has been employed, for the first time with femtosecond pulses. An important first step was to demonstrate the applicability of the technique in the simpler case of optical transparency, i.e., without plasmonic doping. Indeed, the setup was tested on pure water and ethanol. It was shown that the output optical signal does not exhibit a step-like function response versus the input power as usually expected when nanosecond or picosecond pulses are employed, yet it features the underlying physics of the transformation of the pulses into nonlinear conical waves. The response was systematically studied, and it was demonstrated how the Kerr nonlinearity can be reliably evaluated.

As a next step, gold nanorod colloids of varying concentration were studied by the same technique. The peak of the plasmon resonance of the samples was purposely chosen to lie near the employed optical wavelength. It was demonstrated how the Kerr nonlinearity can be fully determined by use of the proposed technique in conjunction with (i) optical transmittance measurements, to evaluate

the imaginary part of the nonlinearity, (ii) spectroscopic analysis, to estimate particle deformation effects and (iii) numerical simulations, to model the experimentally obtained optical collapse conditions. Physically, it was shown that the samples exhibit saturation of optical absorption well before the self-focusing threshold, yet considerable particle deformation occurs concurrently only near the foresaid threshold. Effectively, the "plasmon-enhanced" Kerr nonlinearity of the composite is strongly saturated near the optical collapse threshold. This is because of the ultrafast generation of a large population of nonthermal electrons near the surfaces of the metallic nanoparticles, which destroy plasmon-oscillation coherence and field amplification, by drastically modulating the electronic energy-level structure of the metal and its dielectric permittivity.

Contrarily, nonlinear propagation of high-repetition rate femtosecond pulses through metallic nano-colloids is governed by a quasi-cw self-channeling effect (a phenomenological diffraction-free propagation) above a threshold power. Particularly under cw illumination, the observed self-channeling effect has been attributed to occur due to either gradient optical forces exerted on the particles, inducing a local refractive index modulation through mass transport, or due to absorption, giving rise to temperature gradients and a nonlinear thermal lensing effect. Here it is shown that under typical focusing conditions reported in the literature, self-channeling is in fact a nonlinear thermal lensing effect even for an illumination wavelength far from the plasmon resonance. Notably, under cw illumination, gradient forces can only become dominant through spatial thermal confinement by employing tighter focusing conditions. The above observations are generalized for the case of high-repetition rate femtosecond pulses (quasi-cw self-channeling). Importantly, through time resolved observations of high-power thermal lensing, it is further shown that femtosecond pulses, as opposed to cw illumination, can be used to achieve spatiotemporal thermal confinement. A detailed discussion shows how the latter can potentially be optimized through the repetition rate parameter with the possibility of promoting self-channeling through gradient forces.

TABLE OF CONTENTS

LIST OF TABLES

LIST OF FIGURES

LIST OF SYMBOLS AND ABBREVIATIONS

Abbreviations

BGO	Bismuth Germanate
CW	Continuous Wave
DMSO	dimethyl sulphoxide
fG	functionalized Graphene
FME	Forward Maxwell Equation
FWHM	Full Width at Half Maximum
HRF	Hache-Ricard-Flytzanis
HRFR	Hache-Ricard-Flytzanis-Rautian
LP^2L	Laser Processing and Plasmonics Laboratory
NC	Nanocubes
ND	Decorated Nanodiamonds
NLSE	Non-Linear Schrödinger Equation
NO	Nanooctahedra
NP	Nanoparticle
NR	Nanorod
Nshells	Nanoshells
Nstars	Nanostars
NTP	Nanotriangle Prisms
OL	Optical Limiting
rGO	reduced Graphene oxide
RSA	Reverse Saturable Absorption
SA	Saturable Absorption
SEM	Scanning Electron Microscopy
SPM	Self-Phase Modulation
SPR	Surface Plasmon Resonance
SVEA	Slowly Varying Envelope Approximation
THG	Third Harmonic Generation

Latin symbols

$a(I)$	Intensity-dependent absorption coefficient
a_0	Linear absorption coefficient
a_{ns}	Non-Saturated absorption coefficient
a_s	Sommerfeld constant
a_R	Particle polarizability
a_V	Thermal expansion coefficient
a_2^e	Nonlinear second-order absorption coefficient of the effective medium

A	Normalized intensity-dependent absorption coefficient
A_0	Normalized linear absorption coefficient
A_{ns}	Normalized non-saturated absorption coefficient
$\mathcal{A}$	Normalized fitting parameter
b	Dimensionless parameter of self-focusing collapse dynamids
c	Speed of light in vacuum
C_e	Electron heat capacity
d	Particle size (diameter)
d_c	Duty cycle
d_f	Arbitrary distance in the far-field
d_i	Image plane distance
d_o	Object plane distance
D	Electric displacement field
D_f	Spectral filter of gain medium
D_g	Dispersion filter of gain medium
D_m	Diffusion coefficient
d	Distance of geometrical focus from input beam
$\mathcal{D}$	Distance between beam waist at X and Y axis
dn/dT	Thermo-optic coefficient
e	Elementary charge
e_f	Ellipticity
E	Complex electric field
E_0	Input electric field
E_1	Electric field in the particle
E_F	Fermi energy
E_g	Ground state energy
E_{in}	Input pulse energy
e	Normalized complex electric-field amplitude
$\mathcal{E}$	Complex electric-field amplitude
f	Volumetric filling factor
F	Normalized focusing parameter
F_3	Dimensionless function
F_{in}	Input fluence
F_{scat}	Scattering force
$\mathcal{F}\{\}$	Fourier transform
g	Gravity acceleration
g_3	Dimensionless function associated with the density of states
$G(I)$	Function of laser cavity gain and losses

G_{e-ph}	Electron-phonon coupling parameter
$g(I)$	Gain of laser cavity
$\mathcal{G}$	Arbitrary dimensionless parameter
h	Sample thickness (composite material)
h_{eff}	Effective thickness
$\hbar$	Convective heat transfer coefficient
$\hbar$	Reduced Planck constant
I	Laser intensity
I_0	Input laser intensity
I_1	Laser intensity in particles
I_{OL}	Optical limiting intensity
I_s	Saturated intensity
I_s^{δ}	Saturated intensity at a detuning from resonance
J	Complex current density
J_B	Complex current density due to bound charges
J_E	Complex current density due to critical plasma
J_f	Complex current density due to free carriers
J_P	Complex current density due to direct photoionization
$\mathcal{J}$	Complex current density amplitude
k	Wavenumber
k_0	Central wavenumber
k_BT	Thermal energy
k_{eff}	Complex wavevector in the effective medium
$k_{\perp}$	Transverse wavevector
$k_0^{(2)}$	Second-order dispersion (group velocity dispersion)
K	Number of simultaneously absorbed photons
K_T	Thermal conductivity
$\hbar$	Thermal diffusivity
l	Characteristic atomic scale
l_c	Length of laser cavity
l_p	Propagation distance of the pulse in the medium
L	Local field factor
L_d	Diffraction length
L_f	Characteristic thermal diffusion length of a focused beam
L_{DS}	Dispersion length
L_{SF}	Characteristic distance of self-focusing
ℓ	Losses in laser cavity
$\mathcal{L}$	Dimensionless beam width

m	Beam stretching factor
m_e	Mass of electron
M	Number of nanoparticles
$M^2_{(X,Y)}$	Beam propagation factor (along X and Y axes)
MA	Magnification of the optical system (with sample)
MA_0	Magnification of the optical system (air)
$\mathscr{m}$	Topological charge
n	Intensity-dependent refractive index
n_0	Linear refractive index
$n_{0,eff}$	Linear refractive index of the effective medium
n_2	Nonlinear refractive index
$n_{2,g}$	Nonlinear refractive index of the gain medium
n_d	Linear refractive index of the surrounding dielectric
n_e	Electron density
$n_{e,c}$	Critical plasma density
n_m	Linear refractive index of the metal
n_n	Neutral species density
n_2^e	Nonlinear refractive index of the effective medium
n_2^h	Nonlinear refractive index of the host dielectric
$n_{2,0}^e$	Nonlinear second-order refractive index of the effective medium
n_4^e	Nonlinear fourth-order refractive index of the effective medium
n_6^e	Nonlinear sixth-order refractive index of the effective medium
N	Sum of all equilibrium-state population in a nanoparticle
N_{12}	Difference of population of ground-excited states in a two-level system
$\mathscr{n}$	Beam compression factor
OD	Optical density
p	Interparticle distance
p_{abs}	Absorbed laser power
p_i	Induced individual particle polarization
P	Complex induced polarization density
P_0	Power of thermal self-collimation
P_{cr}	Critical power for self-focusing
$P_{cr,0}$	Critical power for self-focusing (ideal beam)
P_h	Induced polarization in the host dielectric
P_{in}	Input power
P_{SC}	Supercontinuum onset power
P_{th}	Threshold power for self-focusing
P^L	Complex linear induced polarization density

P^{NL}	Complex nonlinear induced polarization density
P_{cr}^{e}	Critical power for self-focusing of the effective medium (without absorption)
P_{cr}^{h}	Critical power for self-focusing of the host dielectric
P_{cr}^{Townes}	Critical power for self-focusing (strict definition of Townes profile)
P_{OB}^{eth}	Onset power for optical breakdown in ethanol
P_{th}^{e}	Threshold power for self-focusing of the effective medium
$P_{th}^{Gaussian}$	Threshold power for self-focusing for Gaussian profile
$P_{th,exp}^{Gaussian}$	Threshold power for self-focusing for Gaussian profile (experimental)
P_{th}^{h}	Threshold power for self-focusing of the host dielectric
$(P_{th})^{abs}$	Threshold power for self-focusing accounting for absorption losses
$\mathscr{P}$	Normalized self-focusing nonlinearity
$\mathcal{P}^{NL}$	Complex nonlinear induced polarization density amplitude
$q(I)$	Optical response of nanocomposite in laser cavity
Q	Function related to collapse dynamics
r	Radial coordinate
r_p	Radius of particle
R	Radius of curvature
$\mathcal{R}$	Townes profile complex field envelope
$\mathscr{r}$	Normalized radial coordinate
s	Normalized saturation intensity
s_f	Surface area of the volume of focused laser beam
$S(t, k_\perp)$	Far-field electric field amplitude distribution
$\mathcal{S}$	Characteristic surface area for heat diffusion
t	Time
t_B	Characteristic time of Brownian motion
t_{e-e}	Electron-electron coupling characteristic time
t_{e-ph}	Electron-phonon coupling characteristic time
t_{FWHM}	Laser pulsewidth (Full Width at Half-Maximum)
t_{NR}	Non-radiative plasmon lifetime
t_p	Laser pulsewidth ($1/e^2$ for Gaussian profile)
t_R	Radiative plasmon lifetime
t_d^m	Characteristic time for mass diffusion
t_d^{th}	Characteristic time for thermal diffusion
T	Temperature
$\hat{T}$	Self-steepening operator
T_0	Initial electron temperature
$T_{1,2}$	Relaxation lifetime of excited population and induced moment, respectively
T_e	Electron temperature

T_λ	Optical transmittance
$T_{\lambda,0}$	Initial optical transmittance
$T_{\lambda,ns}$	Non-saturated optical transmittance
$\mathcal{T}$	Integrated time
u	Convective fluid flow velocity
u_B	Characteristic velocity due to Brownian motion
u_g	Group velocity
u_{scat}	Velocity due to scattering forces
u_d^m	Velocity due to gradient forces (convective particle velocity)
U	Overall heat transfer coefficient
U_i	Ionization potential
v_f	Volume of focused laser beam
v_F	Fermi velocity
v_p	Depolarization factor
V	Volume of particle
V_m	Volume of composite material
w	Beam width
$w_{0,(X,Y)}$	Input beam width (along X and Y axes)
w_f	Focused beam width waist
$w_{i,(X,Y)}$	Imaged beam width waist
w_I	Impact ionization rate
w_m	Multiphoton ionization rate
$w_{f,(X,Y)}^{ideal}$	Ideal focused beam width waist
W	Figure of merit for optical switching
$\mathcal{W}$	Lambert function
z	Propagation distance
z_0	Input beam Rayleigh length
z_f	Position of focusing plane
z_i	Position of imaging plane
z_{NL}	Nonlinear beam waist position
$z_{R,(X,Y)}$	Rayleigh length (along X and Y axes)
$z_{R,f}$	Rayleigh length of the focused beam
$z_{R,i}$	Rayleigh length of the imaged beam
Z_c	Beam collapse distance
$Z_c^{(F)}$	Focused beam collapse distance

Greek Symbols

β	Linear absorption
β_K	Cross section of multiphoton absorption
γ	Plasmon decoherence rate (Drude)
γ_0	Plasmon decoherence rate (bulk)
γ_{e-e}	Electron-electron collision relaxation rate
γ_{e-ph}	Electron-phonon collision relaxation rate
γ_{ib}	Interband electron relaxation rate
γ_s	Surface scattering relaxation rate
Γ	Plasmon decoherence rate
$\Gamma_{1,2}$	Phenomenological relaxation rates of population and moment coherence
δ	Ratio between diffraction over dispersion lengths
δ_s	Skin depth
δn	Refractive index modulation
δN_{eq}	Steady-state population difference in a two-level system
$\delta T_{\lambda,p-v}$	Normalized recorded peak to valley transmittance difference
δy	Downward beam displacement
$\delta\varphi_i$	Initial phase-front curvature
$\delta\varphi_T$	Thermal self-induced phase
$\delta\Phi$	Nonlinear phase-shift
∇_T^2	Transverse Laplace operator
ε	Dielectric permittivity
ε_0	Permittivity of free space
ε_d	Dielectric permittivity of surrounding dielectric medium
ε_{eff}	Dielectric permittivity of the effective medium
ε_m^D	Drude dielectric permittivity of metal
ε_m^{ib}	Interband transition contribution to dielectric permittivity of metal
ζ	Normalized propagation distance
η	Dynamic viscosity
θ	Beam divergence
θ_0	Beam divergence in linear regime
θ_{diff}	Diffraction angle
θ_{sf}	Self-focusing angle
Θ	Angle between input beam wavevector and metamaterial slab
$\kappa(\omega)$	Transformed wavevector due to group velocity
κ_0	Linear extinction coefficient
λ	Wavelength
λ_0	Central wavelength
λ_p	Wavelength associated with plasma frequency

μ	Kinematic viscosity
μ_0	Vacuum permeability
μ_{21}	Induce dipole moment of transition
ξ	Parameter that determines the type of NLSE (critical, subcritical, supercritical)
$\rho(I)$	Intensity dependent particle concentration
ρ_0	Initial particle concentration
σ	Absorption cross section of particle
$\sigma_f(\omega)$	Complex frequency dependent cross section of collision of free carriers
τ	Normalized time
τ_c	Electron collision time
φ	Phase argument
$\chi^{(1)}$	First-order susceptibility
$\chi^{(3)}$	Third-order susceptibility
$\chi^{(3)}_{xxxx}$	Component *xxxx* of third-order susceptibility tensor
$\chi^{(3)}_{eff}$	Third-order susceptibility of the effective medium
$\chi^{(3)}_{m}$	Third-order susceptibility of metallic particle
ψ	Dimensionless factor related to the beam profile distribution
ω	Radial frequency
ω_0	Central radial frequency
ω_{21}	Radial frequency difference associated to energy levels of a two-level system
ω_b	Maximum pulse broadening toward bluer radial frequencies
ω_{ib}	Threshold radial frequency of interband transitions
ω_r	Maximum pulse broadening toward redder radial frequencies
ω_p	Plasma radial frequency

LIST OF APPENDICES

CHAPTER 1 INTRODUCTION

The use of plasmonics for the purpose of modulation of electromagnetic wave propagation in engineered metamaterials and waveguides has been the subject of research for over 30 years. The principal motivation was mainly fueled by the objective of either development of all-optical switching and communication devices based on free-electron, Kerr-type nonlinearities, or observation of plasmon-mediated coherent nonlinear responses [1-3]. Both involve the enhancement of the nonlinear interaction of an optical field with an optical medium, which has indeed been predicted by early theoretical studies, specifically focused on the formulation of the effective nonlinear susceptibility of plasmonic nanocomposites [4-7] (i.e., plasmonic nanoparticles embedded in a dielectric host). However, as it turns out there exist major constraints imposed by the real physical picture framing the proposed theory, which account mainly for (i) whether the nonlinearity is "fast" or "slow" (or equivalently, whether it involves virtual or real electronic transitions, respectively), (ii) the losses related to resonant interactions and (iii) the existence of optical saturation or damage [1, 2].

The first constraint is related to the origin, time response and strength of the nonlinearity. If the induced nonlinear polarization involves virtual transitions, the response is ultrafast and coherent, yet intrinsically weak. Conversely, nonlinearities due to excitation of electrons to real states ensue latency due to all involved relaxation processes, however, bringing about the advantage of typically stronger responses. Quite encouraging has been the fact that, in metallic nanoparticles, ultrafast incoherent nonlinearities have been observed under intense pumping [8-12]. Still, for the case of optical phase-switching with plasmonics, latency is not the only concern, since a significant amount of the incident field energy is stored as electromechanical energy of excited electrons (especially near the plasmon resonance) [13], which in turn complicates phase-switching over one extinction length of wave propagation in the composite medium [1, 2, 14]. Finally, ultrafast, and localized optical field-enhancement near metallic nanoparticles under intense pumping is limited by saturation effects [15-21] or by thresholds of thermodynamic transitions both in the host material and the metallic inclusions of the composite, eventually leading to optical damage [1, 2, 22-26].

Despite all above constraints, there have been still numerous developments related to waveguide-free nonlinear electromagnetic wave propagation in plasmonic nanocomposites within the framework of effective medium properties. For instance, metallic nanoparticles have been

employed, due to their thermal nonlinear absorption properties, for the development of absorption modulation optical components or optical limiting technologies [27-34]. Additionally, experiments in plasmonic nanocomposites (specifically in the picosecond pulsed regime) have showed that they possess customizable, determined by the volumetric metal concentration, nonlinear responses due to management of high-order nonlinearities [35]. Also, plasmonic nanocomposites have demonstrated capabilities of configurable nonlinearities and self-induced waveguiding in soft-matter systems [36-39]. Among others, all above advancements will be discussed in detail in Chapter 4 of this thesis.

Of principal interest of the author is the investigation of features of nonlinear propagation of femtosecond laser pulses in metal nanoparticle aqueous suspensions (considered a specific case of a plasmonic nanocomposite). In this context, two interaction regimes of long-scaled, diffraction limited propagation are identified: one of the instantaneous response of a single, high energy (~1 μJ) femtosecond pulse propagation and another one, quasi-steady state propagation regime, arising from accumulation of high repetition rate, low energy (~1 nJ) femtosecond pulses.

The first type of nonlinear propagation involves the effects of femtosecond filamentation [40, 41] and supercontinuum generation [42, 43], which have been extensively studied and understood in the past 20 years for the case of optical transparency. These effects were reported for the first time in a plasmonic nanocomposite (Ag nanoparticle aqueous suspension) in 2007 [44]. A promising observation was noted therein, the one of the enhancement of supercontinuum generation in the presence of nanoparticles in comparison with the undoped dielectric. The effect was attributed to enhancement of the Kerr self-focusing nonlinearity on the presence of nanoparticles, however, without clear insights related to the physical constraints discussed above. Other theoretical works have followed on the modelling of nonlinear propagation of femtosecond pulses in glasses doped with plasmonic nanoparticles, reporting also on the possibility of low-threshold and enhanced supercontinuum, under non-resonant pumping conditions and for propagation distances of the order of the Rayleigh length [45-47]. However, more recently, a contradictory experimental observation has been reported in the case of filamentary propagation of femtosecond pulses in colloidal Au; that of overall power dissipation as incoherent electronic kinetic energy in each nanoparticle upon beam collapse and transformation into nonlinear, conically emitted supercontinuum [48-52].

A major concern based on the foregoing discussion is the optical characterization of the nonlinear susceptibility, which is typically very weak in the femtosecond regime [2]. For instance, results obtained by the widely employed z-scan technique indicate that the self-focusing nonlinearity of plasmonic nanocomposite materials is hardly distinguishable from their dielectric host. Accordingly, examination of whether the origin of the reported supercontinuum enhancement (if any) is attributed on the plasmon-enhanced Kerr nonlinearity of a doped dielectric, urges the determination of the critical power for self-focusing upon femtosecond filamentation. In return, one benefits from an alternative to z-scan, and more direct in this case, optical characterization approach, by gaining further insights on the effect itself and tackling at the same time issues related to the z-scan technique, e.g., beam walk-off and limitations ensued by the thin sample approximation (to avoid filamentation) [53].

When femtosecond pulses of high repetition rate are employed, the working mechanisms of nonlinear propagation in colloidal media are entirely different. Phase-front modulation is expected to arise from diffusive ("slow") nonlinearities as a result of accumulative effects. As a point of reference, let us invoke the numerous recent studies of steady-state, continuous wave (cw) self-channeling (i.e., observation of phenomenologically diffraction-free propagation over several diffraction lengths) in plasmonic soft-matter since utilization of high-repetition rate femtosecond pulses in the same framework has yet to be explored. In those studies, self-channeling has been attributed to two seemingly opposing physical mechanisms; either (i) mass transport induced by gradient optical forces [39, 54-57] or (ii) temperature gradients induced by optical absorption and heating of the solvent [37-39, 58, 59]. A clear demonstration of self-phase modulation arising from mass transport effects in metallic nanoparticle suspensions has not been reported to this day, while experimental evidence and interpretation of self-channeling as a result of thermal lensing, thus, self-collimation of an externally focused beam due to absorption, appears to be more robust.

The work presented in this dissertation aims to:

1. Provide (a) an overview of state-of-the art theoretical background of nonlinearities in plasmonic metamaterials and (b) a compendium of recent experimental advances and theoretical modelling related to nonlinear propagation of laser light in plasmonic nanocomposites within the effective medium approximation.

2. Characterize and gain insights on the Kerr self-focusing nonlinearity of plasmonic nanocolloids in the regime of femtosecond laser filamentation.
3. Explore the utilization of high-repetition rate femtosecond laser pulses (as opposed to cw illumination) for the purpose of laser self-channeling in plasmonic nanocolloids induced by either mass or thermal diffusion effects.

In the remainder of this section, a brief synopsis of each chapter is presented as related to the above problems.

Chapter 2 provides an overview of the theory of self-focusing in transparent materials, which will be later useful for the description of processes involving nonlinear light wave propagation in the case of plasmonic nano-colloids, such as self-trapping, optical collapse, laser filamentation, etc.

Chapter 3 presents the scientific reasoning of this work and general organization of the thesis, indicating the coherence of the presented articles with respect to the research objectives.

Chapter 4 presents a synthesis of most important works in recent literature related to the topic of nonlinear laser light propagation in plasmonic nanocomposites. Even though the theory of nanocomposites constitutes a more general case (including the cases of both colloidal and solid-state matter metamaterials), it is useful to examine since it provides insights on the influence of the dielectric environment on the discussed nonlinearities. Most importantly, the purpose of Chapter 4 is to clarify the fundamentals of optical nonlinearities in bulk metals, metallic nanoparticles and their composites, organise information on recent applications and identify gaps in the existing literature of the field. This Chapter is a paper submitted for publication to *Laser & Photonics Reviews* journal.

Thereafter, the main body of this work is divided into two parts: The first part consists of Chapter 5 and Chapter 6, which deal with the development of a power limiting method in the femtosecond filamentation regime. Chapter 5, published in *Scientific Reports* journal, sets the foundations of the technique in the framework of optical transparency, while Chapter 6, published in *Optics Express* journal, demonstrates the applicability of the method in the presence of nonlinear absorption, for the characterization of the Kerr nonlinearity of gold nanorods.

Chapter 7, published in *Nanophotonics* journal, constitutes the second part of the main body of this work, addressing the case of self-channeling in plasmonic nanocolloids. The main idea is to introduce the use of high repetition femtosecond laser pulses to alleviate accumulative thermal effects and promote self-channeling by means of mass transport, i.e., by induced optical forces acting at the particles.

A general discussion of this dissertation is presented in Chapter 8. Several aspects of self-focusing of femtosecond laser pulses in normal-dispersion and absorptive media are discussed, as related with the development of the proposed characterization technique (presented in Chapter 5 and Chapter 6). Further, Chapter 8 discusses the main conclusions drawn by the work presented in Chapter 7, providing further strategies for the realization of optical force-induced self-channeling effect in plasmonic nano-colloids.

CHAPTER 2 LITERATURE REVIEW ON THE THEORY OF SELF-FOCUSING IN TRANSPARENT MATERIALS

To describe with clarity nonlinear laser light propagation in plasmonic metamaterials, I present in this Chapter several key fundamental concepts of nonlinear optics and of the self-focusing theory for the case of optical transparency, i.e., the electric susceptibility of the propagation medium is considered a *real* quantity (a fair approximation for dielectric materials). The present chapter was compiled by a synthesis of related topics found in the following bibliography [40-42, 53, 60-65], also recommended to the interested reader for further studying.

2.1 Nonlinear wave interactions

Consider the electric field of an electromagnetic wave $\vec{E}(\vec{r},t)$ which is incident to a nonlinear medium. A cardinal principle of the interaction between light and matter is that the dielectric susceptibility of the medium and therefore, its electromagnetic response, is dependent on the strength the external applied electric field $\vec{E}(\vec{r},t)$. Accordingly, under irradiation with intense laser pulses, the response of an optical medium is described by the induced, instantaneous polarization density $\vec{P}(\vec{r},t)$, which can be expressed as

$$\begin{aligned}\vec{P}(\vec{r},t) &= \vec{P}^{(1)}(\vec{r},t) + \vec{P}^{(2)}(\vec{r},t) + \vec{P}^{(3)}(\vec{r},t) + \cdots \\ &= \varepsilon_0\left[\overleftrightarrow{\chi}^{(1)} \cdot \vec{E}(\vec{r},t) + \overleftrightarrow{\chi}^{(2)} \cdot \vec{E}^2(\vec{r},t) + \overleftrightarrow{\chi}^{(3)} \cdot \vec{E}^3(\vec{r},t) + \cdots\right]\end{aligned} \tag{2.1}$$

where $\vec{P}^{(n)}(\vec{r},t)$ denotes the various orders of the induced polarization, ε_0 is the vacuum dielectric permittivity and $\overleftrightarrow{\chi}^{(n)}$ represents the various orders of susceptibility. Even though the optical susceptibilities are in principle represented by a tensor of $(n+1)$ order that depends specifically on the medium atomic or molecular crystal structure, in the case of isotropic and homogeneous materials, there are cases where we can isolate a specific component of the nonlinear susceptibility that contributes in a nonlinear process, and treat it as a scalar. In general, the electric field $\vec{E}(\vec{r},t)$ and induced first order polarization $\vec{P}^{(1)}(\vec{r},t)$ can be represented as the sums of their frequency components ω_m

$$\left\{\vec{E}(\vec{r},t),\vec{P}^{(1)}(\vec{r},t)\right\}=\sum_{m}\left\{\vec{E}_m(\vec{r}),\vec{P}_m^{(1)}(\vec{r})\right\}e^{-i\omega_m t}+c.c.$$
$$=\sum_{m}\frac{1}{2}\left\{\vec{\mathcal{E}}_m,\vec{\mathcal{P}}_m^{(1)}\right\}e^{i(\vec{k}_m\cdot\vec{r}-\omega_m t)}+c.c. \qquad 2.2$$

where $\vec{\mathcal{E}}_m(\vec{r}),\vec{\mathcal{P}}_m^{(1)}$ are the complex amplitudes of the electric field and the induced first order polarization respectively and $\vec{k}_m$ their corresponding wavevectors. For a single monochromatic laser beam, the electric field, and the induced polarization can be viewed as comprised by a single frequency component ω_0, which denotes the optical frequency of the field.

In the generalized case that the susceptibility is treated as a tensor, for materials that are characterized by inversion center symmetry (centrosymmetric media), transformation operations over all the even-order nonlinear susceptibility tensors impose that the only way for the latter to remain unchanged, is to vanish to zero. The odd-order susceptibilities however do not incur this constraint; on the contrary, inversion transformations leave them unchanged. Thus, in the case of centrosymmetric materials, where the second order susceptibility vanishes, the third order one will be the first non-zero nonlinear term in the expansion of polarization described by Equation 2.1. The third order nonlinear polarization is then described by the inner product of the third order susceptibility tensor with all the involved input electric fields in the summation of Equation 2.2. Thus, the third order susceptibility is a 4th rank tensor of $81(=3^4)$ independent components by reason of all the combinations of the different vectoral components (analyzed in a coordinate system, e.g., Cartesian) of the three interacting fields $\vec{E}(\vec{r},t)$ to yield the induced third order polarization $\vec{P}^{(3)}(\vec{r},t)$.

However, due to various inversion symmetries that characterize centrosymmetric isotropic media (liquids, gases, amorphous solids), the number of independent components of the third order susceptibility tensor reduces to only three. The discussion simplifies even further when we consider permutations of the input fields (since the order that the susceptibility tensor acts on the three input fields does not matter if some of them are indistinguishable) and the superposition of input fields travelling parallel to each other, linearly polarized, inducing a nonlinear polarization parallel to

them. In that case we may treat the fields, but most importantly the third order susceptibility, as scalars.

In that framework, let us assume the three fields $\vec{E}(\vec{r},t)$, each of them comprised by different frequencies ω_m, involved in a $\chi^{(3)}$ process in a nonlinear medium. Accordingly, the induced nonlinear polarization $\vec{P}^{(3)}(\vec{r},t)$ will be comprised by a linear combination of terms, each oscillating at a specific frequency that corresponds to a contribution of a resulting combination of the interacting fields of various frequencies as shown in Equation 2.2 since

$$\vec{P}^{(3)}(\vec{r},t)=\varepsilon_0\overleftrightarrow{\chi}^{(3)}\cdot\left[\sum_m\vec{E}_m(\vec{r})e^{-i\omega_m t}+c.c.\right]^3=\frac{\varepsilon_0\overleftrightarrow{\chi}^{(3)}}{8}\cdot\left[\sum_m\vec{\mathcal{E}}_m e^{i(\vec{k}_m\cdot\vec{r}-\omega_m t)}+c.c.\right]^3 \quad 2.3$$

Subsequently, two types of contributions to the nonlinear polarization are revealed. The ones that belong to the first type are characterized by the same wavevector, therefore will be automatically phase matched. Physically, this means that the nonlinear polarization does not lead to energy exchange between the fields. Ultimately, the terms that are automatically phase matched are associated with self-phase or cross-phase modulation of the generated field. The second type of contribution gives rise to a new wave vector, implicating energy exchange between the different fields, or, in other words, phase matching is required. The above becomes clearer by considering the following simple case: a single input monochromatic field is launched into the nonlinear medium, all interacting fields are linearly polarized at the same direction, propagating parallel to each other; thus, we may write in scalar form

$$\begin{aligned}P^{(3)}(z,t)&=\frac{1}{8}\varepsilon_0\chi^{(3)}\left[\mathcal{E}e^{i(k_0z-\omega_0t)}+c.c.\right]^3\\&=\frac{1}{8}\varepsilon_0\chi^{(3)}\left[\mathcal{E}^3e^{i(3k_0z-3\omega_0t)}+3|\mathcal{E}|^2\mathcal{E}e^{i(k_0z-\omega_0t)}+c.c.\right]\\&=\frac{1}{2}\left[\mathcal{P}^{(3)}_{THG}e^{i(3k_0z-3\omega_0t)}+\mathcal{P}^{(3)}_{SPM}e^{i(k_0z-\omega_0t)}+c.c.\right]\\&=P^{(3)}_{THG}(z)e^{-i3\omega_0t}+P^{(3)}_{SPM}(z)e^{-i\omega_0t}+c.c.=P^{(3)}_{THG}(z,t)+P^{(3)}_{SPM}(z,t)\end{aligned} \quad 2.4$$

The expression of the resulting $P^{(3)}(z,t)$ is comprised by two terms, one oscillating at a new frequency $3\omega_0$ [phase matching, and therefore energy exchange between the fields is required, so

that the new wavevector $k_0(3\omega_0)$ satisfies the relation $3k_0(\omega_0) = k_0(3\omega_0)]$ and a second term that oscillates at the fundamental frequency ω_0. In this simple example, the first term corresponds to the effect of third harmonic generation (THG) and the second corresponds to self-phase modulation (SPM) due to refractive index shift in the medium, implicating the manifestation of the self-focusing effect. The latter process is described in the following section.

2.2 Self-focusing and the Nonlinear Schrödinger equation

2.2.1 Stationary Nonlinear Schrödinger equation

2.2.1.1 Derivation

When a linearly polarized electromagnetic wave interacts linearly with a dielectric, the induced electric displacement field D reads (scalar form) $D = \varepsilon_0 E + P^{(1)} = \varepsilon_0\left(1 + \chi^{(1)}\right)E = \varepsilon_0 n_0^2 E$, where n_0 is the linear refractive index of the dielectric. In the case of a SPM process (neglecting THG), the displacement field reads $D = \varepsilon_0 E + P^{(1)} + P_{SPM}^{(3)} = \varepsilon_0\left(1 + \chi^{(1)} + 3\chi^{(3)}|E|^2\right)E = \varepsilon_0 n^2 E$, where $n^2 = n_0^2 + 3\chi^{(3)}|E|^2$, or by series expansion $n \approx n_0 + \frac{3\chi^{(3)}}{2n_0}|E|^2$ when it holds $3\chi^{(3)}|E|^2 \ll n_0$. Physically, our discussion so far assumes $\chi^{(3)}$ related to the distortion of the orbitals of non-resonant bound electrons (arising from interband transitions) in a dielectric. However, it can be generalized for $\chi^{(3)}$ arising from molecular reorientation or electrostriction [61, 64].

Examining Maxwell's equations for the case of light propagation in free space and accounting for the oscillating electric field, the wave equation $\Delta\vec{E}(\vec{r},t) = c^{-2}\partial_{tt}\vec{E}(\vec{r},t)$ is derived. According to the definitions presented in the previous paragraph, one can further derive the linear Helmholtz equation by dropping the time dependence of $\vec{E}(\vec{r},t)$ and retaining only $\vec{E}(\vec{r})$, so that $\Delta\vec{E}(\vec{r}) + k_0^2\vec{E}(\vec{r}) = 0$. For the wavevector in free space, the dispersion relation holds $k_0 \equiv \frac{\omega_0}{c}$.

Assuming propagation along z-axis, we can write $\Delta \equiv \nabla_T^2 + \partial_{zz}^2$ and $k_0^2 = k_\perp^2 + k_z^2$, where ∇_T^2 and $k_\perp$ are the transverse Laplace operator and transverse wavenumber respectively. In the case of paraxial propagation along z axis, it holds that $k_\perp^2 \ll k_z^2$, which also entails $k_z \approx k_0$.

For paraxial propagation in a linear dielectric, it can be shown that Helmholtz equation is identical to the one just presented, with $k_0 \to k = k_0 n_0$. In extent, for a dielectric that responds nonlinearly, it holds $k = k_0 n(|E|^2)$, resulting in the (scalar) nonlinear Helmholtz equation $\Delta E + k_0^2\left(n_0^2 + 3\chi^{(3)}|E|^2\right)E = 0$. Finally, under the paraxial approximation, writing E as a function of the envelope field $E = \frac{1}{2}\mathcal{E}e^{ik_0 z}$, and by substituting to the nonlinear Helmholtz equation, the stationary 2D nonlinear Schrödinger equation (NLSE) is derived:

$$2ik\partial_z \mathcal{E} + \nabla_T^2 \mathcal{E} = -\frac{\omega_0^2}{c^2}\frac{\mathcal{P}_{SPM}^{(3)}}{\varepsilon_0} \qquad 2.5$$

NLSE generally provides a good approximation for the physical interpretation of the effect of self-focusing in the case of cw laser beams, under the assumption of paraxial propagation. Such analyses are described in what follows.

2.2.1.2 Self-trapping

The notion of self-trapping was introduced by Chiao et al. [66]. A physical argument was developed to interpret early experimental observations of damage in fused silica in the form of ~ cm filaments (induced by high power laser radiation), considerably higher than the diffraction limit. Indeed, under a SPM process, it is possible for a laser beam to self-focus in a medium that responds nonlinearly to the incident field, so that the refractive index n changes depending on the magnitude of the product $3\chi^{(3)}|E|^2$. In this context, it was argued in [66] that when an optical beam obtains a critical power, the induced nonlinearity balances the diffraction term of the NLSE. Thus, it was argued the beam is self-trapped and propagates as a soliton wave.

The critical power for self-trapping was estimated by considering that the diffraction angle (derived from Fraunhofer diffraction theory) $\theta_{diff} \approx 1.22\lambda/(2w_0 n_0)$, where λ is the optical wavelength and w_0 denotes the radius of a Top-hat profile distribution, balances out a self-focusing angle θ_{sf}, which "traps" the beam by means of a total internal reflection mechanism (according to Snell`s law). The result of the balance provides an estimate of the critical power for self-trapping $P_{cr} \approx \varepsilon_0 n_0 c\pi\,(1.22\lambda)^2/\left(6\chi^{(3)}\right)$. Although this result was a crude estimation of the critical power for self-focusing (here, for self-trapping), Chiao et al. [66] introduced a radial solitary-wave solution

of the NLSE, where nonlinearity and diffraction balance perfectly each other along propagation. The solution (under cylindrical symmetry governed by r, z coordinates) was given in the form of the function $\mathcal{R}(\sqrt{\omega}r) = \frac{\mathcal{E}(r,z)}{\sqrt{\omega}}e^{-i\omega z}$, which was demonstrated to be the solution of the equation $-\mathcal{R} + r^{-1}\partial_r r\partial_r\mathcal{R} + \mathcal{R}^3 = 0$, known as the Townes profile [60, 64].

An important aspect of the self-trapping soliton of the NLSE is its stability. It turns out the soliton solution of the NLSE is unstable to perturbations, leading to either diffraction or optical collapse (discussed next). Interestingly, by defining the parameter ξ, Equation 2.5 constitutes the so-called critical NLSE ($\xi = 1$), which is determined by the nonlinearity term, when written as $\propto |\mathcal{E}|^{2\xi}\mathcal{E}$. In the case where $\xi < 1$, the NLSE becomes subcritical and is inherently stable, whereas for $\xi > 1$ one deals with the supercritical NLSE (unstable) [64].

2.2.1.3 Optical collapse

The notion of optical collapse following self-focusing was first introduced by Kelley [67]. The author considered the case, where self-focusing in a transparent dielectric overcomes diffraction, and the solution of the NLSE blows up. The characteristic self-focusing length L_{SF} was introduced and estimated for the first time, scaling as $L_{SF} \sim \frac{w_0^2}{\sqrt{P_{in}}}$, where P_{in} denotes the input beam power. Accordingly, the critical power for optical collapse was determined by the condition that $L_{SF} \geq L_d$, where L_d denotes a characteristic diffraction length.

Quite remarkably, both Chiao et al. [66] and Kelley [67] noted that the critical quantity for optical collapse induced by self-focusing is the optical power and not the field intensity as one would intuitively expect. Therefore, application of a powerful lens shall not affect the required amount of optical power to observe collapse, which is because both self focusing and diffraction scale as $\sim w_0^2$.

As explained in ref. [64, 68], in theory, the strict definition of the *critical* power for self-focusing is formed in terms of the Townes profile. The critical power in that case has been calculated numerically by solution of $\int |\mathcal{R}|^2 r dr$, which yields $P_{cr} \equiv P_{cr}^{Townes} = 1.8625\frac{\lambda^2}{4\pi n_0 n_2}$, (where the nonlinear refractive index is defined as $n_2 \equiv \frac{3}{4n_0^2\varepsilon_0 c}\chi^{(3)}$) and sets a "lower bound" of optical collapse. However, for any other profile, optical collapse occurs at a somewhat larger power. The

latter power, according to Fibich [64], sets an "upper bound" for optical collapse and it defines the *threshold* power for self-focusing (or filamentation) for any profile other than the Townes. For example, for Gaussian profiles it has been calculated $P_{th}^{Gaussian} = 1.8962\frac{\lambda^2}{4\pi n_0 n_2}$ [1]. The *threshold* power for self-focusing $P_{th} > P_{cr}^{Townes}$ ("upper bound" value) has also been derived for various input spatial beam profile distributions [68].

2.2.1.4 The aberration-free (or Geometric optics) approximation

To analyze self-focusing, Akhmanov et al. [69] have employed the aberration-free approximation to the NLSE. Specifically, the field envelope was written by use of its eikonal and re-introduced in the NLSE. Thus, the authors significantly reduced the partial differential NLSE problem, to a system of three ordinary differential equations, one of which expresses the evolution of the normalized beam width $\mathcal{L}$ as

$$\mathcal{L}_{zz} = \left(\frac{1}{L_d^2} - \frac{1}{L_{SF}^2}\right)\frac{1}{\mathcal{L}^3}. \qquad 2.6$$

Importantly, within the aberration-free approximation, the value of P_{cr} has been determined by the condition that the optical collapse is self-similar, i.e., the beam profile retains its functional form while spatially becomes narrower [64]. Nonetheless, in truth, this physical picture is exact only for the case of the Townes profile, while any other profile that undergoes self-focusing "re-organises" gradually its functional form to the Townes profile before the optical collapse. The latter statement suggests that there is always a power transfer from the high-intensity collapsing core to the lower-intensity non-collapsing "tail" of the beam during the foresaid re-organization process of a beam profile to the Townes functional [64]. This is exactly the process that establishes the threshold power mentioned in the previous section as the upper bound of optical collapse. Additionally, this

---

[1] Note that this is exactly Equation 5.1 (also in Equation 5.2), in which the notation P_{cr} has been used—due to convention, or, according to [64], confusion in the literature. Technically, the notation P_{th} (*threshold* power*)* should have been used instead since P_{cr} (*critical* power) should correspond solely to the Townes profile.

is the reason why the aberration-free approximation (i.e., self-similar collapse description) leads to overestimation of the threshold power for self-focusing in the case of Gaussian beam profiles.

2.2.2 The Nonlinear Schrödinger equation in the case of ultrashort laser pulses

Starting from Maxwell equations to describe an electromagnetic wave propagating in a dielectric medium that responds nonlinearly, one can derive the following extended NLSE for the case of ultrashort laser pulses [62-64][2]:

$$2ik\partial_z\mathcal{E} + 2k\sum_{n=2}^{\infty}\frac{k_0^{(n)}}{n!}(i\partial_t)^n\,\mathcal{E} + \hat{T}^{-1}\nabla_T^2\mathcal{E} = -\frac{\omega_0^2}{c^2}\hat{T}\frac{\mathcal{P}_{SPM}^{(3)}}{\varepsilon_0} \qquad 2.7$$

where the operator $\hat{T} \equiv 1 + \frac{i}{\omega_0}\partial_t$ and a dispersion term ($k_0^{(n)}$ denotes the n^{th} order dispersion) were introduced. It is evident in this relation that the collapse dynamics differ significantly in the case of self-focusing of femtosecond laser pulses since, as the beam collapses, it undergoes space-time focusing and self-steepening, which is modeled by action of the operator $\hat{T}$ on the diffraction and SPM terms, respectively. These effects become significant typically for fs pulses shorter than 100 fs for propagation of laser light of frequencies in the visible-NIR spectrum in most bulk dielectrics. Evidently, the afore-mentioned result of the critical power for self-focusing, derived in the case of the stationary NLSE, is only used by most authors as a reference for optical collapse, rather as a strict demarcation. A discussion on this aspect is further developed in Sections 5.4.1.4 and 8.1.1.

A remarkable consequence of self-focusing of ultrashort laser pulses in transparent dielectrics is the manifestation of laser filamentation, which is typically accompanied by a broadband supercontinuum generation. Laser filamentation is essentially perceived as a phenomenologically

---

[2] This equation is written in accordance with the Slowly Evolving Wave Approximation, while Equation 5.3 is written in the context of the Minimal Approximation (see ref. [63]). The main differences between the two, is that in the former approximation, (i) a small correction on the dispersion term is neglected (see Generalized Few-cycle Envelope Approximation), and (ii) the self-steepening operator $\hat{T}$ replaces all κ/k operators included in the latter approximation (κ is defined in section 4.6.6), which introduces a slight distortion in the space-time focusing effect.

diffraction-free propagation, along which, a low-density plasma channel is formed. The plasma channel does not reach optical breakdown during the course of the pulse duration since the peak intensity of the pulse ionizes the medium only via a highly-nonlinear multiphoton ionization process, while optical breakdown can only be reached via avalanching (unless very strong external focusing is imposed, or the beam is spatially confined by an interface [41, 70-72]). Evidently, for pulses shorter than 1 ps, there is no sufficient time for avalanching to affect pulse dynamics. However, the low-density plasma induced by multi-photon ionization counter-acts self-focusing, forcing the pulse to undergo focusing-defocusing cycles. Effectively, there is a balanced field intensity that can be reached in the formed plasma channel core, termed clamped intensity, for which the magnitude is determined by the band gap of the dielectric, thus the order of multiphoton absorption [40, 41].

The band gap of a given dielectric, hence the magnitude of intensity clamping, has been shown to affect the extent of the induced supercontinuum [43]. The latter is initiated by the SPM process, introducing a broadening $\delta\omega$ on the frequency bandwidth of the femtosecond pulse. Specifically, the leading and trailing fronts of the pulse acquire redder and bluer frequencies, respectively.

Consequently, in a normally dispersive medium, while the pulse undergoes spatio-temporal self-focusing (various frequency components propagate at different velocities), the pulse splits into two sub-pulses, since redder and bluer frequency components accumulate (due to increasing velocities at these frequencies in view of normal dispersion) toward the leading and trailing fronts. It has been shown by numerical simulations that a steep temporal gradient is formed on the intensity profile of the trailing edge of the trailing sub-pulse, referred to as an “optical shock”, accompanied also by temporal chirp accumulation, while the leading sub-pulse undergoes a significantly less steep “optical shock” on the opposite direction. These effects have been evoked to interpret supercontinuum generation (observed as a typically asymmetrically large broadening of the pulse spectrum at the anti-Stokes wing, as opposed to the Stokes wing), when an ultrashort pulse propagates in transparent dielectrics at the normal dispersion regime. In the anomalous dispersion regime, the pulse is self-compressed rapidly since both trailing bluer frequencies and leading redder frequencies move along the center of the beam during self-focusing. Accordingly, such strong self-compression gives rise to an extremely broad continuum generation, typically observed in the anomalous dispersion regime of various transparent materials [42, 62].

CHAPTER 3 RESEARCH APPROACH AND ORGANIZATION

This chapter describes the research approach, motivation, and reasoning in the process of addressing the problems introduced in Chapter 1. It further presents the organization of the presented herein peer-reviewed articles, or articles submitted in peer-reviewed journals, produced during my candidacy, and establishes a clear link between them.

3.1 Motivation and research approach

Experiments that involve the interaction between femtosecond laser pulses and plasmonic nano-colloids are frequently performed in the laboratory facilities of the Laser Processing and Plasmonics Laboratory (LP^2L) research group. The rather distinct effect of laser filamentation and supercontinuum generation at the output of a sample of plasmonic nanoparticles (through a ~5-10 mm thick cell) is readily attainable when the input power of a single (amplified) femtosecond pulse surpasses the critical power for self-focusing of the solvent of the colloidal solution. Typically, this type of nonlinearity is undesirable in the context of biomedical applications developed by our research group. In fact, assuming that truly self-focusing nonlinearity enhancement is attained within an irradiated tissue area by plasmonic doping, unwanted effects related to laser filamentation might potentially be exacerbated during a laser-induced surgical treatment. Thus, a requirement for a deep understanding of the origins of the effect itself has been a principal trigger, allowing myself to initiate investigation within the general framework and problematic of this work.

There are two major components of the described (in Chapter 1) physical problem, which I closely approached and explored throughout this research project. Firstly, the nonlinear response of a plasmonic nano-colloid to laser illumination (and all accompanying laser operation parameters) since it is the key for interpreting the strength of the interaction and potentially engineer an application. Secondly, the mathematical formulation of self-focusing and the nonlinear propagation equation of the Schrödinger type, tailored appropriately to model the most important physical contributions in the studied problem. Indeed, the latter is a powerful tool for gaining insights on laboratory observations; therefore, for the quantification of measurable nonlinear properties of the examined materials as well.

A plasmonic nano-colloid, namely a colloidal solution of plasmonic nanoparticles, constitutes a metal-dielectric nanocomposite, a metamaterial of artificial (nonlinear) optical properties. Given the complexity of the examined materials, it is required to review first the nonlinear properties of metals, metallic nanoparticles, and metal nanocomposites at various laser excitation timescales. It is indeed extremely important to account for the origins of nonlinear laser-material interaction to assess its strength. For instance, in the present work, interactions of femtosecond laser pulses with plasmonic nano-colloids have been principally explored. Despite the ultrafast transient interaction in the case of a single pulse, femtosecond oscillator systems provide high repetition rate running operation leading to nonlinearities by means of accumulative effects (for example, heating or free carrier generation). Thus, establishing the theoretical foundations of laser-material interaction in a wide temporal (from femtosecond to cw illumination) and spatial (from nanometric objects to effective medium properties) range is needed to assess the means of the experimental approach of nonlinear characterization in the two examined cases of amplified or high repetition rate femtosecond illumination.

In each case, having understood the origins of nonlinear response of plasmonic nano-colloids formulated by effective (macroscopic) medium properties, the mathematical description of laser light propagation was approached through the nonlinear Schrödinger equation. In the case of single pulse transient interaction, one must deal with the problem of femtosecond filamentation. However, the examined materials are semi-transparent in contrast to the extensively studied case of optical transparency. Consequently, the critical power for self-focusing (a key parameter of the present work) must be assessed numerically and only approximated by analytical formulas accounting for the effects of absorption, chromatic dispersion and external focusing on the process. In the case of femtosecond pulses of high repetition rate, the problem of nonlinear propagation can be formulated in the steady state. Nevertheless, attention is required on assessing experimentally the nature of the nonlinearity by dynamic monitoring of the system while it approaches stationarity; both thermal and mass transport effects were considered but also transient effects related to electron dynamics.

In the following section, I will go through the organization of the produced, during my candidacy, research articles as presented in this thesis, conforming to what has been discussed so far.

3.2 Organization and coherence of articles

The thesis is structured in 4 articles, which are presented in the context of the approach described in the previous paragraphs to address the research problematic.

The first article, submitted to *Laser & Photonics Reviews*, is entitled "Nonlinear propagation of laser light in plasmonic nanocomposites" and it constitutes an in-depth critical literature review of this thesis. More specifically, the article covers in detail the most recent developments on the understanding of the nonlinear response of metals, metallic nanoparticles and plasmonic nanocomposites in various temporal regimes. Furthermore, it provides a synthesis of their experimentally determined third-order properties obtained by various standard experimental techniques, among with practical considerations. It subsequently presents computational models used for the theoretical formulation of nonlinear wave propagation in plasmonic nanocomposites, corresponding to applicable concepts. Most recent developments in related applications are concisely summarized, indicating the directions of increasing interest in the field, and outlining shortcomings.

The next two articles deal with the development of a characterization technique, namely, an optical power limiting method, in the femtosecond filamentation regime. Therefore, this part of the thesis is devoted on the use of amplified, single femtosecond pulse nonlinear propagation and interaction with a plasmonic nano-colloid. The studied technique is employed to address the problem of the characterization of ultrafast Kerr nonlinearity of metal nano-colloids by evaluation of the critical power for self-focusing. This is done in two steps: firstly, the applicability of the technique is demonstrated in the case of optical transparency, which is the main subject of the second article of this thesis entitled "Optical power limiter in the femtosecond filamentation regime" published in *Scientific Reports*. Secondly, the developed technique is further employed for the full characterization of a gold nanorod colloid in the filamentation regime, as presented in the third article entitled "Femtosecond nearly resonant self-focusing in gold nanorod colloids" published in *Optics Express*.

Finally, the fourth article entitled "Nonlinear thermal lensing of high repetition rate ultrafast laser light in plasmonic nano-colloids", published in *Nanophotonics,* provides a broad description of the phenomenon of self-focusing and nonlinear propagation through various plasmonic nano-colloids

by use of either femtosecond pulses of high repetition rate or cw illumination. A principal idea this part attempts to explore is whether alleviation of accumulative thermal heating upon laser illumination of the studied samples can be achieved by means of temporal localization between each femtosecond pulse as opposed to cw illumination. Such effect can potentially be advantageous toward the so-called nonlinear self-trapping induced by mass transport effects.

CHAPTER 4 ARTICLE 1: NONLINEAR PROPAGATION OF LASER LIGHT IN PLASMONIC NANOCOMPOSITES

Review article submitted to Laser & Photonics Reviews in 2022.

4.1 Authors and author contributions

Leonidas Agiotis and Michel Meunier. L.A. conducted the literature review, analysed literature data, performed critical and numerical analyses, and wrote the main manuscript. M.M. discussed the work and reviewed/commented the main manuscript.

4.2 Introduction

Nonlinear propagation of laser light in optical media has been a subject of intense research over the past decades. From a fundamental point of view, this type of propagation differs from the linear electromagnetic wave propagation, in the sense that the field amplitude exhibits other than first degree dependence on time and space as it propagates through an optical medium. This arises from the nonlinear response of a medium to a laser's electric field and various accompanying self-action effects, which can be Kerr-type, thermal, orientational, photorefractive, quadratic and others [53, 61, 73, 74]. In this context, significant advancements have emerged in the field of nonlinear optics such as the development of all-optical switching and modulation devices [75, 76], optical limiters [77] and laser mode-locking technologies [78]. In the regime of continuous wave and long-pulsed laser irradiation, the observation of optical solitons, has led to applications such as waveguiding, beam-splitting, frequency conversion and others [74]. In the case of ultrashort pulses, new phenomena have been observed due to the finite time response of plasma formation in an optical medium, giving rise to the effect of femtosecond laser filamentation [40, 41]. The latter has triggered research in accompanying effects such as supercontinuum generation [42], pulse compression [79], parametric processes [80], terahertz generation [81, 82] spectroscopy [83], remote sensing [84] and others.

A cardinal role for the engineering of applications based on the concepts just discussed plays the use of tailored optical materials. The significant progress made over the past decades in the fabrication of such "metamaterials" entails the emergence of unique nonlinear phenomena and

applications [36, 85]. Notably, plasmonic nanocomposites, namely, metallic structures with nanometric sizes embedded in dielectric hosts, constitute such metamaterials due to their ability to confine optical energy in the nanoscale [13]. Indeed, in the context of effective medium approximations, early theoretical studies in plasmonic nanocomposites indicated enhanced nonlinear responses due to confined local fields [4, 6]. Nonetheless, phase switching through such media is limited due to either strong absorption or local-field saturation [1, 36]. Deeper understanding of the time-dependent nonlinear response of bulk metals and plasmonic composites, gained over the past decades, demonstrated that their ultrafast nonlinearities are mainly of thermal origin [8, 9]. Thus, coherent enhancement would be typically attainable in sophisticated nanometric structures and at low excitation regimes [3, 36, 86, 87].

Despite all above limitations, numerous studies still demonstrated the unique potential of engineered nonlinear properties of plasmonic nanocomposites. Several examples constitute the reconfigurable nonlinearities in soft-matter systems due to optical control over particle diffusion [36, 39, 55-57, 88], judicious adjustment of the nonlinear response of plasmonic nanocomposites depending on metallic concentration [35], waveguiding by optical vortices [38, 59, 89], engineered optical limiting [32, 90, 91], ultrafast spectroscopy [49, 51], and laser mode-locking [28, 29, 34].

The primary objective of this work is to provide an overview of the underlying physics of nonlinear propagation of light in plasmonic nanocomposites, within the effective medium description, and present in this context a compendium of relevant recent applications. To that end, in Section 4.3 we introduce related fundamental concepts of linear nano-plasmonic and nonlinear optics. In Section 4.4, we discuss in detail most recent advancements on the understanding of the origins of the nonlinear response of metals and plasmonic nanocomposites on different timescales, from femtosecond pulsed to continuous wave interactions. In Section 4.5, we analyze reported experimental evaluations of nonlinearities of metals and metallic nanocomposites at various timescales and provide a synthesis of recent results and figures of merit. In Section 4.6, we present an overview of most recent numerical models of nonlinear wave propagation in plasmonic nanocomposites in the context of a subset of novel nonlinear processes and proposed applications. The latter are categorized in Section 4.7 according to the interaction timescales of the involved nonlinearities, dictated by the duration of applied pulsed photoexcitation.

4.3 Basic concepts

In this section, we cover the fundamental principles of linear nano-plasmonics, the effective medium approximation and elements of nonlinear optics (the latter, based on a synthesis from several exceptional selected textbooks [53, 61, 65]) that focus on the requirements of the present work.

4.3.1 Linear nano-plasmonics

4.3.1.1 The localized surface plasmon resonance

For the sake of briefly reviewing several fundamental concepts of nano-plasmonics, let us restrict ourselves to a system of a single plasmonic nanoparticle embedded in a dielectric matrix and exposed to an externally applied optical field. Due to the nanometric size d of the particle, an applied optical field of wavelength $\lambda \gg d$, can penetrate the structure and drive an electro-mechanical in nature collective oscillation of the electron gas (i.e., a plasmon) of the nanometric metallic object [13, 92, 93]. This oscillation is bound by the particle's surfaces; thus, a resonance frequency, widely referred to as the localised surface plasmon resonance (SPR) is determined by how the particle's geometry affects the electron gas motion. The term "surface" is used due to the intrinsic difference between this type of resonance and the bulk medium "volume" plasma frequency ω_p. The term "localised" is used to indicate that the surface plasmon oscillation is bound in space by a nanometric-sized object, which in turn is different from "propagating" surface plasmons observed at an interface between a metal and a dielectric.

4.3.1.2 Factors that influence the localised surface plasmon resonance

The existence of surface plasmons depends entirely on the condition that the real part of the dielectric function of the nano-object is negative (case of noble metals). [13, 93]. This condition is related to the opposite sign of the phase of the electronic oscillations across the nanomaterial upon excitation by an incoming optical field. Moreover, plasmon oscillations become pronounced when the imaginary part of the dielectric function of the nano-object is small compared to its real counterpart. This condition ensures slower decay of the mode. The type (order) of excited modes is dictated by the skin depth δ_s, which is relevant to the field's penetration depth and the optical

energy's localization [13]. For example, if we consider a spherical particle, when its size gets smaller than its skin depth (typically 25 nm for noble metals [13]), plasmon oscillations can be treated as a quasi-static problem, hence solution of Laplace's equation suffices for its description [93]. For larger particles electromagnetic retardation must be considered and the Lorenz gauge should be used instead. Gustav Mie has solved this problem analytically by a special technique (for spherical particles) and provided the solution in a set of normal excited plasmon modes [92].

A sufficiently small spherical plasmonic particle can be envisaged as a dipole plasmon mode. At the SPR, the involved electronic transitions match energetically the frequency of an incident field, and energy exchange between the field and the plasmon modes becomes maximum. It follows that the SPR condition necessitates understanding of the involved electronic transitions and the determination of the dielectric function of the metal, over a range of frequencies. Let us assume that the dielectric function of the metal follows Drude's model [93]:

$$\varepsilon_m(\omega) \approx \varepsilon_m^D(\omega) = 1 - \frac{\omega_p^2}{\omega^2 + i\gamma\omega} \qquad 4.1$$

where ω denotes the incident photon radial frequency, ω_p is the plasma frequency and γ is the plasmon damping frequency (discussed in Section 4.4.1.1). In the quasi-static regime and accounting for small $Im\varepsilon_m^D$, one can arrive to an expression for the polarizability in the case of a metallic sphere and find a resonance condition of a dipole plasmon mode to be [92, 93]

$$Re\varepsilon_m^D = -2\varepsilon_d \qquad 4.2$$

where ε_d denotes the dielectric function of the surrounding medium. Assuming that ε_m is described by Drude's model and $\omega \gg \gamma$, resonance occurs at a frequency $\omega_0 = \omega_p/\sqrt{1+2\varepsilon_d}$, where ω_p is the plasma frequency. This result was derived considering the geometry of the nanoparticle (here spherical), the dielectric environment, and the frequency dependent dielectric function of the metal (here it follows Drude's model). Thus, SPR highly depends on these parameters.

As for the dielectric function of metals, an accurate description accounts for interband transitions contribution ε_m^{ib} at high photon energies, which can be added to Equation 4.1. Typically, ε_m^{ib} is calculated by using band structure theoretical models of the studied metal, and then by integration

over all the involved transition dipole matrix elements and probabilities that describe excitations from bound states to quasi-free states due to absorption of a probe beam photon energy [8, 9]. For the case of Au and Ag (and their alloys) simple analytical expressions have been deduced [94] (Figure 4.1).

Conclusively, for a nanometric particle of specific dielectric properties (governed by the material it consists of), the energy of its SPR is configurable depending on the particle's geometry in the presence of an applied field and the influence of the dielectric environment. These effects have established nano-plasmonics as an extremely versatile platform for a broad spectrum of applications in linear optics and disciplines within the domain of nanotechnology [95].

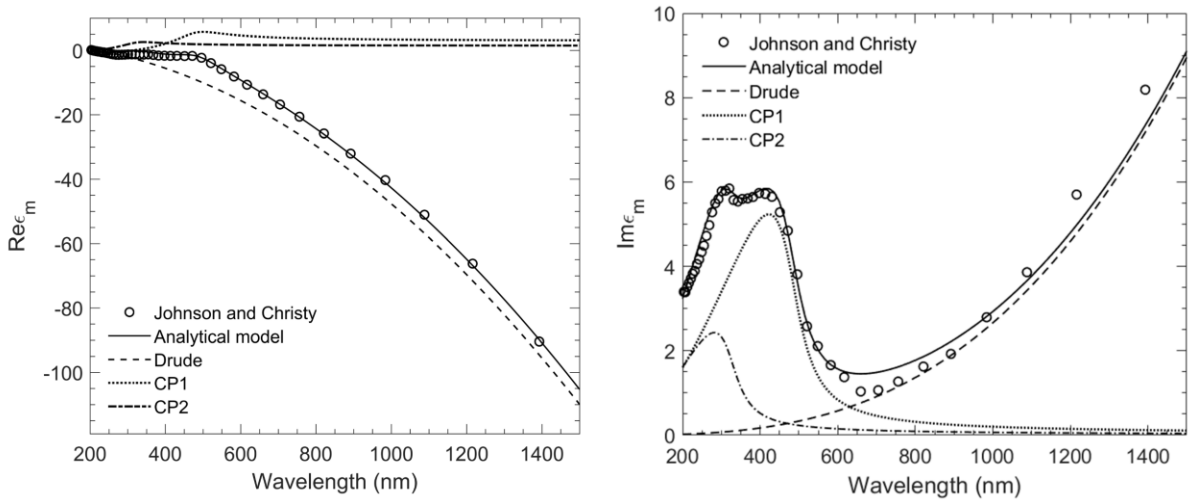

Figure 4.1 The dielectric function of Au. Open circles indicate measured data by Johnson and Christy [96]. The solid curve corresponds to the analytical model described in [94], which is comprised by sum of Drude's model and two interband contributions. The interband contributions are expressed as parametric functions derived from integration over the joint density of states of Au around two different types of critical points CP1 (at X symmetry point) and CP2 (at the L symmetry point) [94].

4.3.1.3 Local Fields

One of the most important consequences of the excited surface plasmon modes at metallic nano-inclusions embedded in a dielectric material, is the localization of optical energy in the vicinity of each nano-inclusion. For a metallic spherical particle, under the influence of an applied field $\vec{E}_0$, the homogeneous local electric field $\vec{E}_1$ inside the particle reads [93, 97]

$$\vec{E}_1 = \frac{3 \quad d}{\varepsilon_m + 2\varepsilon_d}\vec{E}_0 \qquad 4.3$$

a result obtained by classical electrostatics. This simple result indicates the existence of a local field factor $L = \frac{3\varepsilon_d}{\varepsilon_m + 2\varepsilon_d}$, by which, the applied field is enhanced. Minimization of the denominator of this factor occurs at the resonance Equation 4.2, in accordance with what described above. Additionally, the local field outside, in the vicinity of the nanosphere, is enhanced. Importantly, local fields will greatly influence the nonlinear optical properties of the composite material since higher power electric-field interactions will carry the factor *L* to the correspondent power.

4.3.1.4 The effective medium within the Maxwell-Garnett approximation

A nanocomposite material is a heterogeneous medium, meaning, it consists of two different kinds of materials; the first corresponds to a host matrix and the second to nanometric-dimension inclusions [6, 98, 99]. Over the years, several homogenization theories have been implemented to describe effective optical properties, characteristic of the composite [100]. Here, we will focus on nanocomposites consisting of nanostructures of dimensions typically smaller than 100 nm embedded in a dielectric host. Additionally, low volumetric filling factors $f \ll 1$ will be considered. These assumptions allow for the use of Maxwell Garnett's effective medium approximation because of the way the latter is formulated; no time dependence is assigned since the particles bear features smaller than any electromagnetic length scale ($\lesssim \lambda/4$). Further, the considered topologies impose that λ is also larger than the mean distance between particles (Figure 4.2a). Alternative mixing formulas are described in [99], however, they refer to different geometries than the ones described in this work.

Maxwell Garnett's approximation considers a medium where spherical inclusions are randomly distributed in a dielectric host matrix The medium is characterized by an effective dielectric permittivity ε_{eff} calculated by a formula that requires as inputs the dielectric functions of the nano-inclusions ε_m and the host ε_d, and the volumetric filling factor f. Maxwell Garnett's formula is further generalized considering anisotropy. The generalization can be performed by assuming an ensemble of uniformly distributed and similarly oriented ellipoids (particles), and integration over

a region of elliptical shape of same ellipticity. Accounting for a depolarization factor v_p (where $v_p = 1/3$ for spherical symmetry), the generalized Maxwell Garnett's formula reads [100]

$$\varepsilon_{eff} = \varepsilon_d \frac{\varepsilon_d + [v_p(1-f)+f](\varepsilon_m - \varepsilon_d)}{\varepsilon_d + v_p(1-f)(\varepsilon_m - \varepsilon_d)} \qquad 4.4$$

A numerical example is shown in Figure 4.2b. For details on the Maxwell Garnett formula we refer the interested reader to reference [100]. For calculations related to local field factor in composite materials an excellent review is found in [99].

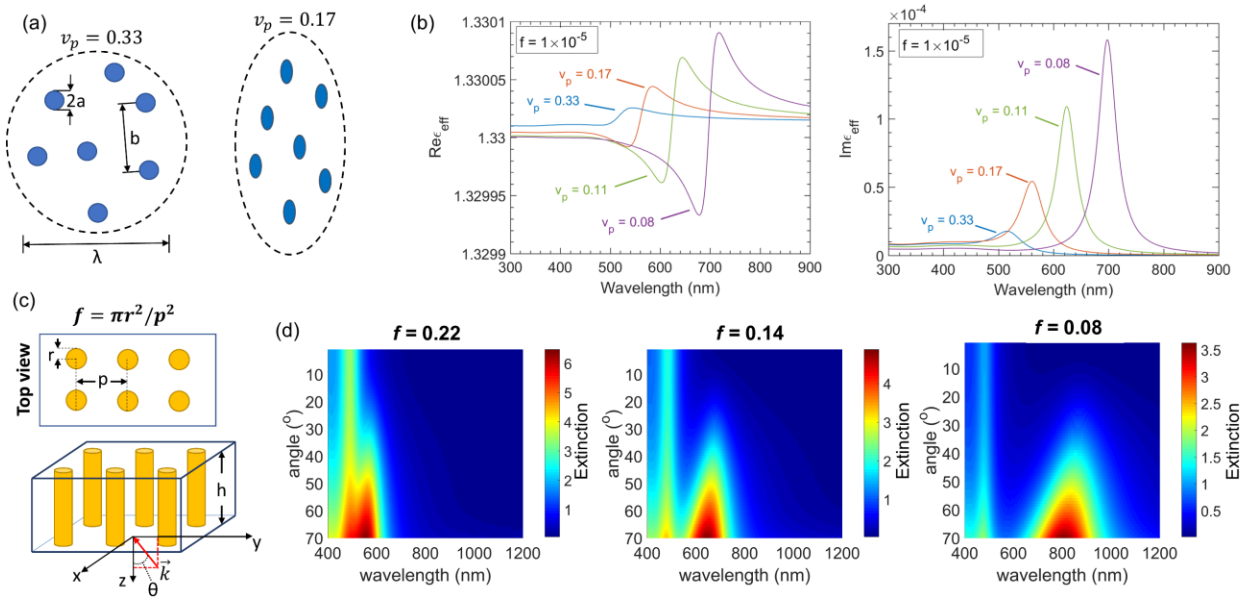

Figure 4.2 (a) Simplified schematics of the topology of the composite material within Maxwell-Garnett's formalism for two different values of depolarization factor v_p. Note that the shape of the integration area (dashed curve) has the same shape as the nanometric inclusions of the composite. (b) Numerical example of the generalized Equation 4.4. An effective medium is assumed to be comprised by Au nanoparticles suspended in water as shown in (a). The analytical formula of Au dielectric function shown in Figure 4.1 was used in the calculations. (c) Schematic representation of an array of vertically aligned Au nanorods, as introduced in [101, 102]. (d) Angular dispersion and volumetric filling factor f dependence of the metamaterial slab of $h = 150$ nm as shown in (c). All calculations have been performed according to formulations and methodologies described in reference [102] .

Notably, the effective permittivity of an array of vertically aligned Au nanorods embedded in a dielectric matrix (Figure 4.2c) has been formulated within the Maxwell Garnett formalism. Such metamaterials possess unique spatial dispersion properties, arising from anisotropy in their

dielectric permittivity dispersion (hyperbolic). Hence, the response of a hyperbolic metamaterial slab (thickness h) depends on the angle Θ that is formed between the $\vec{k}$-vector of an impinging wave and the x-y plane surface of the slab and on the concentration f of the nanorod array, as shown for example in Figure 4.2c, d. In turn, unique nonlinear optical Kerr responses have been engineered with such metamaterials as discussed in [102] and references therein.

4.3.2 Nonlinear propagation and the Kerr nonlinearity in absorbing media

4.3.2.1 Nonlinear wave propagation in absorbing materials

Based on effective medium optical properties, a plasmonic nanocomposite can be viewed as a low-absorption or semi-transparent medium. From Maxwell's equations, we can derive the vectoral wave equation of a light beam (field $\vec{E}$) propagating along z-axis in a nonlinear medium that reads

$$\nabla^2\vec{E} - \nabla\left(\nabla\cdot\vec{E}\right) - \frac{1}{c^2}\frac{\partial^2}{\partial t^2}\vec{E} = \mu_0\frac{\partial^2}{\partial t^2}\vec{P} \tag{4.5}$$

where $\vec{P}$ denotes the induced polarization density, t defines time, c and μ_0 stand for the free-space speed of light and permeability, respectively. In centrosymmetric materials, by neglecting wave-mixing and second-order effects, $\vec{P}$ can be written as the summation of linear and nonlinear polarizations as $\vec{P} = \vec{P}^L + \vec{P}^{NL}$. The corresponding linear part $\vec{P}^L$ and nonlinear part $\vec{P}^{NL}$ describe the response of the material to an electric field $\vec{E}$, as

$$\begin{aligned}\vec{P}^L &= \varepsilon_0\overleftrightarrow{\chi}^{(1)}\cdot\vec{E},\\ \vec{P}^{NL} &= \varepsilon_0\overleftrightarrow{\chi}^{(3)}\cdot\vec{E}\cdot\vec{E}\cdot\vec{E}\end{aligned} \tag{4.6}$$

where ε_0 denotes the free-space permittivity. Let us assume the case of a material irradiated by a single, monochromatic, linearly polarized wave on the x axis. Neglecting harmonic generation and accounting for Equation 4.6, the induced nonlinear polarization is reduced to scalar representation, written (conveniently) in the frequency domain

$$\hat{P}^{NL} = 3\varepsilon_0\chi^{(3)}(\omega)\left|\hat{E}\right|^2\hat{E} \tag{4.7}$$

where $\chi^{(3)}(\omega)$ now denotes the complex tensor component $\chi^{(3)}_{xxxx}(\omega;\omega,\omega,-\omega)$.

Due to bound charges (for example plasmon modes of metallic nano-inclusions) for both linear and nonlinear parts of polarization densities, an additional polarization density current should be accounted for $\vec{J}_b = \frac{\partial}{\partial t}\vec{P}$. Hence, without loss of generality, this term is added in the right hand of Equation 4.5 to account for the imaginary parts of the linear and nonlinear susceptibilities. If ionization occurs in the host, additional free charges J_f should be considered [63].

We can drop the tensor notation for the complex susceptibility under the assumption of medium isotropy and write $\varepsilon(\omega) = 1 + \chi^{(1)}(\omega) = n^2(\omega)$, where $\varepsilon(\omega)$ expresses the relative permittivity of the medium and $n(\omega)$ the refractive index. Equation 4.5 is rewritten in the form

$$\nabla^2\hat{E} - \nabla\left(\nabla\cdot\hat{E}\right) + \frac{\omega^2}{c^2}\varepsilon(\omega)\hat{E} = -\mu_0\left(\omega^2\hat{P}^{NL} + i\omega\hat{J}\right) \tag{4.8}$$

where $\hat{J} = \hat{J}_b + \hat{J}_f$. Assuming paraxiality and propagation within the slowing varying envelope approximation (SVEA), so that $\nabla\left(\nabla\cdot\hat{E}\right) \approx 0$ and $\nabla^2\hat{E} \approx 2ik(\omega)\frac{\partial}{\partial z}\hat{E} + \nabla_T^2\hat{E}$ (∇_T^2 stands for the transverse Laplace operator), Equation 4.8 becomes

$$2ik(\omega)\frac{\partial}{\partial z}\hat{E} + k^2(\omega)\hat{E} + \nabla_T^2\hat{E} = -\frac{\omega^2}{c^2}\frac{\hat{P}^{NL}}{\varepsilon_0} - i\frac{\omega}{c}\frac{\hat{J}}{\varepsilon_0 c} \tag{4.9}$$

known as the Forward Maxwell Equation (FME) [103]. Steady state is assumed when $\vec{P}$ depends weakly on time; this is a good approximation for continuous wave (cw) irradiation where chromatic dispersion becomes negligible [104]. FME is a carrier resolving paraxial equation, being accurate in the cw regime since there is no significant angular spectrum extent from the central frequency.

4.3.2.2 Kerr nonlinearity in absorbing media

Light propagating through plasmonic nanocomposites undergoes both refractive and absorptive nonlinearities. In this section we will first examine each one of these nonlinearities and then discuss their role in Equation 4.8. The effective linear refractive index $n_{0,eff} = \sqrt{\varepsilon_{eff}}$ of the material may undergo shift $\delta n(I)$ depending on the intensity of the input optical field leading to modulation [53]

$$n(I) = n_{0,eff} + \delta n(I) \qquad 4.10$$

In many occasions the intensity dependent shift $\delta n(I)$ is associated with the nonlinear polarization induced by bound electrons, described by $Re\chi_{eff}^{(3)}$. This is the case of the optical Kerr effect. However, modulation $\delta n(I)$ is also associated with diffusive nonlinearities, e.g. thermal (quasi-Kerr effect) [53]. Equation 4.10 is the master equation of the intensity dependent refractive index, implicating the induction of a self-induced lens effect (self-focusing and self-phase modulation) of a laser beam propagating through a nonlinear medium (see for example Figure 4.3a).

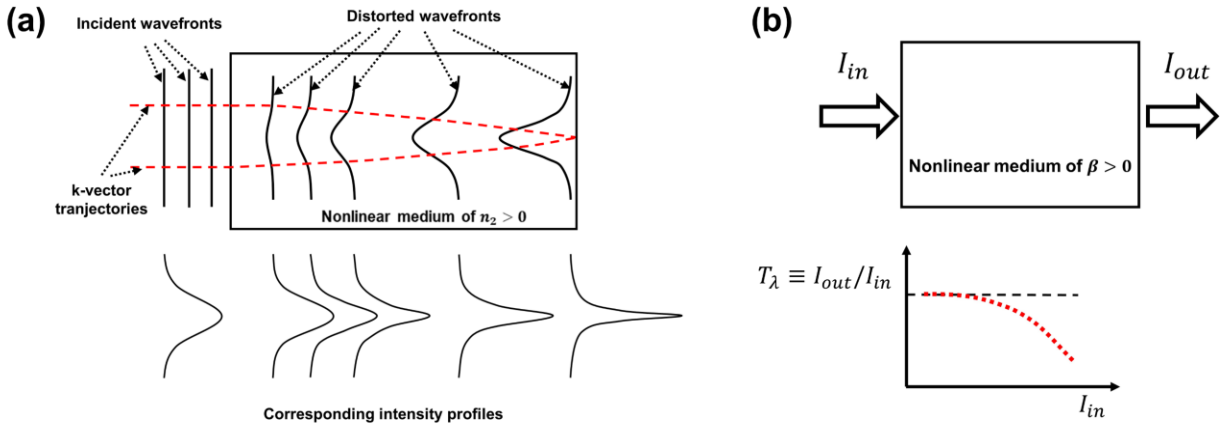

Figure 4.3 (a) Simplified illustration of the effect of a positive Kerr-type nonlinearity (self-focusing). The illustration is shown for a transparent medium for simplicity. The incident wavefront is distorted as the beam propagates through the nonlinear medium due to the intensity dependent phase φ modulation across the Gaussian profile distribution. (b) Optical transmittance of a collimated optical beam propagating through a medium that exhibits nonlinear absorption. A typical curve of the optical transmittance versus the input intensity (red dotted curve) is shown on the bottom figure. The two nonlinearities just described may act concurrently in a plasmonic nanocomposite. Notably, the one influences the other since both effects are intensity dependent.

We shall examine the case of Kerr-type nonlinearities and for convenience, let us assume a monochromatic wave treatment. We first define the electric field $\vec{E}(\vec{r},t)$ of a monochromatic beam propagating along z axis in cylindrical coordinates ($\vec{r}$ is the radial distance from z), the induced nonlinear polarization $\vec{P}^{NL}(\vec{r},t)$ and the induced polarization current $\vec{J}(\vec{r},t)$ in the vector form

$$\{\vec{E}(\vec{r},t), \vec{P}^{NL}(\vec{r},t), \vec{J}(\vec{r},t)\} = \frac{1}{2}\left(\{\mathcal{E}, \mathcal{P}^{NL}, \mathcal{J}\}e^{i[k(\omega_0)z-\omega_0 t]} + c.c.\right)\hat{x} \qquad 4.11$$

Where $k(\omega_0)$ is the wavenumber, carrying information of the optical properties of the propagation medium, ω_0 is the optical frequency of the beam and $\mathcal{E}$ represents the complex amplitude envelope of the field, $\mathcal{P}^{\mathrm{NL}}$ is the complex nonlinear polarization envelope and $\mathcal{J}$ denotes the complex polarization current envelope.

Let us consider only the axial component of Equation 4.8 ($\nabla_T^2 E = 0$) so that $\nabla^2 E \to \frac{d^2}{dz^2}E$, and $\nabla\left(\nabla \cdot \hat{E}\right) \approx 0$. According to the Equation 4.11, Equation 4.8 can be written in the SVEA [65]

$$\frac{d}{dz}\mathcal{E}e^{i[kz-\omega_0 t]} = i\frac{\omega_0^2}{2kc^2}\left\{\frac{3}{4}Re\chi^{(3)}|\mathcal{E}|^2 - i\left(Im\chi^{(1)} + \frac{3}{4}Im\chi^{(3)}|\mathcal{E}|^2\right)\right\}\mathcal{E}e^{i\{(k-k+k)z-\omega_0 t\}} \quad 4.12$$

where we have assumed that all optical properties are considered effective medium properties, $k = \omega_0\sqrt{\varepsilon}/c = \omega_0\sqrt{(1+Re\chi^{(1)})}/c$ is a real quantity and we have included the imaginary part of ε in $\mathcal{J}$ for convenience. Since $\mathcal{E}$ is complex, it can be written in the form $\mathcal{E} = |\mathcal{E}|e^{i\varphi}$, where φ denotes the phase (argument) of $\mathcal{E}$. Therefore Equation 4.12 reads

$$\frac{d}{dz}|\mathcal{E}| + i|\mathcal{E}|\frac{d}{dz}\varphi = i\frac{\omega_0^2}{2kc^2}\left\{\frac{3}{4}Re\chi^{(3)}|\mathcal{E}|^2 - i\left(Im\chi^{(1)} + \frac{3}{4}Im\chi^{(3)}|\mathcal{E}|^2\right)\right\}|\mathcal{E}| \quad 4.13$$

Equation 4.13 can be solved by separating real and imaginary parts, so first we find that the phase φ of the complex amplitude after a propagation length z becomes (Figure 4.3a):

$$\varphi = \frac{\omega_0}{c}\left(n_0 + \frac{3}{8n_0}Re\chi^{(3)}|\mathcal{E}|^2\right)z = \frac{\omega_0}{c}\left(n_0 + \frac{3}{4n_0^2\varepsilon_0 c}Re\chi^{(3)}I\right)z \quad 4.14$$

where the substitution $I = n_0\varepsilon_0 c|\mathcal{E}|^2/2$ was performed. In accordance with Equation 4.10, we find the common definition of the nonlinear refractive index due to bound charges

$$n_2 = \delta n/I = \frac{3}{4n_0^2\varepsilon_0 c}Re\chi^{(3)} \quad 4.15$$

By taking the derivative of the time-averaged intensity $d|\mathcal{E}|/dz = dI/dz \cdot (|\mathcal{E}|/2I)$, the real part of Equation 4.13 gives

$$\frac{dI}{dz} = -\frac{\omega_0}{n_0 c}\left(Im\chi^{(1)} + \frac{3Im\chi^{(3)}I}{2n_0\varepsilon_0 c}\right)I = -(a_0 + \beta I)I \qquad 4.16$$

It follows that the linear absorption coefficient a_0 and the nonlinear absorption coefficient β read

$$a_0 = \frac{\omega_0}{n_0 c} Im\chi^{(1)}, \;\; \beta = \frac{3\omega_0}{2n_0^2\varepsilon_0 c^2} Im\chi^{(3)} \qquad 4.17$$

Thus, we derived the common expressions of Kerr-type nonlinearities $n(I) = n_0 + n_2 I$ and $a(I) = a_0 + \beta I$, where n_0 and a_0 denote linear refractive index and absorption coefficients, respectively.

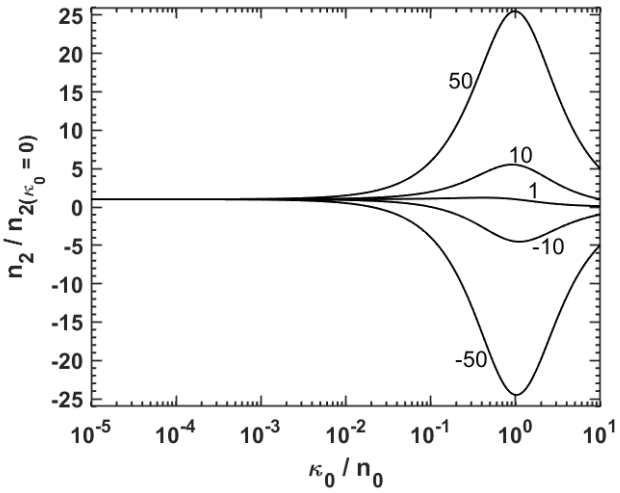

Figure 4.4 Ratio of the exact result of Equation 4.18 over the extensively used Equation 4.15 versus the ratio between linear extinction coefficient over refractive index. Each curve corresponds to varying $Im\chi^{(3)} / Re\chi^{(3)}$ ratios. In the case of plasmonic nanocomposites, at optical frequencies in the visible range and low filling factors (low extinction coefficient), it typically holds $\kappa_0 \ll n_0$, so that the examined n_2 ratio becomes 1, i.e., Equation 4.15 is exact. Produced according to analytical formulas introduced by del Coso and Solis (Ref. [105]).

The simplification that k is a real quantity in an absorptive medium may lead to incorrect description of the wave-propagation equation. Del Coso and Solis have demonstrated that each of the exact expressions of n_2 and β, depend on both $Re\chi^{(3)}$ and $Im\chi^{(3)}$ [105]. Nonetheless, at optical frequencies and for low concentration of metallic inclusions, they can be decoupled with satisfactory accuracy as shown by Equation 4.18. Thus, in the context of wave propagation in plasmonic nanocomposites in the visible-near infrared portion of the electromagnetic spectrum, the nonlinear polarization and density current can be expressed as $\mathcal{P}^{NL} = 2\varepsilon_0 n_0 n_2 I\mathcal{E}$, and $\mathcal{J} =$

$\varepsilon_0 c n_0 a(I)\mathcal{E}$ respectively, where n_2 is here the nonlinear index of refraction of the effective medium, and $a(I)$ is the absorption coefficient of the effective medium. The exact coupling between $Re\chi^{(3)}$ and $Im\chi^{(3)}$ at a wide range of optical frequencies, with the nonlinear index of refraction n_2 and the nonlinear absorption coefficient β reads

$$n_2 = \frac{3}{4\varepsilon_0 c(n_0^2+\kappa_0^2)}\left[Re\chi^{(3)} + \frac{\kappa_0}{n_0} Im\chi^{(3)}\right]$$
$$\beta = \frac{3\pi}{\lambda\varepsilon_0 c(n_0^2+\kappa_0^2)}\left[Im\chi^{(3)} - \frac{\kappa_0}{n_0} Re\chi^{(3)}\right] \quad 4.18$$

Where κ_0 the linear extinction coefficient. Indeed, if $Im\,\chi^{(3)}/Re\chi^{(3)} \sim 1$ then for $f < 10^{-4}$ and at optical frequencies ($\kappa_0 \ll n_0$) it holds $\kappa_0\beta\lambda/(\pi n_0 n_2) \approx \kappa_0 Im\chi^{(3)}/\left(n_0 Re\chi^{(3)}\right) \ll 1$ (Figure 4.4). Hence, under these conditions, one can use Equations 4.15-4.17.

4.4 Nonlinear response of plasmonic nanocomposites

In this section, we will present an overview of recent results on the origins and formulation of the nonlinear response of plasmonic nanocomposites, within the effective medium approximation. Besides the evident influence of field-intensity, we focus on the temporal pulsewidth of the laser source. This is because of the large influence of the laser pulsewidth on the nonlinear response of metallic composites (see Figure 4.5a). In practice, understanding of that influence, is related to the increasing technological interest on the development of photonic devices of ultrafast response.

Section 4.4 is organized as follows: Plasmon dephasing and electron kinetics is discussed in Section 4.4.1. Sections 4.4.2, 4.4.3, deal with the formulation of the electronic nonlinear response of metals, and Section 4.4.4 with the one of the effective medium. In Section 4.4.5, we discuss nonlinear absorption of plasmonic nanocomposites. Section 4.4.6 focuses on the influence of high-order nonlinearities in the effective medium approximation. Finally, Section 4.4.7 is devoted on the formulation of diffusive nonlinear response, of either thermal or mass transport origin.

4.4.1 Interaction timescale considerations and electron kinetics

4.4.1.1 Plasmon dephasing

Under an over-simplified description of a particle-plasmon excitation in the context of a closed two-level atomic approximation, phenomenological non-radiative relaxation lifetimes T_1 and T_2 have been used to express the population relaxation and the coherence dephasing time of the induced polarization, respectively [106]. Following ultrafast laser excitation, localized surface

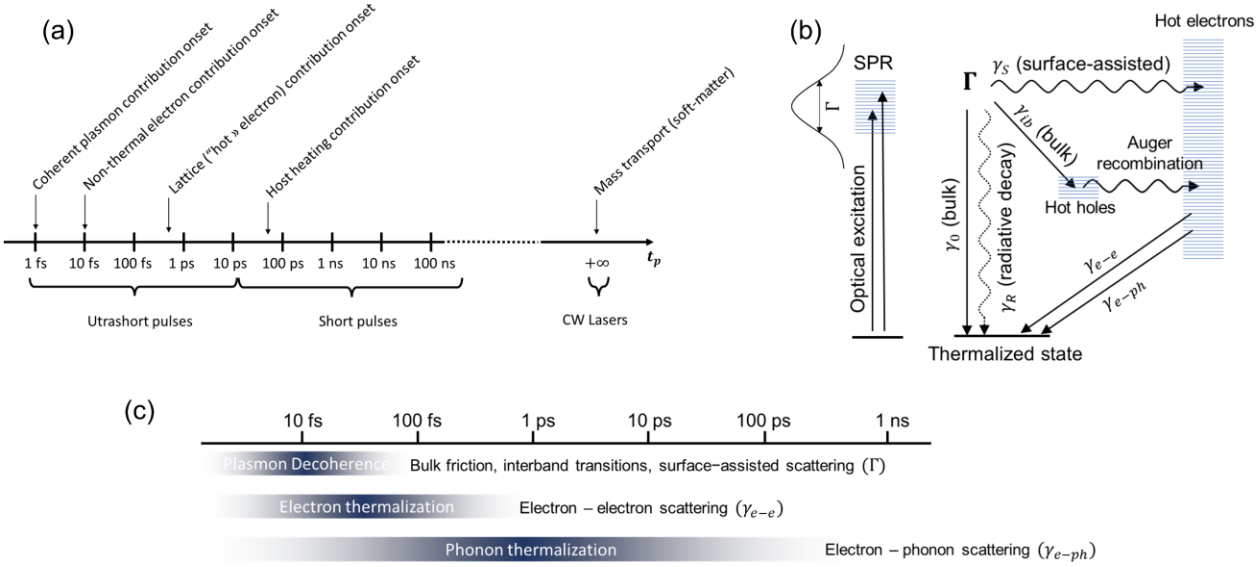

Figure 4.5 (a) Onset of nonlinear contributions depending on the employed laser type interaction with a plasmonic nanocomposite (b) Diagram of the plasmon decay pathways. (c) Representative timescales of excited electron dynamics in a metal or metallic nanoparticle system under ultrashort pulsed excitation.

plasmons typically decay via predominantly non-radiative processes very fast $T_2 = \Gamma^{-1} \sim t_{NR}$<20 fs [106] (Figure 4.5b). The latter is associated with (i) size-independent and inelastic electron-phonon scattering or Umklapp electron-electron scattering, involving intraband transitions within the volume (bulk) of the particle at a rate γ_0 [11], close to the Fermi level, (ii) frequency-dependent, interband electronic transitions within the volume (bulk) of the particle at a rate γ_{ib}, close to the Fermi level [10-12] and (iii) additional scattering at the surfaces γ_S (see next paragraph). Accordingly, it holds $\Gamma = \gamma + \gamma_{ib}$, where $\gamma = \gamma_0 + \gamma_s$ was introduced in Drude's model [Equation 4.1]. Additional relaxation processes occur via radiative decay, having an efficiency that decreases as the particles become smaller [88], in a much longer timescale t_R (~0.1-1 ps), so that $T_2^{-1} =$

$t_{NR}^{-1} + t_R^{-1} \approx t_{NR}^{-1}$. For potential enhancement of ultrafast coherent nonlinear processes in plasmonic systems, the longest possible coherence dephasing time T_2 of the plasmon is a requirement to benefit from the amplified induced polarization discussed earlier.

An open system has been proposed to extend the two-level particle-plasmon decay, via additional non-radiative interactions with the surface of the particle (size-dependent) at a rate γ_s (Figure 4.5b). In other words, in addition to the size-independent processes described in the previous paragraph the plasmon decays and loses its temporal coherence also via collisional interactions with surface defects and impurities into a reservoir of free electron kinetic energy modes and phonon excitations, which slow down relaxation in a much larger timescale [10-12, 88] (Figure 4.5b, c).

Plasmon decoherence timescales may vary dependent on the electronic structure of the metal, and the geometry and chemical environment of a metallic nano-object. Shorter lifetimes occur when the SPR is above the threshold for interband transitions [9]. For this reason, Ag constitutes physically a superior plasmonic material in comparison to Au [13], however, in a Ag cluster (<100 atoms) interband transitions are still possible [107]. In Au nanorods interband transitions are typically far from the energy of the SPR [9] yielding longer phase decoherence [106, 108, 109]. A similar effect has been observed in dendrites [110] and is applicable on the tips of the branches of nanostar geometries, where propagating surface plasmon-polaritons decay. In nanocages or nanoboxes (typically larger than 40 nm) size effects (increased surface scattering) become dominant, resulting in very short decoherence times [88, 111]. Contrarily, in particles smaller than the characteristic length $\frac{v_F}{\omega}$ (typically $< 3\text{nm}$), where v_F is the Fermi velocity, plasmon decays faster into electron-hole pairs and the plasmon quasiparticle becomes indistinguishable from single particle interactions (nonlocality) [13]. In *ab initio* calculations performed in metallic nanoclusters, Ma et al. [107] demonstrated that the two can be distinguished observing that for the plasmon, the amplitudes of the relevant transition coefficients oscillate at the plasmon frequency, whereas for single particle excitation the involved transition coefficient amplitudes vary in frequency. Blocking interband transitions in such systems (for example by alloying with other metals) plasmon decoherence can be temporally extended, ultimately leading (in the ideal case of complete s-p blocking) to Rabi oscillations between plasmon and single particle excitations. The chemical interface also plays an important role on the plasmon decay. Recently, Foerster et al. [112] have

proposed that addition of surface adsorbates induce dipoles inside the metal acting as scattering centers. Further, several studies have shown that in semiconductor-metal interfaces, plasmons may decay directly into interfacial states [113, 114] below the Schottky barrier, yielding generally faster decay times for smaller band-gap interfacial semiconductors [115].

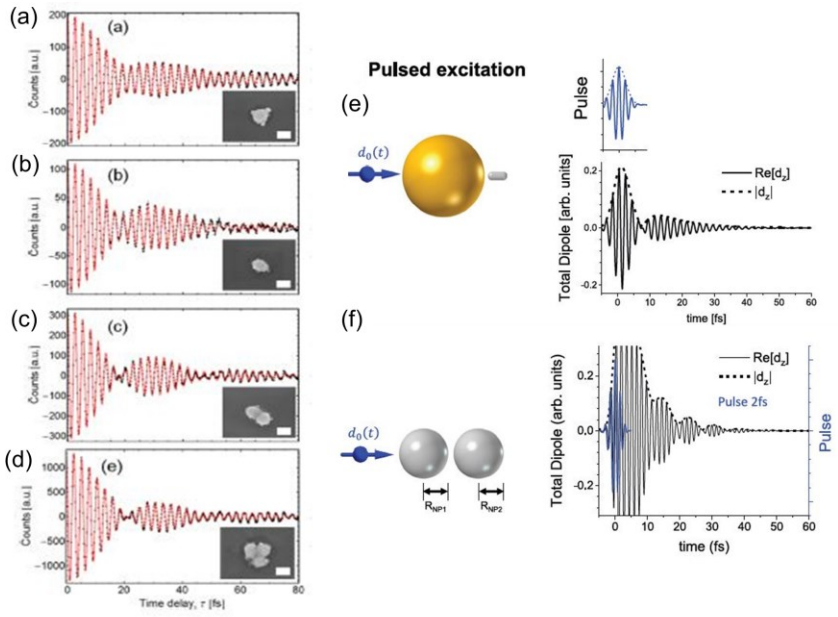

Figure 4.6 Experimentally measured plasmonic decoherence of various aggregations of silver nanoparticles with corresponding SEM images (inset) (a – d). Adapted with permission from [116]. Copyright 2015, American Chemical Society. Theoretical calculations of Fano-type (e) and Rabi-type (f) dimer dynamic decoherence. Adapted under terms of the CC-BY license [117]. Copyright 2020, De Gruyter. Notably, images (a-b) correspond to a system of Ag particles described by a Fano-type interaction, whereas, images (c-d) correspond to a system of Ag particles, which can be described by a Rabi-type interaction.

Recent studies have shown that longer timescales of plasmon decoherence are possible in systems of nanoparticles, such as small agglomerations or dimers. In gold bowtie configuration, Xu et al. [118] have shown dephasing time variations from 7-17 fs depending on the laser polarization. Experiments in small clusters of silver particles have also shown varying plasmon decay rates where the decoherence signal exhibits beatings between two or more frequencies [116] (Figure 4.6a-d). Another recent theoretical study [117] has demonstrated that in dimers decoherence beatings can be observed characterized by a Fano-resonance type (for dimers that consist of two uneven absorption linewidth oscillators) or Rabi-oscillation effects (for dimers that consist of equally narrow absorption lines), as shown in Figure 4.6e-f.

4.4.1.2 Non-thermal (hot) electrons

A photo-excited localized surface plasmon is comprised of two types of electronic excitations: low-energy free carriers (Drude electrons and interband transitions) and high-energy free carriers, due to single-particle electronic excitations (hot electrons) as shown in Figure 4.7a, b [10, 12]. We discussed in the previous paragraphs that the first type is assigned to intraband or interband (if photon energy exceeds the interband threshold) transitions not far above the Fermi level. These carriers are thermalized and their coherent motion in the bulk of the metal decays due to phonon or defect scattering [10, 12]. If interband transitions are present, plasmon decay will be accompanied by excitation of a hot hole population [119, 120] (Figure 4.5b, Figure 4.7b).

The second type of free carriers arises entirely due to surface-assisted optical intraband transitions, which otherwise are forbidden by linear momentum conservation [10, 12, 121]. These transitions are comprised of a significant number of high-energy electrons above the Fermi level, spatially located near the boundaries of a nanoparticle (Figure 4.7a, b). These free carriers are excited concurrently with plasmon decoherence, they are not thermalized and they seek relaxation at somewhat longer timescales [10, 12]. Thermalization occurs principally by electron-electron scattering processes at a rate $\gamma_{e-e} \sim t_{e-e}^{-1}$ (or Auger decay in the presence of hot holes [122]) without significant interaction with the phonons for $t \sim t_{e-e} < 100$ fs [9, 11, 12, 122].

The early dynamics of the non-thermalized distribution function of conduction electrons are described by Boltzmann's transport equation [8, 9, 11, 26, 123]. A source term usually accounts for the laser energy deposition as absorbed by the plasmon, while two collision terms are introduced to represent electron-electron scattering and electron-phonon interaction, the latter being weak for $t < 100$ fs. Other practical models include (i) an extended two-temperature model [12, 124, 125], which considers the energy stored on the non-thermalized electrons and assigns separately temperatures to the thermalized population of conduction electron and phonon sub-systems, and (ii) a revised version of it, a quantum two-temperature model, as presented in reference [12]. First principles calculations have also been recently used [120, 126, 127] to reproduce successfully ultrafast pump-probe measurements [128] of plasmonic nanostructures. An important consequence described by all above models is the ultrafast modulation of the permittivity of metals, which strongly affects the nonlinear response, within timescales as early as < 100 fs.

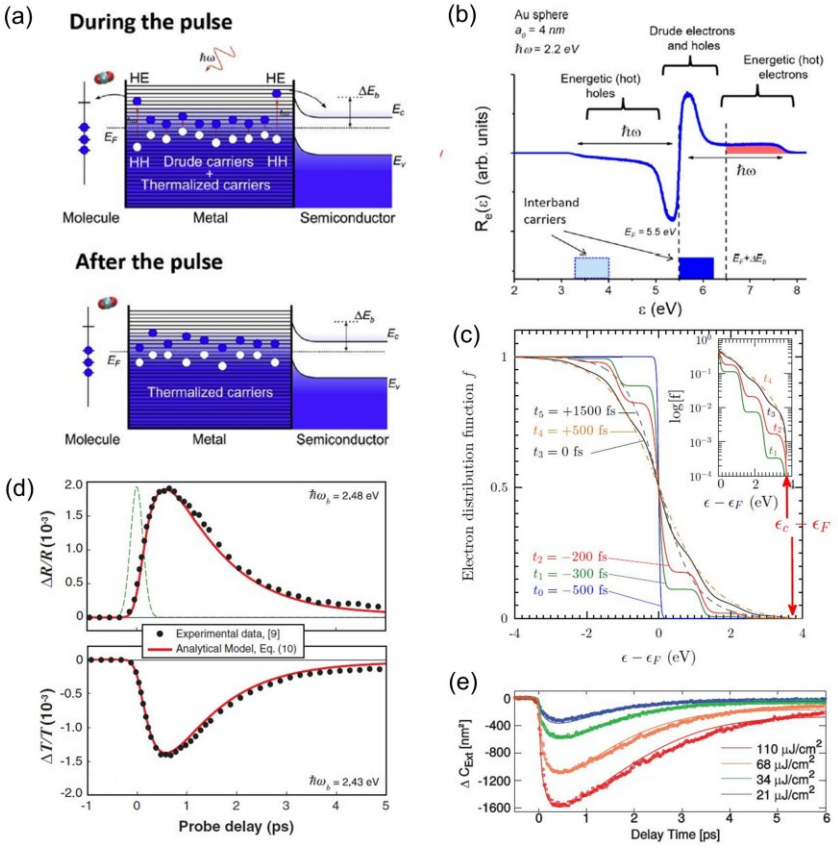

Figure 4.7 (a) Localized non-thermal electron generation near the surfaces of a metallic nanostructure and interactions with a molecule or semiconductor material (host) at the interfaces. Reproduced with permission [10]. Copyright 2019, Elsevier. (b) Electron generation rate at a metallic nanostructure as a function of energy, following a laser pulse interaction. A small yet significant distribution of high energy electrons is produced, by intraband transitions near the Fermi level. Reproduced with permission [12]. Copyright 2017, American Chemical Society. (c) Energy diagram of dynamics of non-thermalized electronic distribution obtained by solution of Boltzmann's transport equation (as described in the text) for the case of irradiation of a gold nanorod by a fs pulse tuned at its longitudinal plasmon resonance. Reproduced with permission [123]. Copyright 2016, American Physical Society. (d) Fitting of theoretical solution of the extended two-temperature model and its fitting to optical transmittance transients obtained by fs pump-probe experiments in Au nanofilms. Reproduced with permission [124]. Copyright 2012, American Physical Society. (e) Ab-initio calculations and their fitting to experimental transients of absorption cross-section obtained by fs pump-probe experiments in colloidal gold nanoparticles. Reproduced with permission by [128]. Copyright 2016, American Physical Society.

Conclusively, the ultrafast generation of surface-induced hot electrons is a deleterious process for plasmon-enhanced coherent nonlinear processes. Thus, there is an interplay between pronounced plasmon response and generation of hot electrons as the size of the particles becomes smaller and energy is confined within the boundaries of a single metallic nanoparticle. Even so, assemblies of

larger particles typically yield higher plasmon quality factors yet facilitate massive hot electron generation within engineered hot spots [119]. Finally, even if plasmon decoherence occurs rapidly, the foresaid ultrafast modulation of the dielectric permittivity of the metal [8, 9, 11, 26, 123, 128], enables engineering of incoherent nonlinear processes, such as Kerr type [3, 8].

4.4.1.3 Electron-lattice coupling

Following electron thermalization into a Fermi-Dirac distribution, energy is transferred to the lattice of the metallic object. The coupling is characterized by a time constant t_{e-ph} (also by the coupling parameter $G_{e-ph} \propto \gamma_{e-ph} \sim t_{e-ph}^{-1}$), evaluated by pump-probe techniques [8, 9, 88]. For instance, for bulk Au and Ag it has been evaluated ~1.15 and 0.85 ps, respectively [8, 9]. For various metals, the dependency of t_{e-ph} on several factors has been the subject of extensive research over the past decades. The electronic structure of the metallic material itself and the electronic temperature has shown to exhibit the most important roles. The dependence of the coupling has been investigated theoretically for the case of various metals, based on first principle calculations [127, 129-131].

In fact, for the case of nanoparticles, spatial confinement is expected to influence t_{e-ph}, due to coupling of electrons with surface phonon modes [88]. Even though this effect has been confirmed in Sb and Cu, in Au and Ag particles, experiments demonstrate constant t_{e-ph}, down to sizes of 10 nm [88], which only exhibit sensitivity to the interband energy threshold in a binary fashion (Figure 4.8b) [132]. Reduction of t_{e-ph} in Au and Ag particles of size below 10 nm (Figure 4.8a) has been assigned to electron spill-out at the surfaces [88] and recently to strong surface dielectric screening [133]. The main reason that t_{e-ph} was observed to be size-independent in Au and Ag was attributed lately to the influence of lattice crystallinity. Indeed, a strong size-dependency in monocrystalline Au nanostructures as opposed to polycrystalline was demonstrated in Ref. [134] (Figure 4.8c). The effect was also demonstrated in earlier studies of epitaxially grown Cu films [135] but also in recent transient absorption studies in Al nanocrystals (Figure 4.8d) [136]. Nano-porosity in Au thin films also highlights the influence of crystal structure in the electron-phonon coupling [137]. Another factor that influences thermal transport dynamics is the environment of the particles, which can be altered by oxidized interfaces [138, 139], surface ligands [133] or even due to solvent's thermal conductivity in soft matter systems [140].

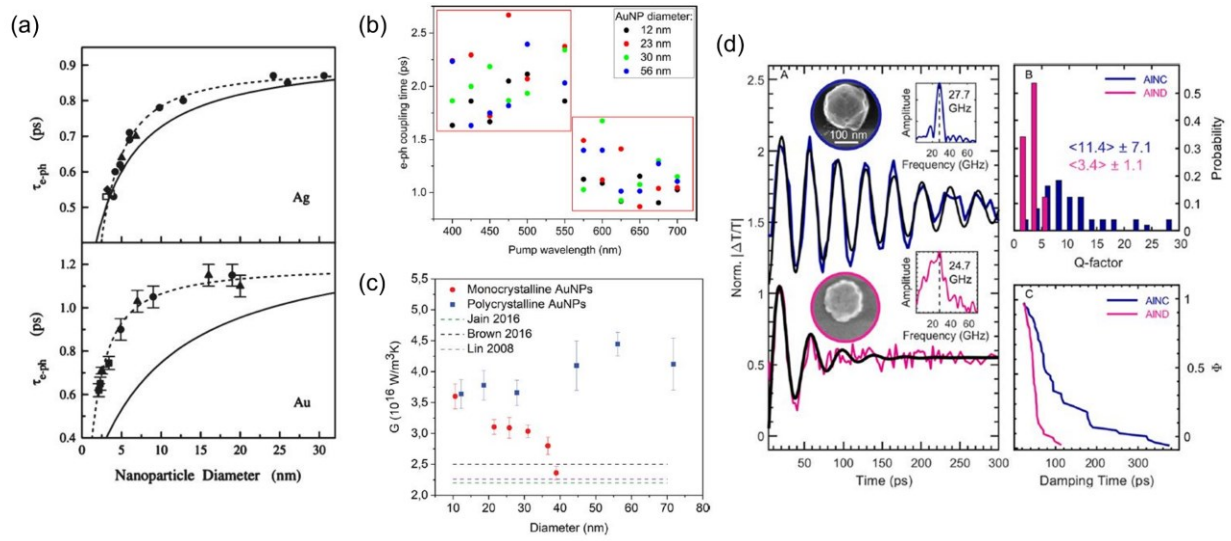

Figure 4.8 Size dependency of electron phonon coupling characteristic time, or constant (G_{e-ph}), in Au and Ag nanoparticles. (a) Reduction of the characteristic time is observed only below a typical size of ~10 nm. Reproduced with permission [141]. Copyright 2003, American Physical Society. (b) Only a binary, size-independent shift is reported in [132] for the case of Au, depending on whether excitation is below or above the interband transition threshold of Au for particles larger than 10 nm. Reproduced with permission. Copyright 2017, American Chemical Society. (c) Electron-phonon coupling is largely influenced by the crystallinity of a Au nanoparticle in conjunction with its size. Reproduced with permission [134]. Copyright 2021, American Chemical Society. (d) The effect of crystallinity in the detection of coherent phononic vibrations and related quality factor in colloidal Al nanocrystals (AlNC) and lithographically fabricated Al nanodisks (AlND) of similar size (~180 nm diameter). Reproduced with permission [136]. Copyright 2020, American Chemical Society.

4.4.1.4 Phonon relaxation and thermal diffusion to the environment

Thermalization of electrons with the phonon sub-system throughout the volume of a nanoparticle occurs typically in several picoseconds [8, 9, 12]. Within this timeframe, the lattice temperature increases to an equilibrium temperature and the particle itself expands. Expansion causes coherent mechanical oscillations of the particles, which can be detected in optical pump-probe measurements because of resulting change of the permittivity of the metal (and therefore, the plasmon resonance) at a certain frequency (corresponding to a vibrational mode) [12, 88, 142]. In turn, such measurements have contributed to the understanding of the mechanical properties of such particles [88] and the development of various applications [143].

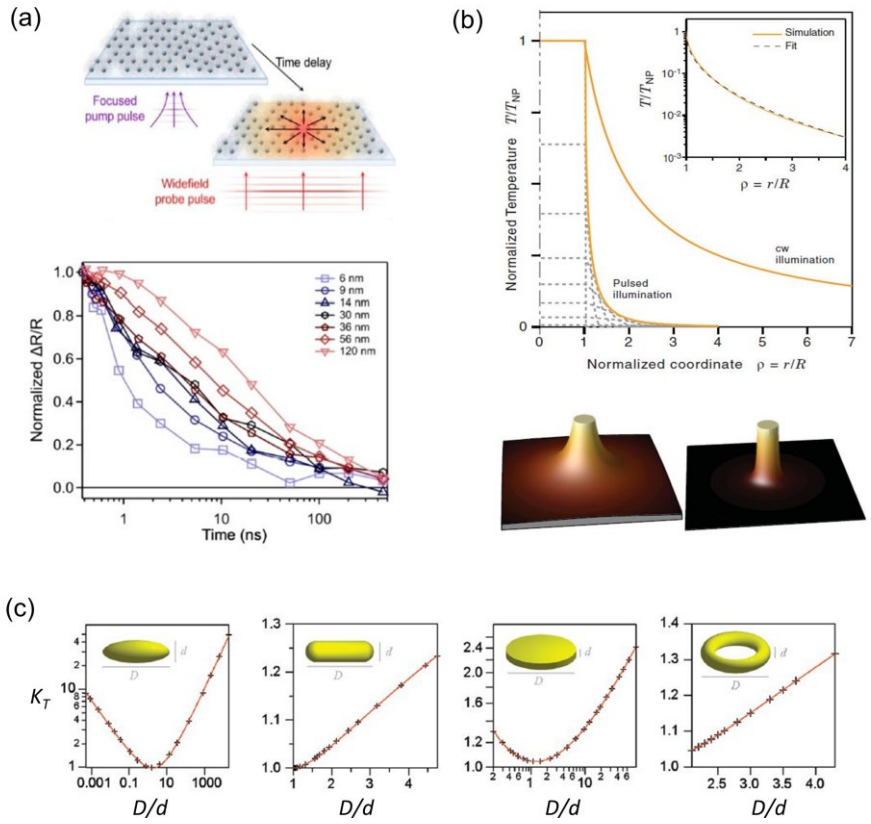

Figure 4.9 (a) Dependency of phonon relaxation and thermal diffusion to the surrounding substrate (glass) on the thickness of thin gold nanoparticle films of varying thicknesses (6-120 nm). Adapted with permission [133]. Copyright 2020, American Chemical Society. (b) Spatial localization of temperature increase in the vicinity of a gold nanoparticle induced by pulsed illumination as opposed to cw. Reproduced with permission [48]. Copyright 2011, American Physical Society. (c). Normalized thermal capacitance K_T dependence on the shape of various geometries of gold nanostructures. Adapted with permission [144]. Copyright 2010, American Chemical Society.

Typically, relaxation of the particle lattice and energy transport to the environment (dielectric matrix) takes place through the particle interface [8, 9]. For very small particles (<10 nm), energy transport may occur directly from interaction of non-thermal electrons with the phonons of the external dielectric matrix itself [8, 9]. For larger nanoparticles (>10 nm) energy exchange between nanoparticle lattice and external dielectric matrix is governed by the thermal resistance of the interface and the diffusion of heat in the surrounding matrix [8, 9]. The timescale of this interaction may vary largely (from 1 ps to 100 ns) because of the multiple interfaces involved (Figure 4.9a) [8, 9, 133] but also due to the dependence of heat flow on the geometry of the particle (Figure 4.9c) [144]. Further, the spatial temperature increase envelope profile, surrounding a nanostructure, is significantly influenced by the timescale of the interaction (Figure 4.9b) [48]. This is because under

very short pulse interaction (up to several ps) energy is deposited and exponentially decays within the nanoparticle before transported to the surrounding matrix. As a result, temperature increase is spatially confined around the irradiated nanostructure compared to a nanosecond pulsed case or continuous wave illumination.

4.4.2 Electronic, coherent nonlinear response of metallic nanoparticles

Although practically not applicable within the framework of modelling of nonlinear propagation and related applications presented in this work (Sections 4.6 and 4.7), the theory presented in this section provides insights on the origins of the coherent nonlinear (third order) response of plasmonic nanoparticles and introduces a clear distinction from the Kerr-type electronic response presented in Section 4.4.3. Notably, there are only a few theoretical works (building on a single, unified quantum theory) relevant to the coherent nonlinear response of metallic nanoparticles, which additionally subject to constraints of spherical geometry and small particle sizes and are based on the perturbative treatment of equation of motion (i.e., weak pump field regimes).

The foundations were introduced by Hache et al. [145] (HRF model) and later, Rautian [146] (HRFR model) further developed the main ideas of the theory by using the correct Hamiltonian. Briefly, the nanoparticle system was treated quantum-mechanically, as a gas of *N* noninteracting electrons within the "particle in a box" model of spherical symmetry. The equation of motion was subsequently solved assuming Fermi statistics for the unperturbed system, expressing the first and third order susceptibilities by nested summation over states. By use of the two-level approximation and assuming that the susceptibilities consist of two contributions (off resonant and resonant), summations could be replaced by integrations leading to the following analytical approximation:

$$\chi_m^{(3)} = \frac{\Gamma_2}{\Gamma_1}\frac{{\alpha_S}^2}{10\pi^3}\left(\frac{d}{l}\right)^2\left(\frac{\lambda_p}{l}\right)^2\left(\frac{\omega_p}{\omega}\right)^2\left[F_3 - i\left(F_3\frac{2\Gamma_2}{\omega} + \frac{\omega^2}{(2\Gamma_2)^2}\left(\frac{2\sqrt{E_F E_g}}{\hbar\omega}\right)^5 g_3\right)\right] \qquad 4.19$$

where, Γ_1 and Γ_2 represent the phenomenological relaxation rate of each level and the coherence rate between two consecutive levels, l is the characteristic atomic scale ($l = V/N$ where V is the volume of the nanoparticle and N is the sum of all the equilibrium-state populations in the particle), a_S is Sommerfeld's constant, λ_p is the wavelength that corresponds to the plasma frequency ω_p,

F_3 and g_3 is a set of dimensionless functions of the order of unity, $\hbar$ is the reduced Planck constant, and E_F and E_g stand for the Fermi energy and the ground state energy respectively.

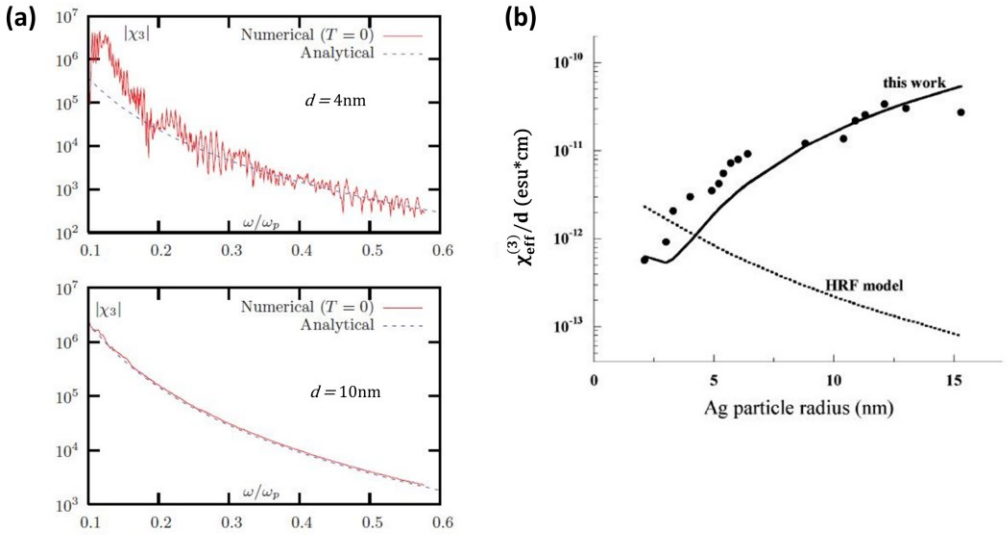

Figure 4.10 Modelling of the intrinsic third order susceptibility of small spherical metallic nanoparticles. (a) Comparison of analytical Equation 4.19 (deduced originally by Rautian) with numerical simulations for two different sizes (here denoted by *d*) of Ag nanoparticles. Adapted with permission [147]. Copyright 2011, American Physical Society. (b) Application of the corrected model of Rautian (HRFR, solid black curve) for small metallic Ag spheres, fitted on experimental data on the effective medium. The dotted lines correspond to the originally proposed formulation developed by Hache et al. [145] (HRF model), which is inversely proportional to nanoparticle size. Adapted with permission [148]. Copyright 2004, American Chemical Society.

Govyadinov et al. [147] expressed the theory in an equivalent form that can be better administrated by numerical calculations, which would be otherwise a rather formidable task in its complex (exact) analytical form. The authors revealed a surprising accuracy and range of applicability of the approximated formulas of HRFR model (see for example Figure 4.10a). They further pointed out several constraints related to its applicability, which include the absence of a clear "bulk" limit and the use of the specific case of $\chi^{(3)}(\omega; -\omega, \omega, \omega)$. Interestingly, in another note, Drachev et al. [148] applied HRFR model to investigate its applicability in a silver nanoparticle nanocomposite's effective $\chi_{eff}^{(3)}$, finding a remarkable accordance between the dependence of $\chi_{eff}^{(3)}/d$ and experimental results found in [149] (Figure 4.10b). Within the same formalism, Drachev et al. [150] interpreted spectra of photoluminescence induced by two-photon transitions in Ag aggregates as a quantum size effect. Numerical calculations for particles with radii up to 30 nm, interpreted

the discrete energy peaks (corresponding to sets of one-photon, two-photon or double (both) resonances), retrieved from experiments [151].

4.4.3 Electronic, incoherent response (Kerr-type)

4.4.3.1 Non-thermal electron contribution

As discussed earlier, the plasmon mode decays very fast (< 20 fs), rendering Equation 4.19 not meaningful beyond the decoherence timescale and within the strong field interaction regime. In fact, the susceptibility of the metal undergoes strong modulation because of the generation of non-thermal free carriers near the surfaces of a particle in a timescale between 10-100 fs. If the incident photon energy does not suffice for the allowance of interband transitions, the foresaid ultrafast modification arises predominantly from electron-electron scattering processes, which results in a broadening of the related rate γ_{e-e} that reads [8, 9, 11, 125, 152, 153]

$$\delta\gamma_{e-e}/\gamma_{e-e} \approx \delta T_e/T_0 \tag{4.20}$$

where δT_e stands for the electron temperature rise and T_0 is their initial temperature. The Drude dielectric function incurs accordingly a modification, (in a timescale < 100fs):

$$\delta\varepsilon_m^D \approx i\delta(Im\varepsilon_m^D) \approx i\frac{\omega_p^2}{\omega^3}\delta\gamma \approx i\frac{\omega_p^2}{\omega^3}\delta\gamma_{e-e} \tag{4.21}$$

To account for interband transitions a contribution $\delta\varepsilon_m^{ib}$ should be computed. In fact, this contribution dominates at lower pump intensities over the intraband (Drude), however the latter becomes important at higher electronic temperatures [8, 9, 11]. Away from the interband transition threshold, typically $\delta\varepsilon_m^{ib}$ is weakly dispersed and its real part prevails over the imaginary part [8, 9] (for example, in Ag or Au nanorods [152, 154]). The interband contribution can be obtained by solution of Boltzmann's transport equation described in Section 4.4.1.2, which yields the distribution function of conduction electrons. Accordingly, the latter is directly associated with modelling of the probability of interband transitions used to evaluate the term ε_m^{ib} so that the ultrafast modulation $\delta\varepsilon_m^{ib}$ contributes (in tandem with $\delta\varepsilon_m^D$) to the nonlinearity in timescales prior to electron thermalization (< 100 fs).

4.4.3.2 Thermalized, "hot" electron contribution (also known as lattice contribution)

Following electron thermalization (> 100 fs), electron-phonon scattering prevails over electron-electron scattering, as energy is transferred to the lattice. The increase of lattice temperature δT_L leads to a modification on the related scattering rate γ_{e-ph}, which in turn affects Equation 4.21 in a longer than 100 fs timescale (while $\gamma_{e-ph} \gg \gamma_{e-e}$) [8, 9, 11, 125]. Another mechanism that is related to δT_L is the modulation of the electronic density affecting mainly the real part of the Drude dielectric permittivity of the metal as [8, 9, 11, 125]

$$\delta(Re\varepsilon_m^D) \approx \frac{\delta\omega_p^2}{\omega} = \frac{\omega_p^2}{\omega} 3\alpha_V \delta T_L \qquad 4.22$$

Where α_V stands for the thermal expansion coefficient of the metal. These mechanisms are typically dominant at higher intensity pumping or away from the interband transition threshold.

At the same time, because of lattice heating at δT_L, the volume of the metal expands so that the Fermi energy undergoes a shift along with the electronic band structures. This modification affects the interband transition threshold $\hbar\omega_{ib}$ and consequently the imaginary part permittivity due to interband transitions according to [8, 9, 11]

$$\delta\left(Im\varepsilon_m^{ib}\right) \cong -\left(\frac{\partial\varepsilon_m^{ib}}{\partial\omega}\right)\left(\frac{\partial\omega_{ib}}{\partial T_L}\right)\delta T_L \qquad 4.23$$

4.4.4 Electronic third order susceptibility of the effective medium

In a plasmonic nanocomposite material the two different constituents possess their own nonlinear susceptibilities. Moreover, the third order susceptibility of metallic nano-inclusions is different compared to the one of the bulk metal, because of their nano-metric dimensions. Essentially, due to finite size effects, the intrinsic $\chi_m^{(3)}$ will be affected by electronic confinement.

An approach, that has been widely used to describe the effective third order nonlinear susceptibility $\chi_{eff}^{(3)}$ in a homogeneous nanocomposite material with inversion symmetry at finite frequencies, was proposed by Stroud and Hui [4]. Under the hypothesis that the applied field frequency is near the

SPR of the nano inclusions, considering a local field factor $L(\vec{r})$, and a volume fraction f of the metallic nano inclusions, the effective third order susceptibility reads

$$\chi_{eff}^{(3)} = f\langle|L(\vec{r})|^2\rangle\langle L^2(\vec{r})\rangle\chi_m^{(3)} \quad 4.24$$

where, the brackets denote average value in the volume of the composite material. In fact, one can exactly evaluate $\chi_{eff}^{(3)}$ near the SPR of the metallic nano inclusions for the special case that they have spherical shape, and their concentration is low.

The discussion presented in Section 4.4.3 suggests that the dielectric function of the metal $\varepsilon_m(I)$ depends strongly on the input intensity *I*, especially for the case of (ultra)short, pulsed illumination. For the case of femtosecond pulses (<500 fs), the dominant contribution is the one ascribed to the generation of nonthermal electrons. For pulses longer than ~500 fs, the lattice contribution becomes dominant. If we account that the absorbed power per unit volume by a single pulse is $p_{abs} = \omega Im\,\varepsilon_m I_1(t)/(n_m\,c)$, where n_m denotes the refractive index of the metal, $I_1(t)$ is the field intensity in the particles, then we can write for spherical nanoparticles

$$p_{abs} = \frac{\omega}{n_m c} Im\varepsilon_m|L|^2 I; \quad L(I) = \frac{3\varepsilon_d}{\varepsilon_m(I) + 2\varepsilon_d} \quad 4.25$$

Accounting for interaction timescale dictated by t_{e-e}, an estimate of the electronic temperature increase after thermalization can be acquired by accounting that $\delta T_e \approx p_{abs} t_{e-e}/C_e$, where C_e denotes the electronic heat capacity. Furthermore, the metal dielectric function modulation is related to the nonlinear polarization induced by bound electrons via $\delta\varepsilon_m \equiv 3\chi_m^{(3)}|E|^2$ (see Equation 4.7), so that locally

$$\chi_m^{(3)} = \frac{2\delta\varepsilon_m n_m \varepsilon_0 c}{3|L[I(t)]|^2 I(t)} \quad 4.26$$

Ultimately, according to the discussion of Section 4.4.3.1 of $\delta\varepsilon_m$ dependency on δT_e and Equation 4.26, it holds for the metal nonlinear susceptibility [124]

$$\chi_m^{(3)} \propto (\partial\delta\varepsilon_m/\partial T_e)\omega\varepsilon_0 Im\varepsilon_m t_{e-e}/C_e \quad 4.27$$

It is noteworthy that Equation 4.24 (combined with Equations 4.25, 4.27) is meaningful only under pulsed illumination, well before heat diffuses in the surrounding matrix (i.e., in a timescale shorter than 1 ns). In the latter case, temperature increase of the dielectric matrix dominates the nonlinear response of the composite material as it will be discussed in Section 4.4.7.1.

4.4.5 Nonlinear absorption of the effective medium

In Section 4.3.2.2, the intensity dependent nonlinear absorption was expressed by Equation 4.16 for Kerr media. Accordingly, dissipative media with nonlinear response are classified in two categories. In the first belong materials with $\beta < 0$, a condition that leads to nonlinear response of a saturable absorber, under the condition $a(I)/a_0 \ll 1$ [97, 155]. The second category is characterized by $\beta > 0$ such that $a(I)/a_0 \gg 1$, classifying such media as optical limiters [97, 155].

4.4.5.1 Saturation of absorption ($\beta < 0$)

Saturation of absorption in a nonlinear medium is a phenomenon during which the transmittance of light, through an absorbing medium, increases with increasing input intensity. The effect can be described in the framework of population redistribution in the ideal case of a two-level atomic system under weak pump excitation [53, 61]. If the population of the ground state is initially N_1 and the one of the excited state is N_2, the system reaches the steady state constant population difference in time with $\delta N^{eq} = N_2 - N_1$. The induced dipole moment of the transition is characterized by $|\mu_{21}|$ and a lifetime T_2 so that the unsaturated linear absorption coefficient a_0 is written as a function of these parameters. Accordingly, solution of the equation of motion (within the perturbative regime) shows that the susceptibility is intensity dependent (saturable) and at the center ω_{21} of the homogeneously broadened linewidth of the transition is written:

$$Im\chi^{(1)} = \left(\frac{a_0}{\omega_{21}}c\right)\frac{1}{1+\frac{I}{I_S}} \qquad 4.28$$

where I_s is termed saturation intensity and can be expressed in terms of the lifetime of the transition and the induced dipole moment.

A plasmon mode, sustained for instance by a small spherical nanoparticle, can be envisaged as an induced dipole moment comprised by a collective of single photon transitions of similar frequency.

Notwithstanding the resemblance to the simple two-level system described by Equation 4.28, the physical picture of transient absorption by a metallic nanocomposite is more complex (accounting for local fields) especially under intense optical pumping. Interestingly, one still encounters the case where transient absorption of the metallic constituents is saturated near the SPR [8, 9, 11]. The effect, however, is a direct consequence of the change in the metal dielectric function and its electronic band structure since the occupation of the electronic states is shifted while a non-thermal free-electron distribution well above the Fermi level is generated. Even after electronic thermalization, electron-phonon collisions or lattice expansion modulate the absorption cross section of the illuminated metallic nanostructures, leading in a transient increase of the effective medium transmittance (as shown for example in Figure 4.11c, e). In other words, under the foresaid regimes, the plasmonic effective medium behaves as a saturable absorber ($\beta < 0$), a property that has attracted increased attention toward the development of optical modulation and laser mode-locking technologies.

4.4.5.2 Nonlinear absorption ($\boldsymbol{\beta > 0}$)

The picture just described is mainly observed for optical pumping located near the SPR. Ultrafast pump-probe experiments over a wide range of optical frequencies have shown that the transient absorption of various plasmonic nanostructures can increase at frequencies away from the SPR (i.e., $\beta > 0$) [21, 156-161]. Nonetheless, even near the SPR, there are conditions where saturable absorption is reversible under intense pumping (typically 10-100 GW/cm^2, 1-10 GW/cm^2 and >1 GW/cm^2 for fs, ps and ns pulses, respectively, depending on the proximity to the SPR among other parameters, see Table A.1, Appendix A). The latter mechanism has been labeled as reverse saturation of absorption (RSA) [32, 33, 162-164]. It is considered to originate from multi-photon processes, photo-injection of electrons, free-carrier absorption (Figure 4.11a), nonlinear scattering or (for colloids) cavitation [32, 97]. It is noteworthy that the opposite effect has been observed in ultrafast (fs) transient transmittance measurements at the wings of the SPR, i.e. it changes sign from negative to positive, at increasing pumping intensities (as shown in Figure 4.11d, f), an effect that has been understood as a broadening of the SPR damping over adjacent optical frequencies as the pumping intensity becomes larger, however, only for intensities <10 GW/cm^2 [21, 158].

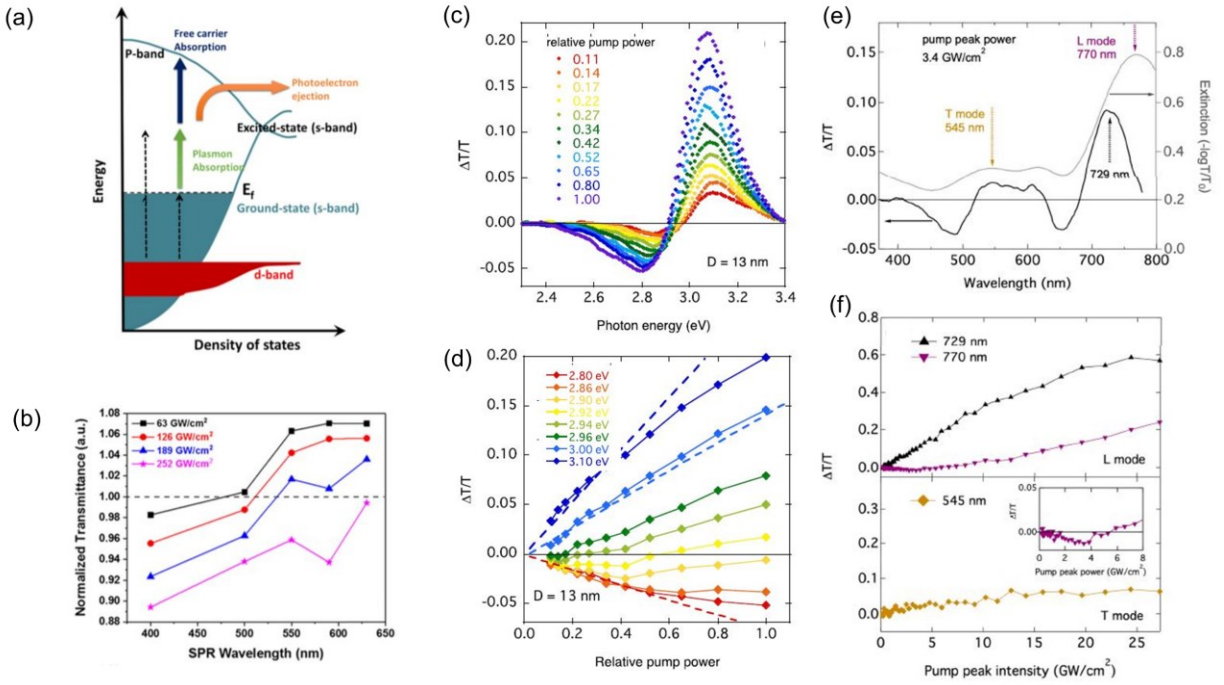

Figure 4.11 (a) Reverse saturation of absorption (RSA) pathways in plasmonic (Ag) hollow nanocubes. (b) As the pumping intensity increases, either multiphoton absorption, free-carrier generation or photoejection of electrons becomes possible, reversing the plasmon bleaching and increasing absorbance (reducing transmittance) due to thermo-modulation of the electronic band structure of the metal. Adapted with permission [32]. Copyright 2020, American Chemical Society. The plasmon band transients and their intensity dependence is shown in (c-f) for Ag nanoparticle (c, d) and Au nanorod (e, f) colloids. It is noteworthy that there are circumstances where the transient transmittance shown in (d) and (f) increases at adjacent frequencies to the plasmon band for increasing pumping intensity due to broadening, which is the inverse picture of the one observed in the RSA case. (c, d) were adapted with permission [158]. Copyright 2015, American Institute of Physics. (e, f) were adapted with permission [21]. Copyright 2019, The Optical Society.

4.4.5.3 Origin of nonlinear absorption

In the case of ultrashort pulse photoexcitation (< 500 fs), the phenomenon of increased transient absorption ($\beta > 0$) has been described as a sequential two-photon absorption. Specifically, in experiments of two-photon induced photoluminescence in Au nanorods, Imura et al. [165] have retrieved spectra indicating two characteristic peaks that correspond to emission stemming from recombination of electrons from the sp bands (near the Fermi level) with holes in the d bands. During photoexcitation, intraband, one-photon transitions near the X and L symmetry points occur in the sp bands, exciting electrons to energies above the Fermi level, leaving back holes in the same band. Subsequently, the initial polarization of electric field having been absorbed, a second,

insensitive to field's polarization transition occurs; a photon is absorbed exciting an electron from the d band to the sp band leaving behind a hole [165] (Figure 4.12a, b). The incoherent nature of two-photon absorption excited photoluminescence in gold nanoparticles has been later confirmed by Jiang et al. [166], and later, dependency of the effect on the shape and crystallinity of the particles rather than the electronic structure of gold was discussed [167, 168] (Figure 4.12c, d, e).

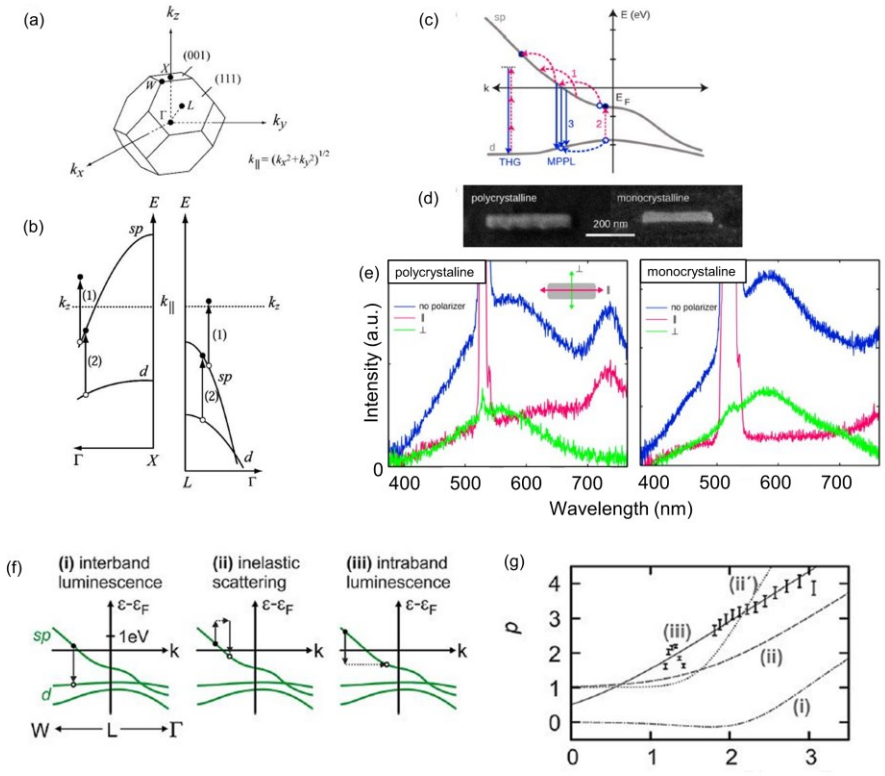

Figure 4.12 Origins of nonlinear absorption in metallic nanoparticles. (a) The first Brillouin zone of Au and the corresponding symmetry points and axes and (b) sequential two-photon absorption initiated by intraband transitions near the X, L symmetry points. Adapted with permission [165]. Copyright 2005, American Physical Society. (c-e) Effect of lattice crystallinity on photoluminescence spectra from gold nanorods. Adapted with permission [168]. Copyright 2014, American Chemical Society. (c) Schematic of how sequential interband transitions result into multiphoton luminescence (filling of hole by interband transition and relaxation of excited state). During third harmonic generation there is no energy exchange with the material, thus, excitation in a real state is not required. (d) SEM images of poly- and monocrystalline gold nanorods and (e) corresponding multiphoton photoluminescence spectra, showing dependency on the crystallinity of the structure for the same material (Au). (f-g) Interpretation of photoluminescence in gold nanorod as radiation from relaxation of the heated electron gas. Adapted with permission [169]. Copyright 2017, American Chemical Society. (f) Mechanisms involved in detection of photoluminescence. (g) Power exponent law fittings of experimental data. Best fitting acquired for intraband luminescence, an indication of relaxation of the thermal electron gas.

The theory just described contradicts with observations by Drachev et al. [148, 150, 151] on the nature of nonlinear absorption, however, the controversy has been reconciled in recent studies. Specifically, coherent two-photon absorption is possible, depending on whether the polarization of the excitation pulse is aligned to the dominant plasmon mode [170], the incident intensity is low [169] and the pulsewidth shorter than plasmon decoherence [171]. Otherwise, broadband emission, typically reported in two-photon absorption photoluminescence experiments, has been assigned to arise from radiative relaxation of the photo-excited hot electron gas (consisting mainly of intraband transitions), observed at high pumping intensities, thus is of thermal nature [169, 172] (see Figure 4.12f, g).

4.4.6 High-order nonlinearities

To account for intrinsic high-order nonlinearities in plasmonic nanocomposites, Reyna et al. introduced a generalized Maxwell Garnett's approximation (quasi-static) for the induced polarization in the effective medium in the presence of an applied field E_0, written in the form $P = P_h + \frac{1}{V_m}\sum_{i=1}^{M} p_i$ [173-175], where P_h is the induced polarization in the host, V_m is the material volume that contains M nanoparticles, and p_i is the induced dipole moment at each one of the nanoparticles. Following that, they expanded the susceptibilities of the particle up to the 7th order with respect to the local field, keeping the nonlinearity of the host up to the 3rd order with respect to the applied field. Later, they performed two separate series expansions in terms of the two different fields to obtain expressions of the susceptibility of the effective medium, due to intrinsic high-order susceptibilities of the inclusions, that finally read

$$\chi_{eff}^{(3)} = fL^2|L|^2\chi_m^{(3)} + \chi_h^{(3)}$$

$$\chi_{eff}^{(5)} = fL^2|L|^4\chi_m^{(5)} - \frac{6}{10}fL^3|L|^4\left[\chi_m^{(3)}\right]^2 - \frac{3}{10}fL|L|^6\left|\chi_m^{(3)}\right|^2 \qquad 4.29$$

$$\chi_{eff}^{(7)} = fL^2|L|^6\chi_m^{(7)} + \frac{12}{35}fL^4|L|^6\left[\chi_m^{(3)}\right]^3 + \frac{3}{35}f|L|^8\left[4|L|^2\chi_m^{(3)} + |L|^2\left(\chi_m^{(3)}\right)^*\right]\left|\chi_m^{(3)}\right|^2$$

The principal physical consequence of these expressions is that $\chi_{eff}^{(3)}$ can be cancelled out by adjusting the filling factor f. Such a process has been named nonlinearity management and its applicability will be discussed in Sections 4.6.2 and 4.7.1.3.

4.4.7 Diffusive nonlinearities

4.4.7.1 Thermal nonlinearity in a plasmonic nanocomposite due to heating of the host

For the cases of cw or long pulsed (~ns) illumination, one ends up heating up the host matrix due to absorption by the nanoparticles. Localized temperature increases and subsequent heat diffusion through interfaces with the host matrix, gives rise to a homogenized temperature δT in the host, *during the course of laser illumination*. Consequently, the laser beam itself undergoes phase modulation as it propagates in the medium due to the nonlinear index shift [39, 176]

$$\delta n = \left(\frac{dn}{dT}\right)\delta T(1-f) \tag{4.30}$$

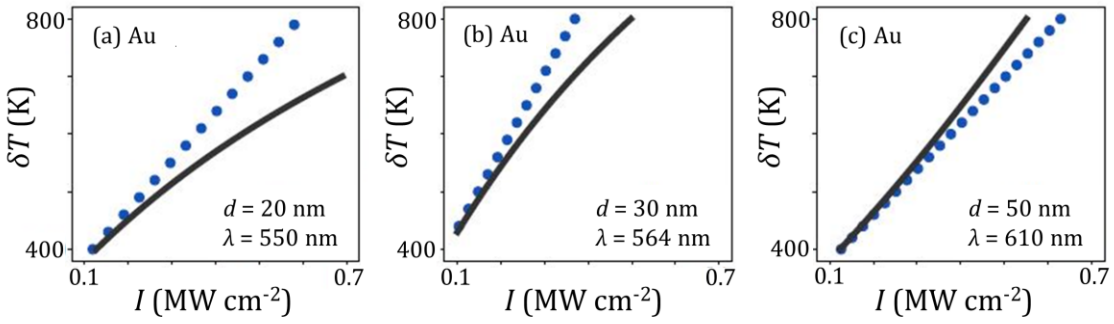

Figure 4.13 Predicted nanoparticle temperature increase versus the input intensity (shown by black solid curves) under cw illumination if thermal conductivity dependence on temperature is considered. The usually employed linear relation (blue dots) is plotted for comparison. Adapted with permission [177]. Copyright 2020, American Physical Society.

where $\left(\frac{dn}{dT}\right)$ denotes the thermo-optic coefficient of the surrounding medium and f the volumetric filling fraction of the nano-inclusions. Interestingly, the same result is observed in quasi-cw illumination induced by accumulation of high repetition rate ultrashort pulses (either fs or ps) [178-180]. The problem of nanoparticle absorption and temperature increase profile has been treated theoretically in references [48, 181]. Recently in references [177, 182], analytical expressions have

been derived related to the temperature increase at the interfaces of plasmonic nanoparticles under cw illumination with emphasis on the temperature dependence of the thermal conductivity of the host (Figure 4.13) and dielectric permittivity of the nanostructure.

4.4.7.2 Nonlinearities induced by mass transport

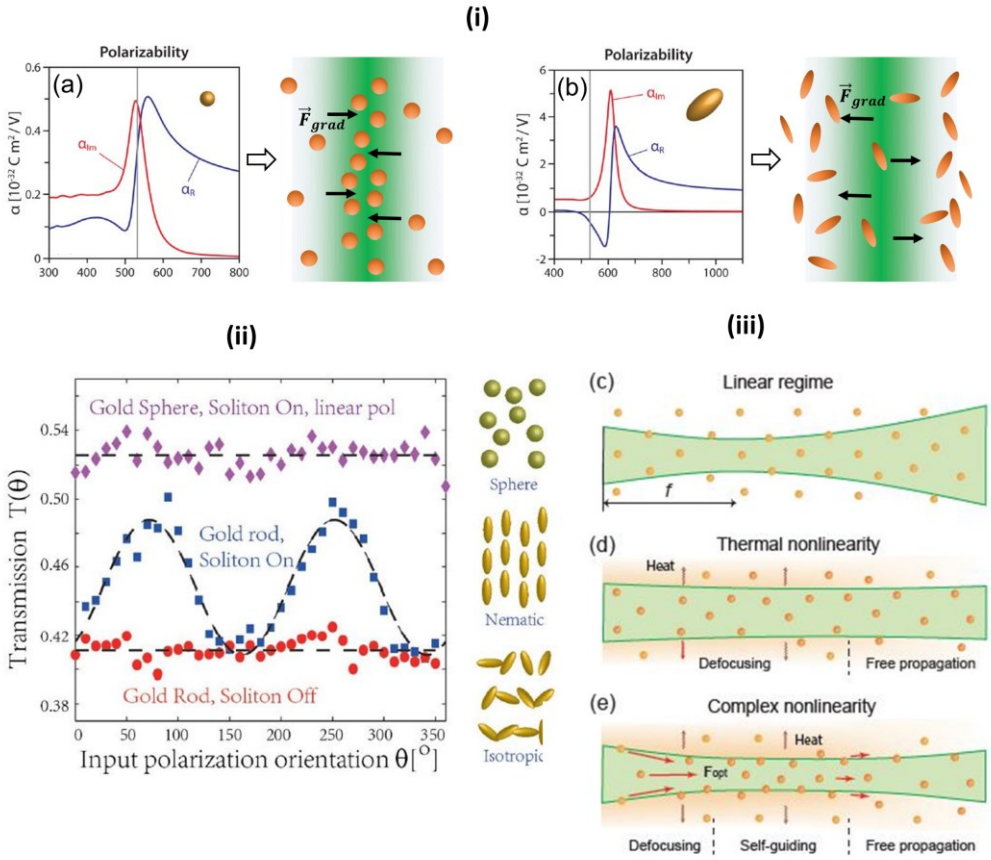

Figure 4.14 (i) Conceptual schematic of mass transport induced nonlinearity and soliton formation in plasmonic colloidal suspensions. Adapted with permission [39]. Copyright 2014, American Chemical Society. In cases (a), (b) nanoparticles of positive or negative polarizability, respectively, are suspended in the solution at the wavelength of the laser beam. As a result, nanoparticles are either attracted toward the beam or repelled away from it, inducing an artificial nonlinear response within the medium due to local modulation of the effective refractive index. (ii) (Top) Conceptual schematic of orientation ordering of suspended nanorods in a colloid along the polarization of a propagating soliton beam when the beam is propagating in the medium. (Bottom) Induced birefringence probed by a coupled beam with the one that orients the particles (see Section 4.7.1.2). Adapted with permission [55]. Copyright 2017, The Optical Society. (iii) Self-confinement and guiding of optical beams due to combined thermal (positive) nonlinearity (absorption of energy by particles and heating of solvent) and concurrent motion of particles due to radiation pressure. Adapted with permission [58]. Copyright 2018, The Optical Society.

In plasmonic soft-matter systems (i.e., colloids), optical forces are exerted on plasmonic nano-inclusions by a cw laser beam, which effectively induces translational or rotational motion of the particles. The exerted forces depend on the sign of the polarizability of the particles, leading to local particle concentration control in the colloid. Such modulation gives always rise to a positive intensity dependent δn of the host. Subcritical or supercritical self-trapping has been shown to be possible for negative or positive particle polarizabilities, respectively [39, 176] (Figure 4.14). The effect becomes appreciable if optical forces are dominant over radiation pressure, or absorption [56]. However, tight focusing conditions are required to limit the foresaid effects [180]. In fact, thermal heating of the nanoparticles may have major influence against mass transport effects, leading to significant modulation of the refractive index of the host and to parasitic convective currents.

4.5 Nonlinear characterization

Several reviews have been published recently with respect to experimental values of nonlinear properties of nanocomposite materials [97, 183-186], mainly involving the three most usual noble metals of choice for plasmonics, namely gold, silver and copper. In this section, we will first briefly discuss the presented results in references [97, 183], which refer to the intrinsic susceptibility of metallic inclusions, to review the influence of the interaction timescale (governed by the radiation pulsewidth) on the nonlinearity. In addition, we will provide a synthesis on recent experimental results with respect to the nonlinear absorption in plasmonic nanocomposites (effective medium) and discuss separately results in the case of high repetition rate femtosecond excitation in conjunction with figures of merit for optical switching.

4.5.1 The intrinsic third-order susceptibility of metallic nanoparticles

Palpant [97] compiled in 2006 a comprehensive review on the third-order nonlinear optical properties of metal nanoparticles near the SPR. In his work, Palpant presented a comparative table of the experimentally obtained intrinsic third-order nonlinear susceptibility $\chi_m^{(3)}$ of Au, Ag, and Cu nanoparticles. The values of the susceptibilities were extracted from the cited therein, measured effective medium susceptibility $\chi_{eff}^{(3)}$, by accounting for the particle volumetric concentration and

local field factors, which implicates appropriate physical assumptions for the examined effective medium. A major impact on the pulsewidth was illustrated in the presented analysis. The same effect was demonstrated in another recent critical analysis by Boyd et al. [183] on the $\chi_m^{(3)}$ value of Au, based on a collection of experimental results. Both analyses showed that the utilization of the experimental technique and laser pulsewidth influence largely the value of $\chi_m^{(3)}$ of noble metals (both bulk and nanoparticle), as shown in Figure 4.15. Importantly, it was illustrated that for experimental measurements performed with pulses < 500 fs, the evaluated $\chi_m^{(3)}$ is in the order of 10^{-10} esu, with pulses 500 fs < t_p < 1 ns, increases in the order of 10^{-9} – 10^{-8}, whereas for pulses > 1 ns, $\chi_m^{(3)}$ can attain values as high as ~ 10^{-6} esu. Recent broadband pump-probe experiments confirm the ultrafast (< 500 fs) $\chi_m^{(3)}$ order-of-magnitude (originating from the non-thermal electron contribution) along with the fact of the significantly different dispersion of $\chi_m^{(3)}$ in the case of nanoparticles as compared to bulk, due to the localized surface plasmon resonance [156, 159].

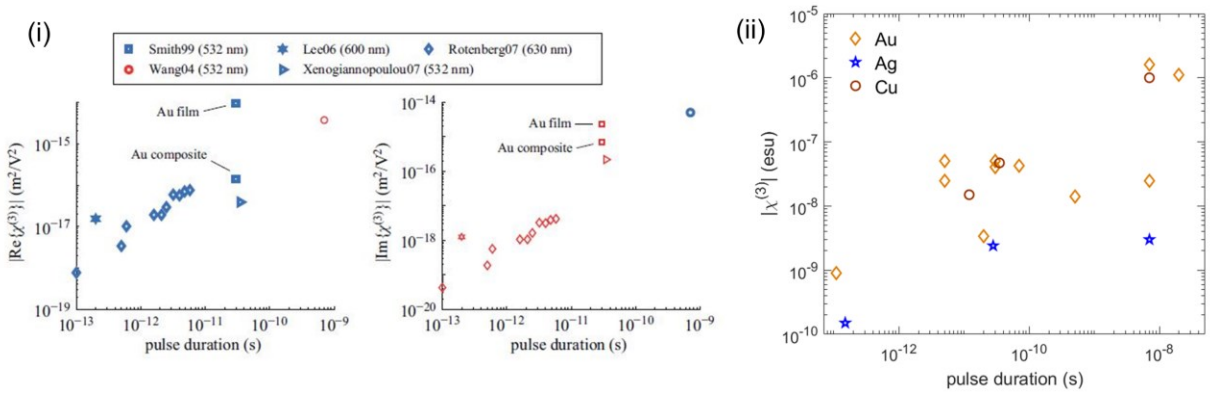

Figure 4.15 Experimental measurements of the dependence of the intrinsic nonlinear susceptibility of metals and metallic nanocomposites on the employed laser pulsewidth. (i) Real and imaginary evaluation of the third order susceptibility of Au. Reproduced with permission [183]. Copyright 2012, Elsevier. (ii) Modulus of the third order susceptibility of Au, Ag and Cu nanoparticles, obtained by experimental measurements in various host materials (matrices), i.e., water, acetone, glass, SiO_2 and Al_2O_3 (not shown in the figure). Produced by data found in Table 1 of Ref. [97] and references therein.

4.5.2 Practical considerations in nonlinear optical characterization

The principal factor affecting the strength of the third-order susceptibility described in the previous paragraph is the temporal dependence of the onset of the various contributing mechanisms of

nonlinearities in metallic composites, i.e., non-thermal electrons, lattice and thermal diffusion in the host contributions, that were discussed in section 4.4 (see also for example Figure 5.6 in ref. [8]). The largest contribution originates from thermal heating of the host induced by short pulses (ns or higher), cw illumination or even high-repetition rate (MHz) ultrashort pulses (fs or ps), during which, heating of electron and phonon subsystems of nanoparticle and host are in thermal equilibrium. Accordingly, since the response of each contribution has a temporal onset, the evaluation of nonlinear properties of metal nanocomposites by techniques such as the z-scan, optical limiting, optical phase conjugation, self-diffraction and others is governed by the laser pulsewidth. Techniques related to nonlinear induced birefringence, e.g., optical Kerr gate or ellipse rotation are not influenced by heating of the host material presumably because they depend on the nonlinear polarization induced along various components of $\chi_{eff}^{(3)}$; contrarily, temperature gradients are developed uniformly within the irradiated volume of thermally isotropic media. This is a typical situation of differences observed for instance between z-scan and optical Kerr gate measurements when MHz ultrashort pulses are employed [187, 188]. Finally, sensitive techniques that are based on coherent nonlinear effects (e.g., harmonic generation or wave-mixing [86, 87, 189]) typically yield smaller values since they originate from ultrafast electronic polarization effects, which in turn are related to plasmon decoherence in metallic nanoparticle composites.

4.5.3 Experimental results from selected studies

In this section, we present an analysis of selected recent experimental results on the nonlinear optical properties of plasmonic nanocomposites, oriented on properties of the effective medium. The summarized results are obtained from studies where the z-scan and optical limiting techniques were employed and are categorized into three groups presented in Table A.1, Table A.2 and Table A.3 (Appendix A). The first group involves the effect of reverse saturation of absorption (RSA), the second group touches the effect of optical limiting (OL) and the third one focuses on saturable absorption (SA).

For femtosecond and picosecond pulses, RSA or OL is typically governed by competition of free-carrier absorption or multiphoton (two-step) absorption against plasmon saturation at high pump intensities (higher than ~ 10 GW/cm^2), since photoexcited conduction electrons relax at a timescale as large as ~ 100 ps [190, 191]. The field-enhancement of the particles and scattering properties

are expected to be affected accordingly. In the nanosecond scale, an onset of nonlinear scattering due to thermodynamic phase transition of the host medium at the interface with the particle has been observed to occur within ~ 0.5 ns [192], which adds an additional nonlinear extinction contribution for the observation of RSA and OL effects. Cavitation bubbles (colloids) or vaporization are likely to occur at elevated fluencies depending on the SPR position, the size and morphology of particles, and the nature of the host. The onset fluence for the observation of cavitation bubbles, is significantly higher for particles smaller than 30 nm ($\gtrsim$ 1000 mJ/cm^2) compared to larger particles (e.g., for 100 nm particles ~ 10 - 100 mJ/cm^2 may suffice) [192, 193].

Notably, several recent studies presented in Table A.1, Table A.2, Table A.3 have demonstrated switching from OL behaviour to enhanced RSA behaviour or enhanced OL by addition of metallic nanoparticles to functionalized graphene dispersions [90, 91, 194-197]. Briefly, in the interface between graphene and metal particles Fermi level is equated between the two materials. Graphene provides thus free carriers to the conduction band of the metal so that relaxation obtains longer lifetimes, resulting to enhanced nonlinear absorption properties of the composite material.

Even though it is a common practice to deduce the value of nonlinear absorption coefficient β of the material, the figure of merit β/α_0 is more meaningful for comparison of the effects of RSA and OL at different timescales. Table A.1 and Table A.2 show that for fs pulses, β/α_0 is in the order of 10^{-2} - 10^{-3} cm^2/GW, for ps pulses it increases in the order of 1 cm^2/GW and for ns pulses it takes values of tens of cm^2/GW. This result illustrates the influence of the underlying temporal onset of all the described participating mechanisms of RSA and OL. In the case of SA, Table A.1 and Table A.3 show that the saturation intensity for fs pulses is in the order of 10 GW/cm^2, for ps pulses is typically a few GW/cm^2 and for ns pulses below 1 GW/cm^2.

For optical modulation and switching devices based on self-phase modulation effect, the figure of merit $W = n_2 I_s/(a_0\lambda)$ is of particular interest. In saturable media, where $\beta \cong -a_0/I_s$, $W > 1$ ensures 180^o phase change of the field over a distance smaller than the absorption length, a desirable property for optical switching devices [14]. Table A.1 shows that there are only a few occasions where W approaches values close or above 1, typically for ns pulses. In fact, relatively high intensities were applied since the z-scan technique was employed. Nonetheless, in recent studies based on the nonlinearity management procedure, conditions of $W > 1$ have been

demonstrated by concentration adjustments in Ag colloids [175]. Moreover, large W values have been reported in studies of high-repetition rate ultrafast laser excitation [187, 188, 198-200]. The involved time response for optical switching in these measurements is however typically larger than thermal diffusion characteristic times and therefore cannot be considered as ultrafast. Finally, in the case of optical switching devices based on SA, plasmonic nanocomposites are still particularly attractive for ultrafast switching in view of the electronic origin of the effect.

4.6 Modelling of nonlinear wave propagation in plasmonic nanocomposites

Equations 4.8-4.9 are the master equations to describe nonlinear wave propagation through an optical medium. In accordance with appropriate and well-justified physical considerations, they can serve as a template for the study of nonlinear phenomena arising in plasmonic nanocomposites. We examine below several recently studied cases of technological interest.

4.6.1 Self-trapping and guiding in soft matter systems due to particle diffusion

In the steady state (cw illumination), the influence of chromatic dispersion on beam propagation is negligible. However, the dispersion term in Equation 4.9, related to the refractive index of the medium, may depend on other parameters [39, 176]. In a nanoparticle suspension, radiation-induced local changes of particle concentration or temperature give rise to intensity dependent refractive index. The first case involves a nonlinearity that depends implicitly on the intensity; electric field gradients exert forces on the particles due to their high polarizabilities a_R. Such forces can be either attracting or repelling, changing locally particle concentration and effective refractive index. The implicit dependency of filling factor f on the intensity was introduced via solution of Smoluchowski equation in the steady state in [176]. Starting from Equation 4.9, a propagation equation for the complex amplitude $\mathcal{E}$ can be written in the time domain [39, 176]

$$i\frac{\partial}{\partial z}\mathcal{E} + k_0(n_m - n_d)V\rho(I)\mathcal{E} + \frac{1}{2k_0 n_0}\nabla_T^2\mathcal{E} = -i\frac{\sigma\rho(I)\mathcal{E}}{2}$$
$$\rho(I) = \rho_0 e^{a_R I/(4k_B T)} \qquad 4.31$$

Where n_m and n_d denote the refractive index of the particles and the surrounding medium, respectively, V is the particle volume, ρ_0 is the unperturbed uniform particle density, σ is the particle absorption cross section, a_R is the particle polarizability and $k_B T$ is the thermal energy.

4.6.2 Nonlinear processes due to management of high-order nonlinearities

Reyna et al. [173, 174] have demonstrated that plasmonic nanocomposites accommodate a nonlinearity management procedure, which means that their nonlinear response can be altered upon concentration adjustments of the volume of nano-inclusions within the volume of the composite material. Their work was focused on the impact of nonlinearity management of high-order nonlinearities in silver nanocolloids on several nonlinear processes, including spatial self-phase or cross-phase modulation [173, 174, 201], optical switching [175], soliton formation and waveguiding [89] and nonlinear birefringence [202]. Equation 4.29 was employed to model nonlinear processes of self-phase or cross-phase spatial modulation in silver nanocolloids that exhibit high-order nonlinear polarization described by the effective susceptibility of Equation 4.29. Chromatic dispersion effects have been ignored in view of picosecond pulsed illumination. Further, both real and imaginary parts of the effective susceptibility can be included in the nonlinear polarization term of Equation 4.8 to account for the nonlinear response of silver nanocolloids described by Equation 4.29. In addition, Reyna et al. [202] have modelled the induced nonlinear birefringence, when a laser field of varying linear polarization, was propagated in a capillary of linear birefringence that was filled with a carbon disulfide suspension of silver nanoparticles. Nonlinear birefringence can be understood as a cross-phase modulation process between two orthogonal components of a laser field in a birefringent fiber optic. In their model Reyna et al. have adopted the formulation of nonlinear birefringence induction presented in [203]. The model ignores diffraction and considers dispersion of second order, and nonlinear polarization (up to fifth order) response of the silver nanocolloids of varying concentration.

4.6.3 Phenomenological self-trapping due to thermal lensing

The effect of nonlinear thermal lensing has been observed since the early days of self-focusing. A nonlinear self-collimation effect has been reported by Askaryan [204], in experiments of nonlinear defocusing of an externally focused beam in a nonlinear medium due to thermal lensing. A similar

effect has been reported in recent studies in plasmonic nanocolloids [37, 38, 58, 180] at very low input powers (tens of mW) under nearly resonant illumination with the SPR. Agiotis and Meunier [180] recently used in this context a steady-state nonlinear propagation equation model to formulate and describe thermal lensing in plasmonic nano-colloids, which reads:

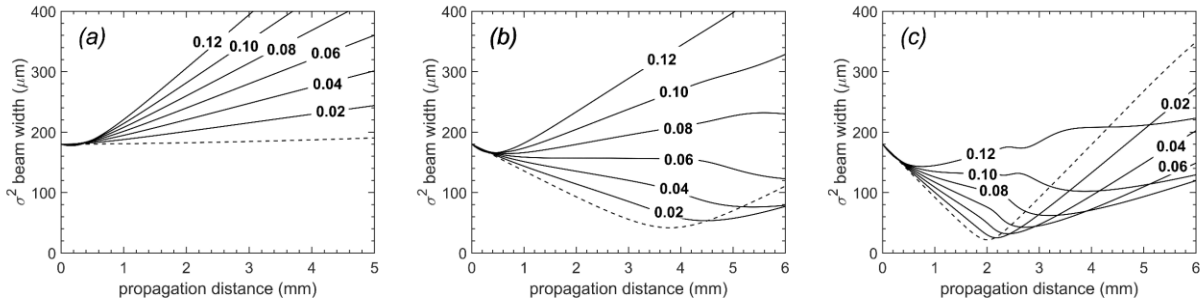

Figure 4.16 Numerical example of the effect of external focusing on the thermal lensing effect. The σ^2 beam width has been evaluated by solution of Equation 3.4.32, considering propagation in a plasmonic aqueous (water) suspension of nanoparticles (e.g., Au nanospheres of $d \sim 10$ - 50 nm) of absorption coefficient $a_0 = 2$ cm^{-1} (depending on size and concentration), thermo-optic coefficient $dn/dT = 10^{-4}$ K^{-1}, thermal conductivity $K_T = 0.6$ W/(Km) and linear refractive index $n_0 = 1.33$. The illumination wavelength has been assumed to be $\lambda = 800$ nm. The input power is shown over each solid-line curve in Watts. Dashed lines indicate the linear regime in all cases. (a) No external focusing. (b, c) The radius of curvature is calculated assuming that the geometrical focus is located at (b) 30 mm and (c) 15 mm in the medium. At all cases the input beam width is $w_0 =$ 180 μm. It is noteworthy that there are conditions where a power-dependent self-collimation effect is observed in cases (b, c) due to thermal lensing.

$$i\frac{\partial}{\partial z}\mathcal{E} + k_0 n_0 \frac{dn}{dT}\delta T\mathcal{E} + \frac{1}{2k_0 n_0}\nabla_T^2\mathcal{E} = -i\frac{a_0\mathcal{E}}{2}$$
$$-K_T\nabla_T^2(\delta T) = a_0 I \qquad 3.4.32$$

where K_T is the thermal conductivity of the solvent. Importantly, the initial condition of the amplitude of the electric field should be defined to account for external focusing, e.g., for a Gaussian beam profile according to the relation

$$\mathcal{E}(r,0) = \sqrt{\frac{2P_{in}}{\pi w_0^2}}exp\left(-\frac{r^2}{w_0^2} - i\frac{k_0 r^2}{2R}\right) \qquad 4.33$$

where P_{in} is the input power, w_0 the input 1/e^2 beam radius and $-i\frac{k_0 r^2}{2R}$ denotes the phase of the input wavefront, with R denoting the radius of curvature of the beam (Figure 4.16).

4.6.4 Reverse saturable absorption and optical limiting

Characterization of nonlinear absorptive properties of plasmonic nanocomposites (e.g., in the context of OL) has been extensively studied by use of a simple nonlinear propagation equation, direct extension of Beer-Lambert's Law [32, 91, 191, 205-207], which reads:

$$\frac{dI}{dz} = -a(I)I \tag{4.34}$$

Evidently, Equation 4.34 constitutes a specific case of the axial propagation Equation 4.16, which was derived in Section 4.3.2.2. The use of Beer-Lambert law is limited in the thin sample approximation, where the beam is considered nearly collimated [several authors however adopted the paraxial relation $I(z) = I_0(1 + z^2/z_R^2)^{-1}$, where z_R is the Rayleigh length, to account for diffraction [91]]. Absorption depends on the incident intensity (nonlinear): in the case of RSA, in accordance with definitions presented in Section 4.4.5, it reads $a(I) = a_0/(1 + I/I_s) + \beta$.

4.6.5 Laser mode-locking

A model for the passive mode-locking of solid-state lasers that use plasmonic nanocomposites as a slow saturable absorber has been proposed in ref. [208]. The laser cavity is characterized by a group velocity dispersion $k_0^{(2)}$, gain $g(I)$ and losses ℓ of the cavity, a Kerr nonlinearity $n_{2,g}$ in the gain medium (and not of the plasmonic nanocomposite), the optical response of the plasmonic nanocomposite $q(I)$, and dispersion of the spectral filter and the gain medium $D_{g,f}$. The model accounts for the wave propagation in a laser cavity of length l_c. and reads

$$l_c\frac{\partial}{\partial z}\mathcal{E} = -i\left(l_c k_0^{(2)}\right)\frac{\partial^2}{\partial t^2}\mathcal{E} + i l_c\frac{\omega_0}{c}n_{2,g}I\mathcal{E} + G(I)\mathcal{E} \tag{4.35}$$

where $G(I) = g(I) - \ell + D_{g,f}\frac{\partial^2}{\partial t^2} - q(I)$ is a function describing the net gain of the cavity per round trip. Equation 4.35 comprises a typical propagation equation model for the studies of laser

mode-locking in slow saturable absorbers (see for example [209] and references therein), however, most interestingly in the context of this review, it incorporates a response function of the plasmonic nanocomposite $q(I) = -i\frac{\omega_0 h}{c^2}\sqrt{\varepsilon_{eff}(I)}$, where h and $\varepsilon_{eff}(I)$ denote the thickness and the effective medium dielectric medium of the plasmonic nanocomposite, respectively. The latter has been described in ref. [208] as a function of time in the context of the extended two-temperature model described in Section 4.4.1.2.

4.6.6 Femtosecond filamentation and continuum generation

In this regime, nonlinear wave propagation, in a semi-transparent medium, results in the manifestation of femtosecond filamentation. Chromatic dispersion cannot be neglected to describe nonlinear wave propagation arising from self-focusing. Rewriting Equation 4.8 in the pulse's local frame, facilitates greatly the problem of the description of the evolution of a propagating pulse over long distances and its interaction with the propagating medium. To do this, the following transformations should be introduced; $z \to z,\ t \to t - z/u_g,\ d_t \to d_t,\ \partial_z \to \partial_z + \omega/u_g$, where $u_g = (\partial k(\omega)/\partial\omega)^{-1}$ denotes the group velocity of the pulse. In addition, $\{E, P^{NL}, J\}$ will be oscillating in the local pulse frame as $\propto \{\mathcal{E}, \mathcal{P}^{NL}, \mathcal{J}\}exp\left[-i\omega_0 t + i\left[\kappa(\omega) - \frac{\omega}{u_g}\right]z\right]$, where $\kappa(\omega) = k_0 + (\omega - \omega_0)/u_g$. Under these transformations the envelope equation reads [63]

$$\frac{\partial^2}{\partial z^2}\hat{\mathcal{E}} + 2i\kappa(\omega)\frac{\partial}{\partial z}\hat{\mathcal{E}} + \left(k^2(\omega) - \kappa^2(\omega)\right)\hat{\mathcal{E}} + \nabla_T^2\hat{\mathcal{E}} = -\frac{\omega^2}{c^2}\frac{\hat{\mathcal{P}}^{NL}}{\varepsilon_0} - i\frac{\omega}{c}\frac{\hat{\mathcal{J}}}{\varepsilon_0 c} \qquad 4.36$$

in which the only simplification made compared to Equation 4.8 is $\nabla(\nabla \cdot E) \approx 0$. Neglecting the ∂_z^2 term, Equation 4.36 yields (depending on various chromatic dispersion approximations) several nonlinear envelope equations for the description and modelling of femtosecond filamentation in transparent media [210-212]. Starting from Equation 4.8, the nonparaxial version of the unidirectional pulse propagation equation can be derived (a carrier-resolving pulse propagation model). Nonparaxiality provides advantage under tight external focusing conditions. For a detailed description of this model, we recommend the specialized on the topic ref. [63].

For transparent media, the term of nonlinear polarization in Equation 4.36 is substituted by $\hat{\mathcal{P}}^{NL} = 2\varepsilon_0 n_0 n_2 \widehat{I\mathcal{E}}$, which is a direct consequence of Equation 4.7 and Equation 4.15. A polarization

current density term $\vec{J}_f$ arises from free charges generated by highly nonlinear ionization processes [40, 60, 63, 213]. The $\vec{J}_f$ term is comprised of currents due to direct photoionization $\vec{J}_P$ and currents related to the dynamic formation of an absorbing electronic density $\vec{J}_E$. The first term is calculated by

$$\frac{\vec{J}_P}{\varepsilon_0 c} = n_0 \beta_K I^{K-1} \vec{E} \tag{4.37}$$

Where β_K is the cross-section of the multiphoton absorption and K denotes the number of simultaneously absorbed photons. The second term obeys the plasma dynamics relation

$$\frac{\partial \vec{J}_E}{\partial t} + \frac{\vec{J}_E}{\tau_c} = \frac{e^2 n_e}{m_e} \vec{E} \tag{4.38}$$

Here, τ_c denotes the electron collision time, n_e the electron density, e the elementary electric charge and m_e the electron's mass. Thus, the solution of this equation can be added as a source term in Equation 4.36 that reads

$$\frac{\vec{J}_E}{\varepsilon_0 c} = \frac{\sigma_f(\omega)}{n_0(\omega)} n_e \vec{E} \tag{4.39}$$

Where $\sigma_f(\omega)$ stands for the complex frequency dependent cross-section for the collision of free carriers. The electron density that appears in this equation can be accordingly calculated by a rate equation of the form

$$\frac{\partial n_e}{\partial t} = w_m(I)(n_n - n_e) + w_I(I) n_e \tag{4.40}$$

Where $w_m(I)$ represents the multiphoton ionization rate, n_n denotes the neutral species density and the $w_I(I)$ stands for the impact ionization rate. Details on femtosecond pulse propagation modelling can be found in other excellent reviews for the interested reader [40, 60, 63].

In the case of an absorptive nonlinear medium (case of plasmonic nanocomposites), losses can be accounted for by the utilization of an additional contribution to $\vec{J}$ that describes the induced

polarization density current due to charges bound in the nanoparticles, which reads (in its envelope form) $\mathcal{J}_b = \varepsilon_0 c n_0 a(I)\mathcal{E}$, in accordance with what described in Section 4.3.2.2.

Features of the model of laser filamentation have been adapted by a few authors [45, 46, 50] for the description of nonlinear propagation of ultrashort pulses in plasmonic nanocomposites (Figure 4.17). In references [45, 46], the FME has been implemented in the pulse's reference to describe off-resonance propagation of fs pulses of optical wavelength of 800 nm in a medium of silver nanoparticles, which reads

$$\frac{\partial}{\partial z}\hat{E} = i\left[k_{eff}(\omega) - \frac{\omega}{u_g}\right]\hat{E} = -\frac{\omega^2}{2k_{eff}(\omega)}\frac{\hat{P}^{NL}}{\varepsilon_0 c^2};\ \hat{P}^{NL} = \varepsilon_0 \chi_{eff}^{(3)}\left|\hat{E}\right|^2\hat{E} \qquad 4.41$$

where $k_{eff}(\omega)$ is the calculated dispersion of the nanoparticle suspension and $\chi_{eff}^{(3)}$ was described by Equation 4.24 (Figure 4.17A). The authors illustrated an expected ultrabroadband supercontinuum generation from such structures after propagation of 8.3 μm, which is mainly attributed to the enhanced real part of the nonlinear susceptibility of the samples. Later, the same group presented a theoretical study on-low threshold supercontinuum generation from silica glasses doped with Ag nanoparticles [45]. For input 20 fs long pulses, the authors observed broadband supercontinuum could be achieved even for low filling factor (10^{-5}) for propagation over about 5 μm. Similar results were obtained for longer input pulse wavelengths (1300 nm and 1550 nm), whereas the authors finally addressed implications of strong pulse compression in such media. Their model however ignored ultrafast modulation (due to non-thermal electrons) of $\chi_{eff}^{(3)}$, which was calculated by Equation 4.41 for unpertubed values of $\chi_{eff}^{(3)}$.

In ref. [50], a unidirectional pulse propagation equation was employed (a paraxial equivalent of Equation 4.36) to describe propagation and supercontinuum generation of fs pulses of 800 nm focused in a gold nanosphere colloidal solution. To reproduce experimental observations on supercontinuum generation, nonlinearities were attributed to pure water properties (Figure 4.17B-E), while the suspended nanoparticles were considered to act only as centers of linear extinction expressed in the $\hat{f}$ term and calculated by the effective medium dielectric permittivity of Equation 4.4. In other words, enhancement on the nonlinear response of the nanoparticles was ignored in

view of the non-resonant interaction and all contributions on the nonlinear ionization terms were attributed to the solvent (water).

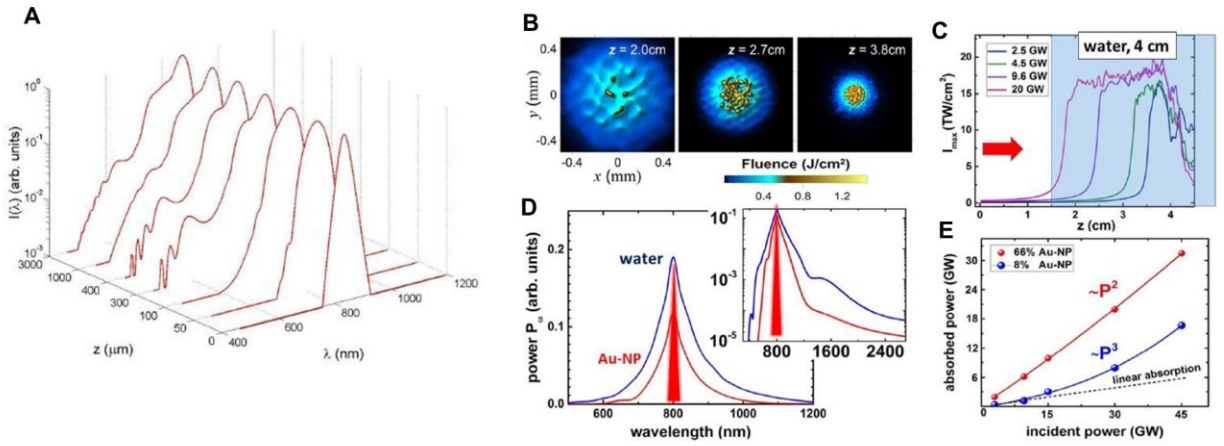

Figure 4.17 Numerical modelling results of supercontinuum generation in plasmonic nanocomposites. (A) Spectral broadening of a 20 fs pulse in a fused silica medium doped with silver nanoparticles of filling factor 10^{-3}, obtained by solution of Equation 4.41. Reproduced with permission [45]. Copyright 2009, The Optical Society. (B-E) Numerical results of filamentation and supercontinuum generation in an aqueous suspension of Au nanoparticles. (B) Transverse fluence profiles. (C) axial profiles of the peak intensity in pure water along propagation for various input pulse powers (D) Spectral broadening comparison between pure water and colloidal gold. Attenuation rather than amplification of supercontinuum is observed. (E) Absorbed power by two colloids of two different concentrations as a function of the incident pulse power. Reproduced with permission [50]. Copyright 2019, The Optical Society.

4.7 Processes and applications

In this section, recent experimental studies on processes and applications related to nonlinear propagation of light in plasmonic nanocomposites are reviewed. The presented studies are categorized into two regimes, due to large differences in the time response of induced nonlinearities. The first, refers to the nonlinear propagation in the CW/short pulse regime, whereas the second category refers to the ultrashort pulse regime.

4.7.1 CW and short pulse regime

4.7.1.1 Plasmonic resonant solitons (self-channeling)

Farfad et al. [39] demonstrated experimentally phenomenological soliton formation in plasmonic nanocolloids for the first time, based on the mechanisms discussed in Sections 4.4.7.2 and 4.6.1. They employed samples containing nanoparticles of either negative or positive polarizabilities at the irradiation wavelength. The authors described how both cases could lead to soliton formation governed by Equation 4.31. Particularly, in the supercritical case of positive polarizability, they proposed that absorption was the key in stabilizing soliton formation. In fact, they indicated that thermal heating of the surrounding medium leads to defocusing of the beam, thus balancing the positive nonlinearity induced by increasing particle concentration. The same group proposed in another study that the coupling of two laser beams at optical frequencies corresponding to opposite polarizability of the nano-inclusions lead to formation of coupled stable solitons for both beams, meaning that their decoupling leads to diffraction limiting propagation of one or the other, depending which beam induces a stronger nonlinearity in the medium [54] (Figure 4.18a-g).

The effect of plasmonic resonant soliton formation was further studied by Shvedov et al. [58] in the case of spherical Au particles of positive polarizability with respect to the applied wavelength. By performing order-of-magnitude calculations they showed that the induced gradient forces in the presence of low intensity laser field are too weak to play a critical role in particle's translation against Brownian motion or radiation pressure. However, radiation forces strongly depend on the size of the particles and they rapidly decrease as the particle's size increases [214]. Shvedov et al. concluded that the highest in value nonlinearity is induced by SPR absorption-mediated thermal heating of the surrounding liquid in agreement with recent observations by Agiotis and Meunier [180], who further compared CW and high-repetition rate fs pulsed illumination in nano-colloids of varying plasmon peaks . The same mechanism was exploited by Ortega et al. [37] to induce self-collimated propagation of CW irradiation (532 nm) in biosynthesized Au nanoparticle colloids (3-5 nm in diameter). The resulted low-divergent beam was further shown that it can be used as a waveguide of beams of a different wavelength. The principle was also recently demonstrated by the same group in ref. [38] (Figure 4.18h). Finally, a conclusion drawn in [180] suggests that thermal lensing can possibly be mitigated by use of high-repetition rate fs pulsed illumination in

conjunction with tight focusing conditions (focused $1/e^2$ radius < 5 μm). Further, soliton formation induced by gradient forces seems more likely if particles of d > 100 nm (decrease Brownian motion) and longest possible illumination wavelength (reduce radiation pressure) are employed.

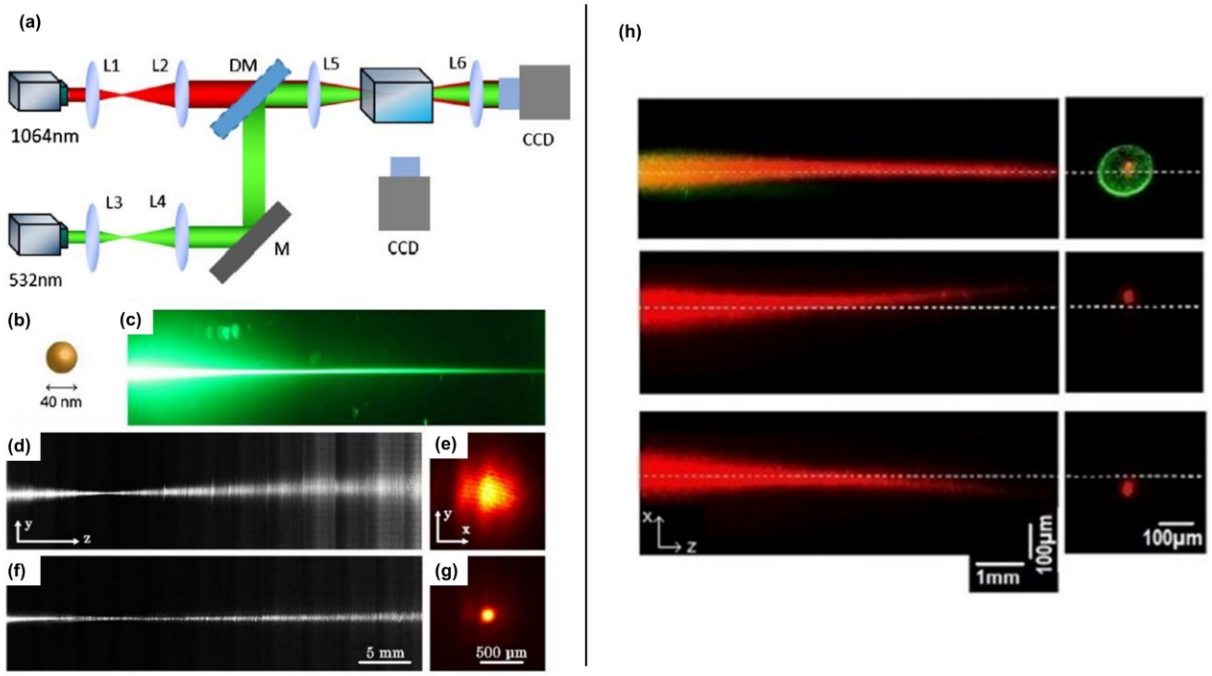

Figure 4.18 Induced waveguiding in plasmonic nanocolloids. (a-g) Demonstration attributed to soliton formation induced by mass transport of particles. (a) The experimental setup. (b) The nanoparticle inclusions of the suspension in which the waveguiding demonstration takes place. (c) Soliton beam (532 nm) (d-e) side and output of the IR probe beam when the soliton beam is absent. (f-g) Same as (d-e), however, with soliton beam present. Adapted with permission [54]. Copyright 2016, The Optical Society. (h) Demonstration attributed to thermal lensing and self-collimation. On the left, shown in red, is a side view of a probe beam steered in a gold aqueous nanosuspension (3-5 nm Au nanoparticles) by a pump beam. Output view of the pump and steered probed beams are shown on the right, in green and red, respectively), which is steered accordingly. Reproduced with permission [38]. Copyright 2021, American Institute of Physics. A demonstration of steering due to thermal lensing in the same context is also shown in [37].

4.7.1.2 Orientation ordering

Considering the conclusions drawn by Farfad et al. [39], an off-resonant laser beam (the SPR of the nanorods does not coincide with the irradiation wavelength) may exert forces on Au nanorods inducing rotational torque on the particles due to their anisotropic polarizability. A soliton beam

induced by optical forces, may potentially align a large ensemble on a specific direction with

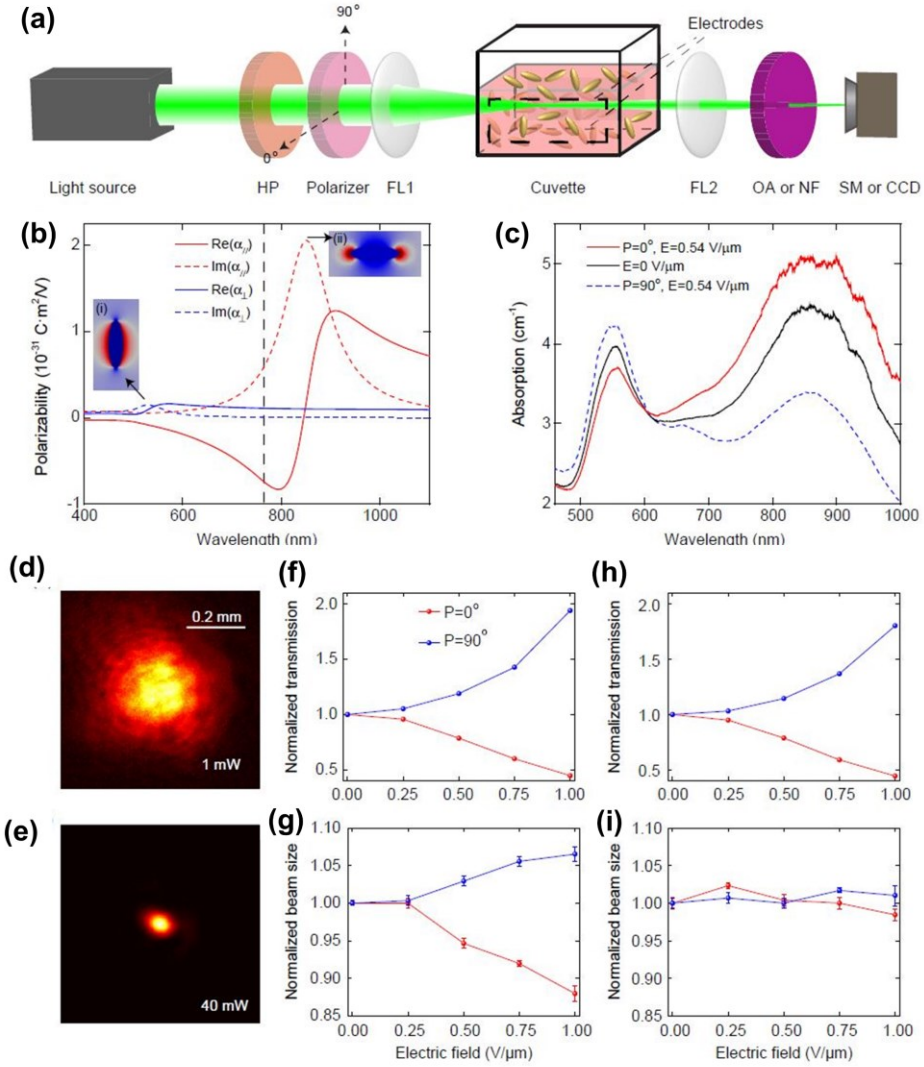

Figure 4.19 Orientation ordering of gold nanorods in a aqueous suspension by an external electric field, and nonlinearity control. (a) Experimental setup. (b) Calculated spectra of polarizability depending on nanorod orientation. (c) Measured absorption spectra when the polarization of the input white light is parallel (red curve) or perpendicular (blue curve) to the applied field. Black curve indicates the absorption spectrum in the absence of the external field. (d-e) Output beam profile of a probe beam for two different input powers. For 40 mW the beam is phenomenologically self-trapped. (f-g) The normalized transmission and output beam size for two different input polarizations of the probe beam of 790 nm wavelength as a function of the applied external field strength. (e-f) Same as (c-d), however for a probe beam of 930 nm wavelength. Adapted under terms of the CC-BY license [57]. Copyright 2021, John Wiley and Sons/Wiley-VCH.

respect to the polarization of the incident field (as shown in Figure 4.14ii). Ultimately, this may lead to artificial, soliton-mediated birefringence. The idea just discussed was developed by Ren et

al. [55] by coupling collinearly to a “soliton beam” formed in a Au nanorod colloid, a weak probe beam (Figure 4.14ii). The polarization of the latter was shifted resulting in optical transmission modulation, implying the orientation ordering of the nanorods along the optical soliton. Such a result has remarkable implications in controlling the nonlinear properties of soft-matter media, being conceptually similar to hyperbolic metamaterials [102, 215, 216]. Nonetheless, as noted by the same group in a more recent study, various mechanisms may hinder orientation ordering, for example, Brownian motion, absorption, or radiation forces [56]. The findings of ref. [56] presumably indicate the manifestation of thermal lensing as in ref. [37, 58, 180]. A possible way to address the problem of orientation alignment of gold nanorods colloids has been recently proposed by means of application of an external electric-field [57] (Figure 4.19).

4.7.1.3 Nonlinearity management

According to what already discussed in Sections 4.4.6, 4.6.2, and the implications of Equation 4.29, Reyna and Araújo [173] demonstrated experimentally a high-order nonlinearity management procedure during which, the filling factor of silver nanocolloids is adjusted toward modification of the refractive and absorptive nonlinear response of the (effective) composite material. The authors have recently presented a comprehensive review of their work, which we refer to for the interested reader [35]. Therein, applications and prospects of the nonlinearity management procedure in plasmonic nanocomposites are illustrated, among others, engineering of spatial-phase modulation [173, 174], nonlinear birefringence [202], soliton formation [201], and all-optical switching [175]. Interestingly, all demonstrations have been performed under picosecond laser excitation regime, where the nonlinearity of the nanoparticles originates from lattice coupling.

4.7.1.4 Optical vortices

An optical vortex is generated when an optical beam’s spatial intensity distribution is twisted around its propagation axis. Such an effect is understood in terms of an angular momentum that any Laguerre-Gaussian beam mode carries. The amplitude of these beams carries an azimuthal angular dependence which readily implies the existence of angular momentum modes in analogy with the quantum mechanical angular momentum operator [217]. Indeed, if one attempts to calculate the angular momentum density per unit volume of a Laguerre-Gaussian distribution, one can arrive with an expression that suggests that the Poynting vector is spiralling around its

propagation axis, due to an angular component. Optical vortices are then said to carry a topological charge m which characterizes the number of spiraling per one wavelength, which can also be expressed as the carried orbital angular momentum $m\hbar$ per photon of the light field. Optical vortices can be produced by various techniques including spiral phase plates, metasurfaces, computer generated holograms and many others, and they have found numerous applications in the fields of optical trapping, optical communications, quantum optics, nonlinear optics, microscopy and others [218, 219]. The stability of vortex solitons in propagating medium has been thus a major subject of investigation over the past decades [218].

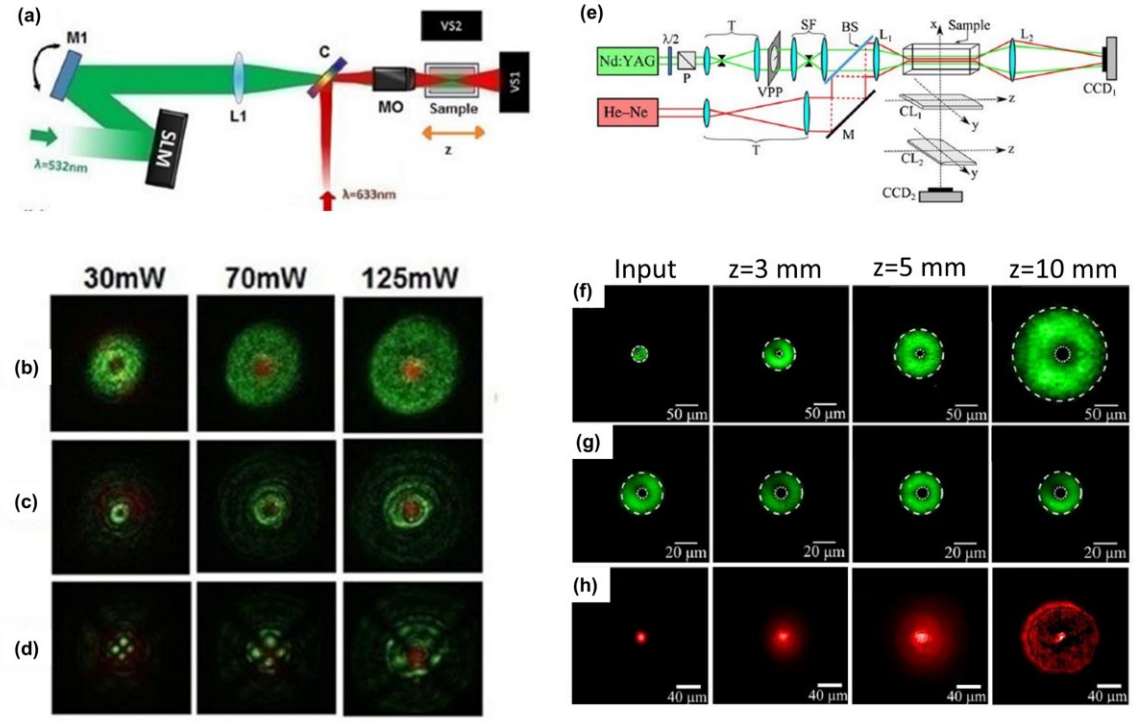

Figure 4.20 Waveguiding with structured light beams in plasmonic nanocolloids. (a-d) Demonstration of a CW vortex pump beam-waveguide, attributed to thermal lensing. (a) The experimental setup. (b-d) Images of the beam profiles at the output face of the cell. Waveguiding of a probe beam (red light) by (b) a simple vortex pump beam (c) a Bessel vortex pump beam and (d) a cosine Bessel vortex beam. Adapted with permission [38]. Copyright 2021, American Institute of Physics. (e-h) Demonstration of a 80 ps pulsed vortex beam-waveguide (soliton beam) attributed to nonlinearity management. (f) Low pump power – soliton beam "off" at the input of an optical cell and after 3, 5 and 10 mm of propagation. (g) Same as (f), however at higher input power, i.e., soliton beam is "on". (h) Coupled probe beam output profile when the soliton beam is "on". Adapted with permission [89]. Copyright 2016, The Optical Society.

Shvedov et al. [58], in their study discussed in Section 4.7.1.1, performed experiments of cw optical vortices propagation in plasmonic nanosuspensions of gold nanospheres and gold nanorods. Their study provided experimental evidence of structural optical stability of vortex solitons in plasmonic nanocolloids in view of the thermally induced nonlinearity. Furthermore, recently, Ortega et al. [38, 59] demonstrated that structured vortex beams can be used to induce stable waveguides in plasmonic nanocomposites due to the thermal lensing effect (Figure 4.20a-d). In a different approach, Reyna and Araújo [89] showed stable, pulsed laser (80 ps pulsewidth, 10 Hz repetition rate, 532 nm wavelength) soliton vortex formation in Ag nanocolloids within the framework of the nonlinearity management procedure (Figure 4.20e-h). Therein, they demonstrated coupling and guiding of a probe cw beam of low intensity with a wavelength of 1064 nm, of which the beam radius matched the dark width of the vortex soliton.

4.7.1.5 Laser Q-switching and mode-locking

Passive laser mode locking by use of plasmonics was first demonstrated by Ganeev et al. in a Nd:glass oscillator at a wavelength of 1054 nm by the utilization of a suspension of platinum nanoparticles acting as a SA in the cavity [34]. In this setup the authors managed to achieve stable 5 ps pulses that exhibit better stability compared to conventional dye films. Later, researchers managed to exploit the saturable absorption properties of gold nanostructures for designing SA elements. In a first demonstration gold nanocrystals were used as a SA for Q-switched pulse generation in an erbium - doped fiber laser [220]. The authors obtained 3.2 μs pulses at 1560 nm with a repetition rate of 24.2 kHz above a threshold pumping power of 30 mW. Furthermore, Wu et al. used a solution of Au nanoparticles into polyvinyl alcohol to form a film which was inserted into a praseodymium doped fiber laser cavity [221]. The authors demonstrated generation of pulses as narrow as 235 ns at a visible frequency with 546.4 kHz repetition rate and maximum output power of 11.1 mW. The geometrically tunable properties of the SPR of metallic nanoparticles has given also further attention to other geometries of nanoparticles, like nanorods. Indeed, gold nanorods exhibited stable performance as SA elements in fiber lasers to produce mode locked pulses [27, 222].

More recently, the ion implantation of Au in a Nd:YAG crystal has been reported to have improved the optical nonlinearity of the latter by 5 orders of magnitude and provided better saturable

absorption properties [223]. Moreover, Pang et al. [28] reported the fabrication of a novel SA in which Au nanoparticles were embedded in a $LiNbO_3$ crystal and demonstrated superior performance compared to previous nanoparticle based SAs due to the combination of the multifunctionality of the $LiNbO_3$ with the SPR of the plasmonic nanoparticles. Further advancements have been reported in the field of plasmonic SA for laser Q-switching by the same group by the ion implantation technique, including Cu embedded in $LiNbO_3$ [30] and $LiTaO_3$ [224] and Ag implanted in $LiNbO_3$ [225] and Nd:YAG [29]. Xian et al. [226] proposed the utilization of refractory titanium nitride nanoparticles as SA and demonstrated mode-locking and generation of minimum pulse duration down to 763 fs (Figure 4.21a-c). Finally, it is noteworthy that utilization of plasmonic metasurfaces with ultrahigh modulation depth have recently exemplified the remarkable potential of plasmonic nanocomposites in laser mode-locking technology [31] (Figure 4.21d-g).

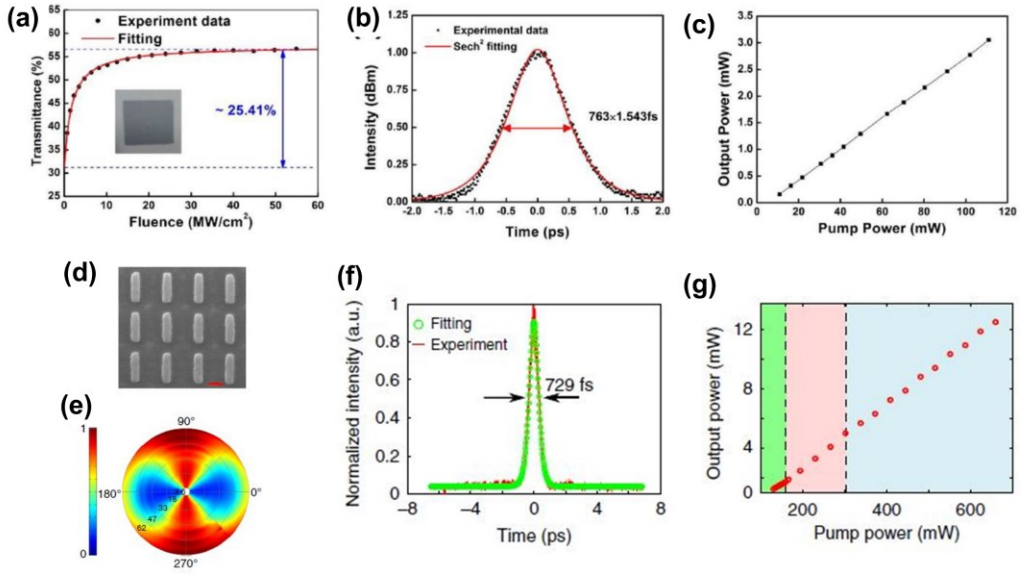

Figure 4.21 (a-c) Q-swithed pulse generation by use of a plasmonic TiN/PVA film as a saturable absorber. (a) The nonlinear transmittance modulation curve. (b) Autocorrelation trace of the generated pulses. (c) The output power curve as a function of the pump power. Adapted with permission [226]. Copyright 2019, John Wiley and Sons. (d-g) Mode-locking in a fiber laser cavity by use of plasmonic nanorod array as a saturable absorber. (d) SEM image of the array. (e) Polarization dependent transmittance through the array. (f) Autocorrelation trace of the mode-locked pulses. (g) The output power of the cavity as a function of the pump power. The shaded regions demarcate single-soliton, single-soliton with cw and soliton molecule regimes with green, red, and blue color, respectively. Adapted under terms of the CC-BY license [31]. Copyright 2020, Springer Nature.

4.7.2 Ultrashort pulse regime

4.7.2.1 Filamentation and supercontinuum generation

Femtosecond filamentation and supercontinuum generation in a plasmonic nanocomposite was first reported in 2007 by Wang and coworkers [44]. The authors employed an amplified femtosecond laser source (50 fs pulsewidth, 1kHz repetition rate, 800 nm wavelength) to observe the nonlinear propagation of pulses in a sample of Ag nanocolloid (10 nm average particle size). Pumping conditions were reported under which the supercontinuum exhibited amplitude enhancement in the Ag-doped water as opposed to neat water, however, without clear insights on the involved mechanisms. Side views of the beam propagation through the samples showed expansion of the spectral broadening towards "bluer" frequencies for increasing input power, by consecutive scattering of orange, yellow, green, and finally bright blue color light off Ag particles in the region of the formed filament's core. Similar results were reported by Cui et al. [227] along with direct observations on the conical emission governed by the characteristics of the SPR of the nanocolloids. Later, Vasa et al. [228] reported on experimental results of supercontinuum generation from water doped with Au nanostructures of varying SPR. Their conclusions focused on observed conditions of increased spectral extent and flat supercontinuum spectra from examined Au colloids, which they attributed to contribution of plasmonic field enhancement on the third order susceptibility of the host.

The latter group further studied experimentally supercontinuum generation in the anomalous dispersion regime of water [229]. Octave spanning supercontinuum expansion was observed despite the stronger absorption of water for wavelengths greater than 1300 μm, which was explained in terms of a phenomenological self-phase modulation model. It was demonstrated that for water doped with gold nanorods (SPR at 626 nm), the supercontinua were significantly modulated in the case of pumping wavelength of 1200 nm, whereas when pumping of 1300 nm was employed, the modulation was less pronounced (Figure 4.22D-E). Thus, the observations implicated resonant interaction with two-photon transitions at the SPR of the samples, possibly affecting the nonlinearity. Notably, in another note, Zhavoronkov et al. [230] reported on supercontinuum generation from a heavy-glass matrix Ag nanocomposite, under a two-photon resonant interaction regime. The authors observed a significant asymmetric broadening of the

pulses in the case of the doped glass as opposed to undoped glass at the same input powers, an effect that they attributed to temporal delay by stimulated Raman scattering, which they considered into numerical simulations of a nonlinear wave propagation equation (Figure 4.22A-C).

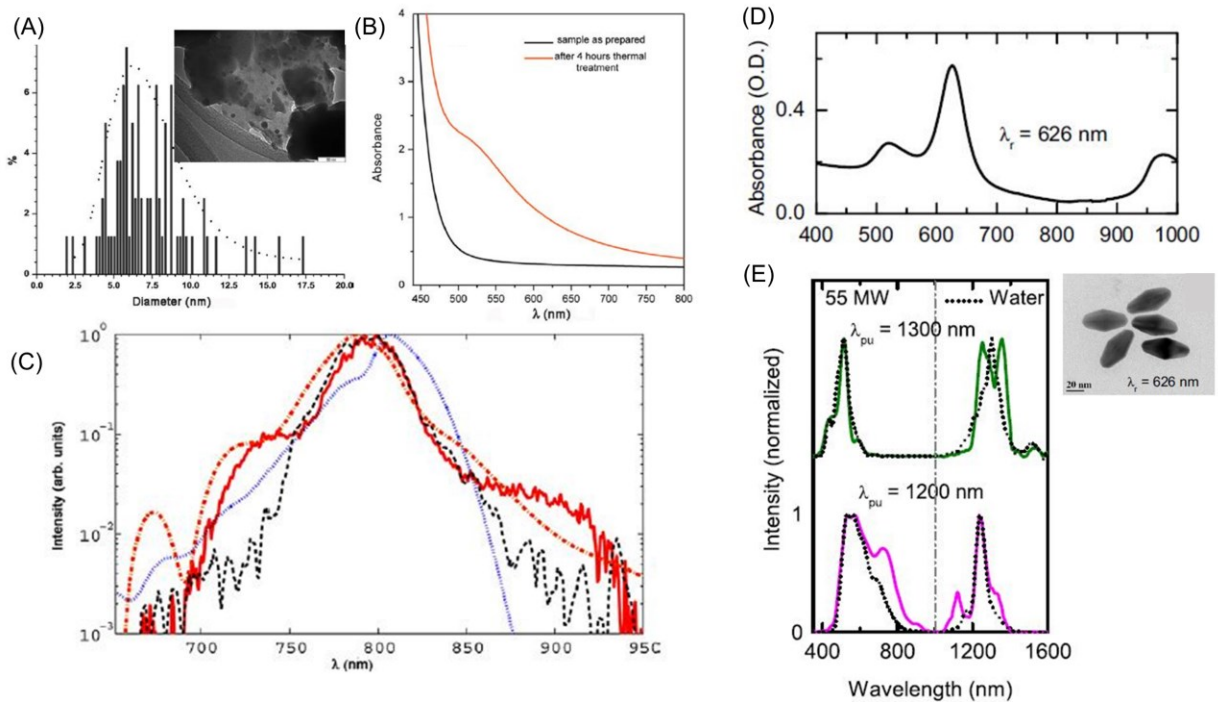

Figure 4.22 Supercontinuum generation in plasmonic nanocomposites under conditions of two-photon resonance with the localized plasmon mode. (A) Size distribution and TEM image of Ag nanoparticles synthesized in a 2 mm WO_3 glass matrix. (B) Absorbance spectra after 4 hours of thermal annealing (red curve). (C) Measured supercontinua (spectral broadening) after propagation through the doped (solid red curve) and undoped (dashed black curve) matrix. The orange dotted and blue dotted curves correspond to numerical calculations accounting for or ignoring a stimulated Raman scattering contribution term, respectively. Adapted with permission [230]. Copyright 2011, Institute of Physics. (D) Absorbance spectra of an aqueous Au nanorod colloidal solution. (E) Measured supercontinua after propagation through a water sample (dashed curves) and the Au nanorod suspension sample (colored curves) in the anomalous dispersion regime of water [pump at 1300 (top figure) and 1200 nm (bottom figure)]. Adapted with permission [229]. Copyright 2013, American Physical Society.

4.7.2.2 Spectroscopy

Kudryashov et al. [50] performed studies of supercontinuum generation from nonlinear propagation of light in Au nanocolloids in the ultrashort pulse regime (femtosecond filamentation) with a different perspective. The authors reported for the first time that in fact, an overall attenuation of supercontinuum generation occurs during femtosecond filamentation in Au

nanocolloids compared to water, owing to strong optical extinction in the former. Nonetheless, they noted that femtosecond filamentation and supercontinuum generation in Au nanocolloids can be utilized for fundamental investigation of their nonlinear response by means of ultrafast broadband nonlinear spectroscopy (Figure 4.23A-C), which reveals features of out-of-equilibrium properties of metallic nanoparticle dielectric function at high pump intensities (SPR quenching, interband threshold red-shift), as observed in their later studies [51, 52, 231] and in ref. [232, 233].

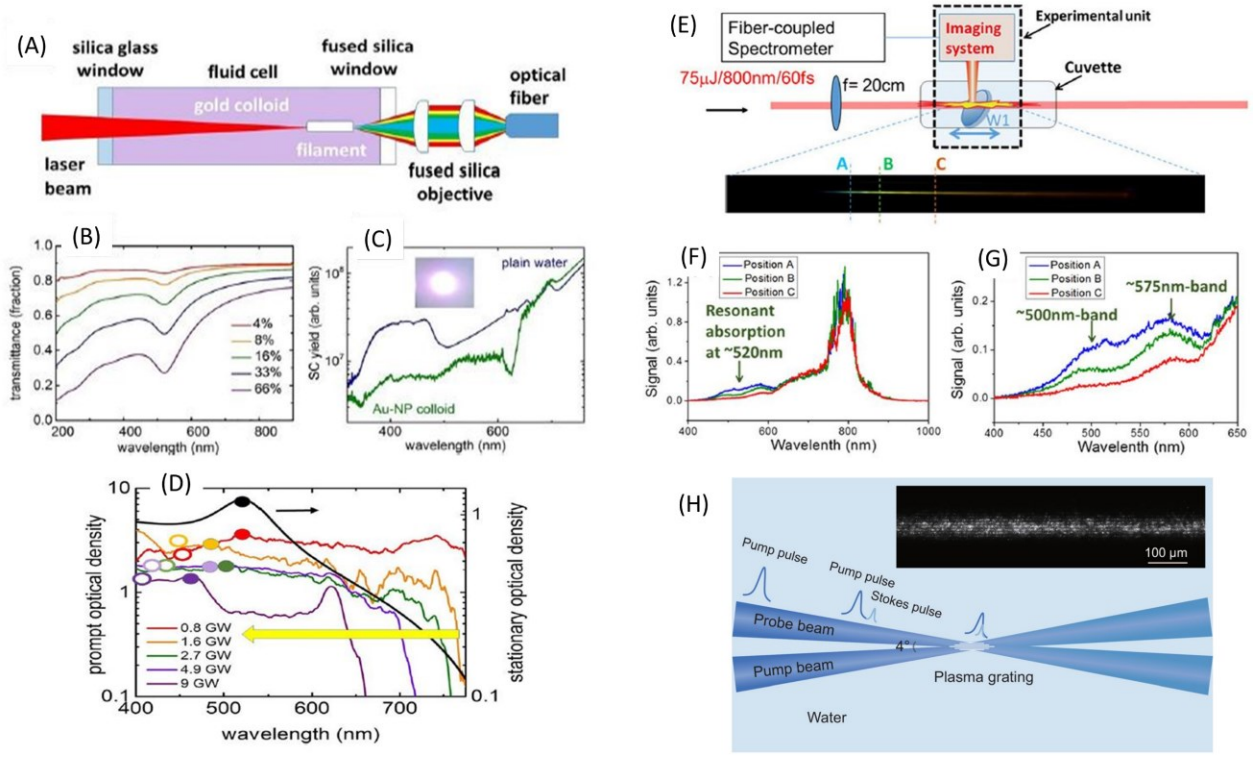

Figure 4.23 Spectroscopic studies in aqueous suspensions of plasmonic nanoparticles. (A-D) Observation of plasmon peak modulation under intense pumping and filamentary propagation. (A) Experimental setup. (B) Linear transmittance of suspensions of different concentrations. (C) Supercontinua obtained for pure water and Au nanocolloid. (D) Optical density spectra obtained by filamentary propagation through Au colloid and normalized over the spectrum of plain water at various pumping intensities (colored curves) and linear optical density (black curve). Adapted with permission [51]. Copyright 2019, American Institute of Physics. (E-G) Spectroscopic measurements at 3 different locations across the propagation axis of a formed filament in Au nanocolloid. Adapted under terms of the CC-BY license [49]. Copyright 2018, Springer Nature. (H) Utilization of Au nanoparticles as contrast agents for imaging filamentary plasma grating in experiments of crossing filament THz generation through a water sample. Reproduced with permission [234]. Copyright 2018, American Institute of Physics.

In another recent note, highly extended filamentation was reported in Au nanocolloids compared to water [49]. However, the observation was related to the fact that the water filament channel is

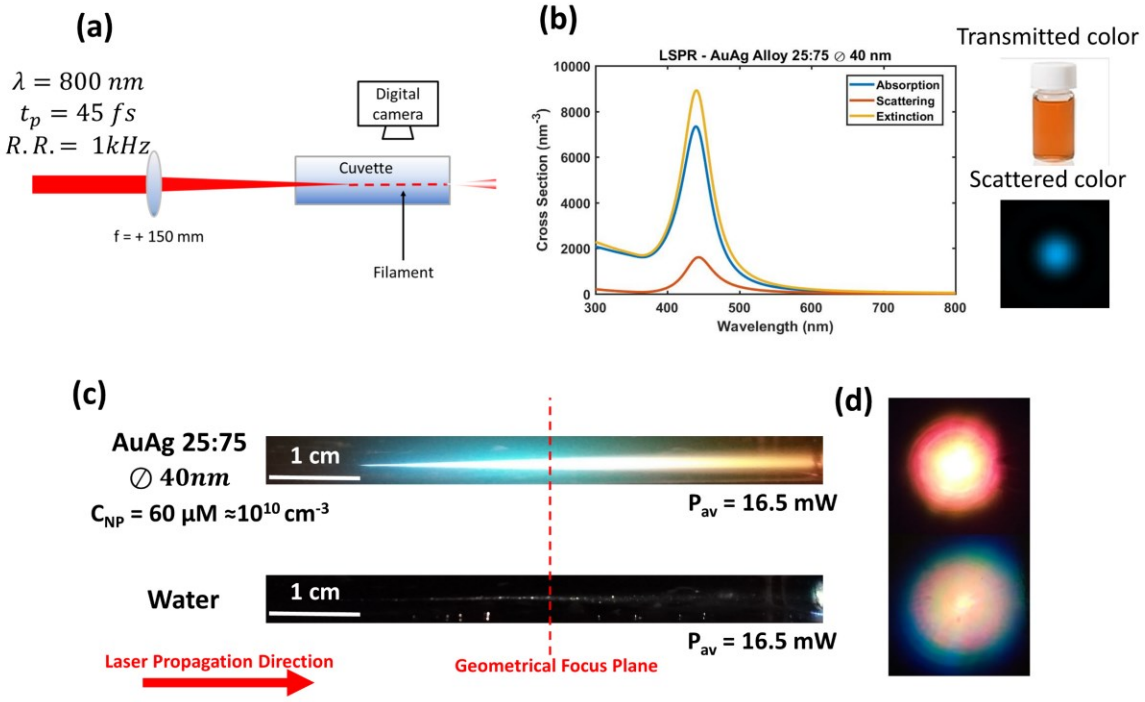

Figure 4.24 Filamentation in a AuAg alloy (25:75) aqueous suspension. The sample preparation is described in [235]. (a) The experimental setup: a 10 cm optical cuvette is filled with the sample. A $1/e^2$ beam radius ~2.4 mm is focused approximately at the middle of the cuvette by a 150 mm positive lens. Side views were collected by a digital camera and far-field output profiles projected on a screen. (b) Calculations of the absorption, scattering and extinction cross sections of the examined nanoparticles. The transmitted and scattered colors are shown in the right top and bottom figures. (c) Side views of filamentation when the cuvette was filled with the plasmonic nano-colloid (top) or water (bottom). Strong phase modulation gives rise to Anti-Stokes wing broadening of the laser spectrum at the incident power (~35 times the critical power of water). Generated frequencies near the plasmon resonance are heavily scattered or absorbed, filtering out the involved frequencies of the laser spectrum at the output as observed in far-field profiles in (d). Scattering of "redder" frequencies is observed near the output face of the cuvette, either due to complete filtering of spectral broadening below 500 nm or due to strong modulation of the dielectric function of the particles (hence, the SPR). Still, the first scenario appears more possible considering reported blue shifting of the SPR under similar conditions of very intense pumping in Au aqueous nano-suspensions [51]. Note that the filament channel observed in the case of water is phenomenologically comparable in length to the one in the case of the plasmonic nanoparticle in contrast to recent reported observations [49].

not visually observable because of its transparency at optical frequencies, whereas highly scattering Au nanoparticles visually enhance the filament's core, making it easily observable to naked eye (Figure 4.24). Yet, experiments presented in [49, 236] provided spectroscopic evaluation of the attenuation by the SPR of the nanoparticles at the spectral shoulder near the SPR region, which typically coincides to the anti-Stokes wing of supercontinuum in water (Figure 4.23E-G). The nonlinear scattering properties of plasmonic nanoparticles were further exploited to achieve imaging of gratings formed in nanoparticle-doped water when interacting filaments cross each other [234, 237, 238] (Figure 4.23H).

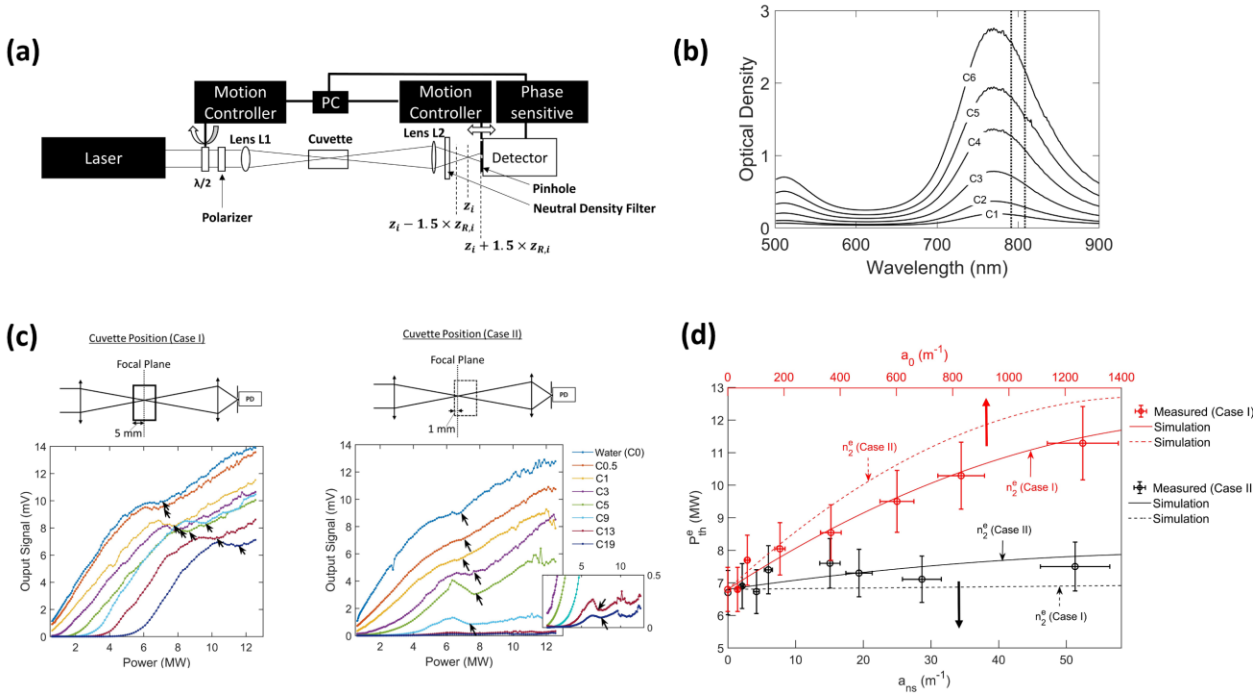

Figure 4.25 Evaluation of the threshold power for self-focusing in Au nanorod colloids by the power limiting method. (a) The experimental setup. Reproduced under terms of the CC-BY license [239]. Copyright 2021, Springer Nature. (b) The examined samples of varying concentration. (c) Typical measurements obtained by the power limiting method in the samples shown in (b) for two different positions of the optical cuvette along the propagation axis. Note that saturation of absorption and partial particle deformation is observed near the threshold power. (d) The experimentally evaluated threshold power for self-focusing versus the absorption of the nanorod colloids. The solid and dotted curves correspond to numerical simulations by solution of a nonlinear propagation equation of Schrodinger type, which accounts for saturation of absorption. Adapted under terms of the CC-BY license [240]. Copyright 2021, The Optical Society.

More recently, Agiotis and Meunier [239] have used an optical power limiting device introduced by Soileau et al. [241-243], originally employed for pulses higher than ~20 ps, to evaluate optical

nonlinearities in transparent media in the filamentation regime, governed by Equation 4.36. They have shown that the technique can be applied in the case of gold nanorod colloids (or any absorbing medium), for the evaluation of their strongly saturable nonlinearity (Figure 4.25). In fact, the authors showed that the self-focusing nonlinearity of the samples increases monotonically, yet only marginally, as the concentration of the nanorods increases. The result has been understood in the context of a synergistic effect of the ultrafast saturable permittivity (thus saturable local-field enhancement) and particle deformation near the threshold of filamentation [240].

4.8 Summary and outlook

The development of plasmonic nanocomposites has allowed fabrication of novel metamaterials with unique effective medium nonlinear properties. Extensive systematic studies on ultrafast electron dynamics in metals and metallic nanoparticles has greatly aided our understanding on the origin of their electronic nonlinear responses and the one of plasmonic composite materials. In this work, we have provided an overview of the most significant and latest advances in the field of ultrafast electron dynamics in metals and plasmonic nanocomposites, and most important approaches to formulate the resulting free electron nonlinearities at various timescales and pumping intensity regimes. Further, we presented a summary of resulting phenomena relevant to absorptive and higher-order responses in these materials. We have moreover referred to latest observations in typically stronger diffusive nonlinearities of slower (or cumulative) response, either due to heat diffusion in the host matrix or mass transport phenomena in soft-matter systems. A quantitative synthesis of measured nonlinearities under various laser excitation regimes has also been presented along with figures of merit, illustrating the importance of fundamental understanding of the origin of the observed nonlinearities. Finally, we provided a compendium on the influence of nonlinear response of plasmonic nanocomposites toward recent advancements in modelling, processes and applications related to nonlinear propagation of laser light in these metamaterials. We note that the presented overview is only relevant to advances within the effective medium approximation and long-range, diffraction-limited nonlinear wave propagation and it did not touch nonlinear processes in nanostructured geometries, for example, harmonic generation in the nanoscale, nonlinear surface waves on interfaces or surface plasmon-polariton solitons.

Overall, enhancement of coherent nonlinear processes related to the collective surface plasmon oscillation are accessible typically only under low-light intensity and ultrafast (< 10-20 fs) regime in nano-scaled geometries. Contrarily, within the effective medium approximation, an important conclusion drawn on the electronic nonlinear response of plasmonic nanocomposites is its predominantly thermal nature, even in the fs timescale. The nonlinear response of metallic nanoparticles, directly related to electronic and lattice temperatures, becomes stronger by increasing the temporal interaction with the incident field. The strongest response is observed by thermal heating of the whole material governed by the thermo-optic properties of the host material during longer pulsed (< 100 ps) or cw illumination.

In the context of fs filamentary propagation, it is unlikely that significant enhancement of Kerr self-focusing, and self-phase modulation processes can be achieved toward the modulation or amplification of supercontinuum generation. Indeed, photo-excited plasmon modes undergo inelastic decoherence and concurrently scatter at the particle interfaces within a timescale < 100 fs to a bath of high-energy kinetic modes, out of thermal equilibrium. Consequently, high intensity fs laser excitation in the resonance of SPR results in strongly saturable nonlinearities. However, it is noteworthy that in this regime scattering and absorptive properties of nanoparticles have been exploited to tailor the spectral extent of generated supercontinua, analyze spectroscopic signatures of the strongly perturbed electronic structure of metallic nanoparticles upon filamentary propagation in colloidal systems, or even for imaging.

Furthermore, studies in the propagation of short pulsed (> 10 ps) and cw irradiation in plasmonic disordered systems has recently revealed a variety of novel nonlinear effects. Judicious adjustments of nonlinear response based on metallic concentration, soft-matter reconfigurable manipulation of nanoparticles, ultrahigh-modulation depth saturable absorbers for laser mode-locking or thermally induced waveguiding optical vortices are several examples. Questions remain open-ended such as the competition of thermal effects against mass transport in soft-matter systems under certain external focusing conditions and size of particles or the stability of spatial solitons in view of high-order nonlinearities. Nonetheless, these sub-fields of nonlinear optics are still relatively young and await new advancements towards the development of plasmonic devices, optical switches, sensors, limiters, waveguides, and others.

CHAPTER 5 ARTICLE 2: OPTICAL POWER LIMITER IN THE FEMTOSECOND FILAMENTATION REGIME

Research article published in Scientific Reports in 2021[3]

5.1 Authors and author contributions

Leonidas Agiotis and Michel Meunier. L.A. designed the research, conducted the experiments, analysed the data, performed theoretical and numerical analysis, and wrote the main manuscript. M.M. supervised and discussed the work and reviewed the main manuscript.

5.2 Abstract

We present the use of a power limiting apparatus to evaluate ultrafast optical nonlinearities of transparent liquids (water and ethanol) in the femtosecond filamentation regime. The setup has been previously employed for the same purpose, however, in a longer pulsewidth (>20 ps) regime, which leads to an ambiguous evaluation of the critical power for self-focusing. The uncertainty originates from the existence of a threshold power for optical breakdown well below the critical power for self-focusing within this timeframe. Contrarily, using the proposed apparatus in the femtosecond regime, we observe for the first time a unique optical response, which features the underlying physics of laser filamentation. Importantly, we demonstrate a dependence of the optical transmission of the power limiter on its geometrical, imaging characteristics and the conditions under which a distinct demarcation for the critical power for self-focusing can be determined. The result is supported by numerical simulations, which indicate that the features of the observed power-dependent optical response of the power limiting setup are physically related to the spontaneous transformation of the laser pulses into nonlinear conical waves.

---

[3] Agiotis, L., Meunier, M. Optical power limiter in the femtosecond filamentation regime. *Sci Rep* **11,** 14270 (2021). https://doi.org/10.1038/s41598-021-93683-x

5.3 Introduction

Prior to the z-scan first demonstration [244], Soileau et al. introduced a passive optical power limiting device that relies on the self-focusing property of liquids [241]. The main idea of passive operation was based on the concept that a focused beam passing through a nonlinear medium will undergo strong phase change on its wavefront at increasing input powers, due to combined laser-induced breakdown and self-focusing inside the nonlinear medium. Thus, by placing an imaging lens after the nonlinear medium, one can observe limited transmission through a pinhole placed at the focus of that lens at high input powers.

In their original paper, the authors have employed their setup using nanosecond and picosecond pulses at an optical wavelength of 1.06 μm to study the nonlinear response of CS_2. Indeed, the device has been tested to exhibit a "step-function"-like transmission for increasing input powers, of which the demarcation was identified as the critical power for self-focusing. The latter is generally defined as the required input peak power of the pulse above which self-focusing overcomes diffraction [40, 64]. Effectively, the beam collapses so that its intensity increases and ionizes the medium. Nonetheless, for a pulse regime typically longer than 1 ps, optical breakdown is reached at a significantly lower power than the critical power for self-focusing within this timeframe due to the comparable times between energetic electron collisions and laser pulsewidth [40, 41]. By contrast, for pulses in the femtosecond regime, self-focusing typically occurs rapidly, before optical breakdown is attained in the medium [41]. Hence, the use of the technique with laser pulses longer than 1 ps, can typically lead to an underestimation of the critical power for self-focusing.

In this work, we employ the foresaid optical power limiter in the femtosecond filamentation regime, and we measure ultrafast optical nonlinearities in deionized water and ethanol. In our proposed approach we introduce to the system a pinhole (~15 μm in diameter), much smaller than the imaged beam waist at this location (~32 μm in diameter), which ensures a significant variation on the recorded output transmittance, related to spatial transformation of the beam profile after the beam collapses into a filament. Thereby, we observe unique features on the optical response of the setup when the pinhole is placed at various positions with respect to the focal plane of the imaging lens and we demonstrate that the critical power for self-focusing, among with other nonlinearities, can

be reliably evaluated by this technique in the femtosecond regime. Further, we discuss a comparison between experimental observations and numerical simulations related to the beam size in the far-field and its transformation into a nonlinear conical wave [245-247] for the well-established case of water.

5.4 Results and Discussion

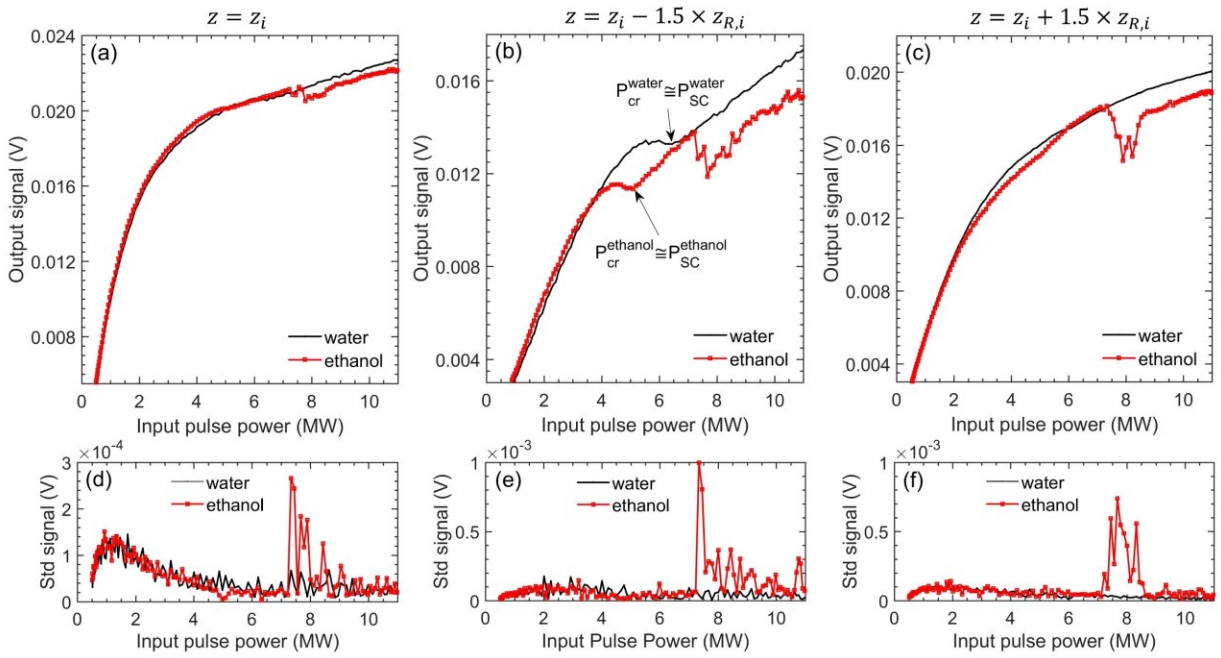

Figure 5.1 Typical experimental measurements in deionized water (black solid lines) and ethanol (red solid lines) by the optical power limiter in the filamentation regime. The top figures (a, b, c) present the output signal averaged over 10 shots and the bottom figures (d, e, f) show the standard deviation of these measurements. Top and bottom figures (presented in column pairs) correspond to different locations of the pinhole: (a, d) $z = z_i$, (b, e) $z = z_i - 1.5 \times z_{R,i}$ and (c, f) $z = z_i + 1.5 \times z_{R,i}$. Distinct features related to collapse of the beam become evident for case (b). In all three cases, a decrease in optical transmission and sudden increase in the standard deviation of the measurement is observed for ethanol at an input power ~7.2 MW, which is identified as an optical breakdown threshold.

We follow a heuristic approach in the experimental procedure, by obtaining measurements for various locations of the pinhole with respect to the imaging plane of the system (Methods). The reasoning lies in the highly dynamic nature of laser filamentation [40], which depends strongly on the beam propagation axis-z. Indeed, near the critical power, a nonlinear focus is initiated in the medium, moving backwards in z as the power increases and the beam collapses into a filament.

Accordingly, the backwards nonlinear focus displacement inside the medium is expected to affect the position of the imaged beam waist in the far-field. In what follows, we present results collected at three different locations of the pinhole: (a) exactly at the imaging plane (the plane that corresponds to the formed focus after lens L2), i.e at $z = z_i$, (b) at 1.5 Rayleigh lengths $z_{R,i}$ before the imaging plane, i.e. at $z = z_i - 1.5 \times z_{R,i}$ and (c) at 1.5 Rayleigh lengths after the imaging plane, i.e. at $z = z_i + 1.5 \times z_{R,i}$. The factor 1.5 is $\sim|MA|^{-1}$, where MA denotes the effective magnification of the system. The latter is noticeably affected by the focal waist position inside the sample, due to linear refraction (Methods/Experimental). Effectively, cases (b) and (c) correspond to the limits of field of focus at the focal plane of lens L1 (Methods/Theoretical).

Figure 5.1 shows typical measurements in the examined liquids (water, ethanol). Case (a) is conceptually the same as the one of the original design of the device [241], however, in the filamentation regime, it appears to bear different features. One cannot distinguish a "step-function"-like transmission, instead, a gradual, monotonic decrease of the latter is observed as the input optical power P_{in} approaches the critical power for self-focusing P_{cr}. In addition, the response of the two liquids appears to be almost identical for both samples for $P_{in} < 7.2MW \equiv P_{OB}^{eth}$, where P_{OB}^{eth} stands for the optical breakdown threshold power for ethanol, which is discussed in the next section. Note that this threshold is evident in the signals of cases (b) and (c).

Contrarily to case (a), in case (b) features related to the collapse of the beam are observed. For both liquids, the optical transmission reaches a plateau (at around ~ 5.3 and $\sim 4.2\ MW$ for water and ethanol respectively), which phenomenologically coincides with a strong phase modulation of the beam. The latter was apparent by visually inspecting the spatial profile of the beam when intercepted by a white card, as it acquires a redder color. After the foresaid plateau is reached, the optical transmission remains almost steady over a small P_{in} interval. Above a critical input power, optical transmission increases monotonically again. It is that power that we identify as the critical power for self-focusing P_{cr}, since, as it will be shown later, it coincides with a beam width transformation and supercontinuum generation threshold P_{SC} in water. The same conclusion can be generalized for the case of ethanol, owing to the similarity of the observed features on the power limiter response and of the qualitative observations on the beam width transformation into white light when intercepted by a white card for both liquids. Indeed, experiments have shown [43] that

the P_{SC} is approximately equal to P_{cr} with $\pm 10\%$ precision for a variety of optically transparent media, which is attributed to the universality of the physics of laser filamentation [41]. Importantly, our analysis, presented in the next paragraphs for the case of water, aims to demonstrate that P_{cr} can be reliably determined by a standalone measurement by the power limiting method operated in case (b) geometry, presumably for a variety of transparent optical media. Finally, note that, despite the common signal features of both examined liquids in case (b), there is a clear difference in the value of P_{in} that these features occur in each one of the samples, indicating the sensitivity of the measurement.

Case (c) exhibited a behaviour more like case (a), nonetheless, the transmitted signals exhibited a smaller slope as a function of P_{in}. In addition, ethanol measurement yielded a slightly weaker optical transmission compared to water at a P_{in} interval before the total collapse of the beam into a filament, however, it was still difficult to identify the features discussed in case (b) for both samples.

Further, we note that the foresaid observed features are not affected significantly by losses related to nonlinear absorption at increasing input powers, which was confirmed in open-apertured optical transmission measurements through the cuvette when filled with the two liquids. Indeed, the optical transmission reduced only by ~1-2% at 6.8 MW for water and at 5.2 MW for ethanol, and by ~5% at 8 MW for water and at 6 MW for ethanol, respectively. Therefore, significant nonlinear losses occur only after the beam collapses into a filament, most likely due to increased plasma generation and direct multiphoton absorption in the liquids.

5.4.1 Evaluation of nonlinearities

5.4.1.1 Optical breakdown

The criterion for the determination of P_{cr} as described by Soileau et al. [241] in their original work, was established by monitoring the standard deviation of normalized transmission measurements through the pinhole (calculated over 5 shots at each input power). The authors observed that the value of the foresaid standard deviation increases by an order of magnitude at P_{cr} and subsequently suddenly drops. A similar behaviour was observed in our experiments solely for the case of ethanol. The event was recorded only after an input pulse power of ~ 7.2 MW, which was accompanied by

a sudden drop on the optical transmission and a spark ignition inside the sample, as visually inspected to have been developed near the geometrical focus, implying the manifestation of optical breakdown.

As was demonstrated for example in [72], typically electron densities of the order of 10^{-18} cm^{-3} are reached during filamentation by pulses of ~50 fs FWHM, via multiphoton ionization in a transparent medium, which is well below the critical plasma density of ~10^{-21} cm^{-3} for optical breakdown. The latter can be reached only by subsequent avalanche ionization, which depends implicitly on the focusing geometry (and explicitly on the developed intensity), on the optical properties of the medium, the ionization potential and the related cross section for cascade ionization [41, 72]. Therefore, we attribute the observed spark ignition to favorable conditions for optical breakdown via avalanching in the case of ethanol at ~7.2 MW. Notably, simultaneous manifestation of both optical breakdown and filamentation is possible under certain focusing conditions inside a given sample, which is characterized by a decrease of the repetition rate of the pulse (here transformed in white light at the specified input power for ethanol), which was observed in our experiments and also reported in Figure 6c of reference [72].

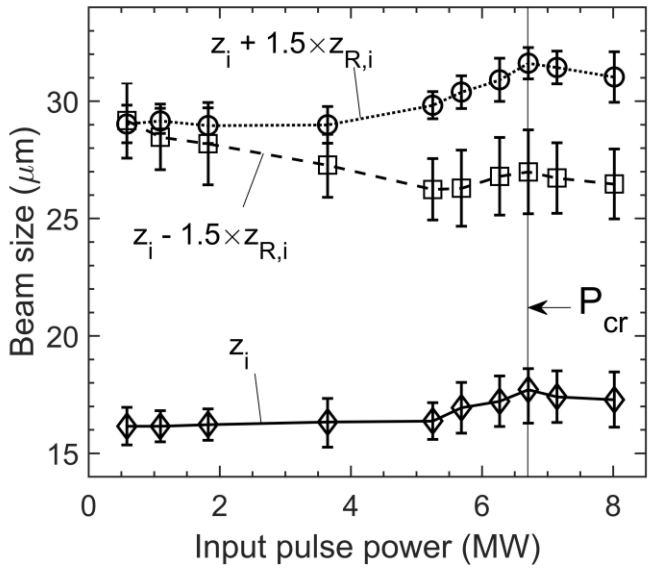

Figure 5.2 Imaged (far-field) beam size dependence on the input pulse power for deionized water at the three examined z-coordinates. In the far-field, a maximum divergence should correspond to a minimum beam size near the focal plane inside the sample. There is a strong implication of beam-width transformation due to the collapse, therefore, the local maximum at 6.7 MW is identified as the critical power for self-focusing P_{cr}.

5.4.1.2 Critical power for self-focusing

Further, we evaluated experimentally the power dependence of the far-field beam size ($1/e^2$) near the imaging plane that is formed after L2 (see schematic in Methods section) when the cuvette is filled with water. The results (Figure 5.2) show how the imaged beam size undergoes a transformation while P_{in} approaches P_{cr}. Initially, it remains almost the same at z_i, it marginally increases at $z_i + 1.5 \times z_{R,i}$, while it reduces at $z_i - 1.5 \times z_{R,i}$ up to an input pulse of $\sim 5.3\ MW$, which coincides with the strong phase modulation observed experimentally. After that point, it increases for all three examined planes, presumably due to a shift in the angular divergence of the beam's wavefront in the presence of strong self-phase modulation. The behaviour persists up to a critical power, (which we identify as P_{cr}) above which it drops for all planes. The initially opposing trend of beam size versus P_{in} for $z = z_i - 1.5 \times z_{R,i}$ compared to the rest two examined z, clarifies the signal behaviour in case (b) of Figure 5.1. The beam size undergoes a sharper shift (reaching a local minimum) for $P_{in} \sim 5.3 MW$, i.e., around the experimentally observed onset power for strong phase modulation of the pulse. Accordingly, such a sharp shift influences the recorded signal on the apertured detector since a larger beam size typically results in a decrease on the axial fluence of the beam. Finally, we note that the experimental $1/e^2$ beam size evaluation is approximate near P_{cr} since the beam is known to be gradually transformed into a nonlinear, Bessel-like conical wave upon collapse into a filament [246-248].

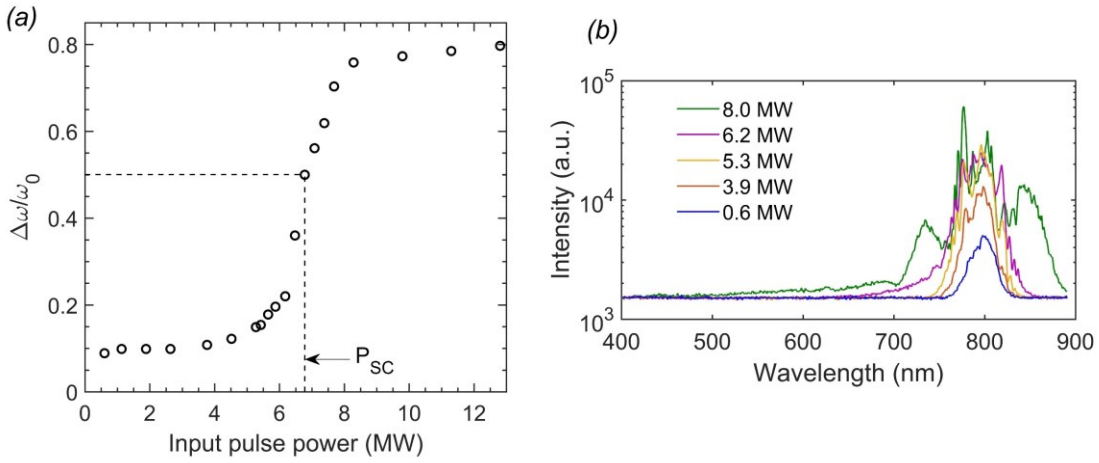

Figure 5.3 (a) Relative spectral broadening of the pulse as a function of the input power in deionized water. The estimation has been performed as in [249]. Note that the authors of [249] have chosen $\Delta\omega/\omega_0(P_{in}=P_{SC}) \approx 0.5$, so here, P_{SC} is close to 6.7 MW. (b) Experimentally obtained supercontinuum spectra for water as a function of the input power.

5.4.1.3 Supercontinuum generation

Importantly, P_{cr} seems to be very close to P_{SC}, defined as the dramatic increase on the pulse spectrum, an assessment that has also been drawn, for example, in references [43, 72, 249]. We illustrate this result by a measurement of the relative spectral broadening of the pulse as a function of the input pulse power in water (as performed in [249]). Based on the above analysis shown in Figure 5.3, we conclude that $P_{cr}^{water} \cong P_{SC}^{water} \approx 6.7\ MW$ and we evaluate $P_{cr}^{ethanol} \cong P_{SC}^{ethanol} \approx 5.2\ MW$ from the optical limiter measurement [case (b) of Figure 5.1].

5.4.1.4 Nonlinear refractive index

Having marked the onset for P_{cr} we derive the nonlinear index of refraction n_2 of the examined liquids from our measurements, accounting for the following: First, as it has been demonstrated by Fibich et al. [64], we assume that the threshold for filamentation, must coincide with the critical power for self-focusing. The same author has demonstrated that for a Gaussian input spatial beam profile the critical power for self-focusing is inversely proportional to the nonlinear index of refraction, according to [64, 68]

$$P_{cr,0} = \frac{3.79\lambda^2}{8\pi n_0 n_2} \tag{5.1}$$

Another factor considered, which significantly affects the critical power for self-focusing, is the beam propagation factor M^2. We use a relation determined by Porras et al. [250], which has been derived through a generalized ABCD propagation law and it reads

$$P_{cr} = P_{cr,0} M^4/\psi \tag{5.2}$$

where ψ is a dimensionless factor related to the beam profile distribution and is equal to 1 for Gaussian profiles. Using Equation 5.1 and 5.2 and , $M^2 = 1.4$ (Methods/Experimental) and the values of the linear refractive index $n_0 = 1.33$ and 1.36 for water and ethanol respectively [251], we have calculated n_2 for the examined liquids. The results are shown in Table 5.1 along with values cited in the literature, obtained by different techniques, for comparison.

Table 5.1 Evaluation of the Kerr nonlinear index of refraction of deionized water and ethanol: A comparison between values in the literature and our measurement. [a] Only the electronic n_2 obtained in [252] is considered. [b] Larger pulsewidths are examined in [253], however, only the smallest value is considered here, to exclude slower contributions on the value of n_2. [c] The value of n_2 in [254, 255] is given in 10^{-13} esu, thus we have calculated $\chi^{(3)}_{xxxx}$(esu) = $n_0 n_2$(esu)/(8π) and converted in m^2/W^2 by applying the relation $n_2(m^2/W^2) = (3.95\times10^{-6})/[n_0^2\chi^{(3)}_{xxxx}(esu)]$ [61]. (NA = Non available)

Reference	Method	$n_2\left(\times 10^{-20} m^2/W\right)$		Wavelength (nm)	Pulsewidth (FWHM)	Repetition rate
		water	ethanol			
[252]	Beam deflection [a]	$2.5 \pm 20\%$	$3.2 \pm 20\%$	800	150 fs	1kHz
[253]	Ellipse Rotation [b]	$3.4 \pm 20\%$	$4.5 \pm 20\%$	790	60 fs	NA
[256]	Spectral Interferometry	$1.9 \pm 10\%$		815	90 fs	1kHz
[255]	Optical Kerr Effect [c]	$1.9 \pm$ NA	$2.4 \pm$ NA	820	130 fs	76 MHz (chopped at NA frequency)
[72]	Supercontinuum onset	$2.0 \pm$ NA		810	45 fs	1kHz
[257]	z-scan	3.5 ± 1.9		1150	90 fs	10 Hz
[254]	Optical Kerr Effect [c]	$1.5 \pm$ NA	$2.9 \pm$ NA	1024	10 ps	150 MHz (100 shots)
Our work	Power limiting	$2.1 \pm 20\%$	$2.7 \pm 20\%$	800	55 fs	50 Hz

In Table 5.1, the ultrafast (isotropic) nonlinear response of the two liquids, as evaluated by the power limiting method herein, is in fair agreement with measurements presented in the literature by various techniques at a wavelength around ~800 nm. For the case of water, at a longer wavelength of 1150 nm, the nonlinear refractive index is expected to increase as demonstrated experimentally in [257], an observation that holds for increasing wavelengths up to 1250 nm. Further, we account that for data at a wavelength of 1024 nm [254], a fair comparison of n_2 can still be performed with our measurements. In terms of pulsewidth excitation, Miguez et al. [253] have demonstrated that for pulsewidth excitation shorter than 200 fs the ultrafast component of the nonlinearity remains almost unchanged for the two liquids. Although that according to that observation one would not expect a significant influence of the pulsewidth on n_2 value within the range of <200 fs, the value of P_{cr} might still be affected due to group velocity dispersion, while Equation 5.1, which is a steady-state result [64], is usually applied as a reference in the case of ultrafast pulses [40, 64]. Further, results presented in [253] imply that for pulses of 10 ps, n_2 can increase up to 40 % (30% increase is discussed for ethanol in [252]) due to contributions from molecular reorientation. However this is not observed when comparing the values of n_2 reported

by [254] with the rest of the reported values shown in Table 5.1. The relative magnitude of the measured nonlinearities between water and ethanol is yet demonstrated. Finally, we should note that direct methods such as the z-scan technique, beam deflection, supercontinuum onset and the power limiting method typically require low repetition rate laser sources (<1 kHz) to ensure that thermal effects are not affecting the evaluated nonlinearities.

5.4.2 Theoretical interpretation

In what follows, we examine theoretically the experimental observations of the imaged (in the far-field) beam size dependency on P_{in} in water. Let us first note that all three examined far-field beam profile distributions near the focal plane of imaging lens L2 are compressed by the same ratio $d_i/d_o \equiv |MA|$, where d_i is the distance from L2 to the imaging far-field plane at z_i, d_o is the distance of lens L2 from the focal plane of lens L1, located at z_f, and MA denotes the linear magnification of the system. The latter remark imposes that, upon lens transformation, the planes near the focal plane of L1 at $z_f \pm z_{R,f}$ correspond to the imaging (far-field) planes at $z_i \mp z_{R,i} \times |MA|^{-1}$ (Methods).

The power dependence of the calculated beam waist size w_f (at the focal plane of L1) inside the propagation medium (Figure 5.4d) exhibits a behaviour different than the one measured at the imaging (far-field) planes, as expected. The imaged far-field beam size w_i versus P_{in} should be calculated instead and compared with the experiment. We first calculated the far-field electric field amplitude distribution $S(t, k_\perp)$ at an arbitrary distance $d_f \gg w_f$ from the examined z coordinates. We integrated in time (since the experimental measurements are time-integrated) to find the radiant energy angular spread distribution (shown in Figure 5.4a,b,c) over a time-averaged instantaneous transverse wavenumber, i.e., $\langle k_\perp \rangle \equiv \frac{1}{\mathcal{T}} \int_0^{\mathcal{T}} dt k_\perp$. From the resulting distributions we have calculated the second moments (twice the standard deviation $\sigma_{\langle k_\perp \rangle}$) of the power dependent $\langle k_\perp \rangle$. Assuming that the pulse undergoes only small spectral modulation before the critical power, we use the relation $\theta \approx k_\perp c/(\omega_0 n_0)$ [248], so that $2\sigma_{\langle \theta \rangle} \approx 2\sigma_{\langle k_\perp \rangle} c/(\omega_0 n_0)$, to calculate the standard deviation of the divergence $\langle \theta \rangle$ at the fundamental frequency ω_0 as a function of P_{in}. Apparently, this is an oversimplification when P_{in} approaches P_{cr}, in view of strong dispersion while the spectrum of the pulse increases (Figure 5.3). Thus, as shown in Figure 5.4e, the divergence

increases versus P_{in}, however, with expected deviations as P_{in} approaches P_{cr}. Even so, as is, w_f and $2\sigma_{\langle\theta\rangle}$ versus P_{in} allow for a first order approximation of the imaged far-field beam size w_i (see Methods), shown in Figure 5.4f.

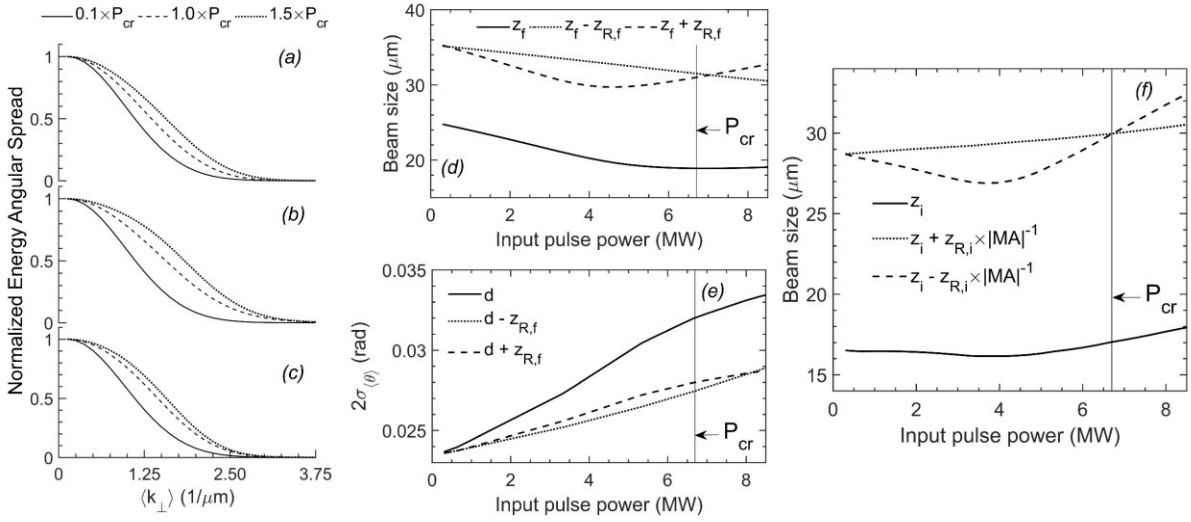

Figure 5.4 Numerical calculations based on Equations 5.3-5.4 (Methods) in water. (a), (b) and (c) show the time-integrated and normalized far-field spectra $S(t, k_\perp)$ versus the time-averaged instantaneous transverse wavenumber $\langle k_\perp \rangle$, calculated by the Hankel transformation of the solution of Equations 5.3-5.4 at (a) $z = z_f - z_{R,f}$, (b) $z = z_f$ and (c) $z = z_f + z_{R,f}$ respectively. The distributions are identified as the radiant energy angular spread, understood as the far-field counterpart of the pulse fluence (radiant energy exposure). (d) Beam size inside the propagation medium (near the focal plane of L1) versus input pulse power. (e) The standard deviation of $\langle k_\perp \rangle$ taken from (a), (b) and (c) has been used to calculate the standard deviation of divergence $\langle \theta \rangle$ of the beam as a function of the input power at a distance d from reference $z = z_f = 0$ (first-order approximation). (f) Calculated imaged beam size in the far-field versus the input pulse power (first-order approximation).

A good agreement is observed between experiment (Figure 5.2) and simulations (Figure 5.4f) up to $\sim$4.5 MW. The agreement gradually breaks down beyond that point, which is a result of the simplification $\langle \theta \rangle \approx \langle k_\perp \rangle c/(\omega_0 n_0)$. In fact, $\langle k_\perp \rangle$ can be related to the instantaneous frequency of the pulse in a self-phase modulation process, leading to the better approximation $\langle \mathrm{k}_\perp \rangle \sim \frac{\omega_0 n_0}{c} \langle \theta(t) \left[1 - \frac{l_p}{c} \partial_t n(t)\right] \rangle$, where $n(t)$ and $\theta(t)$ are respectively the intensity (and implicitly time) dependent refractive index and divergence, and l_p denotes the propagation distance of the pulse. Thus, it becomes evident that the former simplified relation between θ and $\mathrm{k}_\perp$ does not hold as P_{in} approaches P_{cr} in view of the strong modulation of the pulse spectrum $\Delta\omega \propto \frac{l}{c} \partial_t n(t)$ (see Figure

5.3). Dependency of phase modulation on l_p also implies in practice that the observed signal features of the apparatus (Figure 5.1) are dependent on the location of the focal plane inside the cuvette, which in turn is related to the effective magnification of the system due to linear refraction (see Methods).

In effect, upon collapse the beam transforms into a nonlinear conical (Bessel-like) wave and as a result the radiant energy angular spread varies at the generated wavelengths of the expanded spectrum surrounding the fundamental, according to the Fourier-space relation $k_{\perp}(\omega) = k(\omega)\, sin\, \theta(\omega)$ [40, 245-248]. Consequently, the radiant energy angular spread of the fundamental wavelength will be limited upon this transformation beyond the critical point, as energy is transferred at other wavelengths and flows at high angles (X-wave formation for normal dispersion), forming a rim that surrounds the central spot of the generated white light.

5.5 Conclusion

An optical power limiter has been employed to determine ultrafast optical nonlinearities of two transparent liquids (deionized water and ethanol) in the femtosecond filamentation regime. The technique has been utilized in the past only in longer pulse regimes (>1 ps) leading to optical breakdown inside the samples, which typically occurs at optical pulse powers lower than the critical power for self-focusing. In contrast, in the femtosecond regime, the optical response of transparent liquids is governed by distinct features in the context of the studied technique. Particularly, we find that the threshold for self-focusing can be distinguished in the output signal when the apertured detection is located behind the conjugate focal plane of the imaging system, at a distance governed by the field of focus of the first focusing lens and the effective magnification. A presented theoretical analysis indicated how the effect is related to the spontaneous transformation of the beam into a nonlinear conical wave at the onset of filamentation.

Importantly, in this work, we demonstrated that the use of the power limiting setup in the femtosecond filamentation regime can be reliably utilized for future studies of ultrafast optical nonlinearities of various transparent materials, of which the evaluation is a challenging task even with the z-scan technique. Finally, the power limiting setup is anticipated to be a useful tool both

for fundamental studies (e.g., competition between filamentation and optical breakdown) and the development of novel femtosecond laser filamentation based applications.

5.6 Methods

5.6.1 Experimental

Our setup is shown in Figure 5.5. We employed transform-limited pulses of 55 fs pulsewidth (defined by the full width at half maximum FWHM) produced by a Ti:Sapphire amplifier, operating at a repetition rate of 50 Hz. The laser beam, which had a Gaussian spatial profile and initial $1/e^2$ size of ~2.9±1.5% mm, was collected by a lens L1 with a focal length of 200 mm. The beam waist of the focused beam in air was formed at approximately the same position with the focal plane of L1 and was estimated with a knife edge technique to be $w_f \sim 24.5 \pm 3\%\ \mu m$ ($1/e^2$), with a Rayleigh length ~1.680 mm. A second lens L2 with a focal length of 100 mm was positioned at a distance $d_o \sim 300\ mm$ apart from the focal plane of L1. Thus, L2 imaged the focused beam spot after $d_i \sim 150\ mm$ from its center with a magnification $MA_0 \sim -0.5$ (Figure 5.6a). Indeed, the focused beam waist after L2 was estimated to be ~12.4±5% μm with a knife edge technique in air. The beam propagation factor M^2 of the beam was measured to be ~1.4 after both L1 and L2 in air.

A 10 mm thick optical cuvette was positioned so as its center (5 mm from its entrance window along the beam propagation direction) coincided with the focal plane of L1. When filled with the examined liquids, the beam waist was estimated to be formed at $\sim n_0 \times 5$ mm from the entrance window, due to the refractive index difference between the propagation mediums and air in the linear regime. Accordingly, the Rayleigh length at the focal plane of L1 is estimated $z_{R,f} \sim n_0 \times 1.680\ mm$. These effects were confirmed experimentally by measuring the beam radius after the cuvette, when filled with water. Further, the addition of water in the optical cuvette, resulted in a change of the size of the beam collected by L2, a shift of the imaged spot position after L2, and also a change of the dimension of the imaged focal spot ($w_i \sim 16.2 \pm 5\%\ \mu m$) and Rayleigh length at the imaging plane ($z_{R,i} \sim 0.745\ mm$), which were re-estimated by a knife edge technique in the linear regime. Accordingly, a shift of the effective linear magnification $MA \sim -0.67$ is observed (compared to $MA_0 \sim -0.5$). Notably, w_i, $z_{R,i}$ and $|MA|$ increase when the focal plane is located closer to the output window of the cuvette in comparison to locations near the input

window, because linear refraction affects the radius of curvature of the beam inside the examined medium [258].

A pinhole (15 μm in diameter) was positioned approximately at the imaged focal plane formed after L2, when the cuvette was filled with water. The pinhole was placed at a motorized translation stage, which allowed fine adjustments over the beam propagation direction. The portion of beam that passes through the pinhole was collected by a photodetector. A neutral density filter was placed before the pinhole to attenuate the light intensity. The size of the pinhole allowed only a very low signal to pass through. On that account, the photodetector was connected to a lock-in amplifier for sensitive measurement of the generated output signal voltage. A variable attenuation of the beam was set by a combination of a half-waveplate and a polarizer. A motorised rotational stage allowed controlling of the waveplate by a personal computer, which was used to automate the measurements collected by the lock-in amplifier. Data were collected for each input power value and averaged over 10 laser shots. For each mean value of the data points, the standard deviation was calculated to estimate the statistical error. The measurement uncertainties presented in Table 3.1 are conservatively estimated to 20%, which include absolute uncertainties in P_{in}, due to laser energy fluctuations, pulsewidth, M^2 *and* ψ value uncertainties, and relative uncertainties in the determination of P_{cr}.

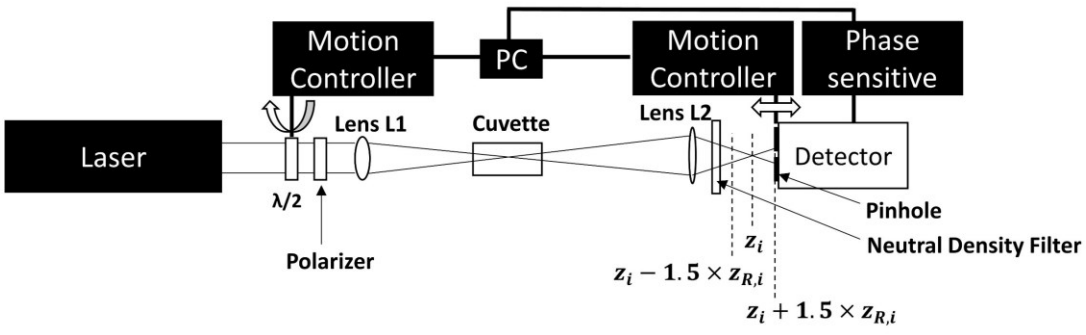

Figure 5.5 The optical power limiter experimental setup. A combination of a half-waveplate and a polarizer are used to control the power of the laser pulses. Two positive lenses are used to focus the beam on the sample and image onto the apertured (by a 15 μm pinhole) photodetector. The setup has been modified by placing a pinhole on a motor stage to allow translation towards z coordinate.

For the measurements of the $1/e^2$ beam width in the far-field as a function of input pulse power, a knife edge technique was used. For the measurements of the relative spectral broadening $\Delta\omega/\omega_0$ presented in Figure 5.3, we have replaced the pinhole and the detector shown in Figure 5.5 with a fiber spectrometer and appropriate neutral density filters to collect the far-field spectrum of the pulse after propagation in water. We followed the methodology reported in [249] so that $\Delta\omega = \omega_b - \omega_r$, where ω_b and ω_r stand for the maximum broadening towards bluer and redder frequencies respectively. The latter are recorded at the frequencies where the signal drops below the detection threshold, which we identify as 10% of the average baseline fluctuations (each measurement has been averaged over 10 shots). As reported in [43], the selected signal level shall not change the result since the signal drops abruptly at the anti-Stokes wing. We further note that the apparatus cut-off on the red side (Stokes broadening) was at ~890 nm, possibly leading to an underestimation of the relative spectral broadening at high input powers (e.g., in Figure 5.3, for $P_{in} > 8$ MW). Nonetheless, we note that beyond that power, no significant further broadening occurs at the anti-Stokes wing for water. Besides, the idea of this approach was to quantify (with some uncertainty) the abstract definition of supercontinuum generation as the dramatic increase of the pulse spectrum when transmitted through the medium [249].

5.6.2 Theoretical

5.6.2.1 Numerical model

We used a theoretical model for the propagation of femtosecond laser pulses inside water (the most studied liquid medium of the above two) [63]. For a pulse propagating along the z axis, whose reference time frame moves at the group velocity u_g, the coupled system of differential equations that give the complex scalar envelope of the electric field $\hat{\mathcal{E}}(r,\omega,z) = \mathcal{F}\{\mathcal{E}(r,t,z)\}$ (written in Fourier space, where $\mathcal{F}\{\ \}$ stands for the Fourier transform, r is the radial coordinate, ω is the radial carrier frequency, t is the retarded time) and the electron density $n_e(r,t,z)$, reads

$$\frac{\partial\hat{\mathcal{E}}}{\partial z} = \frac{i}{2\kappa(\omega)}\nabla_T^2\hat{\mathcal{E}} + \frac{[k^2(\omega)-\kappa^2(\omega)]}{2\kappa(\omega)}\hat{\mathcal{E}} + \frac{k_0}{\kappa(\omega)}\left[i\hat{T}^2\left(\frac{\omega_0}{c}n_2\right)\left|\hat{\mathcal{E}}\right|^2\hat{\mathcal{E}} - \hat{T}\frac{\beta_K}{2}\left|\hat{\mathcal{E}}\right|^{2K-2}\hat{\mathcal{E}} - \frac{i}{2n_0n_{e,c}}\left(\widehat{n_e\mathcal{E}}\right)\right] \quad 5.3$$

$$\frac{\partial n_e}{\partial t} = \frac{\beta_K}{K\hbar\omega_0}\left(1 - \frac{n_e}{n_n}\right)|\mathcal{E}|^{2K} \tag{5.4}$$

Where ω_0, k_0 is the pulse central frequency and central wavenumber respectively, $k(\omega) = \frac{\omega}{c}n(\omega)$, $n(\omega)$ is the linear refractive index of water [259], ∇_T^2 is the transverse Laplacian, $\kappa(\omega) = k_0 - \omega/u_g$, $n_2 = 2.1 \times 10^{-20} m^2/W$ is the experimentally evaluated nonlinear refractive index, $\beta_K = 1 \times 10^{-47} cm^7 W^{-4}$ is the multiphoton absorption cross section of water, $K = 5$ is the required number of simultaneously absorbed photons of energy $\hbar\omega_0$ ($\hbar$ is the reduced Planck's constant) to exceed the ionization potential of water $U_i = 6.5eV$, $\hat{T} = 1 + \frac{i}{\omega}\frac{\partial}{\partial t}$ is the self-steepening operator, $n_{e,c} = \varepsilon_0 m_e \omega_0^2/e^2$ is the critical plasma density (ε_0 is vacuum's dielectric permittivity, m_e is the electron's mass and e is the elementary electric charge) and $n_n = 6.68 \times 10^{22} cm^{-3}$ is the density of neutrals in the medium.

The initial conditions that are given to start propagation and match the experimental conditions, correspond to a Gaussian envelope distribution

$$\mathcal{E}(r,t,0) = \sqrt{\frac{2P_{in}}{\pi w_0^2}} exp\left(-\frac{r^2}{w_0^2} - i\frac{k_0 r^2}{2R} - \frac{t^2}{t_p^2}\right) \tag{5.5}$$

In this relation, $w_0 = 77\ \mu m$ (experimentally evaluated) denotes the input beam radius at the entrance of the cuvette, P_{in} is the input peak power of the pulse, t_p is the pulsewidth (related to the FWHM pulsewidth via $t_{FWHM} = t_p\sqrt{2log(2)}$), $R = d - \frac{z_{R,f}^2}{d}$ is the radius of curvature, $d = n_0 \times 5mm$ is the axial distance that the beam waist is formed in the cuvette with respect to the entrance window and $z_{R,f} = n_0 \times 1.68\ mm$ is the experimentally evaluated Rayleigh distance, where n_0 is the refractive index of the medium at the central frequency (taken as 1 for air and 1.33 for water). To account for the effect of imperfect beam quality, we have multiplied the range of wavelengths λ with the experimentally evaluated factor $M^2 = 1.4$, a transformation that can be used within the paraxial approximation to estimate time integrated quantities, where phase effects are of no consequence [260].

5.6.2.2 Beam size at the focal and at the imaging (far-field) planes

We evaluated the input power dependence of the beam size at the examined z coordinates near the focal plane of L1 inside the propagation medium. To do so, we solved Equations 5.3 - 5.4 and we integrated the solutions in time, to determine the fluence of the pulse at a given z, and subsequently we calculated the beam size according to the second moments definition. Next, we evaluated the far-field distribution of the electric field amplitude $S(t, k_\perp)$ by performing a Hankel transform at the examined z-coordinates. The latter is a good approximation of the Fresnel-Kirchhoff integral, accounting for a plane of observation at a distance $d_f \gg w_f$, where w_f denotes the beam waist at the focal plane of L1.

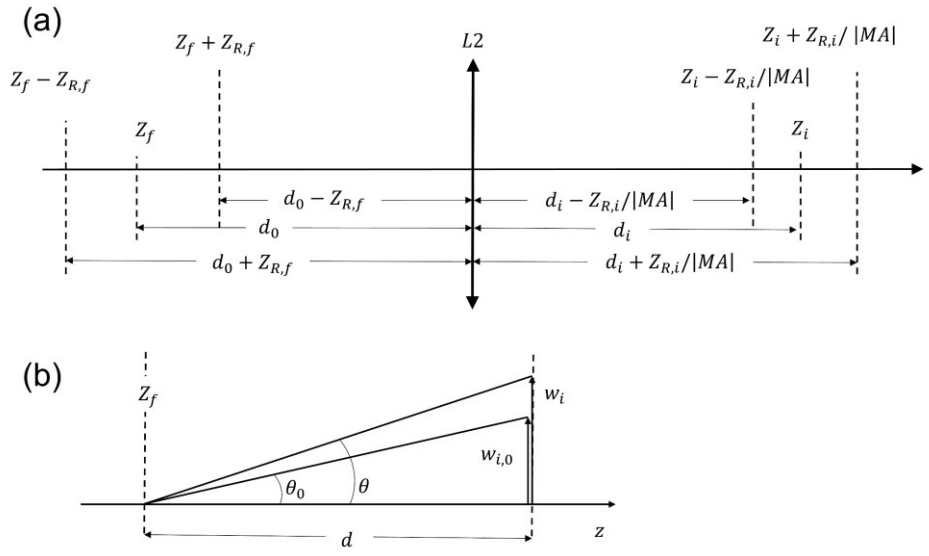

Figure 5.6 Conceptual diagrams used for calculation of the beam size at the imaging (far-field) planes. (a) The correspondence of focal and imaging planes so that the linear magnification of the system MA remains invariant. (b) A diagram that shows how the beam size $w_{i,0}$ at a distance d in the far-field shifts to w_i when accounting for the power dependence of the divergence θ.

5.6.2.3 Observation planes near the focal and imaging planes

The observation planes at $z_f \pm z_{R,f}$ (around the focal plane of L1) are located $d_0 \mp z_{R,f}$ away from L2, where d_o is the distance from the focal plane of lens L1 to lens L2 itself (Figure 5.6a). Therefore, since $z_{R,f} = z_{R,i}/(MA)^2$, the corresponding imaging (far-field) planes should be located at a distance $d_i \mp z_{R,i} \times |MA|^{-1}$ apart from L2, so that the linear magnification of the system $MA =$

$-d_i/d_0$ remains consistent. In other words, the observed electric field amplitude distributions at planes $z = z_i \mp z_{R,i} \times |MA|^{-1}$ (i.e., at $d_i \mp z_{R,i} \times |MA|^{-1}$ away from L2) are equivalent to the ones calculated by the Hankel transform of the electric field amplitude distributions at planes $z = z_f \pm z_{R,f}$ (i.e., at $d_0 \mp z_{R,f}$ behind L2).

5.6.2.4 Imaged (far-field) beam size calculations

The power-dependent divergence θ over the divergence θ_0 in the linear regime, quantifies the imaged far-field beam size change with respect to the linear regime, because $\frac{w_i}{w_{i,0}} \cong \frac{\theta}{\theta_0}$, where $w_{i,0}$ is the imaged far field beam size if $\theta = \theta_0$ (Figure 5.6b). Considering the magnification of the optical system MA in the linear regime, it holds $w_{i,0} = MA \times w_f$. Thus, the imaged spot size can be estimated as

$$w_i(z_i) \cong (MA) \times \frac{\theta}{\theta_0} w_f(z_f) \tag{5.6}$$

Finally, we estimated the beam size at planes $z_i \pm z_{R,i} \times |MA|^{-1}$ starting from

$$w_i\left(z_i \pm z_{R,i} \times |MA|^{-1}\right) \cong (MA) \times \frac{\theta}{\theta_0} w_f\left(z_f \pm z_{R,f} \times |MA|^{-1}\right) \tag{5.7}$$

Applying the paraxial equation $w(z) = \sqrt{1 + (z/z_R)^2}$ for $z_f \pm z_{R,f} \times |MA|^{-1}$ and for $z_f \pm z_{R,f}$, we find:

$$w_i\left(z_i \pm z_{R,i} \times |MA|^{-1}\right) \cong (MA) \times \frac{\theta}{\theta_0} \sqrt{\frac{1}{2} + \frac{1}{2(MA)^2}} w_f\left(z_f \pm z_{R,f}\right) \tag{5.8}$$

We used Equations 5.6-5.8 to plot Figure 5.4f, where we have used data shown in Figure 5.4e so that $\sigma_{\langle\theta\rangle} \to \theta$.

CHAPTER 6 ARTICLE 3: FEMTOSECOND NEARLY RESONANT SELF-FOCUSING IN GOLD NANOROD COLLOIDS

Research article published in Optics Express in 2021[4]. The supporting information for this article is reprinted in Appendix B of this thesis.

6.1 Authors and author contributions

Leonidas Agiotis and Michel Meunier. L.A. designed the research, conducted the experiments, analysed the data, performed theoretical and numerical analysis, and wrote the main manuscript. M.M. supervised and discussed the work and reviewed the main manuscript.

6.2 Abstract

We evaluate the threshold power for self-focusing in gold nanorod colloids of varying concentration by a power limiting method in the femtosecond filamentation regime. The pulses are tuned near the longitudinal plasmon peak of the nanorods, leading to saturation of linear absorption and reshaping of the particles. We evaluated the last two effects by optical transmission measurements and spectroscopic analysis and estimated that considerable particle deformation does not occur before the collapse of the beam. We performed numerical simulations based on the experimental results, and evaluated only a subtle, monotonically increasing enhancement of the nonlinear refractive index of the host material (water) as the nanoparticles concentration increases. The role of higher-order contributions is discussed. Our work provides an alternative characterization approach of ultrafast nonlinearities in absorbing media. It further emphasizes that self-focusing of intense femtosecond pulses in gold nanocomposites is hampered by the ultrafast modulation of the susceptibility of the metal.

---

[4] Femtosecond nearly resonant self-focusing in gold nanorod colloids," *Optics Express* **29**, 39536-39548 (2021). https://doi.org/10.1364/OE.441117

6.3 Introduction

In several recent publications on artificial high-order self-phase modulation in plasmonic nanocolloids under picosecond pulse excitation [35, 89, 173, 174, 261, 262], authors have suggested that these studies can be extended in the femtosecond regime depending on the origin and strength of the nonlinearity. The observation of artificial nonlinear response has been attributed to a judicious management of high-order nonlinearities by varying the concentration of the particles in the suspension. Interestingly, the reported theoretical formulation of the susceptibility of the effective medium is identical to the one that corresponds to instantaneous electronic polarization. However, in the femtosecond timescale the contribution of the metallic nano-inclusions to the effective nonlinear polarization is significantly weaker compared to the picosecond timescale [183, 263], where non-instantaneous effects (i.e., electron-phonon coupling after electron thermalization) give rise to stronger contributions [8, 9, 124, 264, 265]. In addition, possible particle deformation due to energy absorption by the plasmon modes should be considered [22-26, 266-271]. Such limitations hinder major difficulties in the characterization of weak refractive nonlinearities of colloidal gold in the femtosecond timescale by direct methods, such as the z-scan technique. For instance, analytical treatment of z-scan requires thin sample approximation, hence, limitations are introduced by the comparable nonlinearity of the optical cuvette. Further, the latter is usually slightly wedged, which, in conjunction with the requirement of a long translation stage, introduces problems due to beam walk off.

A possible approach to mitigate the problem of optical characterization with a direct method would be to investigate the threshold for self-focusing in thick samples, which alleviates difficulties related to a moving sample and restrictions due to the requirement of thin sample utilization. The theory predicts that an enhancement of the instantaneous Kerr-type nonlinearity of the host material in the presence of nano-inclusions should in principle appear only near the resonance of the latter [4, 5]. Nonetheless, losses due to absorption by the particles (linear or nonlinear) should be accounted for, in the determination of the threshold for self-focusing [64, 272-274]. Effectively, the concentration of particles is a key parameter to explore the possibility of nonlinearity enhancement during self-focusing of femtosecond pulses under nearly resonant interaction with the surface plasmon modes.

In this work, we investigate the threshold for self-focusing in gold nanorod colloidal solutions of varying concentrations under femtosecond laser irradiation, by means of an alternative approach, namely the power-limiting method [239, 272]. We aim to evaluate possible nonlinear refraction enhancement of the host material (water) by considering nonlinear losses (absorption saturation) and particle deformation effects as the particles' concentration increases. The latter has been demonstrated experimentally and theoretically to be a key parameter on the nonlinear response of plasmonic nanocomposite materials since it allows management of higher-order nonlinear contributions to the effective susceptibility, however, only for pulses longer than tens of picoseconds [89, 173, 174]. Here, we discuss in detail this possibility in the femtosecond regime.

6.4 Materials and methods

6.4.1 Sample preparation

We have studied self-focusing in Au nanorod aqueous (water) suspensions (Nanopartz) of 10-nm diameter and 38-nm length with a longitudinal plasmon peak around 770 nm. We have prepared samples of varying concentrations, starting from a sample of concentration $C1 = 6.73 \times 10^{11} ml^{-1}$, given by specifications obtained from the company. Solutions of $C1$ were concentrated approximately 3, 5, 9, 13 and 19 times through centrifugation to produce samples of varying concentrations labelled as $C3$, $C5$, $C9$, $C13$, $C19$ respectively. A sample of concentration labelled $C0.5$ was prepared by diluting a sample of $C1$ approximately 2 times. All solutions were filtered

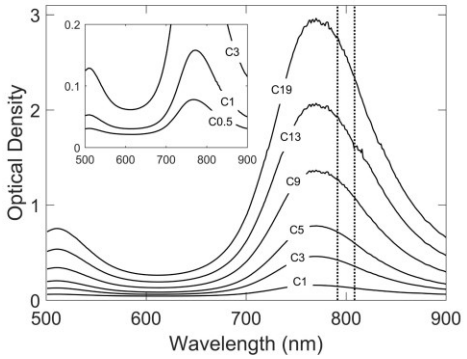

Figure 6.1 Initial optical density spectra of the prepared samples of varying concentration. The dashed lines indicate the FWHM bandwidth of the excitation laser. The inset figure is used for clarity to demonstrate the initial optical density spectra of the diluted sample C0.5, relative to samples C1 and C3. The optical path length of the examined samples is 2 mm.

before and after concentration to remove any possible aggregated samples. Absorbance spectra were measured by a UV/Vis/NIR photo-spectrometer (Epoch Microplate Spectrophotometer, BioTek Instruments, Inc., VT, USA) from 500 nm to 900 nm (Figure 6.1).

6.4.2 Nonlinear optical measurements

We aim for the evaluation of the threshold power for self-focusing in gold nanorod colloids. The threshold was determined experimentally, by the power limiting method, described in detail in reference [239]. A Ti:Sapphire laser, FWHM pulsewidth of 55 fs, repetition rate of 50 Hz, central wavelength of 800 nm was employed in all experiments. The studied material is known to exhibit strong saturation of absorption under nearly resonant ultrafast pulsed laser excitation [15, 17-21] which we evaluated by optical transmission measurements.

Following Mohebi et al. [272], we examined the threshold power for self-focusing by the power limiting method at two different positions of the cuvette (optical path of 10 mm) with respect to the + 200 mm focusing lens, as shown in Figure 6.2(a): focal plane located at (I) 5 mm and (II) 1 mm in front of the input window of the empty cuvette. In case I the initial conditions are identical to the ones described in [239] (~77 μm $1/e^2$ beam radius at the input face of the cuvette). In case II, the $1/e^2$ beam radius at the entrance of the cuvette was determined to be ~30 μm. The apertured detection was placed before the imaging plane by 1.5 times the field of focus [239]. The cuvette was filled with 300 μl of each sample, characterized prior to the measurements (Figure 6.1). Experimental trial scans were repeated several times for each sample by gently stirring the cuvette before each experiment so that large number of particles was exposed to the treatment. Each scan of gradually increasing input power deposition lasted ~10 min., while the general behaviour was nearly reproducible after each trial. For the analysis, we only consider the results of the last set of measurements. Following the treatment, the samples were re-examined spectroscopically for the evaluation of particle deformation effects [268]. Indeed, following Link and El Sayed [267], we used standalone spectroscopic analysis since it has been proposed as a convenient and "time-saving" alternative to TEM for photothermal nanoparticle reshaping analysis. Nonetheless, we note that despite the efforts of exposing a large amount of particles to the power limiting treatment, the exposed volume of samples examined spectroscopically is typically large as opposed to the

irradiated one (at each trial). Accordingly, a detailed discussion is provided in section 6.6.1 on deformation analysis implications.

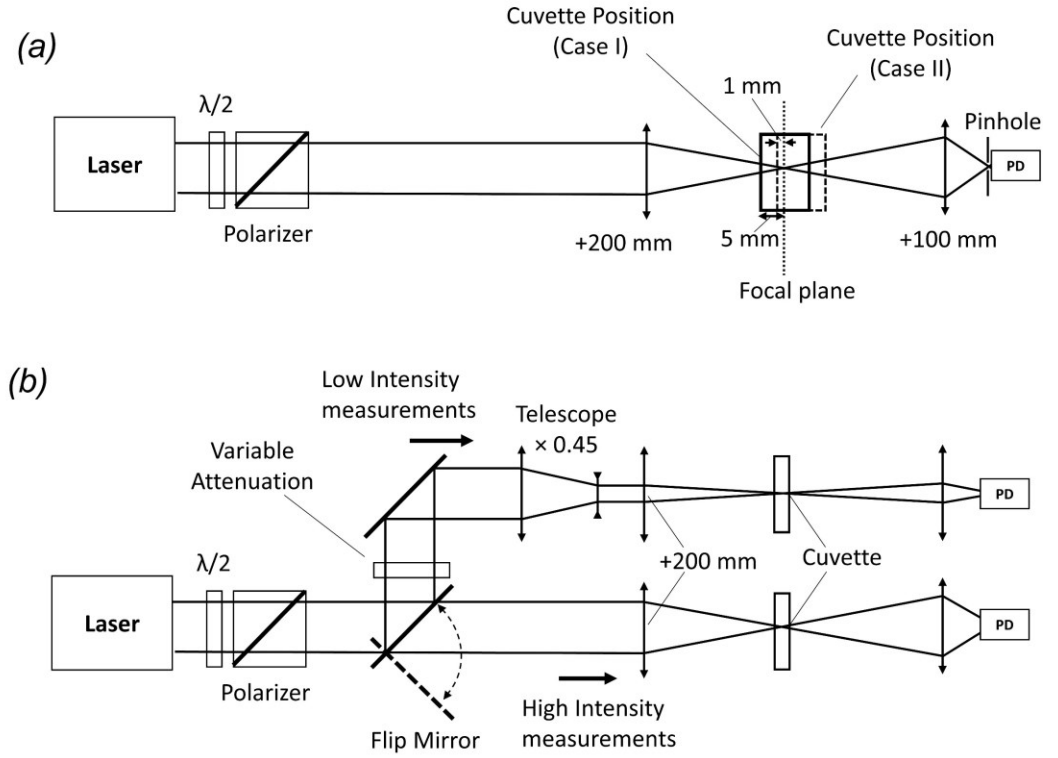

Figure 6.2 (a) The setup of the power limiting method. Two different positions of the optical cuvette with respect to the focus of the +200 mm lens were examined: case I corresponds to the position of the focus at the center of the cuvette (5 mm from the entrance) and case II corresponds to the position of the focus 1 mm in front of the entrance of the cuvette. (b) Optical transmittance setup: For high intensity measurements, the setup of power limiting method was used by removing the pinhole at the imaging plane. For low intensity measurements, a flip mirror was employed to send the beam through a ×0.45 telescope to an identical setup as the one used for high intensity measurements and power limiting.

Subsequently, we conducted optical transmission measurements, which were set up as two independent experiments of high and low input intensity [Figure 6.2(b)]. For high intensity measurements, we have used the configuration of the power limiting method by removing the pinhole placed in front of the photodetector. The thick cuvette was replaced by a cuvette of thickness $h = 2$ mm, of which the center was positioned at the focal plane of the +200 mm lens. The beam was estimated to have a $1/e^2$ radius ~30 μm at the entrance of the cuvette. The cuvette was filled with 300 μl volume of each of the previously examined samples. For low intensity

measurements, the beam was directed with two mirrors to a telescope resulting in a $1/e^2$ beam radius ~1.4 mm. The beam was focused by a +200 nm focal length lens, resulting in a focused beam radius ~55 μm and a Rayleigh length ~8.5 mm (with measured $M^2 = 1.4$). The beam was collected by a photodetector placed in the far field, as in the high intensity configuration. In both cases, for the resulted Rayleigh ranges (in a medium having the refractive index of water ~1.33) it holds $z_R > h$, so that the beam can be considered nearly collimated within the samples. For the optical transmittance measurements, we have used the same samples that were examined by the power limiting method experiments.

6.5 Results

6.5.1 Power limiting measurements

We follow the definitions found in references [272-274] for the threshold power for self-focusing P_{th} and the critical power for self focusing P_{cr} in the case of a medium that exhibits absorption, so that in the absence of absorption (transparent material) it should hold that P_{th} is equal to P_{cr}, and here, for water, the host material (denoted with the superscript *"h"*), it holds $P_{th}^h = P_{cr}^h$. For an absorptive medium, in principle, $P_{th} \geq P_{cr}$ due to absorptive losses. Accordingly, we define P_{th}^e the observed threshold power for self-focusing of the nanorod effective medium, and P_{cr}^e is defined as the critical power for self-focusing of the nanorod effective medium in the absence of absorption, so that $P_{th}^e \geq P_{cr}^e$. It is convenient to do so for our analysis on the enhancement of the self-focusing nonlinearity of the nanorod effective medium n_2^e in comparison to the one of the host material (water) n_2^h, because P_{cr}^e does not depend on absorption but only on n_2^e according to $P_{cr}^e \propto 1/n_2^e$ [64, 273, 274].

In both cases I and II, the critical power for self-focusing P_{cr}^h of the host material (water) was identified to be at 6.8 MW [239] (Figure 6.3). In case I (Figure 6.3a), at low input power P_{in} (below 5 MW), the colloids $C0.5$ and $C1$ were seen to behave almost as linear absorbers, while the slope of the linear region of the output signal versus P_{in} curve, gradually decreased as the nanorods concentration increases from water ($C0$) to $C0.5$ and $C1$. For samples of higher concentrations, strong saturation of absorption was observed, while the slope of the signal tended to approach the corresponding slope of the signal of the neat material (water). The threshold power P_{th}^e was

observed to occur at increasing values of P_{in} as a function of concentration. Effectively, we will show in our following analysis (presented in section 6.6.2) that in these experiments the composite material seemingly exhibited saturable absorption with a Kerr lens coefficient n_2 governed almost entirely by the host (water).

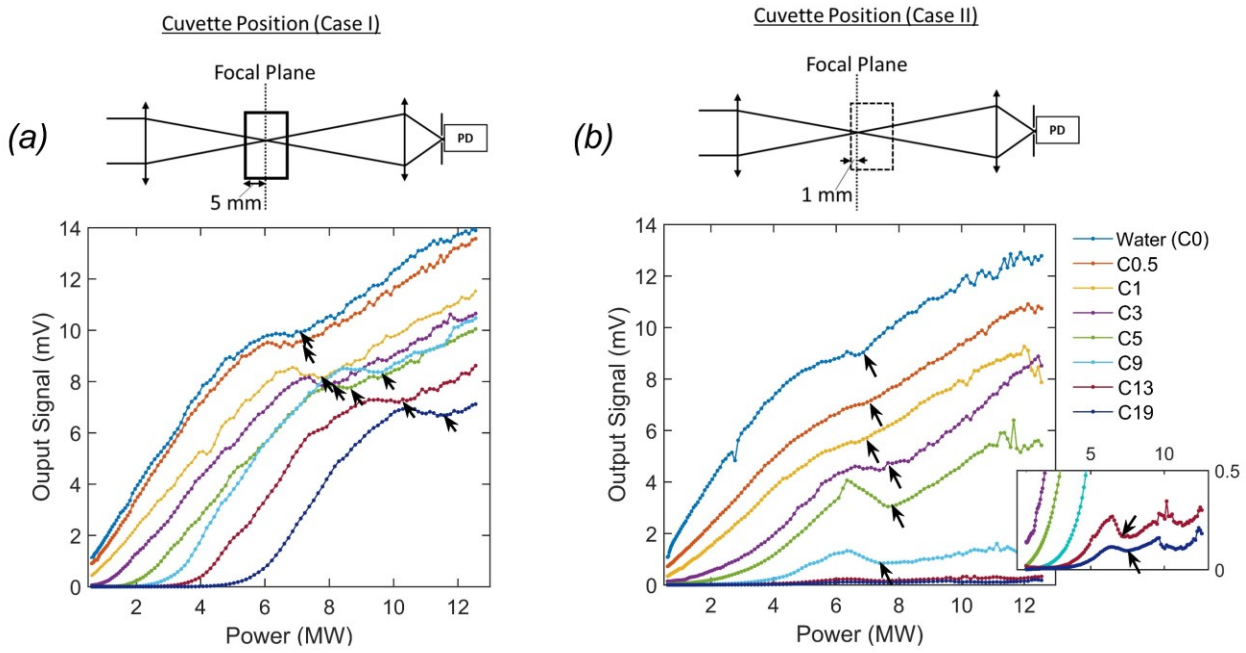

Figure 6.3 (a) Results obtained by using the power limiting setup in the case I configuration. (b) Results from the power limiting setup in the case II configuration. The black arrows indicate the evaluated threshold power for self-focusing $P_{th}{}^{e}$ of the nanorod effective medium, as explained in detail in Ref. [239]. The inset of (b) is a rescaled figure to show more clearly the obtained signals for C13 and C19.

In case II (Figure 6.3b), P_{th}^{e} was confined near P_{cr}^{h} for all samples, as it has also been observed by Mohebi et al. [272]. A large valley was observed at high concentration samples $C9$, $C13$, $C19$ in the output signal as a function of P_{in}, right after the onset of phase modulation of the beam and before the collapse. As demonstrated in [239], the valley is related to the strength of phase modulation, increasing the wavefront divergence on the fundamental frequency. In addition, the optical power arriving at the detection device was significantly reduced, presumably due to the increasing optical path with respect to case I and the various defocusing mechanisms after or prior to the collapse (i.e., multiphoton absorption in the host, dispersion, absorption by the nano-

inclusions and diffraction). In the following paragraphs we shall examine the recorded values of P_{th}^{e} with respect to P_{cr}^{h} in both cases I and II to assess the strength of the nonlinearity in the studied media.

6.5.2 Spectroscopic evaluation of nanorod deformation

We examined possible structural changes of the nanorods in the colloidal suspensions spectroscopically [268] by comparing linear absorption spectra before and after the power limiting measurements (Figure 6.4). The results are similar to the ones reported by Link et al. on nanorod reshaping when moderate femtosecond laser pulse energy excitation was applied with a 20 nm detuning from the resonance (Fig. 2b,c in Ref. [268]). Here, an indicative decrease of the optical density $\delta OD \sim 9 - 17\%$ of the samples was observed at the longitudinal plasmon peak, while the transverse plasmon peak slightly increased. The highest decrease was observed for the highest concentration sample $C19$. Further, the samples exhibited a blue shift of the maximum of the longitudinal plasmon peak of about 9 nm (except for $C0.5$, where blue shift was ~2 nm). Accordingly, the mean aspect ratio of the nanorods that form the longitudinal plasmon peak is expected to have been reduced to an average value of ~3.6 - 3.7, as evaluated by the blue shift of the peak of the plasmon resonance. Finally, the relative broadening of the spectral linewidth was seen to be significantly lower solely for sample $C1$. For the rest of the samples, it was only marginally different. The latter observation does not provide a clear tendency of the relative spectral bandwidth after reshaping of the nanorods. Nonetheless, there is evidence of a structural deformation of nanorods after the power limiting treatment.

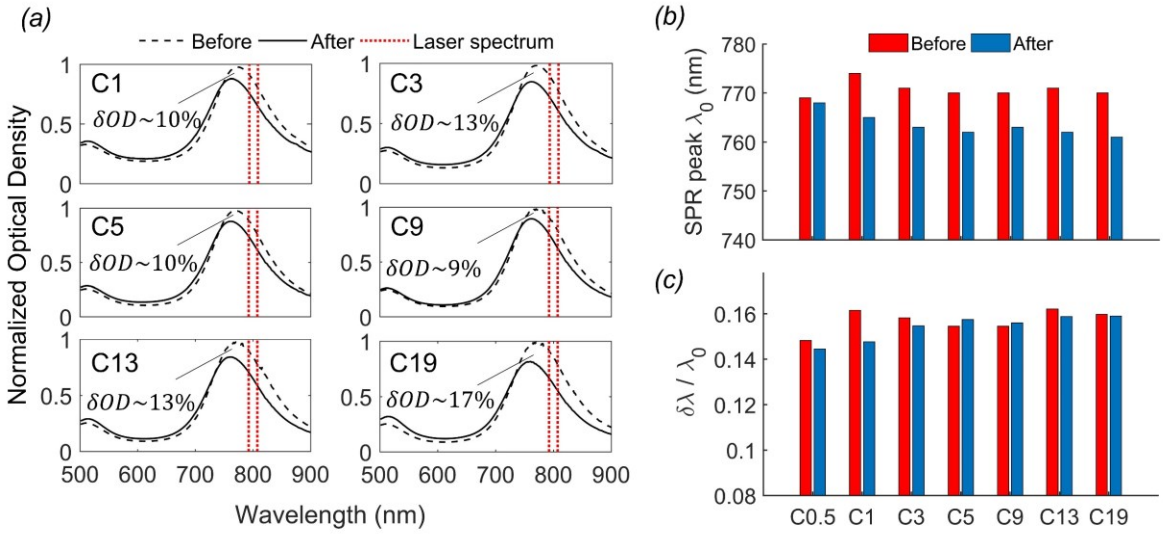

Figure 6.4 (a) Spectroscopic evaluation of nanorod reshaping. The optical density is reduced for all samples after the power limiting treatment. The longitudinal and transverse plasmon mode peaks show a blueshift and an increase of the absorption peak, respectively. The results are indicative of partial, surface melting of a distribution of nanorods, which results in reshaping into shorter nanorods or melting into spherical particles. (b) The average observed blueshift of ~9 nm of the longitudinal plasmon band is consistent with implications of reshaping. (c) Relative spectral broadening of the reshaped longitudinal plasmon band.

6.5.3 Optical transmission measurements

The results of low and high intensity optical transmittance $T_\lambda \equiv I/I_0$ (I denotes the transmitted intensity and I_0 is the input intensity) are shown in Figure 6.5. The observed behaviour was reproducible after each experiment of irradiation at different locations (volumes) of the samples. The low intensity measurements allowed the experimental estimation of linear transmittance $T_{\lambda,0}$, the calculation of the linear absorption coefficient a_0, according to $a_0 = -ln(T_0)/l$ (section B.1 of the Appendix B/Supplemental document, Table B.1), and the evaluation of the detuned saturation intensity I_s^δ (see Equation 6.3). At higher intensities, the optical transmittance was strongly modulated and reached asymptotically values above 90% for all samples. Accordingly, we determined experimentally the non-saturated transmittance $T_{\lambda,ns}$ (as the foresaid asymptotic value of T_λ for each sample) and we evaluated the corresponding non-saturated absorption coefficient a_{ns} according to the relation $a_{ns} = -ln(T_{\lambda,ns})/h$ data shown in section B.1 of the Appendix B/Supplemental document, Table B.1).

The applied pulsewidth is adequately short (55 fs FWHM) so that the saturable optical absorption of the nanoparticles can be described in a context similar to a simple two-level system. Conceptually, the absorbed energy of the longitudinal plasmon mode results in a nearly bleaching of the distribution of participating one-photon electronic transitions, from a given ground state to an excited state [275]. The effect has been better understood as a strong damping of the coherent plasmon oscillation as the "driving force" is increasing [15]. The exact mechanism behind that observation has been interpreted in the context of confinement effects (generation of high-energy "hot" electrons at the surfaces) and activation of nonlinear damping mechanisms of the plasmon mode [9, 12, 26, 123, 276]. One would expect that under such conditions of high pump intensity, energy absorption by the plasmon mode gradually becomes less efficient [123, 269]. Finally, even though saturation appears to be detrimental for the enhancement of coherent third-order processes (e.g., third harmonic generation) at high laser intensities, higher-order contributions cannot be ruled out [148, 276].

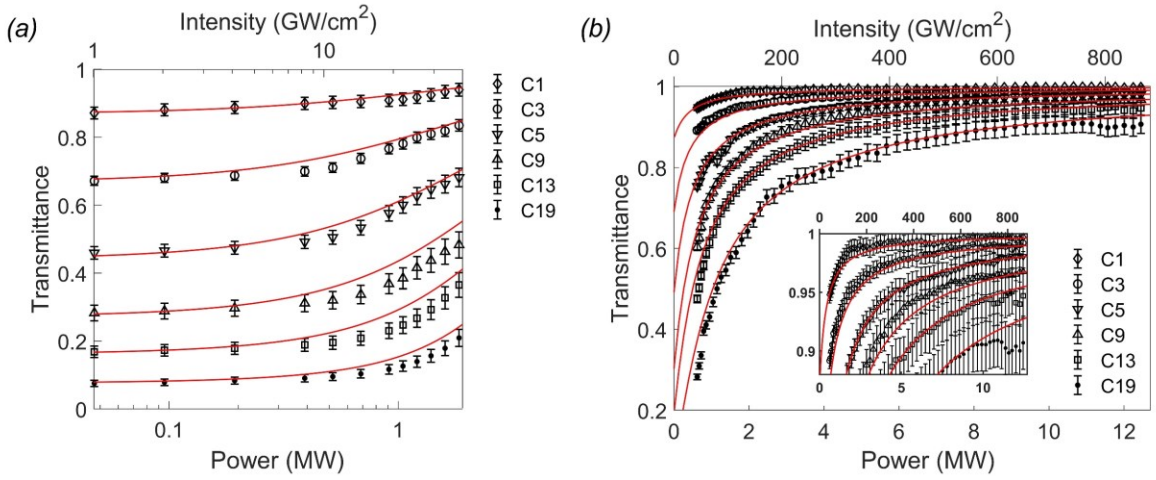

Figure 6.5 (a) Low intensity optical transmittance measurements. At low input pulse power, the absorption is linear. The saturation intensity is observed around 25 GW/cm^2, which corresponds to an input pulse power of ~1 MW (at a 55 μm beam spot size). (b) High intensity optical transmittance measurements. A strong modulation on the optical transmittance is observed, which reaches an almost constant value at high input intensities. We use this constant value to define the non-saturated absorption a_{ns}. In both (a) and (b) the red lines are theoretical fittings of Equation 6.3 to the data of both graphs.

In the case of the examined nanorods, the transverse plasmon mode is seen to be adequately far from 760 nm and the broadening of the absorption spectrum behaves as nearly homogeneous,

which has been seen in time-resolved pump-probe experiments of resonantly pumped gold nanorods at ~800 nm [18]. The intensity I-dependent absorption coefficient $a(I)$ of the nanocomposite can accordingly be written as [18, 277]

$$a(I) = \frac{a_0}{1 + \frac{I}{I_s^{\delta}}} \tag{6.1}$$

The transmittance T_λ through the cuvette can be calculated starting from Beer's law by [53]

$$\frac{T_\lambda}{T_{\lambda,0}} = exp\left[\frac{I_0}{I_s^{\delta}}(1 - T_\lambda)\right]. \tag{6.2}$$

After some algebra, the relation can be expressed more conveniently in terms of T_λ by use of Lambert's function $\mathcal{W}$ (defined as $\mathcal{W}(x)exp[\mathcal{W}(x)] = x$) as

$$T_\lambda = \frac{\mathcal{W}\left[\frac{I_0}{I_s^{\delta}} T_{\lambda,0} exp\left(\frac{I_0}{I_s^{\delta}}\right)\right]}{\frac{I_0}{I_s^{\delta}}} \tag{6.3}$$

Equation 6.3 is well-fitted (with ~95% confidence interval) to the experimental measurements in Figure 6.5a and b, giving an estimation of $I_s^{\delta} \approx 25\ GW/cm^2$ (see section B.1 of the Appendix B/Supplemental document for a discussion on the fitting of Equation 6.3). Implications of nonlinear absorption at very high intensities are noted only for the sample $C19$ (since the predicted transmittance of the fitted curve appears to be slightly higher compared to the experimental data), however, we consider that the occurrence of this deviation of the data values from the fitted curve was not significant, since it does not exceed the applied margin of error (5%).

6.6 Discussion

6.6.1 Saturation of absorption or nanorod reshaping?

We further evaluated the absorbed energy by a single nanorod in the optical transmission measurements and compared with the observations reported by Link and El-Sayed [268] on the

required absorbed energy for total melting of nanorods (average size 11×44 nm) by a single femtosecond pulse. The authors of Ref. [268] have determined a required absorbed energy of ~65 fJ per nanorod (or ~800 J/g), so that the nanorods will be completely melted and ~12 fJ per nanorod (or ~150 J/g), so that they will be reshaped under femtosecond excitation. A more recent experimental evaluation, reported by Taylor et al. [23], accounts for ~340 J/g required absorbed energy for complete reshaping of nanorods of ~3.7 aspect ratio (~15.5 mm wide), when irradiated by a 150 fs pulse at a wavelength of 830 nm. For comparison, we also note that in larger particles (average size of 92×32 nm), Zijlstra et al. [270] have determined an energy onset for reshaping of ~150 fJ per nanorod (or ~105 J/g) and a melting energy threshold of ~260 fJ (or ~180 J/g), by light scattering spectroscopy and electron microscopy experiments on a single nanorod after application of 100 fs pulses tuned at the peak of plasmon resonance. Finally, Hou et al. [26] , by performing optical transmittance measurements with 800 nm wavelength, 100 fs pulses coupled with cw irradiation of 808 nm wavelength in a colloidal solution of smaller nanorods (~12.5 nm diameter and ~4 aspect ratio), have estimated a reshaping onset energy threshold of ~12 fJ per nanorod (or ~100 J/g).

A linear absorption coefficient a_0 has been determined by our low intensity transmittance measurements. Based on the reduction of the plasmon peak intensity shown in the results of Figure 6.4(a), we estimate that after completing the power limiting measurements the concentration of nanorods for sample $C1$ was ~10 % lower than the specification value. Accordingly, we evaluated the concentration for the rest of the samples as a linear function of absorption a_0 (section B.1 of the Appendix B/Supplemental document, Table B.1). Following the methodology of Link and El-Sayed [268], we estimated the absorbed energy by a single nanorod (section B.1 of the Appendix B/Supplemental document, Table B.1). We found that at the saturation intensity, the absorbed energy values ranged from 0.1-1.0 fJ per nanorod (or ~7-18 J/g) (section B.1 of the Appendix B/Supplemental document, Table B.2). These values are quite lower than the reported value by Link and El-Sayed [268] of ~12 fJ per nanorod (or ~150 J/g) required for the onset of reshaping of nanorods.

Notably, in their experiments, Link and El-Sayed [268] have observed reshaping of particles at applied pulse energies >0.5 μJ with 100 fs defined at FWHM (or $t_p = t_{FWHM}/\sqrt{2log(2)} \approx 130\ fs$ for Gaussian pulses), which means that the peak power of the pulses (expressed by $P_{in} =$

$E_{in}/\left(t_p\sqrt{\pi/2}\right)$ reached ~3 MW. Further, this power was focused at a diameter of ~250 μm, which yields peak intensity ~13 GW/cm^2, i.e., half the value of saturation intensity that we estimate here. It is unknown what was the saturation intensity for the samples and conditions applied in [268], however, the authors reported therein a 45% absorbance at the peak intensity of ~13 GW/cm^2 that implies that most likely saturation was not reached at their examined input energy deposition, which emphasizes the importance of laser pulsewidth. Presumably longer pulsewidth (100 fs FWHM in [268]) results in more efficient energy absorption, since damping effects of the plasmon modes, depending on the peak intensity of the pulse (see also [26, 269] on the role of saturation and laser pulsewidth), are expected to be weaker compared to same energy pulses of smaller pulsewidth (55 fs FWHM in our experiments).

At our high intensity measurements, absorption was fully bleached at the highest applied 12 MW input power [Figure 6.5(b)]. By following the foresaid methodology and accounting that the absorption of the samples is characterized by a_{ns}, the calculated absorbed energy per nanorod varied between ~1.4-2.6 fJ (or ~24-46 J/g) (section B.1 of the Appendix B/Supplemental document, Table B.2). Nonetheless, if we consider in these calculations the initial absorption a_0 of the sample and *assume that no absorption saturation occurs at the maximum applied power (12 MW),* the calculated absorbed energy per nanorod ranges from ~16-41 fJ (or ~280-710 J/g), which exceeds several of the foresaid reshaping/melting thresholds. Moreover, various absorption saturation models have been cited in the literature; under the assumption of inhomogeneously broadened linewidth, $a(I) \propto \left(1 + I/I_s^{\delta}\right)^{-1/2}$ [19]. The semi-empirical relation $a(I) \propto \left(1 + \sqrt{I/I_s^{\delta}}\right)^{-1}$ has also been proposed for the interpretation of z-scan technique results [17, 278]. For these models, lower modulation on the optical transmittance is expected at high intensities in comparison to the $a(I) \propto \left(1 + I/I_s^{\delta}\right)^{-1}$ [18, 277] dependence (Eq. 6.1). Consequently, for the interpretation of the strong transmittance (and absorption/losses) modulation observed in the experiments of the high intensity regime [Figure 6.5(b)], besides the saturable behaviour of the samples due to plasmon damping, one should also consider effects related to partial reshaping of nanorods within the irradiation volume [267], ultrafast modification of the absorption cross section due to photo-

excited, high energy non-thermal electrons [26, 123] in the ensemble of randomly oriented particles, and free carrier screening [266].

Importantly, our optical transmission experiments demonstrate that, whether particle deformation occurred or not within the samples, the intensity dependent losses follow in good agreement the model of Equation 6.1, which allows for the theoretical formulation of the pulse propagation and the nonlinear interaction with the medium (Appendix B/Supplemental document, section B.2). Furthermore, in our view the structural deformation and melting of particles recorded right after the power limiting treatment, is not associated with the saturation behavior prior to the collapse of the beam observed in those experiments. It is seen that the longitudinal plasmon mode is nearly saturated just before the collapse and the absorbed energy by the nanorods is not very different compared to the energy absorbed at the saturation intensity. A similar effect was observed in reference [269] for the case of gold nanoparticles, where saturation of absorption at high pump intensities has been reported to prohibit the nanoparticle system to reach temperatures higher than the melting point. Considering all above calculations and experimental results, we conclude that significant particle deformation rather occurred only for $P_{in} \sim P_{th}^{e}$, where the beam collapses into a filament, in the presence of rapidly increasing intensities of the order ~1 TW/cm^2 and the formation of low-density plasma channels ~10^{-18} cm^{-3} within the samples [245].

6.6.2 Evaluation of nonlinearities

On Figure 6.6, we plot P_{th}^{e}, experimentally determined from Figure 6.3, as a function of the linear absorption coefficient a_0 in case I and as a function of the non-saturated absorption a_{ns} in case II. The reason that in case II P_{th}^{e} is plotted versus a_{ns} is that the latter can be considered a constant (since a is asymptotic to a_{ns} at the applied intensities near P_{th}^{e}), which simplifies the beam propagation and collapse analysis. Furthermore, the beam width at the entrance of the cuvette is nearly the same as at the focus and the beam collapses at a distance much smaller than the Rayleigh range. Therefore, in case II, the problem can be adequately described by self-focusing of a collimated beam in a cubic nonlinear medium with linear damping equal to a_{ns}.

We performed a theoretical analysis to interpret the results presented in Figure 6.6 (the theoretical model is described in the Appendix B/Supplemental document, section B.2). We note that the observations drawn by Mohebi et al. [272], imply that the collapse occurs if the critical power is

delivered at the focus after accounting for all absorption losses. In other works, the problem of self-focusing with linear absorption has also been treated in the steady state [64] or within the aberration-free approximation [273, 274]. Here, we consider the effect of saturable absorption observed in our experiments (described by Equation 6.1) and we examine by numerical calculations the beam collapse conditions (threshold power) to assess whether enhancement of the refractive nonlinearity of water is observed.

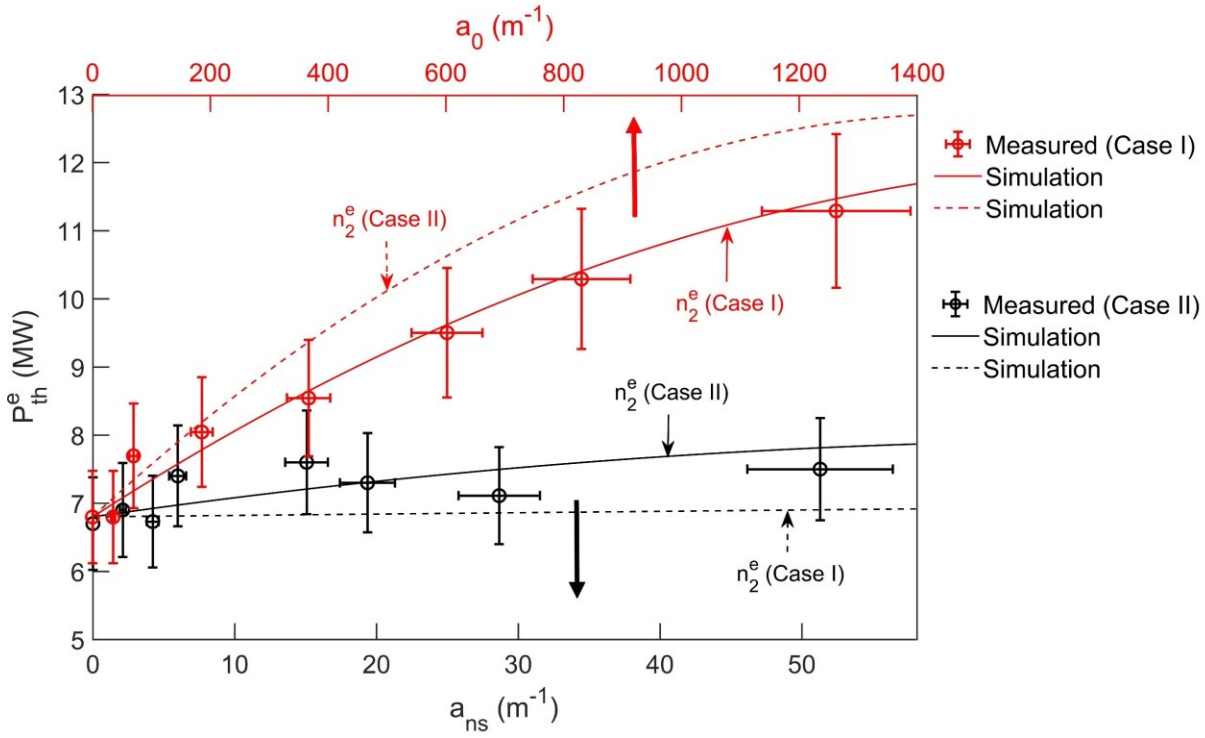

Figure 6.6 . Experimentally evaluated threshold power for self-focusing of the effective medium P_{th}^{e}. The data of case I (red circles) are plotted against the linear absorption coefficient a_0, whereas the data of case II (black circles) are plotted against the non-saturated absorption a_{ns}. The solid lines correspond to numerical evaluation of P_{th}^{e} accounting for the enhancement of the nonlinear refractive index as the concentration of particles (absorption) increases obtained by our numerical treatment for each case respectively. The dashed lines correspond to numerical evaluation of P_{th}^{e} accounting for the nonlinear refractive index values extracted by case I treatment and applied for case II theoretical solution and vice versa (details of the calculations are presented in Appendix B/Supplemental document, section B.3).

The solution of the numerical model (based on all experimental conditions) indicated that a subtle, monotonically increasing enhancement of the nonlinear refractive index n_2^e (real part) as the

concentration of particles (absorption) increases, should be considered to acquire the fitting to our experimental results as demonstrated in Figure 6.6. We have evaluated the real part of the complex nonlinear refractive index n_2^e based on these calculations (the details are shown in the Appendix B/Supplemental document, section B.3) and for the calculation of the imaginary part, we use the relation $a_2^e \cong -a_0/I_s^\delta$. The results are shown in Figure 6.7 as a function of the particle concentration of the examined samples.

With respect to the origin of the refractive (self-focusing) nonlinearity, we rule out the lattice contribution (due to electron-phonon coupling after thermalization of the photo-excited electrons [8, 9, 124, 183, 263-265]), which is a non-instantaneous process. Moreover, ultrafast excitation of non-thermal electrons has seemingly a detrimental influence on the coherently enhanced, plasmon-induced nonlinear polarization of the particles, resulting in ultrafast damping of the plasmon and modulation of the dielectric permittivity of the metal. Nonetheless, the foresaid mechanism still contributes to incoherent (e.g. Kerr type) nonlinear processes [3, 8].

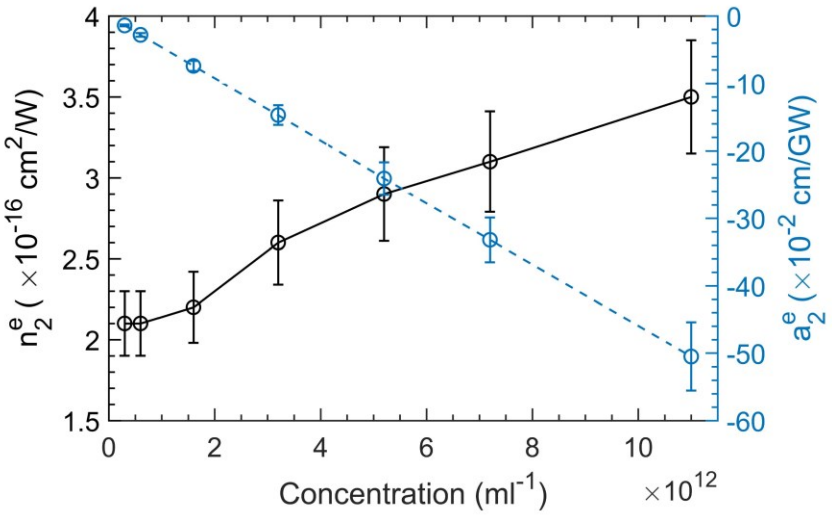

Figure 6.7 Evaluation of the effective nonlinear refraction and absorption of the examined gold nanorod colloids as a function of the concentration. Only the values of n_2^e obtained from the case I treatment are presented on the grounds of the better fitting of the theoretical model solution on the experimental data of both case I and II, as shown in Figure 6.6. The values of n_2^e obtained by the case II treatment are presented in Table B.4 of the Supplemental document for completeness.

In our view, the refractive nonlinearity of water is marginally enhanced in the presence of (saturable) plasmonic amplification of the electric field in the vicinity of the particles, which in

turn affects the laser-induced distorted position of non-resonant electrons in water. The effect is expected to increase monotonically with the increase of nanorod concentration, as it is also implied in the result of Figure 6.7. The time response of this effect is nearly instantaneous so that it can follow the laser pulse amplitude rise time; same for the absorptive properties of the composite, for which ultrafast saturation is observed. Accordingly, the field enhancement is expected to be also saturable [123, 148], with possibility of contributions from higher-order nonlinearities on the susceptibility of the metal, as has been noted by Drachev et al. [148]. This possibility is further supported by observations on the response of the power limiting method signal (case II). Indeed, the deep valleys recorded near the critical power (Figure 6.3b) at higher concentrations of particles, are associated with stronger wavefront (and phase) modulation of the pulse.

Lastly we note that in theory, the behaviour of nonlinear refraction and linear absorption saturation can be equivalently formulated as a higher order cubic-quintic nonlinearity [64]. Experiments in colloidal solutions for picosecond irradiation have shown that if septimal nonlinearities are also considered at high intensities, the saturation of the absorptive behaviour persists (saturable), whereas nonlinear refraction benefits from a small focusing septimal contribution [173, 174]. This generates implications of high-order contributions that might explain the gradual enhancement of self-focusing in our experiments as the concentration of particles increases, which we quantified by a single effective third-order term n_2^e and can be mathematically expressed up to the seventh-order as $n_2^e(I) = n_{2,0}^e + n_4^e I + n_6^e I^2$, with $n_{2,0}^e, n_6^e > 0$ and $n_4^e < 0$ for modelling saturable cubic and focusing septimal nonlinearities. Finally, note that in picosecond regime experimental demonstrations [173, 174], the signs of the high-order refraction coefficients are opposite to the ones just mentioned, implicating stronger non-instantaneous contributions (electron-phonon coupling) to the effective susceptibility.

6.7 Conclusion

We have used for the first time to our knowledge an alternative method (power limiting) to evaluate the enhancement of nonlinear refraction in gold nanorod colloids under near-resonant excitation in the femtosecond filamentation regime. Spectroscopic evaluation showed that considerable particle deformation occurred after the collapse of the beam into a filament, in view of high peak intensities and plasma channel formation. Below the critical power, particle deformation is seemingly small

due to low energy-induced saturation of the linear absorption of the nanorods. By modelling the experimentally observed saturable absorption of the samples, we performed numerical simulations to evaluate the threshold for self-focusing. The results showed that the nanorods subtly enhance the nonlinearity of water as their concentration increases. We attribute the enhancement to the saturable (due to ultrafast generation of "hot" electrons at the surfaces), near field amplification in the vicinity of the nanorods and we determine the complex refractive index of the composites. Our findings reconcile, in the regime of ultrafast excitation <100 fs, with the theory of control over the effective higher-order susceptibility of plasmonic nanocomposites by concentration adjustments. In our view self-focusing of femtosecond pulses below ~100 fs in gold nanorod colloids is undermined by the ultrafast modification of the permittivity of gold, due to excitation of non-thermal electrons and plasmon damping, and not affected by (stronger) non-instantaneous contributions typically observed following the thermalization of the photo-excited free electron kinetic energy modes in the nanoparticle system.

CHAPTER 7 ARTICLE 4: NONLINEAR THERMAL LENSING OF HIGH REPETITION RATE ULTRAFAST LASER LIGHT IN PLASMONIC NANO-COLLOIDS

Research article published in Nanophotonics journal in 2022[5]. The supporting information for this article is reprinted in Appendix C of this thesis.

7.1 Authors and author contributions

Leonidas Agiotis and Michel Meunier. L.A. designed the research, conducted the experiments, analysed the data, performed theoretical and numerical analysis, and wrote the main manuscript. M.M. supervised and discussed the work and reviewed the main manuscript.

7.2 Abstract

We report on experimental observations of phenomenological self trapping in plasmonic colloids of varying plasmon peaks in the visible/near infrared. A femtosecond (fs) oscillator is used in both pulsed (35 fs, 76 MHz) and continuous wave (cw) operation for comparison. We show that for both modes and for all examined colloids (and under typically applied external focusing conditions in self-trapping studies in colloidal media) nonlinear propagation is governed by thermal defocusing of the focused beam, which precedes the steady-state regime reached by particle diffusion, even far from the plasmon resonance (or equivalently for non-plasmonic colloids, even for low absorption coefficients). A strategy for the utilization of high repetition fs pulses to mitigate thermal lensing and promote gradient force-induced self-trapping is discussed. Notably, nonlinear thermal lensing is further accompanied by natural convection due to the horizontal configuration of the setup. Under resonant illumination, for both fs and cw cases, we observe mode break-up of the beam profile, most likely due to azimuthal modulation instability. Importantly, time-resolved observations of the break-up indicate that in the fs case, thermal convection heat transfer is reduced

---

[5] Agiotis, Leonidas and Meunier, Michel. "Nonlinear thermal lensing of high repetition rate ultrafast laser light in plasmonic nano-colloids" *Nanophotonics* **11**, (2022). https://doi.org/10.1515/nanoph-2021-0775

in magnitude and significantly decoupled in time from thermal conduction, presumably due to temperature increase confinement near the particles. We anticipate that our findings will trigger interest toward the use of high repetition fs pulses for self-channeling applications in nano-colloids.

7.3 Introduction

Nonlinear self-trapping of laser light in soft-matter systems, such as dielectric [279-283] or plasmonic colloids [37-39, 54-58, 89, 284] as well as biological media [285-289], has attracted increased attention over the past decade. The effect is described as diffraction-less propagation of laser light, trapped over many diffraction lengths by virtue of the intensity-dependent nonlinear refractive index of the medium. Indeed, the possibility has been noted of tuning the nonlinear response of soft-matter systems via laser-induced local refractive index modulation, leading to the observation of novel self-action effects. Consequently, soft-matter systems provide a unique platform for the fundamental investigation of nonlinear effects and for prototypical applications based on self-focusing and instability beam break-up [36, 286].

In the case of plasmonic nanocolloids, several studies have reported that self-trapping of laser light is possible by virtue of particle concentration gradients arising from the enhanced particle polarizabilities and exerted on them optical forces [39, 54-57]. Others have demonstrated in the same context that the beam is not self-trapped; in fact, a self-channeling effect (a phenomenological self-trapping) is observed because of nonlinear thermal lensing, giving the impression of a self-trapped beam, particularly when the laser field is tuned near the plasmon resonance [37, 38, 58]. In this case, the medium acts as a laser-induced (due to optical absorption by the particles) thermal lens, which tends to collimate the externally focused beam, much like an optical telescope. Thus, the conditions that demarcate the dominance of either thermal or particle diffusion (due to optical forces) effects, especially far from the plasmon resonance, in the context of self-channeling in plasmonic colloids remain unclear.

Further, most studies of self-trapping of optical beams have been conducted by use of cw laser sources. Interestingly, under certain focusing conditions, fs laser pulses of high repetition rate can be used to generate quasi-continuous wave interactions due to cumulative effects [290-294]. Additionally, in the case of plasmonic systems, fs pulses lead to higher localization of thermal effects [48]. Therefore, the use of high repetition fs pulses in plasmonic nano-colloids in this

context and how it compares to cw interaction is particularly interesting and has not been explored yet.

The objectives of this work are the following:

1) Study the phenomenological self-trapping (self-channeling) of high repetition rate fs laser pulses in plasmonic nanocolloids of varying plasmon peaks with respect to the incident field wavelength, by applying commonly reported focusing conditions. We show that the effect exhibits characteristics of thermal self-defocusing of a focused beam (for both cw and fs operation) even far from the plasmon resonance and is generalized for any absorbing medium of given thermal properties. We discuss conditions under which optical force-induced self-trapping can be achieved as opposed to nonlinear thermal lensing by means of high repetition rate fs pulses.

2) Explore the features of the observed nonlinear thermal lensing induced by high repetition fs pulses as opposed to cw laser light, under plasmon-resonant interaction. We specifically aim to explore if thermal effects are alleviated under fs illumination. To this end, we analyzed distinct features in the dynamics of a beam spatial mode break-up and thermal distortion (blooming) at high input powers, when resonant samples are excited by either cw or fs illumination, and their association to the thermal response of the nanoparticles.

7.4 Results

7.4.1 Nonlinear thermal lensing (fs pulses)

A series of experiments were performed to understand the origin of the self-channeling effect under fs illumination in plasmonic nanocolloids. We evaluated the power-dependent full width half maximum (FWHM) far-field beam width and divergence of an externally focused beam as it emerged from a 20 mm optical cuvette that contained each of four examined plasmonic nano-colloids (samples S1, S2, S3, S4 as shown in Table 7.1). Images of the FWHM far-field beam width were collected by a CMOS camera placed at two different positions in the far-field (Figure 7.1a). A Ti:Sapphire laser in fs operation (wavelength 800 nm, pulsewidth 35 fs, repetition rate 76 MHz) was used. The laser oscillator could run in both fs and cw modes. The focused beam $1/e^2$ radius was elliptical, evaluated $w_{0,Y}$~2.8 mm along Y axis (vertical) and $w_{0,X}$~2.4 mm along X axis

(horizontal). We defined the distance d between the entrance of the cuvette and the beam waist in the medium (Figure 7.1b). Additionally, we performed optical transmittance and z-scan measurements on the examined samples under fs illumination. All samples exhibited linear absorption in the range of the applied input powers (1-280 mW) for all examined positions d. The z-scan showed negative refractive nonlinearity, presumably due to thermal lensing, governed by the thermo-optical coefficient $\frac{dn}{dT}$ of the solvent (water) for all colloids. All methods are described in detail in the Appendix C/Supplemental Material (sections C.1.1 and C.1.2). Table 7.1 summarizes the results of optical characterization.

Table 7.1 Linear absorption and thermo-optic coefficients of the examined plasmonic nanocolloids, characterized by optical transmittance and z-scan measurements by fs irradiation at 800 nm. [a] Width × length. [b] Diameter. [c] Longitudinal, [d] Transverse.

Sample	Average Size (nm)	Surface Plasmon Resonance Wavelength (nm)	$a_0(\lambda_0 = 800\ nm)\ (cm^{-1})$	$\frac{dn}{dT}\left(\frac{10^{-5}}{^oC}\right)$
S1 (Au Nanorods)	10×38 [a]	780[c], 510[d]	2.10 ± 0.10	-3.2 ± 0.4
S2 (Au Nanorods)	10×50 [a]	900[c], 510[d]	0.84 ± 0.09	-2.7 ± 0.4
S3 (Au Nanospheres)	50 [b]	525	0.24 ± 0.05	-2.8 ± 0.3
S4 (Au-Ag Alloy:15-85 Nanospheres)	40 [b]	450	0.06 ± 0.02	-2.9 ± 0.3

First, we examined the influence of the position parameter d in the case of the resonant sample S1. Three values of d were examined, summarized in Figure 7.2. Initially, at low power and for all cuvette positions, the FWHM beam width was ~1.9 mm at the Y direction and ~1.6 mm at the X direction at a distance ~10.5 cm (Position 1) away from the focus, and ~1.6 mm at the Y direction and ~1.4 mm at the X direction at a distance ~8.5 cm (Position 2) away from the focus, which yields a divergence ~15 mrad.

The following qualitative observations can be made: As the input power increased, the beam width gradually decreased for all cuvette positions, retaining a nearly Gaussian profile. The behaviour continued up to a critical power value where a diffraction ring was formed on the background, presumably because of strong thermal aberration (phase-front spatial interference of Airy function-type). The onset of this transition was recorded and is shown in Figure 7.2 marked by a shaded, light-blue area.

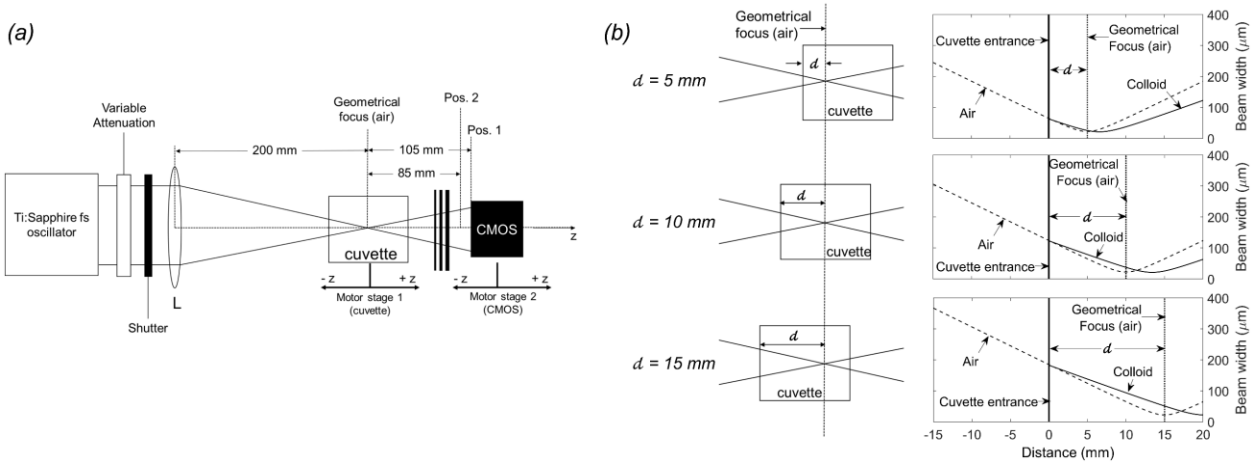

Figure 7.1 The experimental setup (detailed in Appendix C/Supplemental Material). (b) The figures on the left show the three examined cuvette positionings with respect to the geometrical focus of lens L in air, as defined by the parameter d. The figures on the right indicate quantitatively the shift of the actual beam waist position inside the 20 mm long cuvette, when filled with the examined colloids (linear regime). This is because of the difference between the refractive index of air ($n_0 \approx 1$) and colloids ($n_0 \approx 1.33$). The values in air (dashed curves) correspond to experimentally measured beam width along X-axis (shown in Figure C.1b, Appendix C/Supplemental Material). The values in the colloids (solid curves) have been evaluated by Equation C.1b (Appendix C/Supplemental Material) for $n_0 = 1.33$.

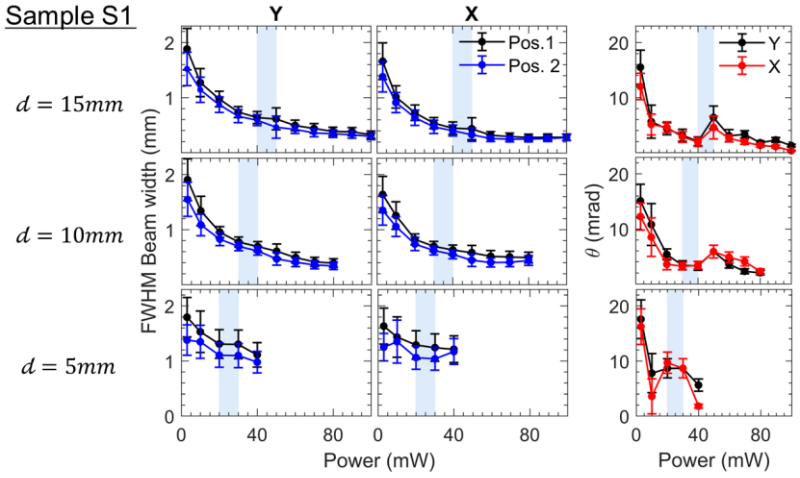

Figure 7.2 Experimental measurements of the far-field FWHM beam width and divergence θ for sample S1 as a function of power for three different values of d (15, 10 and 5 mm). The beam width was determined at two different positions in the far field (shown in Figure 7.1a and in Figure C.1a of the Appendix C/Supplemental Material) to evaluate θ. Results over both Y and X axis are presented. The shaded, light-blue areas indicate the observed power onset of Airy function-type diffraction interference on the beam profile.

The FWHM of only the central Airy disk was evaluated at higher powers than the onset of the foresaid transition. The central Airy disk was seen to gradually shrink and decay at increased input powers (> 40 mW for $d = 5\ mm$, >80 mW for $d = 10\ mm$ and >110 mW for $d = 15\ mm$) while outer rings gained higher radiation densities. Thus, estimation of its FWHM was not performed beyond these powers. In addition, convection currents arose as the liquid was heated, resulting in a downward beam deflection, which became more pronounced as the input power increased.

We make the following quantitative evaluations on the beam width and the divergence of the beam as a function of input power (<100 mW) for all three examined d values (shown in Figure 7.2): For $d = 5\ mm$ the FWHM beam size obtained values >1 mm at the far-field. When the focus was positioned deeper inside the cuvette, a smaller minimum beam width was obtained (down to ~350 μm for $d = 10\ mm$ and ~250 μm for $d = 15\ mm$).

The divergence of the beam for $d = 15\ mm$ exhibited rapid three-fold decrease, from ~15 mrad to ~5 mrad within ~1-10 mW. At higher powers, it decreased on average down to ~8 mrad when $d = 5\ mm$ and to ~2-4 mrad when the focus was positioned deeper in the cuvette. Beyond the onset power of Airy-type interference, the divergence was seen to monotonically decrease for all positions. Specifically, for $d = 15\ mm$, both divergence and spot size attained overall minimum values (~1 mrad and ~280 μm respectively). Conclusively, the minimum values of divergence and beam size were higher as the focus was located closer to the input of the cuvette.

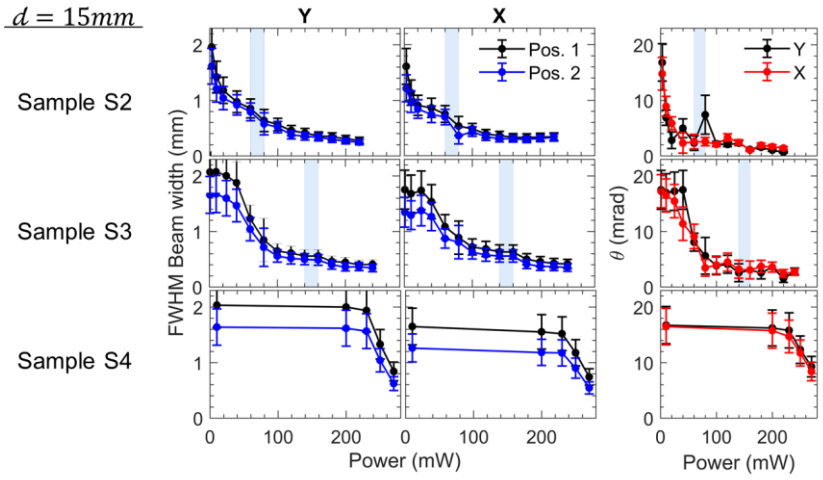

Figure 7.3 Same as Figure 7.2, for the samples S2, S3 and S4 and for $d = 15\ mm$.

For the rest of the samples, we performed experiments for $d = 15\ mm$. The choice was based on the observed minimization of the divergence and beam width for sample S1. The results are shown in Figure 7.3. Similar features of the nonlinear thermal lens were observed for each sample. For comparison, the onset for observation of thermal aberration Airy-type interference (diffraction rings) for sample S2, required $\sim 1.5\times$ higher power compared to S1, while for sample S3 a $\sim 3.5\times$ power increase relative to S1 was needed. Notably, the minimum values of far-field beam width and divergence are evaluated to be smaller as the excitation wavelength is closer to the resonance of the samples (i.e., for higher absorption coefficient).

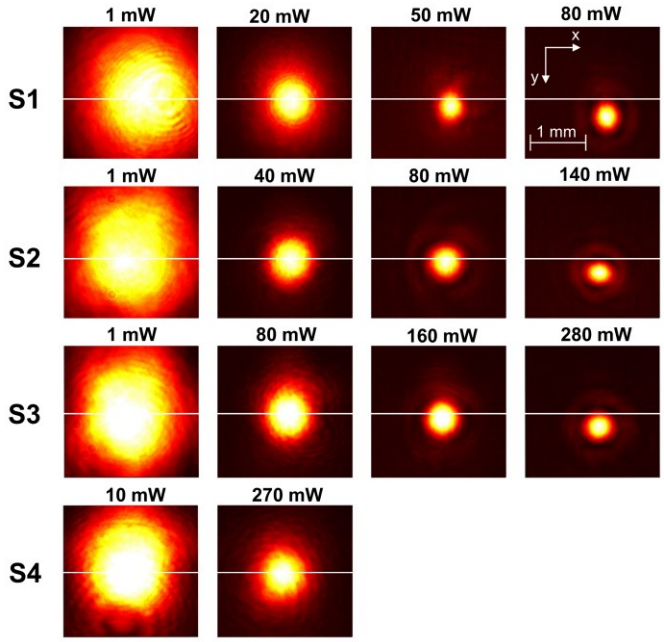

Figure 7.4 Far-field beam width profiles under fs excitation of samples S1, S2, S3 and S4 for various optical input powers recorded at Position 1 and d = 15 mm. The figure demonstrates similar behaviour for all samples: The first column shows the initial profile, the second column shows the required power for shrinking of the beamwidth to approximately half of the initial, the third column shows the appearance of Airy-type diffraction interference, and the fourth column shows further shrinkage of the central Airy disk and downward displacement δy of the beam profile due to convection currents. The horizontal line shows the initial position of the beam center on the Y direction. The inset scale and axes apply for all figures. The x axis is horizontal, and the y axis is vertical and pointing downwards to define the positive direction of δy.

For sample S4, it was not possible to determine the onset of Airy function-type interference since not enough power was available by our laser source (<280 mW). However, we observed the

characteristic reduction (as described for all other samples) of the far-field beam profile and divergence above ~220 mW. The power dependencies of the far-field beam width for each sample are qualitatively depicted in Figure 7.4.

7.4.2 Comparison of resonant nonlinear thermal lensing between fs and cw operation

7.4.2.1 Nonlinear defocusing

In cw operation, the resonant sample S1 exhibited increased absorption (15% higher than fs excitation). This is presumably due to the monochromatic excitation of the plasmon mode, as opposed to the spreading of energy over the optical frequencies of the fs spectrum. Indeed, the latter is expected to result in less efficient mode-matching with the surface plasmons. We have performed comparison of the two cases (fs and cw) when $d = 15\ mm$ (Figure 7.5).

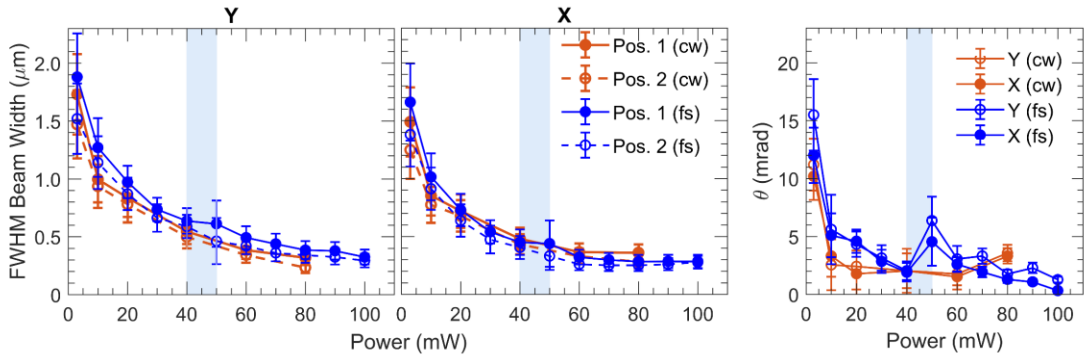

Figure 7.5 Comparison between use of cw and fs excitation on the experimental measurements of the far-field FWHM beam width and divergence θ for sample S1, as a function of power for d = 15 mm.

In cw mode, the FWHM beam width obtained lower values at the same input power compared to the fs case up to ~30 mW. For higher powers, this trend continued only on the Y axis, while in the X axis, no significant difference was observed between cw and fs operation beam widths. On the other hand, in the power interval between 3 - 40 mW, the divergence of the beam obtained smaller values in cw operation down to about 1.5-3.0 mrad. Formation of Airy function-type interference

was observed above ~40 mW. At optical power ~70 mW, the beam divergence increased for cw operation, which opposes the observations of fs operation.

7.4.2.2 Convection and thermal blooming.

Figure 7.6 shows images of the profiles at various powers for fs and cw excitation. Evidently, induced convection currents caused a downward deflection of the beam along the y axis.

Similar features on a beam profile break-up under cw operation preceded in optical power the ones acquired under fs operation. Specifically, break-up of the first outer ring was observed, at an onset of ~100 mW and ~120 mW for cw and fs operation, respectively. The first outer ring clearly breaks up into four bright spots, at ~120 mW input power for both cases. As the power increased in cw operation, the thermal blooming effect [295] manifested itself (at ~160 mW). Contrarily, in fs operation the profile retained its axial symmetry along x and y axes obtaining yet a complex structure, while it was elongated along the x axis up to ~200 mW.

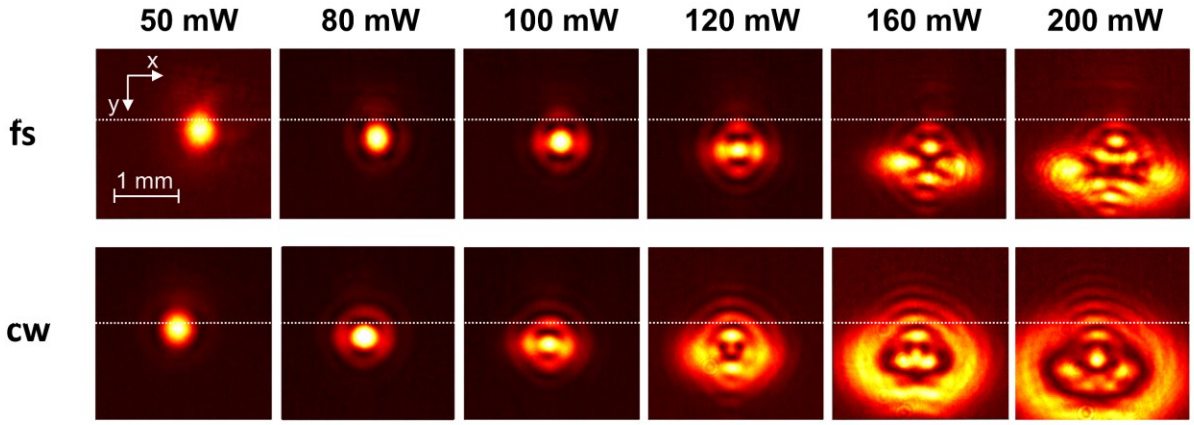

Figure 7.6 Far-field beam width profile under fs and cw excitation of sample S1 for high input powers recorded at Position 1 and d = 15 mm. Beam profile break-up effects are observed beyond 120 mW for both cases. Pronounced beam break-up is observed under cw excitation at lower input power and strong thermal blooming beyond 160 mW with a characteristic highly asymmetric lower half-portion. In the case of fs operation, a less asymmetric, yet complex profile is observed. The downward displacement can be compared in the two cases with respect to the low-input-power position of the center of the beam (white horizontal line).

We have obtained time-resolved images of the far-field beam profile (see Methods, section C.1, Appendix C/Supplemental Material) for the specific cases of input power of 120 mW and 140 mW

input power in cw and fs pulsed operations, respectively. The images were used to analyze the difference in the dynamics of the mode break-up. Results of images taken for both cases are shown in Figure 7.7.

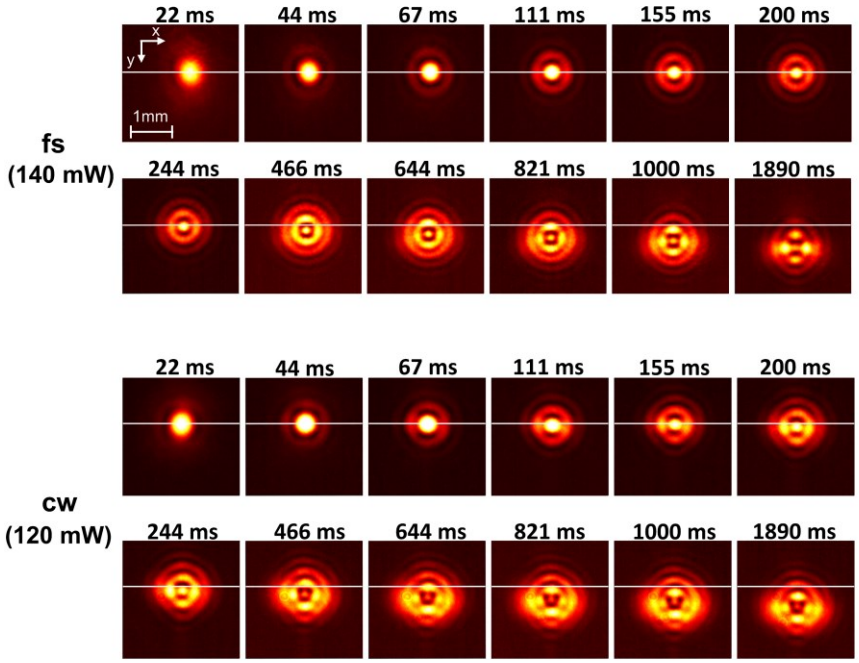

Figure 7.7 Time-resolved far-field beam width profile under fs and cw excitation of sample S1 for input powers of ~140 mW and ~120 mW, respectively, recorded at Position 1 and d = 15 mm. The selection of the foresaid input power leads to a fair comparison between the two profiles due to the 15% higher absorption coefficient calculated in the case of cw operation. Note the subtle downward displacement of the beam core and onset of beam break-up just after 200 ms for the case of cw operation. Contrarily, for fs operation, downward displacement is observed only after ~466 ms and the onset of beam break-up is observed after ~821 ms. Finally, a drastic beam profile break-up is observed for the fs case between the time interval of 1000 and 1890 ms (Supplemental Video).

For the fs case, observable growth of the break-up of the first outer ring surrounding the decaying core occurred only after ~1 s as opposed to the cw case for which the same effect was observed after ~200 ms from the opening of the shutter. Further, the beam profile break-up in the fs case became pronounced after the beam acquired its final position, under convection-induced displacement. In the cw case, the onset of profile displacement subtly preceded in time the one in the fs case (compare for example the central core displacement in the two cases after ~200 ms and ~244 ms from the opening of the shutter). Finally, the break-up was observed to be typically accompanied with stochastic, small-scale motion of the profile around the center of the beam

(Supplemental Video). For the case of cw excitation, such stochastic motion was observed as early as ~200 ms, and was generally more pronounced, whereas, in the fs case it became observable only after ~1 s from the opening of the shutter.

7.5 Discussion

7.5.1 Nonlinear thermal lensing (fs pulses)

The phenomenological self-trapping observed experimentally was compared theoretically to a model based on the stationary nonlinear Schrödinger equation with thermal nonlinearity (Equations C.3a-C.3b, Appendix C/Supplemental Material). We first evaluated σ^2 near-field beam width for $d = 15$ mm as a function of P_{in} after $h = 30\,mm$ of propagation in media characterized by absorption coefficient a_0, thermal conductivity K_T and thermo-optic coefficient dn/dT (Appendix C/Supplemental Material, Section C.1.3). The results are shown in Figure 7.8a for the four different values of a that correspond to the nano-colloids examined experimentally and for K_T, dn/dT of water. The σ^2 near-field beam width at the output $w(z = h)$, exhibits a parabolic behaviour as a function of P_{in}, quantitatively different for each a_0. An inflexion point is formed at an optimum power $P_o(a_0)$ that demarcates thermal aberration in the far-field. The inflexion point has a simple physical interpretation. The initial phase-front curvature of the focused beam, which reads $\delta\varphi_i = \frac{\pi}{\lambda R} w_0^2$ (R , w_0, denote the radius of curvature and beam width at the input, respectively), is compensated by the thermal self-induced phase. The latter is estimated as $\delta\varphi_T(r) = \frac{\pi}{\lambda}\int_0^{z_{NL}} \frac{\delta n(r,z)}{n_0} dz$, where $z_{NL}(P_{in})$ is the distance between the entrance of the cuvette and the nonlinear beam waist, and $\delta n(r,z) = \frac{dn}{dT}\delta T(r,z)$ (where $\delta T(r,z)$ denotes local temperature increase), so that the inflexion point appears when $\delta\varphi_i \approx \delta\varphi_{T,max}$. Evidently, in the linear regime, the beam waist is located at $z_f = n_0 \times d$ (n_0 is the refractive index of water), and for $P_{in} \to P_0$, in the nonlinear regime, the beam waist is moving (increasing) monotonically at $z_{NL}(P_{in}) > z_f$. We observed that, at the inflexion point ($P_{in} = P_0$), the σ^2 nonlinear beam waist $w(z_{NL})$ was expanded compared to the σ^2 linear beam waist w_f in each medium by the same factor m, independently of a_0, which was estimated $m \equiv w(z_{NL})/w_f \sim 1.75$. For $P_{in} > P_0(a_0)$, it holds $\delta\varphi_{T,max} > \delta\varphi_i$. The beam begins to defocus and as a result the σ^2 beam width at the output $w(z = h)$ increases (Figure

7.8a). The position z_{NL} moves further towards the output of the cuvette for increasing P_{in} so the curve of the $w(z_{NL})$ gradually approaches $w(z = h)$ (Figure 7.8a). Figure 7.8b summarises the behaviour of $P_0(a_0)$. We repeated the process for d = 10 mm with similar observations and determined the corresponding $P_0(a_0)$ (Appendix C/Supplemental Material, Section C.2). We further found that in this case $m \sim 1.5$ which shows that m depends on $\delta\varphi_i$, i.e., the initial focusing condition, but not on a_0.

Importantly, P_0, for which it holds $\delta\varphi_i \approx \delta\varphi_{T,max}$, can be estimated experimentally by recording the value of P_{in} *that coincides with the appearance of Airy function type diffraction rings in the far-field*. A fair agreement is observed between simulations and experimental values, where P_0 was further determined numerically for three more a_0 values ($1.40, 0.54$ and $0.12\ cm^{-1}$) in Figure 7.8b.

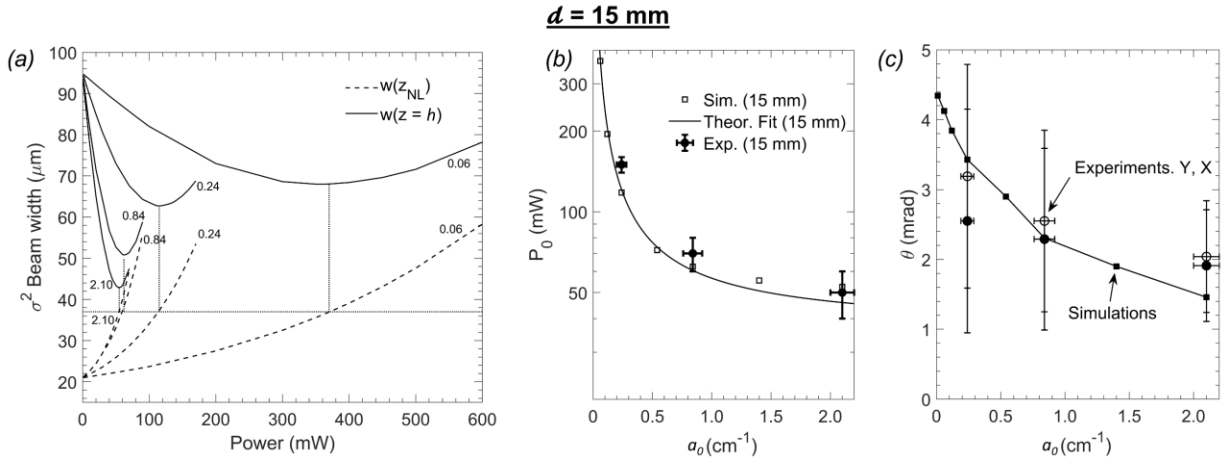

Figure 7.8 Results of numerical simulations based on the nonlinear Schrödinger equation with a thermal nonlinearity (Equations C.3a-C.3b, Supplemental Material) and comparison with experimental observations for d *= 15 mm.* (a) Numerical evaluation of the σ^2 beam width at the output $w(z = h)$ (solid curves) and of the σ^2 nonlinear beam waist $w(z_{NL})$ (dashed curves) as a function of P_{in}. The calculations correspond to the values of absorption coefficient a_0 of the examined samples (in cm^{-1}, shown close to each curve). Dotted lines indicate that at the inflexion points of $w(z = h)$ (i.e., at $P_{in} = P_0$) the nonlinear beam waist $w(z_{NL})$ is stretched by the same factor $m \sim 1.75$ compared to the linear beam waist w_f = 21 μm. (b) Comparison of $P_0(a_0)$ by numerical simulation (squares), fitting of analytical expression (2) for m = 1.75 (solid line) and experimental values (circles). (c) Comparison of $\theta(a_0)$ between numerical simulations (squares) and experimental measurements (circles).

The behaviour of $P_0(a_0)$ can be interpreted in accordance to the theoretical analysis of reference [296] addressing the problem of thermal self-focusing within the aberration-free approximation. The analysis showed that for input power P_{in}, beam compression n is obtained due to positive thermal self-focusing that depends on a critical power p_{cr}, the diffraction length $L_d \equiv z_R$ and a_0 of the medium. The foresaid relation reads

$$P_{in} \approx p_{cr}\left(\frac{n^2-1}{a_0 L_d ln(n^2)} + \sqrt{n^2-1}\right) \qquad 7.1$$

While the problem was solved implying positive nonlinearity, the reduced propagation equation (e.g., Equation 21 in [296]) is identical for negative nonlinearity if also an external focusing initial condition is considered ($\partial_z w|_{z=0} = -w_0/R$) , so that n expresses beam waist stretching instead of compression for a given P_{in}. Accordingly, at P_0, the beam waist stretches by the factor m defined above. By numerical simulations, we used the ansanz of Equation 7.1 for the examined problem, and found that P_0 can be determined, accounting for a fitting dimensionless parameter $\mathcal{A}$, by

$$P_0 \approx \frac{K_T k_0 \lambda^2}{n_0 \left|\frac{dn}{dT}\right|}\left(\frac{\mathcal{A}(m^2-1)}{a_0 L_d ln(m^2)} + \sqrt{\mathcal{A}(m^2-1)}\right) \qquad 7.2$$

where, we have assumed $p_{cr}[in\ W] = K_T k_0 \lambda^2/(n_0 \left|\frac{dn}{dT}\right|)$ and $L_d = k_0 {w_f}^2/2$ (k_0 is the free-space wavenumber). The fitting is plotted in Figure 7.8 for $m = 1.75$ ($d = 15\ mm$) and for $\mathcal{A} = 1/100$, which shows a good agreement between simulations and experiments. We consider parameter $\mathcal{A}$, as a correction factor under the applied approximations (aberration-free approximation, initial external focusing condition, L_d taken at the linear waist). The p_{cr} is a reduced critical power since, in a thermal self-action process, the usual relation of critical power $P_{cr} \propto \frac{\lambda^2}{n_0|n_2|}$ (with $n_2 \propto \frac{dn}{dT} a_0 L_d/(K_T k_0)$ [61]) depends on geometrical characteristics of the beam. For strong absorption ($a_0 L_d \gg 1$), P_0 is independent of a_0, however m clearly depends on the initial focusing condition, so that $P_0 \approx p_{cr}\sqrt{\mathcal{A}(m^2-1)}$. As discussed in [296], this can be understood by the fact that a limited "thin thermal lens" developed at the entrance of a strongly absorbing medium determines balancing of the initial wavefront phase.

Further, we evaluated numerically the divergence of the beam at P_0 versus various values of a_0. The divergence was then calculated according to $[w_{\sigma^2}(h) - w_{\sigma^2}(z_{NL})]/(h - z_{NL})$. A comparison with the experimental results is shown in Figure 7.8. Overall, there is good agreement between the model described by Equations C.3-C.4 and our experimental observations. Accordingly, we conclude that the phenomenological self-trapping by both high repetition rate fs pulses and cw illumination is mainly attributed to steady-state nonlinear thermal self-defocusing of the externally focused beam. The latter effect is caused by optical absorption by a given colloidal solution and governed by the thermal properties of the solvent (here water). Consequently, if the wavelength of the propagating light exactly matches the plasmon resonance of a given nano-colloid, the thermal lensing effect is expected to be further enhanced due to higher absorption cross section of the suspended particles.

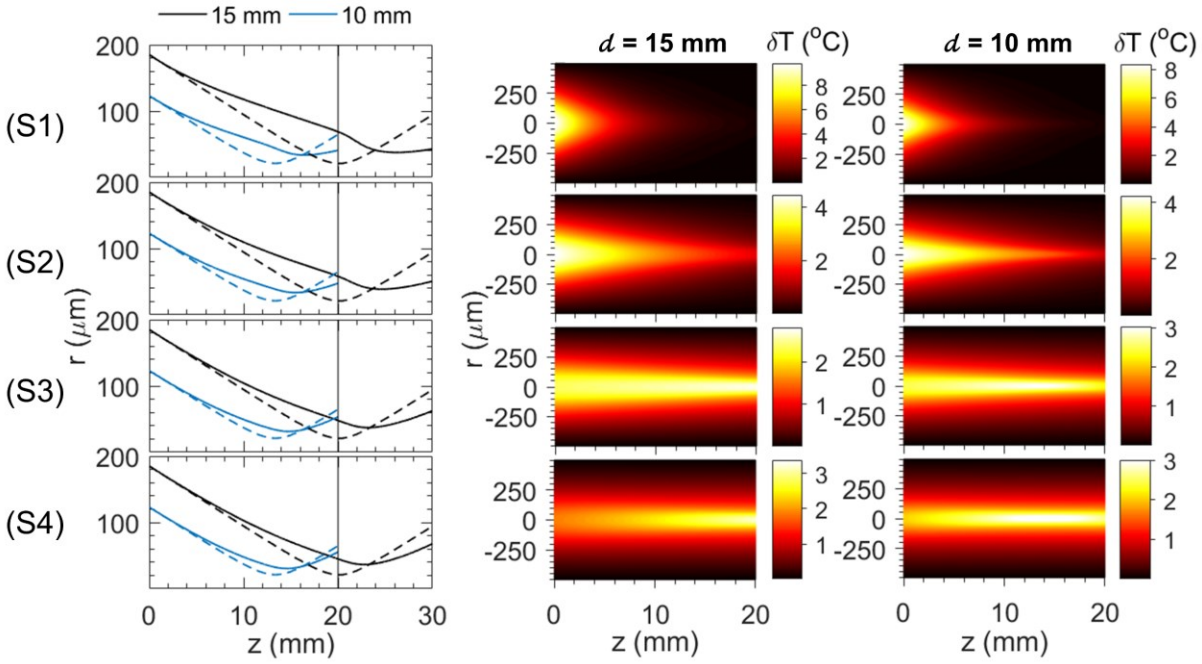

Figure 7.9 Numerical simulation results at $P_{in} = P_0$ for (S1) $a_0 = 2.10$, (S2) $a_0 = 0.84$, (S3) $a_0 = 0.24$ and (S4) $a_0 = 0.06$ cm^{-1} First column shows the σ^2 beam width as a function of z for $d = 15$ mm (black lines) and 10 mm (blue lines). The dashed lines correspond to the linear case (low input power ~0.1 mW). The second and third column show the calculated spatial temperature profiles at $P_{in} = P_0$ for $d = 15$ mm and 10 mm, respectively.

In Figure 7.9, the characteristic-needle like propagation is simulated as a function of propagation z. A nonlinear focus is formed due to temperature-induced refractive index changes in the medium that creates the self-channeling effect, reducing θ at the output. In addition, the δT profiles of all

four cases of a_0 varies significantly. Transverse temperature gradients are extended at larger radius near the input when a is larger. For small values of a_0, increased δT is confined in the vicinity of the focus, where $|\mathcal{E}|^2$ gets higher. This effect has possibly an impact on the development of convective fluid flow due to temperature gradients.

Notably, we have performed an order-of-magnitude comparison between the characteristic times of mass diffusion t_d^m and heat diffusion t_d^{th} (Appendix C/Supplemental Material, Section C.3). We have considered reportedly applied focusing conditions of self-channeling experiments in plasmonic nanocolloids. The calculations showed that, in this context, mass diffusion due to optical forces is a much slower process compared to heat diffusion, so that the latter typically becomes dominant. Nonetheless, the use of high repetition fs pulses exhibits a potential advantage toward mitigation of thermal effects; for instance, if one focuses a beam at a waist of ~1 μm (to overcome Brownian motion) and applies a repetition rate of ~1 MHz, t_d^{th} becomes comparable to the time between each pulse δt_p. In this case, heat accumulation can be alleviated. Contrarily, t_d^m remains much larger than δt_p so that cumulative optical forces are still expected to trap or repulse particles. In other words, it is possible to engineer an interaction where $t_d^{th} \sim \delta t_p \ll t_d^m$ to facilitate gradient force-induced self-trapping in plasmonic nanocolloids by use of fs pulses. However, that would still require considerably high concentrations of particulate material in case of tightly applied focusing [281].

7.5.2 Comparison of resonant nonlinear thermal lensing between fs and cw operation

Experiments on resonant sample S1 demonstrated small differences in the far-field FWHM beam width and divergence between cw and fs operations. The differences may be attributed to the 15% higher absorption coefficient in the case of cw excitation since both the far-field FWHM beam size width and divergence acquire slightly smaller values at the same input power. Nonetheless, at input power of ~80 mW (well above P_0), an increase of the divergence of the central Airy disk was observed in cw operation. This fact, in conjunction with the distinct features in the dynamics of the beam profile for the two laser operation modes (Figure 7.7) indicate an additional contribution to thermal aberration of the beam, presumably due to convective heat transfer.

The breakup of the first diffraction ring, observed in fs and cw operation at P~140 and ~120 mW respectively, exhibits small yet important differences in its dynamics and features. The effect itself bears similarities with the break-up of optical vortices propagating in colloidal media [297]. In the latter case, break-up has been attributed to azimuthal modulation instability due to the exponential grown of a perturbation with an orbital angular momentum of specific charge [297, 298]. Here, we used an elliptical, astigmatic Gaussian beam, which is known to possess orbital angular momentum [299]. Additionally, it is possible that transverse convective currents (see for example in Fig. 3, horizontal setup, of ref. [300]) contribute to wavefront twisting (in addition to downwards translation). Accordingly, we consider that here, an azimuthal modulation instability led to the first diffraction ring breakup much like for the case of an optical vortex.

We analyzed time-resolved images of the beam profile for both fs and cw operation as a function of the input power. Figure 7.10a shows the recorded vertical displacement δy of the core of the beam after the opening of the shutter. We recorded the value of δy as a function of the input power for both cases after $t_1 \approx 0.2\ s$, when the beam is marginally displaced, and after a time delay $t_2 \approx 1.1$ s, when the beam appears to decelerate at its final position. The results clearly indicate consistently smaller δy at early times ($t_1 \approx 0.2\ s$) in the case of fs operation as compared to cw operation. In addition, δy after t_2 is higher for fs operation, suggesting that the beam was displaced with a higher average velocity $\langle u \rangle$ under the induced convective flow within t_2.

Balancing the forces of buoyancy and viscous drag force, leads to an estimation of the average downward velocity of the induced flow [295]

$$\langle u \rangle = \frac{a_V g \pi w_0^2 \delta T}{16 \mu} \tag{7.3}$$

where $a_v \approx 2.1 \times 10^{-4}\ {}^{o}C^{-1}$ is the thermal expansion coefficient of the solvent (water), g is the gravity acceleration, w_0 is the input beam width and $\mu \approx 0.8 \times 10^{-6} m^2/s$ denotes the kinematic viscosity of the solvent (water). Assuming that at the entrance of the medium δT~$8^{o}C$, as seen in the simulations for P_0~$40\ mW$ as seen in Figure 7.9, we find $\langle u \rangle \approx 130\ \mu m/s$, in fair agreement with our observations (Figure 7.10a). Noting that $\delta T \approx \frac{a_0 I w_0^2}{K_T} = 2\frac{a_0 P_{in}}{\pi K_T}$ the flow velocity can be written in the form

$$\langle u \rangle = \frac{a_0 a_V g w_0^2}{8\mu K_T} P_{in} \tag{7.4}$$

Equation 7.4 shows that the relation between $\langle u \rangle$ and P_{in} is linear. In addition, the slope of this relation depends linearly on a_0. Noting that every parameter besides a_0 remains the same for the two laser operation modes, one expects higher $\langle u \rangle$ under cw operation, which is not the case. The effect implicates a difference in the combined thermal conduction and convection heat transfer between the two operation modes, which can be expressed by a δT-dependent, overall heat transfer coefficient $U(\delta T)$. Accounting that heat conduction and convection act in series along y axis, the overall heat transfer coefficient U reads

$$\frac{1}{U(\delta T)S} = \frac{1}{\hbar(\delta T)\mathcal{S}} + \frac{w_0}{K_T \mathcal{S}} \tag{7.5}$$

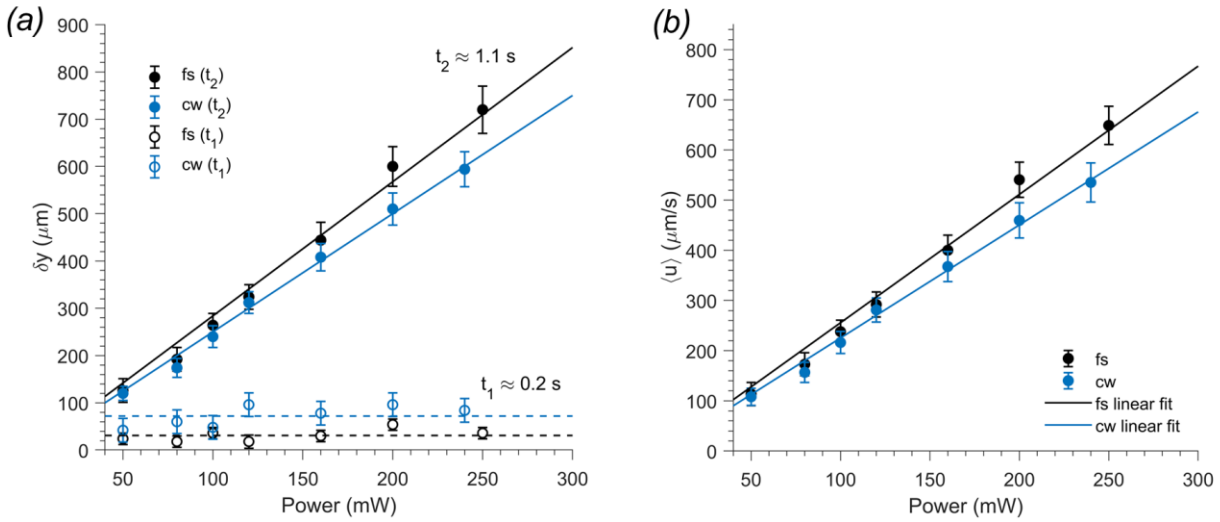

Figure 7.10 Comparison of (a) the displacement δy, and (b) the average velocity $\langle u \rangle$ of the beam profile due to convection under fs and cw operation on sample $S1$ and d = 15 mm as a function of input power. The δy values are shown for two different times t_1 and t_2 after the opening of the shutter. The solid lines are linear fittings and the dashed lines in (a) show the average value of data taken for t_1 at each case. The $\langle u \rangle$ values are calculated for time t_2 after the opening of the shutter.

where $\hbar(\delta T)$ denotes the convection heat transfer coefficient. We also scale the characteristic area $\mathcal{S} \sim \frac{w_0}{a_0}$, so that $\frac{1}{Uw_0} = \frac{1}{\hbar w_0} + \frac{1}{K_T}$. Equation 7.4 is rewritten as

$$\langle u \rangle \approx \frac{a_0 a_V g w_0}{8\mu U} P_{in} \qquad 7.6$$

Equation 7.6 shows that for $\left(\frac{U}{a_0}\right)_{cw} > \left(\frac{U}{a_0}\right)_{fs}$ the value of $\langle u \rangle$ is reduced for the cw case as seen experimentally. Under an oversimplified approach of constant U for both modes, we estimate $1.14\langle u \rangle_{cw} \sim \langle u \rangle_{fs}$ (linear fit data of Figure 7.10b). Accounting also for $(a_0)_{cw} \sim 1.15(a_0)_{fs}$, we find through Equation 7.6 that $(U)_{cw} \sim 1.31(U)_{fs}$, showing that the overall heat transfer coefficient in the fs case is significantly lower. Notably, for $P_{in} \geq 80\ mW$, the $\hbar$ convection coefficient in principle increases due to its dependence on local δT [301] , however, at a different rate between the two modes as shown in Figure 7.10. For $P_{in} < 80\ mW$, it is almost zero, so that $\langle u \rangle_{cw} \approx \langle u \rangle_{fs}$.

Overall, strong thermal aberrations at increased powers, appear to be limited in the case of fs illumination, which is evident on (i) the analysis just described, (ii) the thermal blooming features shown in Figure 7.6, and (iii) the weaker stochastic motion of the beam (Supplemental Video). A possible explanation can be given by the fact that, under excitation by fs pulses, temperature rise is highly confined in the vicinity of the nanoparticles [48]. The temperature increase profile decreases rapidly in space away from the surface of the particle as $\propto r^{-3}$ (ideal case of point source), as opposed to the $\propto r^{-1}$ dependency for cw operation [48]. This is because in the fs case the deposited energy, absorbed by the plasmon mode after each pulse, decays exponentially in time during thermalization of the electrons with the phonon subsystem of the particle before it is transferred through the particle interface to the surrounding solvent. Accordingly, under cw excitation and at short time delays, temperature increase in the medium by heat conduction is less localized compared to the case of fs operation. Homogeneous temperature increase is established faster in the medium so that the effect induces convective currents and beam deflection at slightly shorter time delays (t_1) compared to fs operation at a wide range of powers (Figure 7.10a), which confirms that the effect cannot be attributed to linear absorption difference. Effectively, in the fs case, overall thermal resistance due to convective heat transfer is higher at increasing P_{in}, which affects the vertical deflection of the beam, break-up dynamics and thermal distortion (blooming).

7.6 Conclusion

We have studied phenomenological self-trapping of high repetition rate fs laser pulses in plasmonic nanocolloids of varying plasmon resonance under typically reported external focusing conditions. The excitation regime resulted in cumulative effects, exhibiting a quasi-cw behaviour. Experimental observations of the far-field beam width and divergence indicated similarity for all samples up to a critical power. They further implied phenomenological self-trapping due to stationary, photo-absorption thermal defocusing of an externally focused beam, confirmed for both cw and fs excitation. A good agreement between numerical experiments and the experimental observations supported the foresaid model suggesting that the effect can be generally observed in any absorbing medium.

An important element of the studied effect in a soft-matter system is the induction of convective currents that causes beam downward deflection in a horizontal illumination configuration. Under resonant fs and cw excitation of plasmonic colloids we observed that beam deflection was further accompanied by beam spatial mode break-up at increasing input powers, most likely due to the ellipticity of the beam. By analyzing the dynamics of the effect for both cases, we conclude that under fs excitation, convective heat transfer appears to be, relatively to the cw excitation, reduced in magnitude and decoupled in time from conductive heat transfer. This is presumably because fs illumination as opposed to cw, results typically in spatial temperature increase confinement near the particles. Effectively, delayed beam break-up and reduced beam axial asymmetry due to thermal blooming at increased power are observed.

Finally, according to our analysis, we conclude that the (high) repetition rate of fs pulses in conjunction with tight focusing (high numerical aperture) constitute dominant parameters for alleviating thermal effects and promoting observation of nonlinear self-trapping induced by gradient optical forces in plasmonic nanocolloids.

CHAPTER 8 GENERAL DISCUSSION

8.1 Some aspects of the critical power for self-focusing in the case of ultrashort pulses

8.1.1 Chromatic dispersion

In Chapter 5, the threshold power for self-focusing and filamentation was evaluated experimentally using the power limiting method in the case of optical transparency. Following that, an estimation of the nonlinear index of refraction n_2 was deduced by use of Equation 5.1, which in fact is a steady-state regime result of the solution of the 2-D NLSE, meaning that the influence of chromatic dispersion is ignored in Equation 5.1. Therefore, it should be clarified that the estimation of n_2 of a transparent material by the determination of the critical power in the filamentation regime (case of ultrashort pulses) requires caution.

In Chapter 5, I have further used a result derived from the ABCD formalism that accounts for the influence of M^2 propagation factor on the threshold power for self-focusing. Despite having been formulated within the aberration-free approximation, the latter result is presented as a simple factorization of the threshold power [250]. This is directly related to the fact that the influence of M^2 on the estimation of time-integrated quantities, such as the optical power of the beam, is accurately accounted for when M^2 is multiplied with the optical wavelength in the propagation equation [260]. Thus, the M^2 correction is applied without changing the physical meaning and mathematical derivation of the threshold power $P_{th}^{Gaussian}$. Still, chromatic (normal) dispersion, is expected to further increase $P_{th}^{Gaussian}$ (or P_{th} of any profile) in the case of ultrashort pulses.

In practice, our experimental evaluation provides what Fibich refers to as an "upper bound" for optical collapse in the case of a Gaussian pulse considering a correction due to the M^2 propagation factor, *but also under the influence of chromatic dispersion.* Let us define it as $P_{th,exp}^{Gaussian}$. The relation between the threshold power and n_2 through Equation 5.1 sets equivalently a lower bound for the evaluation of n_2 since it appears that the steady state $P_{th}^{Gaussian}$ is somewhat overappreciated by equating it to what was measured, i.e., to $P_{th,exp}^{Gaussian}$. This is because it should hold $P_{th}^{Gaussian} \leq P_{th,exp}^{Gaussian}$, accounting for the influence of normal chromatic dispersion discussed earlier. To better

evaluate this experimental overestimation, one should in practice examine the influence of chromatic dispersion in conjunction with the applying external focusing conditions. The former can be examined briefly by comparison of the characteristic diffraction length L_d and dispersion length L_{DS} (see Appendix B, Section B.2 and Table B.3 for definitions) by the parameter $\delta \equiv L_d/L_{DS}$.

Based on numerical results presented by Luther et al. [302] and as stated in [40], when $\delta \ll 1$, Equation 5.1 provides a fair estimation of the critical power, even for the case of ultrashort pulses. To test further this hypothesis, I benchmarked the solution of Equation B.2 (Appendix B) for $A = 0$ with the analytical approximation introduced by Luther et al. [302], assuming a collimated beam at the input (Figure 8.1). As a numerical experiment, the same model was also solved accounting for the initial focusing condition of the physical experiment ($F = 0.36$). The result (Figure 8.1) shows that the effect of dispersion is significantly weaker against combined diffraction and nonlinearity when the beam is focused by a lens at the input. Most likely this occurs because in the case of small normal dispersion, the various temporal cross sections of the beam collapse in singularity points Z_c that vary as a function of time t, forming a singularity curve $Z_c(t)$ [64]. Therefore, under the influence of a lens, all singularity points of the same t transform into a new singularity function $Z_c^{(F)}(t)$ (for instance, within the aberration-free approximation, it should hold that $Z_c^{(F)}(t) \sim Z_c(t)F/[Z_c(t)+F]$ [64]) so that the singularity curve $Z_c(t)$ changes substantially (becomes confined in space) and so do the collapse dynamics. Similar conclusions were drawn in [303] on the effects of external focusing and chromatic dispersion in the case of the critical power for optical collapse in the case of ultrashort pulses. Most importantly, Figure 8.1 shows that for the parameters used in the experiments of Chapter 5 (2δ~0.4), the value of the threshold power is at most 10% higher than the one evaluated by Equation 5.1, which remains well within the limits of the margin of error of n_2 presented in Table 5.1.

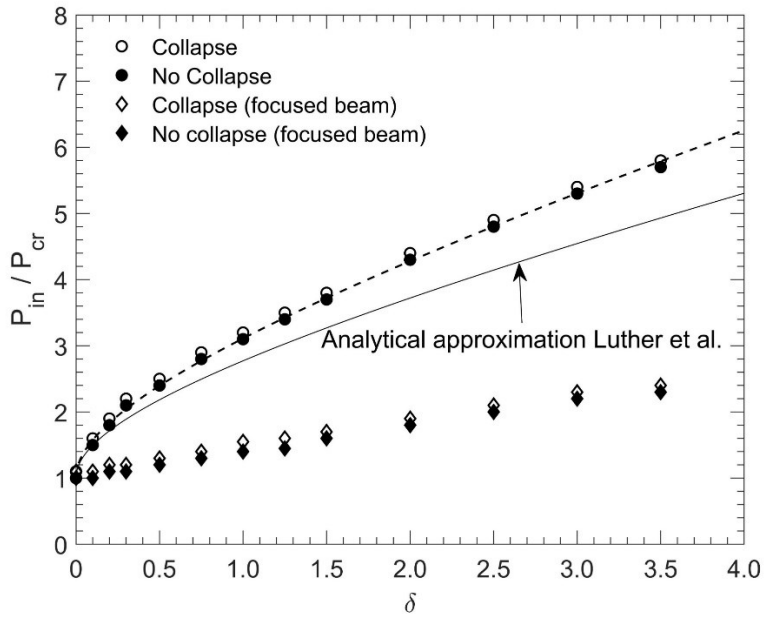

Figure 8.1 Results of numerical simulations by solution of Equation B.2 (A = 0), (Appendix B). The black solid line shows the analytical approximation by Luther et al. [302]. Notably, the latter underestimates the threshold calculated numerically for a collimated beam (open and closed circles) as δ becomes large, which is also demonstrated by Luther et al. [302]. A linear correction by 3/4 (black dashed line) shows however a remarkable agreement with the numerical solution. Importantly, chromatic dispersion has a significantly weaker influence on the threshold power when external focusing is applied (open and closed diamonds), (F = 0.36), matching the experiment, as discussed in Appendix B).

8.1.2 Absorption

Chapter 6 dealt with the case of self-focusing in an absorbing medium (Au nanorod colloids). The examined plasmonic material constitutes a particular case; it exhibits saturation of linear absorption under intense pumping conditions accompanied by deformation effects near the optical power collapse region. Bypassing the physical picture of what is happening to the material itself and for the shake of simplifying the optical collapse condition (threshold power for self-focusing), I shall examine in this section what is happening to the propagating field. I focus on the case 2 of the experiments described in Chapter 6 (i.e., the case that the geometrical focus is located near the input face of the cell containing the samples), where the general problem of optical collapse of an externally focused beam can be reduced to that of a collimated beam and linear absorption (non-saturable) with satisfactory accuracy. If additionally chromatic dispersion is ignored by virtue of

the focusing conditions discussed in the previous section, solution of the steady-state Schrodinger equation with linear damping can provide a fair approximation of the optical collapse threshold.

An interesting approach has been introduced by Butylkin et al. [274], within the aberration-free approximation, to determine an analytical expression of the threshold intensity for self-focusing in the case of linear absorption. The reduced equations of the NLSE that represent the evolution of dimensionless beam width $\mathcal{L}$ as a function of propagation z read

$$\mathcal{L}_{zz} = \left(\frac{1}{L_d^2} - \frac{1}{L_{SF}^2} e^{-za_0}\right)\frac{1}{\mathcal{L}^3}. \tag{8.1}$$

where L_{SF} is the characteristic self-focusing distance. The problem has been divided and studied into two regions, that of weak and strong absorption ($A \ll 1$ and $A \gg 1$, respectively, A as defined in Appendix B). In fact, in our case the weak absorption solution proves to be sufficient. A derived analytical expression provides an estimate of the threshold power for self-focusing in the presence of linear absorption and has been normalized over the critical power for self-focusing as

$$\frac{(P_{th})^{abs}}{P_{cr}} \approx 1 + \frac{2A^2}{3ln\left[1 + \frac{2}{3}\left(\frac{4}{5}A^2\right)^{\frac{2}{3}}\right]}. \tag{8.2}$$

Even though the aberration-free approximation typically leads to significant overestimation of the critical power for self-focusing, Equation 8.2 is written in a normalized form over some P_{cr}. The failure of the aberration-free approximation to calculate exactly P_{cr} is that it considers the quantity $b = (L_d^{-2} - L_{SF}^{-2})$ to be a constant, while in reality it decays as a function of z because of power transfer during re-organization of the beam profile to the Townes functional [64]. Considering Equation 8.1 in the weak absorption regime, it holds that $\mathcal{L}_{zz} \approx [L_d^{-2} - L_{SF}^{-2}(1 - \alpha z)]\mathcal{L}^{-3} = -b'(z)L^{-3}$, so the dynamics of optical collapse are governed by $b_z' = -aL_{SF}^{-2} = -Qa$, where $Q = L_{SF}^{-2} > 0$ is constant. Asymptotic analysis of the reduced equations in the case of linear damping presented in [64] show that the dynamics of collapse are governed in fact by the ansatz $b_z' = -Q(z)a$, where the $Q(z) > 0$ function reduces as $z \to Z_c$, amounting for the power transfer from the collapsing core to the outer tail of the beam. The latter is not considered in the aberration-free

approximation employed by Butylkin et al. [274]. However, Q is independent of linear absorption a in b_z' for both cases. Thus, one could apply the threshold power determined experimentally in the absence of absorption (or the theoretical $P_{th}^{Gaussian}$ in the absence of absorption if chromatic dispersion is negligible) as the normalization parameter P_{cr} (which is in principle different than the theoretical overestimated expression of P_{cr} within the aberration-free approximation) expecting that this "correction" on Equation 8.2 to yield a fairly accurate evaluation of $(P_{th})^{abs}$.

A comparison between the result of the numerical simulations and the "corrected" use of Equation 8.2 is shown in Figure 8.2, which demonstrates a fair agreement between the two. Conclusively, the presented analysis suggests that Equation 8.2 can be used with appropriate caution as an analytical expression for a fair estimation of the threshold power for self-focusing by the power limiting method in the presence of "weak" absorption, provided that the critical power in the absence of absorption has first been evaluated experimentally and chromatic dispersion effects are subtle as imposed by the examined medium and the applied focusing conditions.

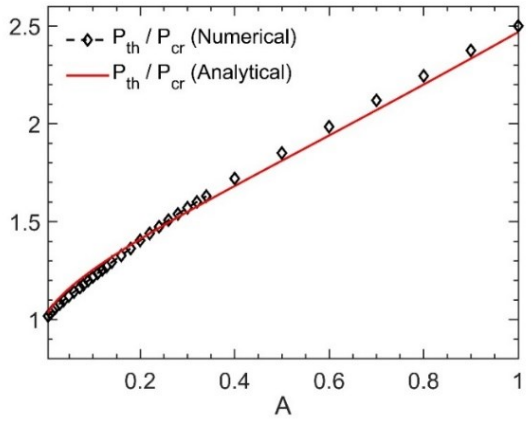

Figure 8.2 The results of numerical simulations of Equation B.2 compared with the analytical approximation proposed by Butylkin et al. [274] (Equation 8.2).

8.2 Considerations on steady-state self-channeling in plasmonic nano-colloids

A major question raised in Chapter 7 is how, in a soft-matter system, self-channeling of laser light due to mass transport (scattering) can be experimentally realised as opposed to nonlinear thermal lensing in the presence of absorption. Generally, demonstrations of self-channeling (either due to

scattering or absorption) in the literature are based on the following experimental techniques: (i) imaging the side view of the scattered radiation by the particles along the formed, diffraction-free channeling effect, (ii) monitoring the output beam profile transformation at the output face of the cuvette or the far-field and (iii) monitoring the output power versus the input power.

It is rather surprising that, in the literature, the dynamics of self-channeling are scarcely examined experimentally. In fact, according to the analysis presented in Appendix C the temporal evolution of the beam profile transformation should, in principle, differ significantly when governed by either mass transport or thermal effects (much slower in the first case). For instance, in reference [300], mass transport effects due to thermophoresis have been distinguished from thermal conduction with an all-optical method as a delayed response. A similar approach can be adopted for the case of the self-channeling problem described above.

For instance, in the proposed model of Equation 4.31, it is suggested that supercritical self-focusing due to local concentration modulation occurs provided that particles have positive polarizability (in the case of negative polarizability, self-focusing nonlinearity becomes subcritical). Since positive polarizability results in trapping particles along the high-intensity core of the beam, it is accordingly thought that optical collapse will be prevented and balanced eventually by increasing local absorption, which in turn shall result in heating up the medium and establishing a negative thermal lens that defocuses the beam. Accordingly, this hypothesis can be verified by analyzing the dynamics of the output beam profile transformation, first, at early stages of self-action, i.e., for low input power and second, at increasing input power, i.e., when thermal distortion or displacement of the beam due to convective currents become observable. However, to my knowledge, the approach I just described has not been performed experimentally in the context of self-channeling in colloidal matter.

Another aspect that appears to be problematic, is the way Equation 4.31 is implemented in the literature, and specifically, the applied initial conditions of the input field. Reportedly, most experimental demonstrations of self-guiding attributed to optical gradient forces in colloidal suspensions have been performed under conditions of external focusing by a positive lens (one exception is ref. [304], where an optical fiber was employed). A positive lens introduces an initial phase-front curvature of $\sim\frac{\pi}{\lambda R}w_0^2$, which must be considered in the numerical model supporting the

experiment. The initial conditions imposed in numerical experiments for instance in [176, 280, 285, 287] suggest that the beam was initially collimated. Such assumption may lead to substantial misrepresentation of the physical picture; thus, one cannot expect that the experiment is accurately reproduced. For instance, modelling of the nonlinear self-collimation of laser beams due to the thermal lensing effect described in Section 4.6.3 necessitates application of appropriate external focusing condition.

Having that much out of the way, and as a continuation of what has been discussed in Chapter 7, let us examine strategies toward realisation of self-channeling of laser light in a plasmonic nano-colloid induced by optical forces. It is common practice in reported self-channeling experiments to use an applied $1/e^2$ beam waist larger than 10 μm. In this context, a major obstacle against metallic nanoparticle trapping is beam bending away from the irradiation volume due to thermal heating effects, prohibiting the formation of sufficiently steep intensity gradients near the beam waist. Temperature gradients are developed because of optical absorption by the particles, locally heating the surrounding solvent within a much shorter timescale compared to the characteristic time required for mass transport. Hence, in practice, one might first consider that the SPR should be located adequately far from the applied optical wavelength to reduce the absorption cross-section of each particle. Nonetheless, as shown in Figure 7.9, even a local temperature increase by 3 K may have a significant impact on beam bending, as demonstrated also experimentally in Chapter 6 by use of AuAg alloy nanoparticles of 20 nm radius and volumetric filling factor $<10^{-5}$ (concentration $\rho \approx 3 \times 10^{17} m^3$).

A way that the physical picture can change rather drastically is the application of a more powerful lens to reduce the effective length of thermal diffusion and the corresponding characteristic time near the beam waist, so that, in the steady state, power dissipation as heat toward the heat bath of the surrounding solvent becomes comparable or higher than the energy storage in the irradiated volume and local temperature remains unchanged. However, accounting for a mean distance between particles $p \approx \rho^{-\frac{1}{3}} \approx 1.5\ \mu m$ (as applied in the previous example), such choice comes at the expense of the requirement of a higher particle concentration since the modulation of refractive index of the colloid exhibits saturation when the beam width approaches p [304] . For instance, a

×10 concentration increase of the above value shall reduce p close to the diffraction limit (at ~0.7 μm) when 800 nm wavelength and NA = 0.6 are applied.

In Chapter 7 I discussed how the choice of a high-repetition ultrashort pulsed laser source may also contribute to alleviating thermal effects by temporal confinement of energy deposition. Taking the idea presented in Figure C.5 of Appendix C a step further, let us ignore absorption-related effects and consider how mass transport compares to limitations imposed by Brownian motion of the particles and radiation pressure. In the Rayleigh regime $\lambda \gg r_p$ and based on the same arguments and parameters presented in Appendix C, it can be shown that the velocities developed due to scattering force and gradient force scale as $u_{scat} = D_m F_{scat}/k_B T = 14.2\pi^3 P_{in}\varepsilon_m {r_p}^5/\left(vc\lambda^4 {w_f}^2\right)$ (as presented in [58, 214]) and $u_d^m = w_f/t_d^m = {r_p}^2 P_{in}/\left(3\pi vc {w_f}^3\right)$ (from the analysis presented in Appendix C), respectively. Furthermore, in a stationary fluid medium, a strict criterion considers that displacement r due to Brownian diffusion scales as $t_B = {r_p}^2/D_m$ [305] so that the time averaged velocity due to Brownian motion scales as $u_B = D_m/r_p$. For instance, we can estimate the maximum beam waist above which velocity due to Brownian motion overcomes gradient forces, as $w_f \lesssim \sqrt[3]{2{r_p}^4 P_{in}/(ck_B T)}$. According to this relation, if optical power of 1 W is delivered at the focus, one is hardly expected to trap a particle of $2r_p = 40\ nm$ with a beam waist higher than $w_f \approx 0.65\ \mu m$, a value much lower than what is usually employed in "self-trapping induced by gradient-forces" experiments. In truth, for the same optical power and by employing a beam width no more than $w_f \approx 5.5\ \mu m$, nanoparticles of at least $2r_p = 200\ nm$ are likely to respond to gradient forces, however, such particle sizes lie in the limits of the Rayleigh regime, so in this case the presented calculations are only applicable for wavelengths higher than 800 nm.

Additionally, equating u_{scat} and u_d^m provides an estimate of the maximum beam waist $w_f \lesssim \mathcal{G}\,\lambda^4/{r_p}^3$ (where $\mathcal{G} = (42.7\pi^4\varepsilon_m)^{-1}$), which can be applied to ensure that gradient forces dominate over scattering. Evidently, this condition necessitates the highest possible λ (scattering reduction) and the smallest possible particle size r_p to maximize the applied beam waist, which contradicts the previous criterion related to Brownian motion and shifts the diffraction limit at larger values. One can easily verify for instance that for delivered optical power of 1 W at the focus and optical

wavelength of 1000 nm, nanoparticles of size $2r_p = 140\,nm$ are not likely to be trapped with a beam waist higher than 3.5 μm. Conclusively, considering all above estimations, the longest wavelength possible (as limited by increasing optical absorption in the solvent) in conjunction with a small beam waist (< 3-4 μm) and adequate particle concentration ($\rho \gg {w_f}^{-3}$) of nanoparticles of diameter ~100-200 nm are prescribed for observation of self-trapping in plasmonic nanocolloids. Employing smaller nanoparticles, would typically require stronger external focusing, which might even approach the diffraction limit. In any case, the negative polarizability regime [176] seems accordingly preferable (as opposed to the positive one) since it leads to subcritical self-focusing, thus it is inherently stable. At such proximity to diffraction limits, realization of the proposed by Fardad et al. [39] positive polarizability scenario seems highly unlikely due to its supercritical nature.

Another aspect I did not touch in Chapter 7 is the fact that the refractive index of water (the solvent of the colloid) exhibits a temperature dependence that changes its monotonicity below 0 K. In fact, the slope of the thermo-optic coefficient dn/dT of water is almost 0 [306, 307] (local maximum of $n(T)$) for a range of temperatures between 3-5 K, i.e., within its liquid phase. Even within the range of 5-10 K, the absolute value of dn/dT of water, despite being negative, is typically ~5-6 times lower than the absolute value at the room temperature [306-308], which means that ~5-6 times larger input power must be applied in experiments similar to those that correspond to Figure 7.2, Figure 7.3 and Figure 7.4 to obtain the same effects. Thus, this observation provides possibly an interesting way to mitigate temperature rise-mediated refractive index modulation in aqueous plasmonic colloids when kept at low temperatures.

CHAPTER 9 CONCLUSION

9.1 Review

This thesis focused on the understanding of nonlinear propagation of femtosecond laser pulses in metallic nanoparticle colloids and its association in the development of related applications. An important first step toward this goal, was to organize existing knowledge on the origin of nonlinearities in plasmonic nanocomposites to clarify their temporal response, strength, and potential practical capabilities. Within the formalism of the effective medium approximation, and particularly in the femtosecond regime, metallic nanocomposites possess an ultrafast nonlinearity arising from the gained kinetic energy of a large and out-of-equilibrium electronic distribution generated near the surfaces of the nano-inclusions ~10 fs after pulse-medium interaction. This means that excited plasmons lose their coherence during the foresaid process. Effectively, observed nonlinearities under the inherently intense pumping conditions of femtosecond pulses lead to saturation effects due to the drastic modulation of the metal's dielectric permittivity, undermining local-field enhancement effects. It is important to point out that the physical picture just described refers to a composite medium of effective properties formulated by homogenization theories and thus, is applicable to macroscopic electromagnetic field propagation. In mesoscopic or nanoscopic systems (below the diffraction limit), the potential of coherent nonlinear responses has been explored in the context of non-perturbative (low-intensity field) quantum-mechanical formalism. Returning to the effective-medium picture, under longer laser field-medium temporal interaction t, another two important regimes can be distinguished: (i) 500 fs $\lesssim$ $\lesssim$ 10 ps: in this regime, nonlinearities are related to the thermalization of electrons with the lattice of the metallic nano-inclusions (intrinsic) and (ii) $t \gtrsim$ 10 ps: diffusive nonlinearities (typically stronger) arise in the dielectric matrix (extrinsic) of the composite.

The research presented in this thesis was divided into two distinct directions, based on the running operation of modern ultrafast laser systems: (i) the propagation of pure femtosecond, single pulse of high-energy (by use of a femtosecond amplifier) leading to the effect of femtosecond filamentation, and (ii) a quasi-static propagation regime due to accumulation of low energy, high-repetition rate femtosecond laser pulses (by use of a mode-locked femtosecond oscillator). Within

the overall scope presented in Chapter 1 and the two distinct directions just mentioned, the following contributions were reported:

(i) In Chapter 5, an optical power limiting technique was employed, for the first time, in the femtosecond filamentation regime, for the purpose of evaluating optical nonlinearities in transparent liquids. Comprehensive experimental demonstration of the technique in water and ethanol indicated the importance of the location of far-field apertured detection of the setup in the case of ultrashort laser pulses so that a standalone measurement can reliably yield quantitative information on the self-focusing nonlinearity and weigh the interplay between possible optical breakdown against filamentary propagation through a transparent material. A theoretical background was developed to interpret the response of the technique within the context of the theory of transformation of the ultrafast beam into a nonlinear conical wave upon optical collapse into a filament of light.

In Chapter 6, the use of the power limiter apparatus in the femtosecond filamentation regime was further demonstrated in the more complex case of Au nanorod colloids (i.e., an optical medium that exhibits saturable nonlinearities as discussed through Chapter 1). Accordingly, the measurements were combined with optical transmittance characterization for the evaluation of the imaginary part of the nonlinearity, but also particle deformation effects were carefully examined. Detailed nonlinear propagation analysis in conjunction with all previous experimental evidence showed that the Kerr nonlinearity of gold nanorod colloids is strongly saturated near the power of optical collapse, while also particle deformation effects are observed. The measurements presented therein clearly indicate that the plasmon-mediated local fields are undermined by the ultrafast generation of non-thermal electrons, thus contributing to an insignificant increase of the Kerr nonlinearity of the host dielectric upon filamentation. Lastly, the combined work presented in Chapter 5 and Chapter 6 show that the power limiting method can be employed as an alternative direct characterization technique of ultrafast nonlinearities in a variety of transparent and absorptive media. It is therefore anticipated that these studies will generate interest for researchers working on the development of novel applications based on femtosecond filamentation or in general, on ultrafast, Kerr-type nonlinearities.

(ii) In Chapter 7, the use of high-repetition rate femtosecond laser pulses for the observation of self-channeling in various metallic nano-colloids was compared against cw illumination. This was

done by providing a detailed and broad description of the observed phenomenon, ranging from nonlinear sample characterization and nonlinear propagation analysis to theoretical analysis of both self-focusing and thermal conduction and convection effects. The findings indicated that (a) self-channeling in plasmonic nanocolloids (under either cw or high-repetition rate fs operation) manifests itself principally due to absorption-induced nonlinear thermal lensing and self-collimation of the externally focused beam into the examined media, and (b) the use of fs pulses appear to alleviate thermal distortion effects at high input powers.

The findings presented in Chapter 7 lead to the following important implications: First, since it was demonstrated that nonlinear thermal lensing takes place even far from the plasmon resonance and for low absorption coefficients, the self-channeling effect reported often in the literature as an optical gradient-force-mediated nonlinear effect must be carefully examined experimentally, particularly in dynamic experiments, not only in the case of plasmonic nanocolloids but also for any colloidal system. Most likely, the beam waist, being reportedly >10 μm in diameter in relevant experiments, appears to undermine the possibility of spatial thermal confinement, thus hampering mass transport effects induced by gradient forces. Second, as shown in Chapter 7, the differences observed in the thermally distorted output profiles between the two operation modes point out significant temporal thermal confinement in the case of fs pulses as opposed to cw illumination. Although not having been demonstrated experimentally, this observation prompts to strong implications that the repetition rate of fs pulses is a powerful parameter toward alleviation of thermal effects and promotion of laser-induced mass transport in plasmonic nanocolloids, since the latter is physically a much slower process.

9.2 Directions for future research

The nonlinear propagation equation has been employed extensively throughout this thesis (solved in water and metallic nanocolloids), thus gaining insights on experimental observations within two main propagation regimes: single pulse or high-repetition rate pulses.

In the first regime and in the case of aqueous colloidal gold nanorods, nonlinear propagation was mainly studied near the threshold of optical collapse, while the accompanied effects of femtosecond filamentation and supercontinuum generation were not covered in detail. Nonetheless, a synthesis of results found in the literature, observations made by practical experimentation (e.g., as shown

in Figure 4.24 and in ref. [309]) and measurements of the Kerr nonlinearity obtained by the power limiting method have led the author to draw several conclusions and recommendations with respect to filamentary propagation and supercontinuum generation in plasmonic nanocolloids, as follows:

- No significant enhancement of the self-focusing nonlinearity has been measured or observed when metallic nanoparticles are dispersed in water at an optical wavelength of 800 nm and pulsewidth of > 55 fs. The effect has been quantitatively evaluated for nearly resonant nanorods by the power limiting method. For non-resonant Au nanospheres and AuAg alloy nanospheres, the threshold power was evaluated qualitatively to be consistently above the one of the solvent (water). The corresponding generated supercontinua at the anti-Stokes wing do not differ substantially in spectral extend from the one of pure water and are principally attenuated in amplitude due to (modulated) scattering or absorption by the particles near the SPR frequencies. These observations can be spectroscopically evaluated *quantitatively* by a similar approach to the one proposed in [51] for a variety of plasmonic nanoparticles and excitation regimes, for the purpose of studying SPR quenching and interband threshold shift effects [57, 233]. Systematic spectroscopic investigation of generated supercontinua both in the normal and anomalous dispersion regions of a host dielectric in conjunction with power limiting method measurements are recommended.
- Laser filamentation in plasmonic nanocomposites by employing ultrashort pulses of pulsewidth shorter than plasmon decoherence and excitation of non-thermal electrons (< 10 fs) has yet to be explored. Not only few-cycle fs pulses are faster than the reported response for thermo-modulation of the nanoparticle's permittivity and saturation of field amplification, but also the threshold power for self-focusing in the host dielectric shall be substantially lower energetically in view of increased pulse peak power. Thus, the deposited energy on the system near the threshold power for self-focusing shall further reduce below thermodynamic transitions observed in the particles, favoring their integrity, as discussed in Chapter 6. Nonetheless, one should be mindful of the applied field intensities driving the plasmon oscillation, likely exceeding the perturbative theoretical regime presented by the theory of nonlinear coherent response of small metallic nanospheres (Section 4.4.2).
- The strongest in magnitude nonlinearities in plasmonic nanocomposites are slow and extrinsic, mainly arising from heating of the dielectric host. It would be interesting to

exploit this response and demonstrate “active” control of femtosecond filamentation in plasmonic nanoparticle-doped transparent materials. For instance, light-induced waveguides (refractive index gradients) can be generated by cw or short pulse illumination in plasmonic nanocomposites near the plasmon resonance. Coupling femtosecond filaments through these “waveguides” is expected to yield a powerful tool of supercontinuum control in bulk media. It would be further interesting to experiment with host dielectrics of low thermal expansion coefficients, thus of positive thermo-optic response (e.g., silica or water at low temperatures).

Conclusively, such advances in supercontinuum control through femtosecond filamentation in bulk or colloidal media are highly desirable and expected to bring about advances in the fields of transient pump-probe spectroscopy [42], ultra-resolution microscopy and optical communications [310], and biophotonics [311].

In the second regime, that of high-repetition rate femtosecond pulses, strategies for the realisation of self-channeling induced by optical gradient forces have been thoroughly discussed in Chapter 7 and Chapter 8. These effects hold potential for low-intensity remote communication, controlling light with light technologies and formation of optical waveguides in biological or plasmonic soft-matter. Another possibility to be explored is that of self-channeling through thermophoresis, as for example discussed in [281]. Toward this objective, it is required that plasmonic nanostructures of negative Soret coefficient are engineered (i.e., by surface functionalization or by shell-structured fabrication in a dielectric coating) and tested. Importantly, self-trapping through thermophoresis is most likely to occur in a vertical illumination setup since parasitic induction of convective currents in a soft matter system is otherwise unavoidable.

REFERENCES

[1] J.B. Khurgin, G. Sun, Plasmonic enhancement of the third order nonlinear optical phenomena: Figures of merit, Optics express, 21 (2013) 27460-27480.

[2] J. Khurgin, G. Sun, Third-order nonlinear plasmonic materials: Enhancement and limitations, Physical Review A, 88 (2013) 053838.

[3] A.V. Krasavin, P. Ginzburg, A.V. Zayats, Free-electron optical nonlinearities in plasmonic nanostructures: a review of the hydrodynamic description, Laser & Photonics Reviews, 12 (2018) 1700082.

[4] D. Stroud, P. Hui, Nonlinear susceptibilities of granular matter, Physical Review B, 37 (1988) 8719.

[5] D. Stroud, V.E. Wood, Decoupling approximation for the nonlinear-optical response of composite media, JOSA B, 6 (1989) 778-786.

[6] J. Sipe, R.W. Boyd, Nonlinear susceptibility of composite optical materials in the Maxwell Garnett model, Physical Review A, 46 (1992) 1614.

[7] M.I. Stockman, K.B. Kurlayev, T.F. George, Linear and nonlinear optical susceptibilities of Maxwell Garnett composites: Dipolar spectral theory, Physical Review B, 60 (1999) 17071.

[8] F. Vallée, N. Del Fatti, Ultrafast nonlinear plasmonics, Plasmonics: Theory and Applications, Springer2013, pp. 167-205.

[9] T. Stoll, P. Maioli, A. Crut, N. Del Fatti, F. Vallée, Advances in femto-nano-optics: ultrafast nonlinearity of metal nanoparticles, The European Physical Journal B, 87 (2014) 1-19.

[10] L.V. Besteiro, X.-T. Kong, Z. Wang, G. Hartland, A.O. Govorov, Understanding hot-electron generation and plasmon relaxation in metal nanocrystals: Quantum and classical mechanisms, Acs Photonics, 4 (2017) 2759-2781.

[11] A. Crut, P. Maioli, F. Vallée, N. Del Fatti, Linear and ultrafast nonlinear plasmonics of single nano-objects, Journal of Physics: Condensed Matter, 29 (2017) 123002.

[12] L.V. Besteiro, P. Yu, Z. Wang, A.W. Holleitner, G.V. Hartland, G.P. Wiederrecht, A.O. Govorov, The fast and the furious: Ultrafast hot electrons in plasmonic metastructures. Size and structure matter, Nano Today, 27 (2019) 120-145.

[13] M.I. Stockman, Nanoplasmonics: past, present, and glimpse into future, Optics express, 19 (2011) 22029-22106.

[14] M. Sheik-Bahae, D.C. Hutchings, D.J. Hagan, E.W. Van Stryland, Dispersion of bound electron nonlinear refraction in solids, IEEE Journal of quantum electronics, 27 (1991) 1296-1309.

[15] M. Pelton, M. Liu, S. Park, N.F. Scherer, P. Guyot-Sionnest, Ultrafast resonant optical scattering from single gold nanorods: Large nonlinearities and plasmon saturation, Physical Review B, 73 (2006) 155419.

[16] S. Kim, J. Jin, Y.-J. Kim, I.-Y. Park, Y. Kim, S.-W. Kim, High-harmonic generation by resonant plasmon field enhancement, Nature, 453 (2008) 757-760.

[17] J. Olesiak-Banska, M. Gordel, R. Kolkowski, K. Matczyszyn, M. Samoc, Third-order nonlinear optical properties of colloidal gold nanorods, The Journal of Physical Chemistry C, 116 (2012) 13731-13737.

[18] Y. Hua, K. Chandra, D.H.M. Dam, G.P. Wiederrecht, T.W. Odom, Shape-dependent nonlinear optical properties of anisotropic gold nanoparticles, The journal of physical chemistry letters, 6 (2015) 4904-4908.

[19] Y.-H. Qiu, F. Nan, Y.-F. Zhang, J.-H. Wang, G.-Y. He, L. Zhou, Q.-Q. Wang, Size-dependent plasmon relaxation dynamics and saturable absorption in gold nanorods, Journal of Physics D: Applied Physics, 49 (2016) 185107.

[20] M. Maldonado, H. Baltar, A.S. Gomes, R. Vaia, K. Park, J. Che, M. Hsiao, C.B. de Araújo, A. Baev, P. Prasad, Coupled-plasmon induced optical nonlinearities in anisotropic arrays of gold nanorod clusters supported in a polymeric film, Journal of Applied Physics, 121 (2017) 143103.

[21] R. Sato, J. Henzie, H. Rong, M. Naito, Y. Takeda, Enhancement of the complex third-order nonlinear optical susceptibility in Au nanorods, Optics express, 27 (2019) 19168-19176.

[22] M. Gordel, J. Olesiak-Banska, K. Matczyszyn, C. Nogues, M. Buckle, M. Samoc, Post-synthesis reshaping of gold nanorods using a femtosecond laser, Physical Chemistry Chemical Physics, 16 (2014) 71-78.

[23] A.B. Taylor, A.M. Siddiquee, J.W. Chon, Below melting point photothermal reshaping of single gold nanorods driven by surface diffusion, ACS nano, 8 (2014) 12071-12079.

[24] L. Delfour, T.E. Itina, Mechanisms of ultrashort laser-induced fragmentation of metal nanoparticles in liquids: numerical insights, The Journal of Physical Chemistry C, 119 (2015) 13893-13900.

[25] A. Plech, S. Ibrahimkutty, S. Reich, G. Newby, Thermal dynamics of pulsed-laser excited gold nanorods in suspension, Nanoscale, 9 (2017) 17284-17292.

[26] X. Hou, N. Djellali, B. Palpant, Absorption of ultrashort laser pulses by plasmonic nanoparticles: not necessarily what you might think, ACS photonics, 5 (2018) 3856-3863.

[27] X. Wang, Z. Luo, M. Liu, R. Tang, A. Luo, W. Xu, Wavelength-switchable femtosecond pulse fiber laser mode-locked by silica-encased gold nanorods, Laser Physics Letters, 13 (2016) 045101.

[28] C. Pang, R. Li, Z. Li, N. Dong, C. Cheng, W. Nie, R. Böttger, S. Zhou, J. Wang, F. Chen, Lithium Niobate Crystal with Embedded Au Nanoparticles: A New Saturable Absorber for Efficient Mode-Locking of Ultrafast Laser Pulses at 1 μm, Advanced Optical Materials, 6 (2018) 1800357.

[29] R. Li, C. Pang, Z. Li, N. Dong, J. Wang, F. Ren, S. Akhmadaliev, S. Zhou, F. Chen, Monolithic waveguide laser mode-locked by embedded Ag nanoparticles operating at 1 μm, Nanophotonics, 8 (2019) 859-868.

[30] S. Wang, C. Pang, Z. Li, R. Li, N. Dong, Q. Lu, F. Ren, J. Wang, F. Chen, 8.6 GHz Q-switched mode-locked waveguide lasing based on LiNbO 3 crystal embedded Cu nanoparticles, Optical Materials Express, 9 (2019) 3808-3817.

[31] J. Wang, A. Coillet, O. Demichel, Z. Wang, D. Rego, A. Bouhelier, P. Grelu, B. Cluzel, Saturable plasmonic metasurfaces for laser mode locking, Light: Science & Applications, 9 (2020) 1-9.

[32] B.K. Dadhich, S. Bhattacharya, S. Ballav, B. Bhushan, P.K. Datta, A. Priyam, Femtosecond-Laser-Induced Saturable Absorption and Optical Limiting of Hollow Silver Nanocubes: Implications for Optical Switching and Bioimaging, ACS Applied Nano Materials, 3 (2020) 11620-11629.

[33] S. Wang, Y. Zhang, R. Zhang, H. Yu, H. Zhang, Q. Xiong, High-order nonlinearity of surface plasmon resonance in Au nanoparticles: paradoxical combination of saturable and reverse-saturable absorption, Advanced Optical Materials, 3 (2015) 1342-1348.

[34] R. Ganeev, R. Tugushev, T. Usmanov, Application of the nonlinear optical properties of platinum nanoparticles for the mode locking of Nd: glass laser, Applied Physics B, 94 (2009) 647-651.

[35] A.S. Reyna, C.B. de Araújo, High-order optical nonlinearities in plasmonic nanocomposites—a review, Advances in Optics and Photonics, 9 (2017) 720-774.

[36] N.M. Litchinitser, Nonlinear optics in metamaterials, Advances in Physics: X, 3 (2018) 1367628.

[37] A. Balbuena Ortega, E. Brambila, V. López Gayou, R. Delgado Macuil, A. Orduña Diaz, A. Zamilpa Alvarez, A. Arzola, K. Volke-Sepúlveda, Light control through a nonlinear lensing effect in a colloid of biosynthesized gold nanoparticles, Journal of Modern Optics, 66 (2019) 502-511.

[38] A. Balbuena Ortega, F. Torres-González, V. López Gayou, R. Delgado Macuil, J. Cardoso Sakamoto, A. Arzola, G. Assanto, K. Volke-Sepulveda, Guiding light with singular beams in nanoplasmonic colloids, Applied Physics Letters, 118 (2021) 061102.

[39] S. Fardad, A. Salandrino, M. Heinrich, P. Zhang, Z. Chen, D.N. Christodoulides, Plasmonic resonant solitons in metallic nanosuspensions, Nano letters, 14 (2014) 2498-2504.

[40] A. Couairon, A. Mysyrowicz, Femtosecond filamentation in transparent media, Physics reports, 441 (2007) 47-189.

[41] S.L. Chin, Femtosecond laser filamentation, Springer2010.

[42] A. Dubietis, G. Tamošauskas, R. Šuminas, V. Jukna, A. Couairon, Ultrafast supercontinuum generation in bulk condensed media (Invited Review), arXiv preprint arXiv:1706.04356, DOI (2017).

[43] A. Brodeur, S. Chin, Ultrafast white-light continuum generation and self-focusing in transparent condensed media, JOSA B, 16 (1999) 637-650.

[44] C. Wang, Y. Fu, Z. Zhou, Y. Cheng, Z. Xu, Femtosecond filamentation and supercontinuum generation in silver-nanoparticle-doped water, Applied physics letters, 90 (2007) 181119.

[45] R. Driben, A. Husakou, J. Herrmann, Low-threshold supercontinuum generation in glasses doped with silver nanoparticles, Optics express, 17 (2009) 17989-17995.

[46] R. Driben, A. Husakou, J. Herrmann, Supercontinuum generation in aqueous colloids containing silver nanoparticles, Optics letters, 34 (2009) 2132-2134.

[47] R. Driben, J. Herrmann, Solitary pulse propagation and soliton-induced supercontinuum generation in silica glasses containing silver nanoparticles, Optics letters, 35 (2010) 2529-2531.

[48] G. Baffou, H. Rigneault, Femtosecond-pulsed optical heating of gold nanoparticles, Physical Review B, 84 (2011) 035415.

[49] S. Yuan, F.J. Liu, L.R. Wang, J.Y. Nan, M. Li, B.Q. He, H.P. Zeng, Highly extended filaments in aqueous gold nano-particle colloidals, Scientific reports, 8 (2018) 1-7.

[50] S. Kudryashov, A. Samokhvalov, Y.E. Geints, E. Ageev, V. Veiko, Femtosecond laser filaments in gold colloidal solutions: supercontinuum and ultrasonic tracing, JOSA B, 36 (2019) A125-A130.

[51] S. Kudryashov, A. Samokhvalov, S. Shelygina, V. Veiko, Tuning of localized plasmon resonance in colloidal gold nano-particles by ultrafast interband photoinjection of free carriers: Superplasmonic states?, Applied Physics Letters, 115 (2019) 161903.

[52] S.I. Kudryashov, A.A. Samokhvalov, E. Ageev, V.P. Veiko, Ultrafast Broadband Nonlinear Spectroscopy of a Colloidal Solution of Gold Nanoparticles, JETP Letters, 109 (2019) 298-302.

[53] R.L. Sutherland, Handbook of nonlinear optics, CRC press2003.

[54] T.S. Kelly, Y.-X. Ren, A. Samadi, A. Bezryadina, D. Christodoulides, Z. Chen, Guiding and nonlinear coupling of light in plasmonic nanosuspensions, Optics letters, 41 (2016) 3817-3820.

[55] Y.-X. Ren, T.S. Kelly, C. Zhang, H. Xu, Z. Chen, Soliton-mediated orientational ordering of gold nanorods and birefringence in plasmonic suspensions, Optics letters, 42 (2017) 627-630.

[56] H. Xu, P. Alvaro, Y. Xiang, T.S. Kelly, Y.-X. Ren, C. Zhang, Z. Chen, Plasmonic resonant nonlinearity and synthetic optical properties in gold nanorod suspensions, Photonics Research, 7 (2019) 28-35.

[57] Y. Xiang, G. Liang, P. Alvaro, X. Hu, Y. Liang, T.S. Kelly, Z. Shi, H. Xu, Z. Chen, Resonant Optical Nonlinearity and Fluorescence Enhancement in Electrically Tuned Plasmonic Nanosuspensions, Advanced Photonics Research, 2 (2021) 2000060.

[58] V. Shvedov, K. Cyprych, M.Y. Salazar-Romero, Y. Izdebskaya, W. Krolikowski, Nonlinear propagation and quasi self-confinement of light in plasmonic resonant media, Optics express, 26 (2018) 23196-23206.

[59] A. Balbuena Ortega, F.E. Torres-González, V. López Gayou, R. Delgado Macuil, G. Assanto, K. Volke-Sepulveda, Light Confinement with Structured Beams in Gold Nanoparticle Suspensions, Photonics, Multidisciplinary Digital Publishing Institute, 2021, pp. 221.

[60] L. Bergé, S. Skupin, R. Nuter, J. Kasparian, J.-P. Wolf, Ultrashort filaments of light in weakly ionized, optically transparent media, Reports on progress in physics, 70 (2007) 1633.

[61] R.W. Boyd, Nonlinear optics, Academic press2020.

[62] R.W. Boyd, S.G. Lukishova, Y.R. Shen, Self-focusing: Past and Present: Fundamentals and Prospects, Springer2009.

[63] A. Couairon, E. Brambilla, T. Corti, D. Majus, O.d.J. Ramírez-Góngora, M. Kolesik, Practitioner's guide to laser pulse propagation models and simulation, The European Physical Journal Special Topics, 199 (2011) 5-76.

[64] G. Fibich, The nonlinear Schrödinger equation, Springer2015.

[65] P.E. Powers, J.W. Haus, Fundamentals of nonlinear optics, CRC press2017.

[66] R.Y. Chiao, E. Garmire, C.H.J.P.r.l. Townes, Self-trapping of optical beams, 13 (1964) 479.

[67] P.J.P.R.L. Kelley, Self-focusing of optical beams, 15 (1965) 1005.

[68] G. Fibich, A.L. Gaeta, Critical power for self-focusing in bulk media and in hollow waveguides, Optics letters, 25 (2000) 335-337.

[69] S. Akhmanov, A. Sukhorukov, R.J.S.P.J. Khokhlov, Self-focusing and self-trapping of intense light beams in a nonlinear medium, 23 (1966) 1025-1033.

[70] C.B. Schaffer, A. Brodeur, E.J.M.S. Mazur, Technology, Laser-induced breakdown and damage in bulk transparent materials induced by tightly focused femtosecond laser pulses, 12 (2001) 1784.

[71] L. Sudrie, A. Couairon, M. Franco, B. Lamouroux, B. Prade, S. Tzortzakis, A.J.P.R.L. Mysyrowicz, Femtosecond laser-induced damage and filamentary propagation in fused silica, 89 (2002) 186601.

[72] W. Liu, O. Kosareva, I. Golubtsov, A. Iwasaki, A. Becker, V. Kandidov, S. Chin, Femtosecond laser pulse filamentation versus optical breakdown in H 2 O, Applied Physics B, 76 (2003) 215-229.

[73] J. Zyss, Molecular nonlinear optics: materials, physics, and devices, Academic press2013.

[74] Z. Chen, M. Segev, D.N. Christodoulides, Optical spatial solitons: historical overview and recent advances, Reports on Progress in Physics, 75 (2012) 086401.

[75] Z. Chai, X. Hu, F. Wang, X. Niu, J. Xie, Q. Gong, Ultrafast all-optical switching, Advanced Optical Materials, 5 (2017) 1600665.

[76] V. Sasikala, K. Chitra, All optical switching and associated technologies: a review, Journal of Optics, 47 (2018) 307-317.

[77] D. Dini, M.J. Calvete, M. Hanack, Nonlinear optical materials for the smart filtering of optical radiation, Chemical reviews, 116 (2016) 13043-13233.

[78] G. Pu, L. Zhang, W. Hu, L. Yi, Automatic mode-locking fiber lasers: progress and perspectives, Science China Information Sciences, 63 (2020) 1-24.

[79] S. Skupin, G. Stibenz, L. Berge, F. Lederer, T. Sokollik, M. Schnürer, N. Zhavoronkov, G. Steinmeyer, Self-compression by femtosecond pulse filamentation: Experiments versus numerical simulations, Physical Review E, 74 (2006) 056604.

[80] S. Chin, F. Théberge, W. Liu, Filamentation nonlinear optics, Applied Physics B, 86 (2007) 477-483.

[81] K.-Y. Kim, A. Taylor, J. Glownia, G. Rodriguez, Coherent control of terahertz supercontinuum generation in ultrafast laser–gas interactions, Nature photonics, 2 (2008) 605.

[82] I. Dey, K. Jana, V.Y. Fedorov, A.D. Koulouklidis, A. Mondal, M. Shaikh, D. Sarkar, A.D. Lad, S. Tzortzakis, A. Couairon, Highly efficient broadband terahertz generation from ultrashort laser filamentation in liquids, Nature communications, 8 (2017) 1-7.

[83] J. Odhner, R. Levis, Optical spectroscopy using gas-phase femtosecond laser filamentation, Annual review of physical chemistry, 65 (2014) 605-628.

[84] J. Kasparian, J.-P. Wolf, Physics and applications of atmospheric nonlinear optics and filamentation, Optics express, 16 (2008) 466-493.

[85] W. Cai, V.M. Shalaev, Optical metamaterials, Springer2010.

[86] J. Obermeier, T. Schumacher, M. Lippitz, Nonlinear spectroscopy of plasmonic nanoparticles, Advances in Physics: X, 3 (2018) 1454341.

[87] N.C. Panoiu, W. Sha, D. Lei, G. Li, Nonlinear optics in plasmonic nanostructures, Journal of Optics, 20 (2018) 083001.

[88] G.V. Hartland, Optical studies of dynamics in noble metal nanostructures, Chemical reviews, 111 (2011) 3858-3887.

[89] A.S. Reyna, C.B. De Araujo, Guiding and confinement of light induced by optical vortex solitons in a cubic–quintic medium, Optics letters, 41 (2016) 191-194.

[90] R.K. Yadav, J. Aneesh, R. Sharma, P. Abhiramnath, T.K. Maji, G.J. Omar, A. Mishra, D. Karmakar, K. Adarsh, Designing hybrids of graphene oxide and gold nanoparticles for nonlinear optical response, Physical Review Applied, 9 (2018) 044043.

[91] Y. Yu, J. Si, L. Yan, M. Li, X. Hou, Enhanced nonlinear absorption and ultrafast carrier dynamics in graphene/gold nanoparticles nanocomposites, Carbon, 148 (2019) 72-79.

[92] U. Kreibig, M. Vollmer, Optical properties of metal clusters, Springer Science & Business Media2013.

[93] S.A. Maier, Plasmonics: fundamentals and applications, Springer Science & Business Media2007.

[94] D. Rioux, S. Vallières, S. Besner, P. Muñoz, E. Mazur, M. Meunier, An analytic model for the dielectric function of Au, Ag, and their alloys, Advanced Optical Materials, 2 (2014) 176-182.

[95] L. Wang, M. Hasanzadeh Kafshgari, M. Meunier, Optical Properties and Applications of Plasmonic-Metal Nanoparticles, Advanced Functional Materials, 30 (2020) 2005400.

[96] P.B. Johnson, R.-W. Christy, Optical constants of the noble metals, Physical review B, 6 (1972) 4370.

[97] B. Palpant, Third-order nonlinear optical response of metal nanoparticles, Non-linear optical properties of matter, Springer2006, pp. 461-508.

[98] J.E. Sipe, R.W. Boyd, Nanocomposite materials for nonlinear optics based on local field effects, Optical Properties of Nanostructured Random Media, Springer2002, pp. 1-19.

[99] K. Dolgaleva, R.W. Boyd, Local-field effects in nanostructured photonic materials, Advances in Optics and Photonics, 4 (2012) 1-77.

[100] V.A. Markel, Introduction to the Maxwell Garnett approximation: tutorial, JOSA A, 33 (2016) 1244-1256.

[101] R. Atkinson, W.R. Hendren, G.A. Wurtz, W. Dickson, A.V. Zayats, P. Evans, R.J. Pollard, Anisotropic optical properties of arrays of gold nanorods embedded in alumina, Physical Review B, 73 (2006) 235402.

[102] A.D. Neira, N. Olivier, M.E. Nasir, W. Dickson, G.A. Wurtz, A.V. Zayats, Eliminating material constraints for nonlinearity with plasmonic metamaterials, Nature communications, 6 (2015) 7757.

[103] A. Husakou, J. Herrmann, Supercontinuum generation of higher-order solitons by fission in photonic crystal fibers, Physical Review Letters, 87 (2001) 203901.

[104] J. Marburger, Self-focusing: theory, Progress in quantum electronics, 4 (1975) 35-110.

[105] R. Del Coso, J. Solis, Relation between nonlinear refractive index and third-order susceptibility in absorbing media, JOSA B, 21 (2004) 640-644.

[106] C. Sönnichsen, T. Franzl, T. Wilk, G. von Plessen, J. Feldmann, O. Wilson, P. Mulvaney, Drastic reduction of plasmon damping in gold nanorods, Physical review letters, 88 (2002) 077402.

[107] J. Ma, Z. Wang, L.-W. Wang, Interplay between plasmon and single-particle excitations in a metal nanocluster, Nature communications, 6 (2015) 1-11.

[108] Y. Nishiyama, K. Imaeda, K. Imura, H. Okamoto, Plasmon dephasing in single gold nanorods observed by ultrafast time-resolved near-field optical microscopy, The Journal of Physical Chemistry C, 119 (2015) 16215-16222.

[109] T. Zhao, J.W. Jarrett, J.S. Johnson, K. Park, R.A. Vaia, K.L. Knappenberger Jr, Plasmon dephasing in gold nanorods studied using single-nanoparticle interferometric nonlinear optical microscopy, The Journal of Physical Chemistry C, 120 (2016) 4071-4079.

[110] M. Bosman, E. Ye, S.F. Tan, C.A. Nijhuis, J.K. Yang, R. Marty, A. Mlayah, A. Arbouet, C. Girard, M.-Y. Han, Surface plasmon damping quantified with an electron nanoprobe, Scientific reports, 3 (2013) 1-7.

[111] M. Hu, J. Chen, M. Marquez, Y. Xia, G.V. Hartland, Correlated Rayleigh Scattering Spectroscopy and Scanning Electron Microscopy Studies of Au− Ag Bimetallic Nanoboxes and Nanocages, The Journal of Physical Chemistry C, 111 (2007) 12558-12565.

[112] B. Foerster, V.A. Spata, E.A. Carter, C. Sönnichsen, S. Link, Plasmon damping depends on the chemical nature of the nanoparticle interface, Science advances, 5 (2019) eaav0704.

[113] K. Wu, J. Chen, J.R. McBride, T. Lian, Efficient hot-electron transfer by a plasmon-induced interfacial charge-transfer transition, Science, 349 (2015) 632-635.

[114] S. Tan, A. Argondizzo, J. Ren, L. Liu, J. Zhao, H. Petek, Plasmonic coupling at a metal/semiconductor interface, Nature Photonics, 11 (2017) 806-812.

[115] B. Foerster, M. Hartelt, S.S. Collins, M. Aeschlimann, S. Link, C. Sönnichsen, Interfacial states cause equal decay of plasmons and hot electrons at gold–metal oxide interfaces, Nano letters, 20 (2020) 3338-3343.

[116] R. Mittal, R. Glenn, I. Saytashev, V.V. Lozovoy, M. Dantus, Femtosecond nanoplasmonic dephasing of individual silver nanoparticles and small clusters, The journal of physical chemistry letters, 6 (2015) 1638-1644.

[117] O. Ávalos-Ovando, L.V. Besteiro, Z. Wang, A.O. Govorov, Temporal plasmonics: Fano and Rabi regimes in the time domain in metal nanostructures, Nanophotonics, 9 (2020) 3587-3595.

[118] Y. Xu, Y. Qin, B. Ji, X. Song, J. Lin, Polarization manipulated femtosecond localized surface plasmon dephasing time in an individual bowtie structure, Optics express, 28 (2020) 9310-9319.

[119] P. Christopher, M. Moskovits, Hot charge carrier transmission from plasmonic nanostructures, Annual review of physical chemistry, 68 (2017) 379-398.

[120] R. Sundararaman, P. Narang, A.S. Jermyn, W.A. Goddard III, H.A. Atwater, Theoretical predictions for hot-carrier generation from surface plasmon decay, Nature communications, 5 (2014) 1-8.

[121] J.B. Khurgin, Hot carriers generated by plasmons: where are they generated and where do they go from there?, Faraday discussions, 214 (2019) 35-58.

[122] M. Bauer, A. Marienfeld, M. Aeschlimann, Hot electron lifetimes in metals probed by time-resolved two-photon photoemission, Progress in Surface Science, 90 (2015) 319-376.

[123] T. Labouret, B. Palpant, Nonthermal model for ultrafast laser-induced plasma generation around a plasmonic nanorod, Physical Review B, 94 (2016) 245426.

[124] M. Conforti, G. Della Valle, Derivation of third-order nonlinear susceptibility of thin metal films as a delayed optical response, Physical Review B, 85 (2012) 245423.

[125] M. Zavelani-Rossi, D. Polli, S. Kochtcheev, A.-L. Baudrion, J. Béal, V. Kumar, E. Molotokaite, M. Marangoni, S. Longhi, G. Cerullo, Transient optical response of a single gold nanoantenna: the role of plasmon detuning, ACS photonics, 2 (2015) 521-529.

[126] A.M. Brown, R. Sundararaman, P. Narang, W.A. Goddard III, H.A. Atwater, Nonradiative plasmon decay and hot carrier dynamics: effects of phonons, surfaces, and geometry, ACS nano, 10 (2016) 957-966.

[127] A.M. Brown, R. Sundararaman, P. Narang, W.A. Goddard III, H.A. Atwater, Ab initio phonon coupling and optical response of hot electrons in plasmonic metals, Physical Review B, 94 (2016) 075120.

[128] A.M. Brown, R. Sundararaman, P. Narang, A.M. Schwartzberg, W.A. Goddard III, H.A. Atwater, Experimental and ab initio ultrafast carrier dynamics in plasmonic nanoparticles, Physical review letters, 118 (2017) 087401.

[129] A. Giri, M.V. Tokina, O.V. Prezhdo, P.E. Hopkins, Electron–phonon coupling and related transport properties of metals and intermetallic alloys from first principles, Materials Today Physics, 12 (2020) 100175.

[130] P. Ji, Y. Zhang, Ab initio determination of effective electron–phonon coupling factor in copper, Physics Letters A, 380 (2016) 1551-1555.

[131] Z. Lin, L.V. Zhigilei, V. Celli, Electron-phonon coupling and electron heat capacity of metals under conditions of strong electron-phonon nonequilibrium, Physical Review B, 77 (2008) 075133.

[132] E. Minutella, F. Schulz, H. Lange, Excitation-dependence of plasmon-induced hot electrons in gold nanoparticles, The journal of physical chemistry letters, 8 (2017) 4925-4929.

[133] B. Guzelturk, J.K. Utterback, I. Coropceanu, V. Kamysbayev, E.M. Janke, M. Zajac, N. Yazdani, B.L. Cotts, S. Park, A. Sood, Nonequilibrium thermodynamics of colloidal gold nanocrystals monitored by ultrafast electron diffraction and optical scattering microscopy, ACS nano, 14 (2020) 4792-4804.

[134] Y.U. Staechelin, D. Hoeing, F. Schulz, H. Lange, Size-Dependent Electron–Phonon Coupling in Monocrystalline Gold Nanoparticles, ACS Photonics, 8 (2021) 752-757.

[135] X. Shen, Y.P. Timalsina, T.-M. Lu, M. Yamaguchi, Experimental study of electron-phonon coupling and electron internal thermalization in epitaxially grown ultrathin copper films, Physical Review B, 91 (2015) 045129.

[136] B. Ostovar, M.-N. Su, D. Renard, B.D. Clark, P.D. Dongare, C. Dutta, N. Gross, J.E. Sader, C.F. Landes, W.-S. Chang, Acoustic vibrations of Al nanocrystals: size, shape, and crystallinity revealed by single-particle transient extinction spectroscopy, The Journal of Physical Chemistry A, 124 (2020) 3924-3934.

[137] Q. Zheng, X. Shen, K. Sokolowski-Tinten, R. Li, Z. Chen, M. Mo, Z. Wang, S. Weathersby, J. Yang, M. Chen, Dynamics of electron–phonon coupling in bicontinuous nanoporous gold, The Journal of Physical Chemistry C, 122 (2018) 16368-16373.

[138] K.J. Smith, Y. Cheng, E.S. Arinze, N.E. Kim, A.E. Bragg, S.M. Thon, Dynamics of energy transfer in large plasmonic aluminum nanoparticles, ACS Photonics, 5 (2017) 805-813.

[139] M.-N. Su, P.D. Dongare, D. Chakraborty, Y. Zhang, C. Yi, F. Wen, W.-S. Chang, P. Nordlander, J.E. Sader, N.J. Halas, Optomechanics of single aluminum nanodisks, Nano letters, 17 (2017) 2575-2583.

[140] H. Gogoi, B.G. Maddala, F. Ali, A. Datta, Role of Solvent in Electron-Phonon Relaxation Dynamics in Core-Shell Au-SiO2 Nanoparticles, ChemPhysChem, DOI (2021).

[141] A. Arbouet, C. Voisin, D. Christofilos, P. Langot, N. Del Fatti, F. Vallée, J. Lermé, G. Celep, E. Cottancin, M. Gaudry, Electron-phonon scattering in metal clusters, Physical review letters, 90 (2003) 177401.

[142] A. Ahmed, M. Pelton, J.R. Guest, Understanding how acoustic vibrations modulate the optical response of plasmonic metal nanoparticles, ACS nano, 11 (2017) 9360-9369.

[143] J. Cunha, T.L. Guo, G. Della Valle, A.N. Koya, R. Proietti Zaccaria, A. Alabastri, Controlling light, heat, and vibrations in plasmonics and phononics, Advanced Optical Materials, 8 (2020) 2001225.

[144] G. Baffou, R. Quidant, F.J. García de Abajo, Nanoscale control of optical heating in complex plasmonic systems, ACS nano, 4 (2010) 709-716.

[145] F. Hache, D. Ricard, C. Flytzanis, Optical nonlinearities of small metal particles: surface-mediated resonance and quantum size effects, JOSA B, 3 (1986) 1647-1655.

[146] S. Rautian, Nonlinear saturation spectroscopy of the degenerate electron gas in spherical metallic particles, Journal of Experimental and Theoretical Physics, 85 (1997) 451-461.

[147] A.A. Govyadinov, G.Y. Panasyuk, J.C. Schotland, V.A. Markel, Theoretical and numerical investigation of the size-dependent optical effects in metal nanoparticles, Physical Review B, 84 (2011) 155461.

[148] V.P. Drachev, A.K. Buin, H. Nakotte, V.M. Shalaev, Size dependent χ (3) for conduction electrons in Ag nanoparticles, Nano letters, 4 (2004) 1535-1539.

[149] K. Uchida, S. Kaneko, S. Omi, C. Hata, H. Tanji, Y. Asahara, A. Ikushima, T. Tokizaki, A. Nakamura, Optical nonlinearities of a high concentration of small metal particles dispersed in glass: copper and silver particles, JOSA B, 11 (1994) 1236-1243.

[150] V.P. Drachev, E. Khaliullin, W. Kim, F. Alzoubi, S. Rautian, V. Safonov, R. Armstrong, V.M. Shalaev, Quantum size effect in two-photon excited luminescence from silver nanoparticles, Physical Review B, 69 (2004) 035318.

[151] V. Drachev, W.-T. Kim, V. Safonov, V. Podolskiy, N. Zakovryashin, E. Khaliullin, V. Shalaev, R. Armstrong, Low-threshold lasing and broad-band multiphoton-excited light emission from Ag aggregate-adsorbate complexes in microcavity, Journal of Modern Optics, 49 (2002) 645-662.

[152] N. Del Fatti, F. Vallee, Ultrafast optical nonlinear properties of metal nanoparticles, Applied Physics B, 73 (2001) 383-390.

[153] C. Voisin, N. Del Fatti, D. Christofilos, F. Vallée, Ultrafast electron dynamics and optical nonlinearities in metal nanoparticles, The Journal of Physical Chemistry B, 105 (2001) 2264-2280.

[154] H. Baida, D. Mongin, D. Christofilos, G. Bachelier, A. Crut, P. Maioli, N. Del Fatti, F. Vallée, Ultrafast nonlinear optical response of a single gold nanorod near its surface plasmon resonance, Physical review letters, 107 (2011) 057402.

[155] O. Plaksin, Y. Takeda, H. Amekura, N. Kishimoto, S. Plaksin, Saturation of nonlinear optical absorption of metal-nanoparticle composites, Journal of Applied Physics, 103 (2008) 114302.

[156] R. Sato, S. Ishii, T. Nagao, M. Naito, Y. Takeda, Broadband plasmon resonance enhanced third-order optical nonlinearity in refractory titanium nitride nanostructures, ACS Photonics, 5 (2018) 3452-3458.

[157] R. Sato, M. Ohnuma, K. Oyoshi, Y. Takeda, Experimental investigation of nonlinear optical properties of Ag nanoparticles: Effects of size quantization, Physical Review B, 90 (2014) 125417.

[158] R. Sato, M. Ohnuma, K. Oyoshi, Y. Takeda, Spectral investigation of nonlinear local field effects in Ag nanoparticles, Journal of Applied Physics, 117 (2015) 113101.

[159] B. Zhang, R. Sato, H. Momida, T. Ohno, M. Chundak, M. Naito, M. Yoshitake, Y. Takeda, Spectral dependence of the third-order optical susceptibility of Au nanostructures: Experiments and first-principles calculations, Physical Review B, 100 (2019) 035446.

[160] B. Zhang, R. Sato, K. Oyoshi, H. Mamiya, M. Ohnuma, Y. Takeda, Dispersion of third-order susceptibility of Au nanoparticles fabricated by ion implantation, Nuclear Instruments and Methods in Physics Research Section B: Beam Interactions with Materials and Atoms, 447 (2019) 38-42.

[161] B. Zhang, R. Sato, M. Tanaka, Y. Takeda, Spectral dependence of third-order susceptibility of Au triangular nanoplates, Scientific reports, 10 (2020) 1-6.

[162] Y. Gao, X. Zhang, Y. Li, H. Liu, Y. Wang, Q. Chang, W. Jiao, Y. Song, Saturable absorption and reverse saturable absorption in platinum nanoparticles, Optics communications, 251 (2005) 429-433.

[163] U. Gurudas, E. Brooks, D.M. Bubb, S. Heiroth, T. Lippert, A. Wokaun, Saturable and reverse saturable absorption in silver nanodots at 532 nm using picosecond laser pulses, Journal of applied physics, 104 (2008) 073107.

[164] H.I. Elim, J. Yang, J.-Y. Lee, J. Mi, W. Ji, Observation of saturable and reverse-saturable absorption at longitudinal surface plasmon resonance in gold nanorods, Applied physics letters, 88 (2006) 083107.

[165] K. Imura, T. Nagahara, H. Okamoto, Near-field two-photon-induced photoluminescence from single gold nanorods and imaging of plasmon modes, The Journal of Physical Chemistry B, 109 (2005) 13214-13220.

[166] X.-F. Jiang, Y. Pan, C. Jiang, T. Zhao, P. Yuan, T. Venkatesan, Q.-H. Xu, Excitation nature of two-photon photoluminescence of gold nanorods and coupled gold nanoparticles studied by two-pulse emission modulation spectroscopy, The journal of physical chemistry letters, 4 (2013) 1634-1638.

[167] N. Gao, Y. Chen, L. Li, Z. Guan, T. Zhao, N. Zhou, P. Yuan, S.Q. Yao, Q.-H. Xu, Shape-dependent two-photon photoluminescence of single gold nanoparticles, The Journal of Physical Chemistry C, 118 (2014) 13904-13911.

[168] V. Knittel, M.P. Fischer, T. de Roo, S. Mecking, A. Leitenstorfer, D. Brida, Nonlinear photoluminescence spectrum of single gold nanostructures, ACS nano, 9 (2015) 894-900.

[169] L. Roloff, P. Klemm, I. Gronwald, R. Huber, J.M. Lupton, S. Bange, Light emission from gold nanoparticles under ultrafast near-infrared excitation: Thermal radiation, inelastic light scattering, or multiphoton luminescence?, Nano letters, 17 (2017) 7914-7919.

[170] C. Molinaro, Y. El Harfouch, E. Palleau, F. Eloi, S. Marguet, L. Douillard, F. Charra, C. Fiorini-Debuisschert, Two-photon luminescence of single colloidal gold nanorods: revealing the origin of plasmon relaxation in small nanocrystals, The Journal of Physical Chemistry C, 120 (2016) 23136-23143.

[171] V. Remesh, M. Stührenberg, L. Saemisch, N. Accanto, N.F. van Hulst, Phase control of plasmon enhanced two-photon photoluminescence in resonant gold nanoantennas, Applied Physics Letters, 113 (2018) 211101.

[172] M.-B. Lien, J.-Y. Kim, M.-G. Han, Y.-C. Chang, Y.-C. Chang, H.J. Ferguson, Y. Zhu, A.A. Herzing, J.C. Schotland, N.A. Kotov, Optical asymmetry and nonlinear light scattering from colloidal gold nanorods, ACS nano, 11 (2017) 5925-5932.

[173] A.S. Reyna, C.B. de Araújo, Nonlinearity management of photonic composites and observation of spatial-modulation instability due to quintic nonlinearity, Physical Review A, 89 (2014) 063803.

[174] A.S. Reyna, C.B. de Araújo, Spatial phase modulation due to quintic and septic nonlinearities in metal colloids, Optics express, 22 (2014) 22456-22469.

[175] A.S. Reyna, C.B. de Araújo, An optimization procedure for the design of all-optical switches based on metal-dielectric nanocomposites, Optics express, 23 (2015) 7659-7666.

[176] R. El-Ganainy, D. Christodoulides, C. Rotschild, M. Segev, Soliton dynamics and self-induced transparency in nonlinear nanosuspensions, Optics express, 15 (2007) 10207-10218.

[177] I.W. Un, Y. Sivan, Thermo-optic nonlinearity of single metal nanoparticles under intense continuous wave illumination, Physical Review Materials, 4 (2020) 105201.

[178] M. Hasanzadeh Kafshgari, L. Agiotis, I. Largillière, S. Patskovsky, M. Meunier, Antibody-Functionalized Gold Nanostar-Mediated On-Resonance Picosecond Laser Optoporation for Targeted Delivery of RNA Therapeutics, Small, 17 (2021) 2007577.

[179] D.A. Hastman, J.S. Melinger, G.L. Aragones, P.D. Cunningham, M. Chiriboga, Z.J. Salvato, T.M. Salvato, C.W. Brown III, D. Mathur, I.L. Medintz, Femtosecond laser pulse excitation of DNA-labeled gold nanoparticles: Establishing a quantitative local nanothermometer for biological applications, ACS nano, 14 (2020) 8570-8583.

[180] L. Agiotis, M. Meunier, Nonlinear thermal lensing of high repetition rate ultrafast laser light in plasmonic nano-colloids %J Nanophotonics, Nanophotonics, DOI doi:10.1515/nanoph-2021-0775(2022).

[181] A.O. Govorov, H.H. Richardson, Generating heat with metal nanoparticles, Nano today, 2 (2007) 30-38.

[182] Y. Sivan, S.-W. Chu, Nonlinear plasmonics at high temperatures, Nanophotonics, 6 (2017) 317-328.

[183] R.W. Boyd, Z. Shi, I. De Leon, The third-order nonlinear optical susceptibility of gold, Optics Communications, 326 (2014) 74-79.

[184] J. Olesiak-Banska, M. Waszkielewicz, P. Obstarczyk, M. Samoc, Two-photon absorption and photoluminescence of colloidal gold nanoparticles and nanoclusters, Chemical Society Reviews, 48 (2019) 4087-4117.

[185] A. Stepanov, Nonlinear optical properties of metal nanoparticles in silicate glass, Glass Nanocomposites, Elsevier2016, pp. 165-179.

[186] Y.-x. Zhang, Y.-h. Wang, Nonlinear optical properties of metal nanoparticles: a review, RSC advances, 7 (2017) 45129-45144.

[187] Z. Li, Y. Yu, Z. Chen, T. Liu, Z.-K. Zhou, J.-B. Han, J. Li, C. Jin, X. Wang, Ultrafast third-order optical nonlinearity in Au triangular nanoprism with strong dipole and quadrupole plasmon resonance, The Journal of Physical Chemistry C, 117 (2013) 20127-20132.

[188] X. Wang, L. Yao, S. Li, M. Cai, Extraordinarily Large Third-Order Optical Nonlinearity in Au Nanorods under Nanowatt Laser Excitation, The Journal of Physical Chemistry C, 124 (2020) 6838-6844.

[189] J. Renger, R. Quidant, N. Van Hulst, L. Novotny, Surface-enhanced nonlinear four-wave mixing, Physical review letters, 104 (2010) 046803.

[190] S. Qu, Y. Gao, X. Jiang, H. Zeng, Y. Song, J. Qiu, C. Zhu, K. Hirao, Nonlinear absorption and optical limiting in gold-precipitated glasses induced by a femtosecond laser, Optics communications, 224 (2003) 321-327.

[191] S. Chen, R. Niu, W. Wu, D. Kong, Y. Gao, Wavelength-dependent nonlinear absorption and ultrafast dynamics process of Au triangular nanoprisms, Optics express, 27 (2019) 18146-18156.

[192] A. Siems, S.A. Weber, J. Boneberg, A. Plech, Thermodynamics of nanosecond nanobubble formation at laser-excited metal nanoparticles, New Journal of Physics, 13 (2011) 043018.

[193] D. Lapotko, Optical excitation and detection of vapor bubbles around plasmonic nanoparticles, Optics express, 17 (2009) 2538-2556.

[194] Z. Li, N. Dong, C. Cheng, L. Xu, M. Chen, J. Wang, F. Chen, Enhanced nonlinear optical response of graphene by silver-based nanoparticle modification for pulsed lasing, Optical Materials Express, 8 (2018) 1368-1377.

[195] S. Biswas, A. Kole, C. Tiwary, P. Kumbhakar, Enhanced nonlinear optical properties of graphene oxide–silver nanocomposites measured by Z-scan technique, RSC advances, 6 (2016) 10319-10325.

[196] D. Tan, X. Liu, Y. Dai, G. Ma, M. Meunier, J. Qiu, A Universal Photochemical Approach to Ultra-Small, Well-Dispersed Nanoparticle/Reduced Graphene Oxide Hybrids with Enhanced Nonlinear Optical Properties, Advanced Optical Materials, 3 (2015) 836-841.

[197] B.S. Kalanoor, P.B. Bisht, S.A. Ali, T.T. Baby, S. Ramaprabhu, Optical nonlinearity of silver-decorated graphene, JOSA B, 29 (2012) 669-675.

[198] H. Dai, L. Zhang, Z. Wang, X. Wang, J. Zhang, H. Gong, J.-B. Han, Y. Han, Linear and nonlinear optical properties of silver-coated gold nanorods, The Journal of Physical Chemistry C, 121 (2017) 12358-12364.

[199] K. Zhang, Z.-L. Huang, H.-W. Dai, Z.-W. Ma, J.-B. Han, H.-M. Gong, Y.-B. Han, Surface plasmon enhanced third-order optical nonlinearity of silver nanocubes, Optical Materials Express, 5 (2015) 2648-2654.

[200] Z. Chen, H. Dai, J. Liu, H. Xu, Z. Li, Z.-K. Zhou, J.-B. Han, Dipole plasmon resonance induced large third-order optical nonlinearity of Au triangular nanoprism in infrared region, Optics express, 21 (2013) 17568-17575.

[201] A.S. Reyna, K.C. Jorge, C.B. de Araújo, Two-dimensional solitons in a quintic-septimal medium, Physical Review A, 90 (2014) 063835.

[202] A.S. Reyna, E. Bergmann, P.-F. Brevet, C.B. de Araújo, Nonlinear polarization instability in cubic-quintic plasmonic nanocomposites, Optics express, 25 (2017) 21049-21067.

[203] G.P. Agrawal, Chapter 6 - Polarization effects, in: G.P. Agrawal (Ed.) Nonlinear Fiber Optics (Sixth Edition), Academic Press2019, pp. 189-244.

[204] G.A. Askarian, M.A. Mukhamadzhanov, Nonlinear defocusing of a focused beam: a fine beam from the focus, ZhETF Pisma Redaktsiiu, 33 (1981) 48.

[205] R. Philip, P. Chantharasupawong, H. Qian, R. Jin, J. Thomas, Evolution of nonlinear optical properties: from gold atomic clusters to plasmonic nanocrystals, Nano letters, 12 (2012) 4661-4667.

[206] H.H. Mai, V.E. Kaydashev, V.K. Tikhomirov, E. Janssens, M.V. Shestakov, M. Meledina, S. Turner, G. Van Tendeloo, V.V. Moshchalkov, P. Lievens, Nonlinear optical properties of Ag nanoclusters and nanoparticles dispersed in a glass host, The Journal of Physical Chemistry C, 118 (2014) 15995-16002.

[207] I. Papagiannouli, P. Aloukos, D. Rioux, M. Meunier, S. Couris, Effect of the Composition on the Nonlinear Optical Response of Au x Ag1–x Nano-Alloys, The Journal of Physical Chemistry C, 119 (2015) 6861-6872.

[208] K.-H. Kim, U. Griebner, J. Herrmann, Theory of passive mode locking of solid-state lasers using metal nanocomposites as slow saturable absorbers, Optics letters, 37 (2012) 1490-1492.

[209] R. Paschotta, U. Keller, Passive mode locking with slow saturable absorbers, Applied Physics B, 73 (2001) 653-662.

[210] T. Brabec, F. Krausz, Nonlinear optical pulse propagation in the single-cycle regime, Physical Review Letters, 78 (1997) 3282.

[211] P. Kinsler, G. New, Few-cycle pulse propagation, Physical Review A, 67 (2003) 023813.

[212] M.A. Porras, Propagation of single-cycle pulsed light beams in dispersive media, Physical Review A, 60 (1999) 5069.

[213] C. Brée, Nonlinear optics in the filamentation regime, Springer Science & Business Media2012.

[214] K. Svoboda, S.M. Block, Optical trapping of metallic Rayleigh particles, Optics letters, 19 (1994) 930-932.

[215] A. Poddubny, I. Iorsh, P. Belov, Y. Kivshar, Hyperbolic metamaterials, Nature photonics, 7 (2013) 948.

[216] C.R. Simovski, P.A. Belov, A.V. Atrashchenko, Y.S. Kivshar, Wire metamaterials: physics and applications, Advanced Materials, 24 (2012) 4229-4248.

[217] L. Allen, M.W. Beijersbergen, R. Spreeuw, J. Woerdman, Orbital angular momentum of light and the transformation of Laguerre-Gaussian laser modes, Physical review A, 45 (1992) 8185.

[218] B.A. Malomed, Vortex solitons: Old results and new perspectives, Physica D: Nonlinear Phenomena, DOI (2019).

[219] Y. Shen, X. Wang, Z. Xie, C. Min, X. Fu, Q. Liu, M. Gong, X. Yuan, Optical vortices 30 years on: OAM manipulation from topological charge to multiple singularities, Light: Science & Applications, 8 (2019) 1-29.

[220] T. Jiang, Y. Xu, Q. Tian, L. Liu, Z. Kang, R. Yang, G. Qin, W. Qin, Passively Q-switching induced by gold nanocrystals, Applied Physics Letters, 101 (2012) 151122.

[221] D. Wu, J. Peng, Z. Cai, J. Weng, Z. Luo, N. Chen, H. Xu, Gold nanoparticles as a saturable absorber for visible 635 nm Q-switched pulse generation, Optics express, 23 (2015) 24071-24076.

[222] Z. Kang, Y. Xu, L. Zhang, Z. Jia, L. Liu, D. Zhao, Y. Feng, G. Qin, W. Qin, Passively mode-locking induced by gold nanorods in erbium-doped fiber lasers, Applied Physics Letters, 103 (2013) 041105.

[223] W. Nie, Y. Zhang, H. Yu, R. Li, R. He, N. Dong, J. Wang, R. Hübner, R. Böttger, S. Zhou, Plasmonic nanoparticles embedded in single crystals synthesized by gold ion implantation for enhanced optical nonlinearity and efficient Q-switched lasing, Nanoscale, 10 (2018) 4228-4236.

[224] C. Pang, R. Li, Z. Li, N. Dong, H. Amekura, S. Wang, H. Yu, J. Wang, F. Ren, N. Ishikawa, Copper nanoparticles embedded in lithium tantalate crystals for multi-GHz Lasers, ACS Applied Nano Materials, 2 (2019) 5871-5877.

[225] C. Pang, R. Li, Y. Zhang, Z. Li, N. Dong, L. Wu, H. Yu, J. Wang, F. Ren, F. Chen, Tailoring optical nonlinearities of LiNbO 3 crystals by plasmonic silver nanoparticles for broadband saturable absorbers, Optics express, 26 (2018) 31276-31289.

[226] Y. Xian, Y. Cai, X. Sun, X. Liu, Q. Guo, Z. Zhang, L. Tong, J. Qiu, Refractory Plasmonic Metal Nitride Nanoparticles for Broadband Near-Infrared Optical Switches, Laser & Photonics Reviews, 13 (2019) 1900029.

[227] Q. Cui, J. Yao, J. Ni, S. Zhang, Direct observation of broadband conical emission along femtosecond-laser-induced rainbow filament in silver-nanoparticle-doped water, Journal of Modern Optics, 59 (2012) 1569-1573.

[228] P. Vasa, M. Singh, R. Bernard, A.K. Dharmadhikari, J.A. Dharmadhikari, D. Mathur, Supercontinuum generation in water doped with gold nanoparticles, Applied Physics Letters, 103 (2013) 111109.

[229] P. Vasa, J.A. Dharmadhikari, A.K. Dharmadhikari, R. Sharma, M. Singh, D. Mathur, Supercontinuum generation in water by intense, femtosecond laser pulses under anomalous chromatic dispersion, Physical Review A, 89 (2014) 043834.

[230] N. Zhavoronkov, R. Driben, B. Bregadiolli, M. Nalin, B. Malomed, Observation of asymmetric spectrum broadening induced by silver nanoparticles in a heavy-metal oxide glass, EPL (Europhysics Letters), 94 (2011) 37011.

[231] S.I. Kudryashov, A.A. Samokhvalov, E. Ageev, V.P. Veiko, Filamentation of an Ultrashort Laser Pulse in a Medium with Artificial Nonlinearity, JETP Letters, 109 (2019) 432-436.

[232] Z. Wang, Z. Kan, M. Shen, Study the plasmonic property of gold nanorods highly above damage threshold via single-pulse spectral hole-burning experiments, Scientific Reports, 11 (2021) 1-10.

[233] X. Zhang, Plasmon extinguishment by bandedge shift identified as a second-order spectroscopic differentiation, Nanophotonics, 10 (2021) 1329-1335.

[234] F. Liu, S. Yuan, B. He, J. Nan, A.Q. Khan, L.e. Ding, H. Zeng, Enhanced stimulated Raman scattering by femtosecond ultraviolet plasma grating in water, Applied Physics Letters, 112 (2018) 094101.

[235] D. Rioux, M. Meunier, Seeded growth synthesis of composition and size-controlled gold–silver alloy nanoparticles, The Journal of Physical Chemistry C, 119 (2015) 13160-13168.

[236] Y. Nie, S. Yuan, Y. Du, M. Yan, J. Wang, Q. Zhang, H. Xu, M. Li, H. Zeng, Colorful light channel for femtosecond laser filamentation in nanoparticle colloidal solutions, AIP Advances, 10 (2020) 065010.

[237] F. Liu, S. Yuan, B. He, J. Nan, M. Jiang, A.Q. Khan, L.e. Ding, J. Yu, H. Zeng, Filamentary plasma grating induced by interference of two femtosecond laser pulses in water, Optics express, 25 (2017) 22303-22311.

[238] B. He, J. Nan, F. Liu, S. Yuan, M. Li, J. Peng, H. Zeng, Terahertz Generation Enhanced by Nonlinear Filaments Interaction in Liquids, IEEE Photonics Technology Letters, 31 (2019) 1369-1372.

[239] L. Agiotis, M. Meunier, Optical power limiter in the femtosecond filamentation regime, Scientific Reports, 11 (2021) 14270.

[240] L. Agiotis, M. Meunier, Femtosecond nearly resonant self-focusing in gold nanorod colloids, Optics express, 29 (2021) 39536-39548.

[241] M. Soileau, W. Williams, E. Van Stryland, Optical power limiter with picosecond response time, IEEE Journal of Quantum Electronics, 19 (1983) 731-735.

[242] W.E. Williams, M. Soileau, E.W. Van Stryland, Optical switching and n2 measurements in CS2, Optics communications, 50 (1984) 256-260.

[243] I. Asselberghs, J. Pérez-Moreno, K. Clays, Characterization techniques of nonlinear optical materials, Non-Linear Optical Properties of Matter, Springer2006, pp. 419-459.

[244] M. Sheik-Bahae, A.A. Said, E.W. Van Stryland, High-sensitivity, single-beam n 2 measurements, Optics letters, 14 (1989) 955-957.

[245] A. Couairon, E. Gaižauskas, D. Faccio, A. Dubietis, P. Di Trapani, Nonlinear X-wave formation by femtosecond filamentation in Kerr media, Physical Review E, 73 (2006) 016608.

[246] A. Dubietis, E. Gaižauskas, G. Tamošauskas, P. Di Trapani, Light filaments without self-channeling, Physical review letters, 92 (2004) 253903.

[247] M. Kolesik, E.M. Wright, J.V. Moloney, Dynamic nonlinear X waves for femtosecond pulse propagation in water, Physical review letters, 92 (2004) 253901.

[248] D. Faccio, M.A. Porras, A. Dubietis, F. Bragheri, A. Couairon, P. Di Trapani, Conical emission, pulse splitting, and X-wave parametric amplification in nonlinear dynamics of ultrashort light pulses, Physical review letters, 96 (2006) 193901.

[249] F. Ilkov, L.S. Ilkova, S. Chin, Supercontinuum generation versus optical breakdown in CO 2 gas, Optics letters, 18 (1993) 681-683.

[250] M.A. Porras, J. Alda, E. Bernabeu, Nonlinear propagation and transformation of arbitrary laser beams by means of the generalized ABCD formalism, Applied optics, 32 (1993) 5885-5892.

[251] S. Kedenburg, M. Vieweg, T. Gissibl, H. Giessen, Linear refractive index and absorption measurements of nonlinear optical liquids in the visible and near-infrared spectral region, Optical Materials Express, 2 (2012) 1588-1611.

[252] P. Zhao, M. Reichert, S. Benis, D.J. Hagan, E.W. Van Stryland, Temporal and polarization dependence of the nonlinear optical response of solvents, Optica, 5 (2018) 583-594.

[253] M.L. Miguez, T.G. De Souza, E.C. Barbano, S.C. Zilio, L. Misoguti, Measurement of third-order nonlinearities in selected solvents as a function of the pulse width, Optics Express, 25 (2017) 3553-3565.

[254] P. Ho, R. Alfano, Optical Kerr effect in liquids, Physical Review A, 20 (1979) 2170.

[255] G. Qi-huang, L. Jian-liang, Z. Tie-qiao, Y. Hong, Ultrafast third-order optical nonlinearity of organic solvents investigated by subpicosecond transient optical Kerr effect, Chinese physics letters, 15 (1998) 30.

[256] Z. Wilkes, S. Varma, Y.-H. Chen, H. Milchberg, T. Jones, A. Ting, Direct measurements of the nonlinear index of refraction of water at 815 and 407 nm using single-shot supercontinuum spectral interferometry, Applied Physics Letters, 94 (2009) 211102.

[257] C.B. Marble, J.E. Clary, G.D. Noojin, S.P. O'Connor, D.T. Nodurft, A.W. Wharmby, B.A. Rockwell, M.O. Scully, V.V. Yakovlev, Z-scan measurements of water from 1150 to 1400 nm, Optics letters, 43 (2018) 4196-4199.

[258] S. Nemoto, Ray matrix for Gaussian beam propagation in a nonlinear medium: experimental results, Applied optics, 34 (1995) 6123-6129.

[259] A.G. Van Engen, S.A. Diddams, T.S. Clement, Dispersion measurements of water with white-light interferometry, Applied optics, 37 (1998) 5679-5686.

[260] P. Bélanger, Beam propagation and the ABCD ray matrices, Optics letters, 16 (1991) 196-198.

[261] N.l.T. C. Oliveira, M.L. Silva-Neto, A.S. Reyna, C.B. de Araújo, Influence of the Fifth-Order Nonlinearity of Gold Nanorods on the Performance of Random Lasers, The Journal of Physical Chemistry C, 124 (2020) 10705-10709.

[262] E. Falcão-Filho, C.B. de Araújo, J. Rodrigues Jr, High-order nonlinearities of aqueous colloids containing silver nanoparticles, JOSA B, 24 (2007) 2948-2956.

[263] H. Liao, R. Xiao, J. Fu, H. Wang, K. Wong, G. Wong, Origin of third-order optical nonlinearity in Au: SiO 2 composite films on femtosecond and picosecond time scales, Optics letters, 23 (1998) 388-390.

[264] J. Jayabalan, Origin and time dependence of higher-order nonlinearities in metal nanocomposites, JOSA B, 28 (2011) 2448-2455.

[265] A. Marini, M. Conforti, G. Della Valle, H. Lee, T.X. Tran, W. Chang, M. Schmidt, S. Longhi, P.S.J. Russell, F. Biancalana, Ultrafast nonlinear dynamics of surface plasmon polaritons in gold nanowires due to the intrinsic nonlinearity of metals, New Journal of Physics, 15 (2013) 013033.

[266] E.t. Boulais, R. Lachaine, M. Meunier, Plasma-mediated nanocavitation and photothermal effects in ultrafast laser irradiation of gold nanorods in water, The Journal of Physical Chemistry C, 117 (2013) 9386-9396.

[267] G. González-Rubio, P. Díaz-Núñez, A. Rivera, A. Prada, G. Tardajos, J. González-Izquierdo, L. Bañares, P. Llombart, L.G. Macdowell, M.A. Palafox, Femtosecond laser reshaping yields gold nanorods with ultranarrow surface plasmon resonances, Science, 358 (2017) 640-644.

[268] S. Link, M. El-Sayed, Spectroscopic determination of the melting energy of a gold nanorod, The Journal of Chemical Physics, 114 (2001) 2362-2368.

[269] G.V. Hartland, M. Hu, J.E. Sader, Softening of the symmetric breathing mode in gold particles by laser-induced heating, The Journal of Physical Chemistry B, 107 (2003) 7472-7478.

[270] P. Zijlstra, J.W. Chon, M. Gu, White light scattering spectroscopy and electron microscopy of laser induced melting in single gold nanorods, Physical Chemistry Chemical Physics, 11 (2009) 5915-5921.

[271] C.J. DeSantis, D. Huang, H. Zhang, N.J. Hogan, H. Zhao, Y. Zhang, A. Manjavacas, Y. Zhang, W.-S. Chang, P. Nordlander, Laser-induced spectral hole-burning through a broadband distribution of Au nanorods, The Journal of Physical Chemistry C, 120 (2016) 20518-20524.

[272] M. Mohebi, M. Soileau, E.W. Van Stryland, Effect of linear absorption on self-focusing, Optics letters, 13 (1988) 758-760.

[273] P. Qi, L. Zhang, L. Lin, N. Zhang, Y. Wang, W. Liu, Critical power for self-focusing of optical beam in absorbing media, Laser Physics, 28 (2018) 045407.

[274] V.S. Butylkin, A.E. Kaplan, Y.G. Khronopulo, E.I. Yakubovich, Resonant nonlinear interactions of light with matter, Springer Science & Business Media2012.

[275] R. Philip, G.R. Kumar, N. Sandhyarani, T. Pradeep, Picosecond optical nonlinearity in monolayer-protected gold, silver, and gold-silver alloy nanoclusters, Physical Review B, 62 (2000) 13160.

[276] S. Park, M. Pelton, M. Liu, P. Guyot-Sionnest, N.F. Scherer, Ultrafast resonant dynamics of surface plasmons in gold nanorods, The Journal of Physical Chemistry C, 111 (2007) 116-123.

[277] K. Wang, H. Long, M. Fu, G. Yang, P. Lu, Intensity-dependent reversal of nonlinearity sign in a gold nanoparticle array, Optics letters, 35 (2010) 1560-1562.

[278] M. Samoc, A. Samoc, B. Luther-Davies, H. Reisch, U. Scherf, Saturable absorption in poly (indenofluorene):? a picket-fence polymer, Optics letters, 23 (1998) 1295-1297.

[279] O. Brzobohatý, L.s. Chvátal, A. Jonáš, M. Šiler, J. Kanka, J. Jezek, P. Zemánek, Tunable soft-matter optofluidic waveguides assembled by light, ACS photonics, 6 (2019) 403-410.

[280] S. Fardad, M.S. Mills, P. Zhang, W. Man, Z. Chen, D. Christodoulides, Interactions between self-channeled optical beams in soft-matter systems with artificial nonlinearities, Optics letters, 38 (2013) 3585-3587.

[281] Y. Lamhot, A. Barak, O. Peleg, M. Segev, Self-trapping of optical beams through thermophoresis, Physical review letters, 105 (2010) 163906.

[282] W. Man, S. Fardad, Z. Zhang, J. Prakash, M. Lau, P. Zhang, M. Heinrich, D.N. Christodoulides, Z. Chen, Optical nonlinearities and enhanced light transmission in soft-matter systems with tunable polarizabilities, Physical review letters, 111 (2013) 218302.

[283] J. Sun, S.Z. Silahli, W. Walasik, Q. Li, E. Johnson, N.M. Litchinitser, Nanoscale orbital angular momentum beam instabilities in engineered nonlinear colloidal media, Optics express, 26 (2018) 5118-5125.

[284] A.S. Reyna, G. Boudebs, B.A. Malomed, C.B. de Araújo, Robust self-trapping of vortex beams in a saturable optical medium, Physical Review A, 93 (2016) 013840.

[285] A. Bezryadina, T. Hansson, R. Gautam, B. Wetzel, G. Siggins, A. Kalmbach, J. Lamstein, D. Gallardo, E.J. Carpenter, A. Ichimura, R. Morandotti, Z. Chen, Nonlinear Self-Action of Light through Biological Suspensions, Physical Review Letters, 119 (2017) 058101.

[286] R. Gautam, A. Bezryadina, Y. Xiang, T. Hansson, Y. Liang, G. Liang, J. Lamstein, N. Perez, B. Wetzel, R. Morandotti, Nonlinear optical response and self-trapping of light in biological suspensions, Advances in Physics: X, 5 (2020) 1778526.

[287] R. Gautam, Y. Xiang, J. Lamstein, Y. Liang, A. Bezryadina, G. Liang, T. Hansson, B. Wetzel, D. Preece, A. White, Optical force-induced nonlinearity and self-guiding of light in human red blood cell suspensions, Light: Science & Applications, 8 (2019) 1-9.

[288] N. Perez, J. Chambers, Z. Chen, A. Bezryadina, Nonlinear self-trapping and guiding of light at different wavelengths with sheep blood, Optics Letters, 46 (2021) 629-632.

[289] H. Xin, Y. Li, X. Liu, B. Li, Escherichia coli-based biophotonic waveguides, Nano letters, 13 (2013) 3408-3413.

[290] B. Agate, C. Brown, W. Sibbett, K. Dholakia, Femtosecond optical tweezers for in-situ control of two-photon fluorescence, Optics Express, 12 (2004) 3011-3017.

[291] M. Falconieri, Thermo-optical effects in Z-scan measurements using high-repetition-rate lasers, Journal of Optics A: Pure and Applied Optics, 1 (1999) 662.

[292] Y. Jiang, T. Narushima, H. Okamoto, Nonlinear optical effects in trapping nanoparticles with femtosecond pulses, Nature Physics, 6 (2010) 1005-1009.

[293] T.-H. Liu, W.-Y. Chiang, A. Usman, H. Masuhara, Optical Trapping Dynamics of a Single Polystyrene Sphere: Continuous Wave versus Femtosecond Lasers, The Journal of Physical Chemistry C, 120 (2016) 2392-2399.

[294] S.M. Mian, S.B. McGee, N. Melikechi, Experimental and theoretical investigation of thermal lensing effects in mode-locked femtosecond Z-scan experiments, Optics communications, 207 (2002) 339-345.

[295] D.C. Smith, High-power laser propagation: thermal blooming, Proceedings of the IEEE, 65 (1977) 1679-1714.

[296] A. Khachatrian, A. Sukhorukov, Some aspects of thermal self-focusing, Opto-electronics, 3 (1971) 49-55.

[297] S.Z. Silahli, W. Walasik, N.M. Litchinitser, Necklace beam generation in nonlinear colloidal engineered media, Optics letters, 40 (2015) 5714-5717.

[298] A. Vincotte, L. Bergé, Femtosecond optical vortices in air, Physical review letters, 95 (2005) 193901.

[299] J. Courtial, K. Dholakia, L. Allen, M. Padgett, Gaussian beams with very high orbital angular momentum, Optics communications, 144 (1997) 210-213.

[300] R. Rusconi, L. Isa, R. Piazza, Thermal-lensing measurement of particle thermophoresis in aqueous dispersions, JOSA B, 21 (2004) 605-616.

[301] S. Singhal, D. Goswami, Thermal lens study of NIR femtosecond laser-induced convection in alcohols, ACS omega, 4 (2019) 1889-1896.

[302] G. Luther, J. Moloney, A. Newell, E. Wright, Self-focusing threshold in normally dispersive media, Optics letters, 19 (1994) 862-864.

[303] P. Polynkin, M. Kolesik, Critical power for self-focusing in the case of ultrashort laser pulses, Physical Review A, 87 (2013) 053829.

[304] W. Lee, R. El-Ganainy, D. Christodoulides, K. Dholakia, E. Wright, Nonlinear optical response of colloidal suspensions, Optics Express, 17 (2009) 10277-10289.

[305] B. Uma, T. Swaminathan, R. Radhakrishnan, D. Eckmann, P. Ayyaswamy, Nanoparticle Brownian motion and hydrodynamic interactions in the presence of flow fields, Physics of fluids, 23 (2011) 073602.

[306] G. Abbate, U. Bernini, E. Ragozzino, F. Somma, The temperature dependence of the refractive index of water, Journal of Physics D: Applied Physics, 11 (1978) 1167.

[307] G.W. Robinson, C.H. Cho, G.I. Gellene, Refractive index mysteries of water, The Journal of Physical Chemistry B, 104 (2000) 7179-7182.

[308] I. Thormählen, J. Straub, U. Grigull, Refractive index of water and its dependence on wavelength, temperature, and density, Journal of physical and chemical reference data, 14 (1985) 933-945.

[309] L. Agiotis, M. Meunier, Threshold conditions for resonant Kerr self-focusing in plasmonic nano-colloids, Nonlinear Photonics, Optical Society of America, 2020, pp. NpTu2E. 6.

[310] R.R. Alfano, The supercontinuum laser source, DOI (1989).

[311] P. Vasa, D. Mathur, Ultrafast biophotonics, Springer2016.

[312] Y.H. Lee, Y. Yan, L. Polavarapu, Q.-H. Xu, Nonlinear optical switching behavior of Au nanocubes and nano-octahedra investigated by femtosecond Z-scan measurements, Applied Physics Letters, 95 (2009) 023105.

[313] G. Fan, S. Qu, Q. Wang, C. Zhao, L. Zhang, Z. Li, Pd nanoparticles formation by femtosecond laser irradiation and the nonlinear optical properties at 532 nm using nanosecond laser pulses, Journal of Applied Physics, 109 (2011) 023102.

[314] B. Karthikeyan, M. Anija, R. Philip, In situ synthesis and nonlinear optical properties of Au: Ag nanocomposite polymer films, Applied physics letters, 88 (2006) 053104.

[315] R. Li, N. Dong, F. Ren, H. Amekura, J. Wang, F. Chen, Nonlinear absorption response correlated to embedded Ag nanoparticles in BGO single crystal: from two-photon to three-photon absorption, Scientific reports, 8 (2018) 1-8.

[316] E. Cattaruzza, G. Battaglin, P. Calvelli, F. Gonella, G. Mattei, C. Maurizio, P. Mazzoldi, S. Padovani, R. Polloni, C. Sada, Fast nonlinear refractive index of pure and alloy metallic nanoclusters in silica glass, Composites Science and technology, 63 (2003) 1203-1208.

[317] D. Potamianos, I. Papadakis, E. Kakkava, A. Bourlinos, G. Trivizas, R. Zboril, S. Couris, Nonlinear optical response of gold-decorated nanodiamond hybrids, The Journal of Physical Chemistry C, 119 (2015) 24614-24620.

[318] R. Kuladeep, L. Jyothi, P. Prakash, S. Mayank Shekhar, M. Durga Prasad, D. Narayana Rao, Investigation of optical limiting properties of Aluminium nanoparticles prepared by pulsed laser ablation in different carrier media, Journal of Applied Physics, 114 (2013) 243101.

[319] S. Edappadikkunnummal, S.N. Nherakkayyil, V. Kuttippurath, D.M. Chalil, N.R. Desai, C. Keloth, Surface plasmon assisted enhancement in the nonlinear optical properties of phenothiazine by gold nanoparticle, The Journal of Physical Chemistry C, 121 (2017) 26976-26986.

[320] P. Ferrari, S. Upadhyay, M.V. Shestakov, J. Vanbuel, B. De Roo, Y. Kuang, M. Di Vece, V.V. Moshchalkov, J.-P. Locquet, P. Lievens, Wavelength-dependent nonlinear optical properties of Ag nanoparticles dispersed in a glass host, The Journal of Physical Chemistry C, 121 (2017) 27580-27589.

[321] O.M. Bankole, O. Osifeko, T. Nyokong, Enhanced nonlinear optical responses of zinc diaminopyrimidin-2-ylthio phthalocyanine conjugated to AgxAuy alloy nanoparticles, Journal of Photochemistry and Photobiology A: Chemistry, 329 (2016) 155-166.

[322] R. Li, N. Dong, C. Cheng, F. Ren, R. Hübner, J. Wang, S. Zhou, F. Chen, Giant enhancement of nonlinear optical response in Nd: YAG single crystals by embedded silver nanoparticles, ACS omega, 2 (2017) 1279-1286.

[323] Y. Niu, Y. Wang, G. Wang, T. Zhang, C. Liu, Enhanced optical linearity and nonlinearity of Nd: YAG crystal embedded with Ag nanoparticles by prior Zn ion implantation, Optical Materials Express, 8 (2018) 3666-3675.

[324] T. Zhang, Y. Sun, Y. Niu, C. Liu, Enhanced nonlinear absorption of Au nanoparticles embedded into Nd: YAG crystal towards saturable absorber application, Applied Physics Express, 12 (2019) 122014.

[325] O. Sánchez-Dena, P. Mota-Santiago, L. Tamayo-Rivera, E. García-Ramírez, A. Crespo-Sosa, A. Oliver, J.-A. Reyes-Esqueda, Size-and shape-dependent nonlinear optical response of Au nanoparticles embedded in sapphire, Optical Materials Express, 4 (2014) 92-100.

[326] A. Ryasnyanskiy, B. Palpant, S. Debrus, U. Pal, A. Stepanov, Third-order nonlinear-optical parameters of gold nanoparticles in different matrices, Journal of luminescence, 127 (2007) 181-185.

[327] P. Jafarkhani, M. Torkamany, S. Dadras, A. Chehrghani, J. Sabbaghzadeh, Necklace-shaped Au–Ag nanoalloys: laser-assisted synthesis and nonlinear optical properties, Nanotechnology, 22 (2011) 235703.

[328] E. Koushki, A. Farzaneh, Numerical simulation of optical dispersion, group velocity, and waveguide properties of gold and silver nanocolloids and hybrids, Colloid and Polymer Science, 295 (2017) 197-203.

[329] M. Falconieri, G. Salvetti, Simultaneous measurement of pure-optical and thermo-optical nonlinearities induced by high-repetition-rate, femtosecond laser pulses: application to CS2, Applied physics B, 69 (1999) 133-136.

[330] A. Gnoli, L. Razzari, M. Righini, Z-scan measurements using high repetition rate lasers: how to manage thermal effects, Optics express, 13 (2005) 7976-7981.

[331] G. Baffou, Thermoplasmonics: Heating Metal Nanoparticles Using Light, Cambridge University Press, Cambridge, 2017.

APPENDIX A MEASURED NONLINEAR PROPERTIES OF PLASMONIC NANOCOMPOSITES (LITERATURE DATA)

Table A.1 Measured nonlinear optical properties of plasmonic nanocomposites that exhibit reverse saturable absorption. Symbols/Abbreviations; t_p: pulsewidth, λ : wavelength, a_0 : linear absorption coefficient, w_0 : beam waist, F_{in} : input fluence, E_{in} : input pulse energy, I : input intensity, I_s :saturation intensity, β: nonlinear absorption coefficient, NC: nanocubes, NO: nanooctahedra, NP: nanoparticles, rGO: reduced graphene oxide, NR: nanorods, fG: functionalized graphene. [a] Length × Width, [b]Aspect ratio.

Ref.	Laser characteristics			Sample characteristics					Reverse saturable absorption onset conditions					Nonlinear properties		
	t_p	Rep. rate	λ	Material	Type	Avg. NP size	SPR	Thick-ness	a_0 (cm^{-1})	w_0 (μm)	F_{in} (mJ/cm^2)	E_{in} (μJ)	I (GW/cm^2)	I_s (GW/cm^2)	β (cm/GW)	β/α_o (cm^2/GW)
[310]	60 fs	1 KHz	800 nm	Au NC	Colloid	65 nm	530 nm	1 mm	35	40	9.9	0.05	33	12.8	0.161	0.046
	60 fs	1 KHz	800 nm	Au NO	Colloid	49 nm	550 nm		10	40	9.9	0.05	33	25.3	0.244	0.024
[79]	100 fs	1 kHz	800 nm	Au-NP/rGO 2h	Thin Film	17.7 nm	530 nm	100 nm	6600	35	1.3	0.05	26	8.6	0.0057	0.86
[17]	130 fs	1 kHz	725 nm	AuNRs	Colloid	(36.1×10.7) nm[a]	845 nm	1 mm	3.57	35	8.1	0.31	124	50	0.0012	0.003
[32]	150 fs	1 kHz	808 nm	Hollow AgNC	Colloid	33 nm	510 nm		0.62			0.5	63	30	0.0045	0.007
	150 fs	1 kHz	808 nm	Hollow AgNC	Colloid	45 nm	550 nm		1.79			1.0	126	70	0.0065	0.004
	150 fs	1 kHz	808 nm	Hollow AgNC	Colloid	70 nm	590 nm		1.84			1.5	189	80	0.0075	0.004
	150 fs	1 kHz	808 nm	Hollow AgNC	Colloid	100 nm	630 nm		2.07			2.0	252	90	0.0053	0.003
[154]	220 fs	1kHz	800 nm	AuNRs	Colloid	3.8[b]	800 nm	1 mm	3.57	10	0.76	0.003	7	0.5		
[153]	25 ps	250 Hz	532 nm	AgNP	Thin Film	17 nm	430 nm	47 nm	5000	40	35	1.75	2.8	0.375		
[33]	40 ps		1060 nm	AgNP-NaCMC/Quartz	Thin Film	13 nm	525 nm	200 nm	1250	47	389	27.1	19.44	2	2600	2.1
[187]	40 ps	10 Hz	532 nm	AgNP/fG	Colloid	5 nm	450 nm	1 mm		24	260	4.7	13	3.7	812	
	40 ps	10 Hz	1064 nm	AgNP/fG	Colloid	5 nm	450 nm	1 mm		46	480	32	24	2.3	600	
[311]	4 ns	2 Hz	532 nm	PdNPs	Colloid	2-6 nm	440 nm		5.60				0.08	0.033	10	1.79
[197]	4 ns	1-10 Hz	532 nm	$Au_{0.6}Ag_{0.4}$	Colloid	15-20 nm	475 nm	1 mm	2.10		650	6.5	0.08	0.061		
	4 ns	1-10 Hz	532 nm	$Au_{0.2}Ag_{0.8}$	Colloid	15-20 nm	420 nm	1 mm	0.4		1750	18	0.22	0.16		
[195]	5 ns	1-10 Hz	532 nm	AuNP	Colloid	4 nm	525 nm	1 mm	7.5	13	1000	5.3	0.4	0.2	15	2
[181]	6 ns	10 Hz	550 nm	AuTNP	Colloid	(120 × 10) nm[a]	530 nm/700 nm	2 mm	2.5	30	21600	600	7.2	0.62	2.30	0.92
	6 ns	10 Hz	600 nm	AuTNP	Colloid	(120 × 10) nm[a]	530 nm/700 nm	2 mm	1.4	30	21600	600	7.2	0.71	2.60	1.86
	6 ns	10 Hz	650 nm	AuTNP	Colloid	(120 × 10) nm[a]	530 nm/700 nm	2 mm	2.5	30	21600	600	7.2	0.65	1.60	0.64
	6 ns	10 Hz	700 nm	AuTNP	Colloid	(120 × 10) nm[a]	530 nm/700 nm	2 mm	3.1	30	21600	600	7.2	0.7	1.50	0.48
[312]	7 ns		532 nm	AuAgPVA	Thin film	10 nm	450 nm	100 um	39.1			30		0.08	7000	179
[180]	8 ns	10 Hz	532 nm	AuNPs	Thin film	5-20 nm	534 nm	24 um	203.3	40	800	40	0.19	0.0063		
[152]	8 ns	1 Hz	532 nm	Pt-PVP	Colloid	2 nm	Flat		1.43	55	96	9.2	0.024	0.011	32	22.4
[196]	8 ns		480 nm	AgNP	Colloid	2.4 nm	450 nm		5.8	18	540	5.5	0.14	0.001	600	103
	8 ns		480 nm	AgNP	Colloid	2.8 nm	475 nm		8.9	18	120	1.2	0.029	0.007	150	16.9

Table A.2 Measured nonlinear optical properties of plasmonic nanocomposites that exhibit optical limiting behaviour. Symbols/Abbreviations; t_p: pulsewidth, λ : wavelength, a_0 : linear absorption coefficient, w_0 : beam waist, F_{in} : input fluence, E_{in} : input pulse energy, I_{OL} :optical limiting intensity, β: nonlinear absorption coefficient, NShells: nanoshells, NP: nanoparticles, rGO: reduced graphene, BGO: Bismuth Germanate, ND: decorated nanodiamonds, GO: graphene oxide, DMSO: dimethyl sulphoxide.

Ref.	Laser Characteristics			Material Characteristics					Optical limiting threshold conditions				Nonlinear properties		
	t_p	Rep. rate	λ	Material	Type	Avg. NP size	SPR	Thick-ness	a_0 (cm^{-1})	w_0 (μm)	F_{in} (mJ/cm^2)	E_{in} (μJ)	I_{0L} (GW/cm^2)	β (cm/GW)	β/α_o (cm^2/GW)
[18]	90 fs	1 kHz	796 nm	AuNShells	Colloid	120 nm SiO2 + 15 nm Au shell	785 nm	1 mm	6	42	2.7	0.15	60	0.048	0.008
[186]	150 fs	1 kHz	800 nm	AgNPs/rGO	Colloid	2.5 nm	420 nm	1 mm	3.57		3.4			0.2	0.06
[313]	340 fs	100 Hz	515 nm	Ag in BGO	Thin Film	10.7 nm	466 nm	100 nm	5000	15	7.1	0.05	42	3.1	0.001
[314]	6 ps	1 Hz	527 nm	Au3Ag6A	Thin film	14.3 nm	475 nm	2.7 um	26000	20	4.8	0.06	1.6	13000	0.5
[315]	35 ps		532 nm	ND/Au(10%) 0.51 mg/ml	Colloid	8-25 nm		1 mm	2.50	18	658	6.7		4.2	1.7
[195]	5 ns		532 nm	Au_{25} Cluster	Colloid	<1 nm		1 mm	7.50	13	1000	5.3	0.4	20	2.7
	5 ns		532 nm	Au_{38} Cluster	Colloid	<1 nm		1 mm	7.50	13	1000	5.3	0.4	35	4.7
	5 ns		532 nm	Au_{144} Cluster	Colloid	1 nm		1 mm	7.50	13	1000	5.3	0.4	75	10
[78]	5 ns	10 Hz	532 nm	AuNP-GO	Colloid	25 nm	231 nm	1 mm	3.00	17	400	3.6	0.16	100	33.3
	5 ns	10 Hz	532 nm	AuNP-rGO(400)	Colloid	25 nm		1 mm	3.00	17	400	3.6	0.16	122	40.7
	5 ns	10 Hz	532 nm	AuNP-GO(1000)	Colloid	25 nm		1 mm	3.00	17	400	3.6	0.16	64	21.3
	5 ns	10 Hz	1064 nm	AuNP-GO	Colloid	25 nm	231 nm	1 mm	1.50	32	875	28	0.35	59	39.3
	5 ns	10 Hz	1064 nm	AuNP-rGO(400)	Colloid	25 nm		1 mm	1.50	32	875	28	0.35	40	26.7
	5 ns	10 Hz	1064 nm	AuNP-GO(1000)	Colloid	25 nm		1 mm	1.50	32	875	28	0.35	34	22.7
[316]	6 ns	10 Hz	532 nm	AlNP	Colloid (C_6H_5Cl)	23 nm	238 nm	1 mm	3.57	25	410	8	0.14	80.7	22.6
	6 ns	10 Hz	532 nm	AlNP	Colloid ($CHCl_3$)	12 nm	244 nm	1 mm	3.57	25	460	9	0.15	82.9	23.2
	6 ns	10 Hz	532 nm	AlNP	Colloid ($C_6H_5CH_3$)	31 nm	285 nm	1 mm	3.57	25	680	13	0.23	38.9	10.9
	6 ns	10 Hz	532 nm	AlNP	Colloid (C_6H_6)	59 nm	279 nm	1 mm	3.57	25	1090	21	0.36	119.7	33.5
	6 ns	10 Hz	532 nm	AlNP	Colloid (CCl_4)	62 nm	261 nm	1 mm	3.57	25	1380	27	0.46	0.82	0.23
[317]	7 ns	10 Hz	532 nm	Au	Colloid (Phenothiazine)	27.8 nm	530 nm	1 mm	2.23	18	2870	28	0.82	17.4	7.8
[318]	8 ns	10 Hz	460 nm	Ag	In Glass Host	3 nm	460 nm		4.00	16	6400	5.2	0.16	180	45
	8 ns	10 Hz	560 nm	Ag	In Glass Host	3 nm	460 nm		2.70	16	6400	5.2	0.16	140	51.9
	8 ns	10 Hz	660 nm	Ag	In Glass Host	3 nm	460 nm		2.00	16	6400	5.2	0.16	110	55
[196]	8 ns		480 nm	Ag	Colloid	1.2 nm		1 mm	3.20	18	540	5.5	0.14	50	15.6
[319]	10 ns		532 nm	Ag3Au1 in DMSO	Colloid	50 nm	450 nm		3.47		310			214	61.7
	10 ns		532 nm	Ag1Au3 in DMSO	Colloid	50 nm	500 nm	2 mm	3.47		280			260	74.9

Table A.3 Measured nonlinear optical properties of plasmonic nanocomposites that exhibit saturable absorption. Symbols/Abbreviations; t_p: pulsewidth, λ : wavelength, a_0 : linear absorption coefficient, w_0 : beam waist, F_{in} : input fluence, E_{in} : input pulse energy, I_s :saturation intensity, β: nonlinear absorption coefficient. n_2: nonlinear refractive index, NR: nanorods, NStars: nanostars, fG: functionalized graphene, NTP: nanotriangle prisms. [a] Length × Width

Ref	Laser characteristics			Sample characteristics					Saturated absorption onset conditions					Nonlinear properties		
	t_p	Rep. rate	λ	Material	Type	Avg. NP size	SPR	Thick-ness	a_0 (cm^{-1})	w_0 (μm)	F_{in} (mJ/cm^2)	E_{in} (μJ)	I_s (GW/cm^2)	β (cm/GW)	n_2 (cm^2/GW)	$\left\lvert\frac{n_2 I_s}{a_0 \lambda}\right\rvert$
[18]	90 fs	1 kHz	796 nm	AuNR	Colloid	41 × 10 nm[a]	800 nm	1 mm	6.45	42	1.0	0.05	21	-0.307		
	90 fs	1 kHz	796 nm	AuNStars	Colloid	50 nm	800 nm	1 mm	5.53	42	1.8	0.10	40	-0.14		
[17]	130 fs	1 kHz	850 nm	AuNR	Colloid	36.1x10.7 nm[a]	845 nm	1 mm	3.60	35	0.5	0.02	8	-0.023		
[320]	340 fs	100 Hz	515 nm	Ag	Thin film		505 nm	150 nm		15	<1.4	<0.01	<8.3	-360	0.002	
[215]	340 fs	100 Hz	515 nm	Au	Thin film	2.7 nm	561 nm	70 nm		15	<4.2	<0.03	<25	-190		
[184]	340 fs	100 Hz	1030 nm	Ag_2S@Ag-fG	Thin film	35-55 nm				30	0.2	0.006	1.3	-100000		
[321]	20 ps	1 kHz	532 nm	Ag	Thin film	2.18 nm	500 nm	65 nm	1000	22.5	151	0.24	1.5	-69000	-0.71	0.20
	20 ps	1 kHz	532 nm	Zn-Ag	Thin film	5,25 nm	500 nm	35 nm	234000	22.5	207	0.33	2.1	-11000	-0.7	0.11
[322]	20 ps	10kHz	532 nm	Zn-Au	Thin film	7.27 nm	600 nm	35 nm	231000	22.5	673	1.07	6.7	-360		
[323]	26 ps	1-10 Hz	532 nm	Au:Al_2O_3	Thin film	5.1 nm	564 nm	140 nm	957	32	13	0.042	0.1	-8750	0.11	0.21
	26 ps	1-10 Hz	532 nm	Au:Al_2O_3	Thin film	13.4 nm	564 nm	140 nm	1284	32	26	0.084	0.2	-22300	0.11	0.40
	26 ps	1-10 Hz	532 nm	Au:Al_2O_3	Thin film	14.2 nm	564 nm	140 nm	1291	32	26	0.084	0.2	-23400	0.10	0.38
[187]	40 ps	10 Hz	532 nm	AgNP/fG	Colloid	5 nm	450 nm	1 mm	3.04	24	740	1.34	3.7			
	40 ps	10 Hz	1024 nm	AgNP/fG	Colloid	5 nm	450 nm	1 mm	1.74	46	460	3.06	2.3			
[197]	4 ns	1-10 Hz	532 nm	Au	Colloid	15-20 nm	520 nm	1 mm	1.8		1800	18.5	0.23	-17.6	-3.0×10^{-4}	0.72
	4 ns	1-10 Hz	532 nm	$Au_{0.5}Ag_{0.5}$	Colloid	15-20 nm	460 nm	1 mm	0.9		800	8	0.1	-3.4	-1.4×10^{-4}	0.29
	4 ns	1-10 Hz	532 nm	Ag	Colloid	30-40 nm	420 nm	1 mm	0.04		1450	15	0.17	-2	-2.6×10^{-5}	3.30
[181]	6 ns	10 Hz	550 nm	AuNTP	Colloid	120 × 10 nm[a]	530&700 nm	2 mm	2.50	30	4500	12.7	0.15			
	6 ns	10 Hz	600 nm	AuNTP	Colloid	120 × 10 nm[a]	530&700 nm	2 mm	1.40	30	4200	11.9	0.14			
	6 ns	10 Hz	650 nm	AuNTP	Colloid	120 × 10 nm[a]	530&700 nm	2 mm	2.50	30	5700	16.1	0.19			
	6 ns	10 Hz	700 nm	AuNTP	Colloid	120 × 10 nm[a]	530&700 nm	2 mm	3.10	30	7200	20.4	0.24			
[324]	7 ns	10 Hz	532 nm	Ag at Al_2O_3	Thin film	3.1 nm		117 nm	80000				0.16	-1300000	7.6	0.29
	7 ns	10 Hz	532 nm	Ag at ZnO	Thin film	2.6 nm		141 nm	80000				1.5	-120000	3.0	1.06
[325]	10 ns	300 Hz	532 nm	AuAg	Colloid		400&490 nm	1 mm	3	65	900	119	0.18	26.5	-8.1×10^{-4}	0.92

APPENDIX B FEMTOSECOND NEARLY RESONANT SELF-FOCUSING IN GOLD NANOROD COLLOIDS-SUPLEMENTAL DOCUMENT

B.1 Analysis of optical transmittance measurements and evaluation of nanorod reshaping.

Table B.1 Analysis of the results obtained by theoretical fitting of Equation 6.1 to the optical transmittance measurements.

Sample	$T_{\lambda,0}T_0$	O.D.	a_0 (m^{-1})	Concentration (L^{-1})	$T_{\lambda,ns}$	$(O.D.)_{ns}$	a_{ns} (m^{-1})
C1	0.87	0.14	70	6.0×10^{14}	0.992	0.008	4.2
C3	0.69	0.37	186	1.6×10^{15}	0.988	0.012	6.0
C5	0.48	0.73	367	3.2×10^{15}	0.970	0.030	15.1
C9	0.30	1.20	602	5.2×10^{15}	0.962	0.039	19.4
C13	0.19	1.66	830	7.2×10^{15}	0.944	0.057	28.7
C19	0.08	2.53	1260	1.1×10^{16}	0.903	0.103	51.3

Table B.2 Calculated values of energy absorbed per nanorod during the experiments of low and high intensity optical transmittance. [a] Estimated at input pulse power of ~1MW, i.e. approximately at the onset of saturation. [b] Estimated at input pulse power of ~12 MW, i.e., at the maximum applied input power in these experiments. [c] Calculated by accounting that the absorption of the samples is fully saturated, and it is governed by the value a_{ns}. [d] Calculated by considering that no saturation occurs in the samples and that the absorption is governed by the initial (linear) absorption coefficient a_0.

Low intensity measurements					
Beam radius (μm)		Optical length (mm)	Irradiation volume (L)		Energy deposition [a] (nJ)
55		2	1.9×10^{-8}		89
Sample		Number of NR in Ir. volume	Energy absorbed (nJ)		Energy absorbed/NR (fJ)
C1		1.2×10^{7}	12		1.0
C3		3.1×10^{7}	28		0.9
C5		6.0×10^{7}	46		0.8
C9		9.9×10^{7}	62		0.6
C13		1.4×10^{8}	72		0.5
C19		2.1×10^{8}	82		0.4
High intensity measurements					
Beam radius (μm)		Optical length (mm)	Irradiation volume (L)		Energy deposition [b] (μJ)
30		2	5.7×10^{-9}		1.1
Sample	Number of NR in Ir. volume	Energy absorbed [c] (nJ)	Energy absorbed/NR [c] (fJ)	Energy absorbed [d] (nJ)	Energy absorbed/ NR [d] (fJ)
C1	3.4×10^{6}	9	2.6	138	41
C3	9.1×10^{6}	13	1.4	330	36
C5	1.8×10^{7}	32	1.8	554	31
C9	3.0×10^{7}	41	1.4	746	25
C13	4.1×10^{7}	59	1.5	863	21
C19	6.2×10^{7}	104	1.7	980	16

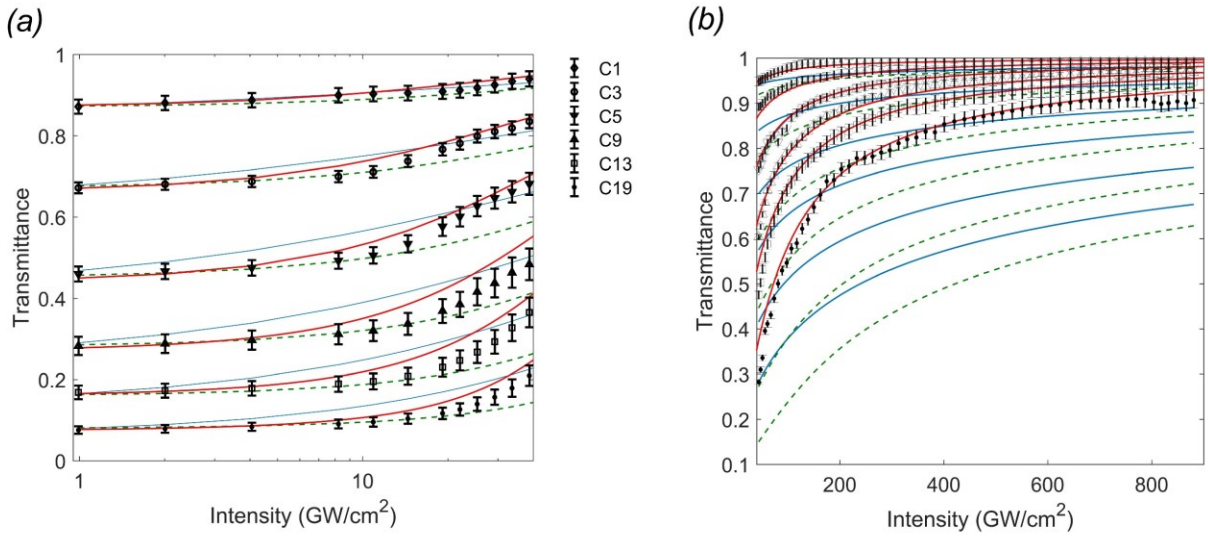

Figure B.1 Goodness of fit evaluation of saturable absorption models $a(I) \propto (1 + I/I_s^{\delta})^{-1}$ (red solid lines), $a(I) \propto (1 + I/I_s^{\delta})^{-1/2}$ (green dashed lines) and $a(I) \propto [1 + (I/I_s^{\delta})^{1/2}]^{-1}$ (blue solid lines) (a) low intensity measurements and (b) high intensity measurements data, as presented in Figure 6.5 of the Chapter 6/main manuscript.

We have performed an analysis on the goodness of fit of Equation 6.2 to the results of Figure 6.5 presented in section 6.5.3 of the Chapter 6/main text. Two additional models of saturable absorption $a(I)$ cited in the literature were tested, namely, $a(I) \propto \left(1 + I/I_s^{\delta}\right)^{-1/2}$[19] and $a(I) \propto \left(1 + \sqrt{I/I_s^{\delta}}\right)^{-1}$ [17, 278] . Each of the tested models was plugged in the propagation equation $\frac{dI}{dz} = -a(I)I$ and solved numerically to produce the fits presented in Figure B.1 by using values of Table B.1. In the low intensity results [Figure B.1(a)], sum of squares estimations for the value $I_s^{\delta} = 25\ GW/cm^2$ indicated a better goodness of fit (minimum sum of squares) for the model of Equation 6.1 compared to the other two models for the samples C1, C3 and C5, and comparable goodness of fit between Equation 6.1 model and the model $a(I) \propto \left(1 + I/I_s^{\delta}\right)^{-1/2}$ for the rest of the samples. Importantly, in the high intensity measurements, the tested models $a(I) \propto \left(1 + I/I_s^{\delta}\right)^{-1/2}$ and $a(I) \propto \left(1 + \sqrt{I/I_s^{\delta}}\right)^{-1}$ deviated significantly from the experimental data and only the model of Equation 6.1 provided a satisfactory fit. Despite the implications of a synergistic

effect between saturation of absorption and particle deformation within the irradiation volume (see discussion in section 6.6.1 of the Chapter 6/main text), the model of Equation 6.1 still provides a satisfactory fit to model nonlinear losses and allow numerical evaluation of the threshold for self-focusing, as presented in the following section.

B.2 Theoretical model description

To determine the threshold power for self-focusing in a medium that exhibits saturable absorption (in our case the gold nanorod colloids), it suffices to restrict ourselves to the damped nonlinear Schrodinger equation (NLSE) [64] within the Slowly Varying Envelope Approximation (SVEA) [63], which considers dispersion at the lowest order (second). It has been illustrated in [245] that chromatic dispersion is not the mechanism that arrests the collapse in most Kerr media of small dispersion, it rather introduces a shift on the steady-state critical power [303]. The model does not include terms relevant to the arrest of the collapse (multiphoton nonlinear absorption and plasma formation) and to post-collapse dynamics (shock terms), and it reads:

$$2ik\frac{\partial \mathcal{E}}{\partial z} + \nabla_T^2 \mathcal{E} - kk_0^{(2)}\frac{\partial^2 \mathcal{E}}{\partial t^2} + 2k^2\frac{n_2}{n_0}|\mathcal{E}|^2\mathcal{E} - ika(I)\mathcal{E} = 0 \qquad \text{B.1}$$

where $\mathcal{E}$ is the complex amplitude of the electric field, n_0 is the refractive index of the medium, $k = k_0\lambda_0 = 2\pi n_0/\lambda_0$ is the medium wavenumber, where λ_0 is the central laser wavelength, z defines the propagation coordinate, $a(I)$ is the nonlinear absorption described by Equation 6.1, $k_0^{(2)}$ is the second order dispersion of the medium and ∇_T^2 is the transverse Laplacian in cylindrical coordinates. Assuming a Gaussian beam, the initial $\mathcal{E}$ profile reads

$$\mathcal{E}(r,0) = \sqrt{\frac{2P_{in}}{\pi w_0^2}}exp\left(-\frac{r^2}{w_0^2} - \frac{t^2}{t_p^2} - i\frac{k_0 r^2}{2R}\right)$$

where P_{in} is the optical pulse power at the entrance of the cuvette, w_0 is the beam radius, $R = d - z_f^2/d$ is the radius of curvature of the focused beam, of which the beam waist is formed at distance d from the entrance window of the cuvette and z_f is the experimentally evaluated Rayleigh length of the focused beam.

It is convenient to write Equation B.1 in a dimensionless form, in pursuance of a numerical determination of P_{th}/P_{cr}. We make the following substitutions:

$$\tau \to \frac{t}{t_p}, \qquad \mathscr{r} \to \frac{r}{w_0}, \qquad \zeta \to \frac{z}{4z_0}, \qquad \delta \to \frac{2z_0 k_0^{(2)}}{{t_p}^2}, \qquad e \to \frac{\mathcal{E}}{\sqrt{\frac{2P_{in}}{\pi w_0^2}}}, \qquad s \to \frac{I_S^{\delta}}{\left(\frac{2P_{cr}}{\pi w_0^2}\right)},$$

$$\mathscr{p} \to 7.58\frac{P_{in}}{P_{cr}}, \qquad A \to \frac{2z_0 a_0}{1+\frac{I}{I_S^{\delta}}} = \frac{A_0}{1+\frac{|e|^2}{s/P_{in}}}$$

Where w_0 denotes the input beam radius, $z_0 = (k_0 n_0 w_0^2)/2$ is the corresponding Rayleigh length and $P_{cr} = \frac{3.79\lambda^2}{8\pi n_0 n_2}$ is the steady-state critical power for self-focusing. The transformation results in

$$i\partial_\zeta e + \nabla_T^2 e - \delta\partial_{\tau\tau} e - iA(|e|^2)e + \mathscr{p}|e|^2 e = 0 \qquad \text{B.2}$$

Defining the dimensionless parameter $F \equiv \frac{R}{z_0} n_0$, the initial beam profile is then given by

$$e(\mathscr{r}, \tau, 0) = \exp\left(-\mathscr{r}^2 - \tau^2 - i\frac{\mathscr{r}^2}{F}\right) \qquad \text{B.3}$$

Accounting for the values $F \approx 0.36$ and $s \approx 0.34$, which correspond to our experimental setup and observations in case I, we conducted extensive numerical simulations of Equation B.2 with the n_2 of water determined experimentally (Table B.3) [239]. These numerical experiments show that, as the peak input power is increased, a P_{th} is reached where self-focusing dominates diffraction, chromatic dispersion and absorption, and the solution blows up (we follow the criterion described in [68]). Accordingly, we can determine the ratio P_{th}/P_{cr} as a function of the normalized linear absorption $A_0 \equiv 2z_0 a_0$ for a direct comparison with the experimental results in case I.

As discussed earlier, in case II, we follow a slightly different approach. The beam is considered nearly collimated so that we can drop the third (phase) term in the exponential of Equation B.3. Further, in Equation B.2 we define the substitution $A \to A_{ns} \equiv 2z_0 a_{ns}$ and we conduct numerical experiments to determine P_{th}/P_{cr} as a function of the normalized non-saturated absorption A_{ns} much like in case (a). The parameters used for the numerical simulations are summarized in Table B.3.

Table B.3 Parameters used for the simulations, which match the experimental conditions.

Parameter	Symbol – Equation	Value
Central laser wavelength	λ_0	= 800 nm
Pulsewidth (FWHM)	t_{FWHM}	= 55 fs
Pulsewidth (1/e^2)	$t_p = t_{FWHM}/\sqrt{2\,log(2)}$	= 71 fs
Second order dispersion (water)	$k_0^{(2)}$	= 248 fs^2/cm
Dispersion length	$L_{DS} = t_p^2/k_0^{(2)}$	= 203 mm
Beam propagation factor	M^2	= 1.4
Linear refractive index (water)	n_0	= 1.33
Nonlinear refractive index (water)	n_2	= 2.1×10^{-16} W/cm^2
Critical power (water)	$P_{cr} = 3.79\,(M^2\lambda_0)^2/(8\pi n_0 n_2)$	=6.8 MW
Case I		
Input beam size	w_0	= 77 μm
Rayleigh length of input beam	$z_0 = \pi n_0 w_0^2/(M^2\lambda_0)$	= 22.1 mm
Diffraction length	$L_d = 2z_0$	= 44.2 mm
Parameter δ	$\delta = L_d/L_{DS}$	= 0.22
Beam waist distance	f	= 6.65 mm
Rayleigh length of focused beam	z_f	= 2.23 mm
Radius of curvature	$R = d - \frac{z_f^2}{d}$	= 5.9 mm
Parameter F	$F = Rn_0/z_0$	= 0.36
Saturation intensity	I_s^δ	= 25 GW/cm^2
Critical intensity	$I_{cr} = 2P_{cr}/(\pi w_0^2)$	=73 GW/cm^2
Parameter s	$s = I_s^\delta/I_{cr}$	= 0.34
Case II		
Input beam size	w_0	= 30 μm
Rayleigh length of input beam	$z_0 = \pi n_0 w_0^2/(M^2\lambda_0)$	=3.36 mm
Diffraction length	$L_d = 2z_0$	= 6.72 mm
Parameter δ	$\delta = L_d/L_{DS}$	= 0.033

Let us now discuss the effect of chromatic dispersion in Equation B.2, which is known to play a decisive role in P_{cr} of transparent materials within the regime of femtosecond filamentation [302, 303]. We can calculate the dispersion length, defined as $L_{DS} = {t_p}^2/k_0^{(2)}$, where $k_0^{(2)} = \frac{\partial^2 k}{\partial \omega^2} \approx 248\,fs^2/cm$ for water at $\lambda_0 = 800\,nm$ [245], and compare it with the diffraction length $L_d \equiv 2z_0$. Thus, for case I it holds that $L_d/L_{DS}{\sim}10^{-1}$ and for case II $L_d/L_{DS}{\sim}10^{-2}$, which shows that in both cases, L_{DS} is at least an order of magnitude larger than L_d. Even so, it is known that small chromatic dispersion does not have a negligible effect near the collapse region, as it enforces power transfer from the collapsing core to the outer tail of the beam at comparable rate with the spatial collapse (non-adiabatic self-focusing [64]). However, here we examine the relative ratio P_{th}/P_{cr} rather than the absolute value of P_{th}, thus, one should rather compare how chromatic dispersion of water is affected by the addition of the nano-inclusions as their concentration increases. The largest filling factor of nano-inclusions in our samples is $\sim 10^{-5}$, therefore, chromatic dispersion increases only marginally compared to neat water for blue-shifted detuning from the plasmon resonance [328]. Besides, one would expect that in the normal dispersion regime, enhancement of chromatic dispersion would increase the absolute values of P_{th} relative to P_{cr}, acting as an opposing

mechanism towards the collapse [303]. In effect, since we do not consider in our analysis the foresaid, marginal group velocity rise as the concentration of particles increases, the evaluation of possible enhancement of the nonlinear refraction becomes further conservative.

B.3 Quantification of nonlinear enhancement

The experimental results (with 10% relative uncertainty in P_{cr}) were normalized over the critical power for self-focusing of the host material (water) $P_{cr}^{h} \approx 6.8\,MW$ and plotted in Figure B.2 versus the normalized (over the diffraction length L_d) linear and non-saturated absorbance A_0 and A_{ns}, corresponding to case I and II (Figure B.2a and Figure B.2b respectively). Along with the experimental results, we have also plotted the corresponding theoretical results of P_{th}/P_{cr} for each case. According to our definitions of P_{cr}^{h}, P_{cr}^{e} and P_{th}^{e} it is expected that in the case that n_2^e is enhanced compared to n_2^h, and by accounting that $n_2^h/n_2^e = P_{cr}^{e}/P_{cr}^{h}$, it should hold $P_{cr}^{e} < P_{cr}^{h}$ and $P_{th}/P_{cr} \equiv P_{th}^{e}/P_{cr}^{e} > P_{th}^{e}/P_{c}^{h}$.

The behaviour of the experimental P_{th}^{e}/P_{cr}^{h} as compared to the solution of our numerical model is similar for both cases I and II; the numerical results exhibit agreement with the three first experimental values of P_{th}^{e}/P_{cr}^{h} (low concentration samples), with a gradual monotonic discrepancy between the theoretical P_{th}/P_{cr} and the experimental P_{th}^{e}/P_{cr}^{h} for the rest of the samples as the concentration of nanorods increases, indicating that the critical power of the nanorod-effective medium P_{cr}^{e} is reduced and the corresponding real part of the nonlinear refractive index n_2^e is enhanced.

We provide an evaluation of the complex, effective-medium nonlinear refractive index of the nanorod colloids $\tilde{n}_2^e = n_2^e + i a_2^e$ (Table B.4 and Figure 6.7 of Chapter 6/main text). For the real part we use data presented in Figure B.2. Since it holds that P_{th}^{e}/P_{cr}^{e} is equal to the numerical prediction P_{th}/P_{cr}, we can evaluate the ratio P_{cr}^{e}/P_{cr}^{h} by the mean experimental values of P_{th}^{e}/P_{cr}^{h} as shown in Figure B.2. Accordingly, the enhanced n_2^e, reads

$$n_2^e = n_2^h \frac{P_{th}/P_{cr}}{P_{th}^{e}/P_{cr}^{h}}$$

For the imaginary part, we have used the relation $a_2^e \cong -a_0/I_s^{\delta}$ [18].

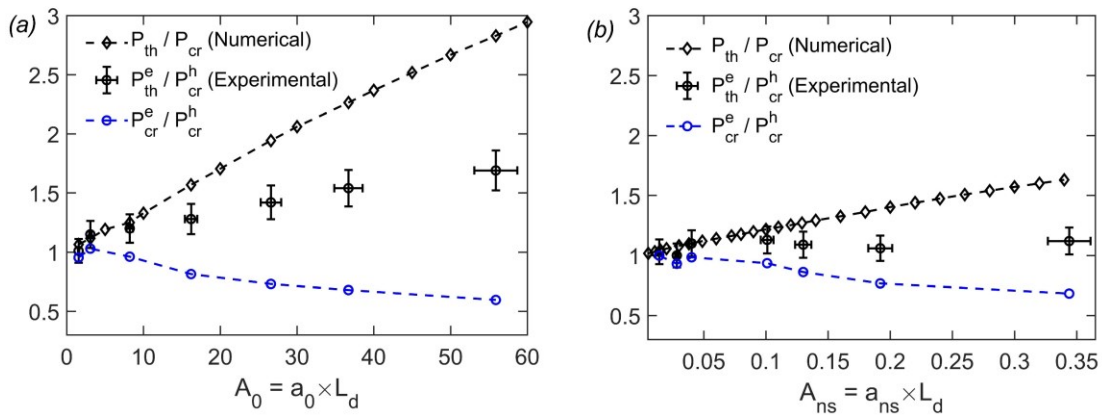

Figure B.2 Evaluation of the enhancement of the self-focusing nonlinearity of the gold nanorod colloids as their concentration (and absorption coefficient) increases. The normalized experimental results of P_{th}^{e}/P_{cr}^{h} are plotted for (a) case I and (b) case II, as a function of (a) the normalized linear absorption A_0 and (b) the normalized non-saturated absorption A_{ns}, which corresponds to the experimental conditions of the power limiting experiments for cases I and II, respectively. The corresponding numerical evaluations of P_{th}/P_{cr} are also plotted in each figure. The ratio P_{cr}^{e}/P_{cr}^{h} (blue circles), was estimated so that the ratio P_{th}^{e}/P_{cr}^{e} coincides with the theoretical curves of P_{th}/P_{cr}. The monotonic decrease of P_{cr}^{e}/P_{cr}^{h} as a function of increasing normalized absorption (higher nanorod concentration) is indicative of the enhancement of the self-focusing nonlinearity.

Based on the values of P_{cr}^{e}/P_{cr}^{h} shown in Figure B.2 and the experimentally determined value of P_{cr}^{h}, we have calculated the absolute numerical fitting of $P_{th}^{e}\left(=\frac{P_{th}}{P_{cr}}P_{cr}^{e}\right)$, shown in Figure 6.6 of the Chapter 6/main text, which now accounts for the gradual enhancement of n_2^e as the concentration of particles (absorption) increases for Cases I and II, respectively (shown in Table B.4).

More analytically, we have calculated $(P_{cr}^{e})_{Case\ I}=\left(\frac{P_{cr}^{e}}{P_{cr}^{h}}\right)_{Case\ I}\times P_{cr}^{h}$ and then estimated $(P_{th}^{e})_{Case\ I}=\left(\frac{P_{th}}{P_{cr}}\right)_{Case\ I}\times(P_{cr}^{e})_{Case\ I}$. Subsequently, we have performed a least square polynomial regression on the data and plotted the result against the experimental data of case I as shown in Figure 6.6 (solid red line). We have followed the same procedure for case II to produce the solid black line shown in Figure 6.6.

Finally, due to the observed differences in the values of n_2^e between cases I and II (Table B.4), we have plotted in Figure 6.6 (dashed lines) the numerical fitting of P_{th}^{e} by solution of Equation B.1

for case I and case II, however, this time for accounting the n_2^e obtained by case II and case I treatments, respectively.

More analytically, instead of using the calculated value $(P_{cr}^e)_{Case\ I}$ to estimate $(P_{th}^e)_{Case\ I}$, we used $(P_{cr}^e)_{Case\ I}$ to estimate $(P_{th}^e)_{Case\ II}$ according to the following relation $(P_{th}^e)_{Case\ II} = \left(\frac{P_{th}}{P_{cr}}\right)_{Case\ II} \times (P_{cr}^e)_{Case\ I}$. Subsequently, we have performed, (as described above) a least square polynomial regression on the data and plotted the result against the experimental data of case II (instead of case I) as shown in Figure 6.6 (dashed red line). To produce the numerical fitting to the experimental results of case I in Figure 6.6 (dashed black line), we have calculated $(P_{cr}^e)_{Case\ II} = \left(\frac{P_{cr}^e}{P_{cr}^h}\right)_{Case\ II} \times P_{cr}^h$ and then estimated $(P_{th}^e)_{Case\ I} = \left(\frac{P_{th}}{P_{cr}}\right)_{Case\ I} \times (P_{cr}^e)_{Case\ II}$, and we have finally performed a least square polynomial regression on the data and plotted the result against the experimental data of case I.

Table B.4 Evaluation of the effective nonlinear refraction n_2^e and absorption a_2^e coefficients of the examined nanorod colloids of varying concentration. The table also shows the nonlinear refraction coefficient n_2^h of the host material (water) evaluated by the power limiting method, the evaluated saturation intensity I_s^δ evaluated by optical transmittance measurements, and the nonlinear absorption coefficient a_2^e.

Sample	n_2^h ($\times 10^{-16}$ cm^2/W)	n_2^e ($\times 10^{-16}$ cm^2/W)		I_s^δ (GW/ cm^2)	a_2^e ($\times 10^{-2}$ cm/GW)
		Case I	Case II		
C0.5		2.1±0.2	2.1±0.2		-1.4±0.2
C1		2.1±0.2	2.2±0.2		-2.8±0.4
C3		2.2±0.2	2.1±0.2		-7.4±1.1
C5	2.1±0.2	2.6±0.3	2.3±0.2	25±5	-14.7±1.8
C9		2.9±0.3	2.4±0.2		-24.1±2.9
C13		3.1±0.3	2.7±0.3		-33.2±4.1
C19		3.5±0.4	3.1±0.3		-50.5±5.3

Notably, a fair agreement is observed when the data of n_2^e for case I are used for the numerical fitting to the experimental data *of both* case I and II, while when the data of n_2^e for case II are used, a less fair agreement is observed when the numerical fitting is plotted against the experimental data of case I. For this reason, we have plotted the results of n_2^e obtained from case I treatment in Figure 6.7 of the Chapter 6/main text.

APPENDIX C NONLINEAR THERMAL LENSING OF HIGH REPETITION RATE ULTRAFAST LASER LIGHT IN PLASMONIC NANO-COLLOIDS – SUPPLEMENTAL MATERIAL

C.1 Methods

C.1.1 Far-field beam width and divergence

In this section, we describe the experimental setup for the evaluation of the far-field FWHM beam size and divergence due to phenomenological self-trapping in plasmonic nano-colloids, shown in Figure C.1(a).

We used a Ti:Sapphire femtosecond oscillator, running at 76 MHz repetition rate. The system initially delivers >35 fs pulses at wavelength $\lambda = 800\,nm$ (measured FWHM bandwidth of ~35 nm). The maximum average output power is ~300 mW. The system can operate as a cw laser by adjustment of a pair of prisms that control the net group delay dispersion of the cavity, so that the phase will not be locked at an emission bandwidth around 800 nm. The transition of fs to cw operation was monitored on a spectrometer and a fast photodiode. At cw operation the system delivers approximately the same average power.

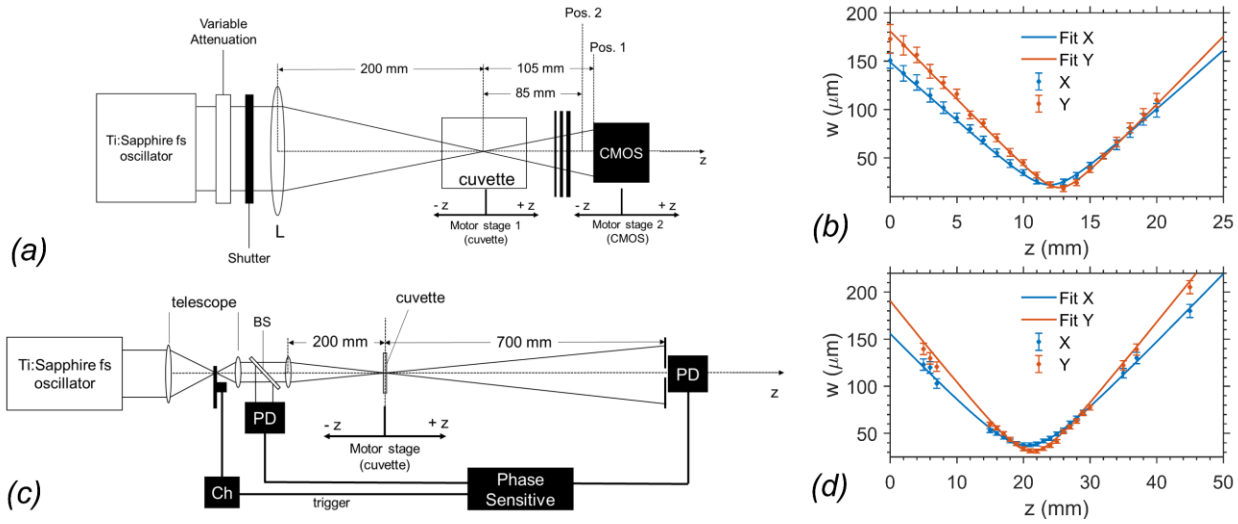

Figure C.1 (a) The experimental setup for the evaluation of far-field beam size and divergence variation as a function of input power in plasmonic nanocolloids. (b) Beam width characterization in air near the geometrical focus of lens L for the setup shown in (a). (c) z-scan characterization setup for the examined plasmonic nanocolloids. (d) Beam width characterization in air near the geometrical focus of the z-scan setup shown in (c).

The input laser beam had an elliptical profile of Gaussian shape along the vertical Y and horizontal X axis that define a plane normal to the propagation direction Z. The initial $1/e^2$ beam radius along the Y axis was $w_{0,Y}$~2.8 mm and along the X axis was $w_{0,X}$~2.4 mm, which yields a beam ellipticity $e_f \equiv \frac{w_{0,Y}}{w_{0,X}} \approx 1.2$. The beam passes through a variable attenuator and a shutter (the latter is used only for time-resolved experiments) and is focused by a positive lens L of focal distance 200 mm. The Rayleigh range $z_{R,Y}$, $z_{R,X}$ of the focused beam in air was determined by a knife edge method, along Y and X axes [Figure C.1(b)]. We evaluated $z_{R,Y}$~1.4 mm, $z_{R,X}$~1.8 mm. The propagation factor $M_Y^2 \approx M_X^2$~1.08 was evaluated by fitting equations

$$w_Y(z) = w_{f,Y}^{ideal}\sqrt{M_Y^2 + M_Y^2\left(\frac{z - z_{f,Y}}{n_0 z_{R,Y}}\right)^2} \qquad \text{C.1a}$$

$$w_X(z) = w_{f,X}^{ideal}\sqrt{M_X^2 + M_X^2\left(\frac{z - z_{f,X}}{n_0 z_{R,X}}\right)^2} \qquad \text{C.1b}$$

on the experimental data, where $w_{f,Y}^{ideal} = \sqrt{\lambda z_{R,Y}/\pi}$, $w_{f,X}^{ideal} = \sqrt{\lambda z_{R,X}/\pi}$ denote the ideal beam waist size, $z_{f,Y}$, $z_{f,X}$ denote the Z coordinates that the beam waist is formed, and n_0 is the refractive index of the medium. The fitting also provides the $1/e^2$ beam waist radii, $w_{f,Y}$~19 μm and $w_{f,X}$~22 μm. Further, we evaluated the distance $\mathcal{D} \equiv z_{f,X} - z_{f,Y}$~0.7 mm. The geometrical focus is approximately at the same location as the beam waists (uncertainty of ~1mm).

A 20 mm long cuvette was positioned on a motorized translation stage near the geometrical focus. The distance between the geometrical focus in air and the entrance window of the cuvette $\mathcal{d}$ varied (between 5, 10 and 15 mm). The cuvette contained each of the four examined samples (described below). The emerged beam was imaged, as a function of input power, on a CMOS camera, positioned at a motorized stage and translated at two different positions, ~85 mm and ~105 mm apart from the geometrical focus. Neutral density filters, placed before the camera, were used to adjust the power density below saturation. The FWHM size of the beam profile w_{FWHM} in the far-field was evaluated by processing the collected images. The divergence of the beam in the far-field was calculated as $\theta(rad) = [w_{FWHM}(105mm) - w_{FWHM}(85mm)]/\left[\sqrt{2ln2} \times 20mm\right]$, accounting for $w_{FWHM} = w_{(1/e^2)}\sqrt{2ln2}$. In dynamic experiments, videos were recorded by the

camera at a framerate of ~45.06 s^{-1} upon opening of a mechanical shutter (~1 ms) placed before lens L.

C.1.2 Sample preparation and optical characterization

We prepared four samples of different plasmonic nanocolloids: (S1) Au nanorods (purchased by Nanopartz) of 10 nm diameter and 38 nm length with a longitudinal peak around 770 nm. (S2) Au nanorods (purchased by Nanopartz) of 10 nm diameter and 50 nm length with a longitudinal peak around 900 nm. (S3) Au nanospheres (purchased by Nanopartz) of 50 nm diameter with a plasmon peak around 525 nm. (S4) AuAg alloy (15:85) (fabricated in our laboratory [235]) of 40 nm diameter with a plasmon peak around 450 nm. The concentration of samples S1, S2 and S3 were (according to specifications) $\rho_{S1} = 6.73 \times 10^{11}\, ml^{-1}$, $\rho_{S2} = 4.93 \times 10^{11}\, ml^{-1}$ and $\rho_{S3} = 3.97 \times 10^{11}\, ml^{-1}$ respectively. The concentration of sample S4 was evaluated $\rho_{S4} \approx 3 \times 10^{11}\, ml^{-1}$.

We performed optical transmittance T_λ measurements for all samples, tested on the setup of Figure C.1(a), under fs operation. We have measured the input and output power after the $h = 20\, mm$ long cuvette by subtracting the influence of the cuvette. The samples were positioned in the three foresaid examined d positions so that the transmittance was evaluated each time as a function of power for each sample and d. No significant difference was observed at every d for a specific sample, while the transmittance exhibited linear behaviour in the examined power range since the beam was always focused deep into the cuvette (>4 mm). The absorption coefficient a of all samples was evaluated according to $T_\lambda = -\ln(a_0 h)$.

Further, we implemented a standard z-scan setup to evaluate the thermo-optical coefficient $\frac{dn}{dT}$ of the examined samples, under fs operation [Figure C.1(c)]. A $0.64\times$ telescope was used to reduce the beam size to $w_{0,Y}$~1.8 mm and $w_{0,X}$~1.5 mm. A mechanical chopper set at a frequency of 20 Hz and a duty cycle d_c~16% was placed on the focus of the telescope, resulting in laser excitation of 8 ms every 50 ms (sufficient time for heat conduction, see for example references [329, 330]). Right after the telescope, a 50:50 beam-splitter directed half of the beam's energy onto a reference photodetector and half on a 200 mm focal length lens. We performed a knife edge characterization of the focused beam in air [the results are shown in Figure C.1(d)]. We evaluated (according to definitions shown above), $z_{R,Y}$~3.5 mm, $z_{R,X}$~5.1 mm, $w_{f,Y}$~30 μm and $w_{f,X}$~36 μm and $D +$

$\mathcal{D}\sim 0.7\ mm$. The samples were contained in an optical cuvette of length $h = 2\ mm$ so that $h < z_{R,Y}, z_{R,X}$. The latter was positioned in a motorized stage and scanned over a length of ~70 mm. An apertured photodetector was placed ~700 mm apart from the focal plane, yielding transmittance $T_\lambda \sim 0.01$ of the central portion of the impinged beam profile. To better read the weak signal, the photodetector was connected to a lock-in amplifier, which was triggered by the chopper's frequency. Accordingly, to determine $\frac{dn}{dT}$ we have used the relations (for 1-photon absorption) [244, 291]:

$$\delta T_{\lambda,p-v} = 0.405|\delta\Phi| \qquad \text{C.2a}$$

$$\frac{dn}{dT} = \frac{\lambda K_T}{a_0 P_{in} d_c h_{eff}} \delta\Phi \qquad \text{C.2b}$$

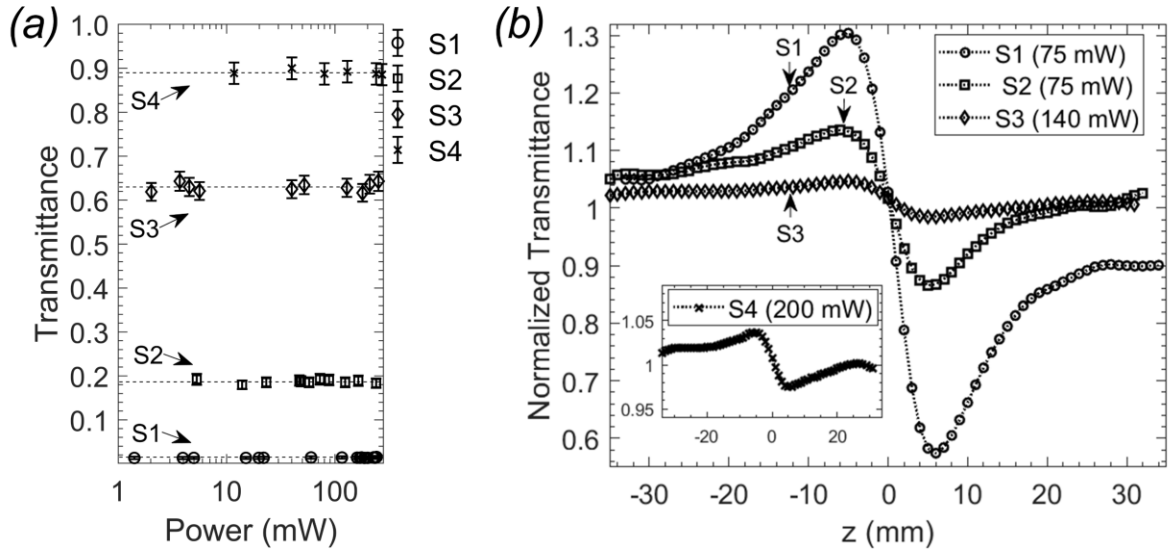

Figure C.2 (a) Optical transmittance measurements on the examined plasmonic nanocolloids as a function of P_{in} and d = 15 mm. The measurements were performed on the setup shown in Figure C.1(a). (b) z-scan signals on the examined plasmonic nanocolloids. Both optical transmittance and z-scan measurements shown here were performed by fs pulsed irradiation.

where $\delta T_{\lambda,p-v}$ is the normalized recorded peak to valley transmittance difference, $\delta\Phi$ is the deduced nonlinear phase shift from Equation C.2a, K_T is the thermal conductivity of water, a_0 is the absorption coefficient of the samples, P_{in} is the average optical power of the fs laser after the mechanical chopper and the effective length reads $h_{eff} = (1 - e^{-a_0 h})/a_0$. Our measurements

confirm a negative thermal nonlinearity for all samples (even far from the resonance) and the value of $\frac{dn}{dT}$ does not vary significantly since it is an intrinsic property. The volumetric filling factor f of all samples is $\ll 1$ so that $\frac{dn}{dT}$ is governed by the solvent (water). All values are reported in Table 7.1.

C.1.3 Numerical simulations

We compare our experimental observations with a thermal lensing model. We performed numerical simulations of the steady-state (with respect to heat conduction) nonlinear Schrodinger equation with a thermal nonlinearity and linear absorption. The model reads:

$$2ik_0n_0\partial_z\mathcal{E} + \nabla_T^2\mathcal{E} + 2k_0^2n_0^2\frac{dn}{dT}\delta T\mathcal{E} - ik_0n_0a_0\mathcal{E} = 0 \quad \text{C.3a}$$

$$-\kappa\nabla_T^2(\delta T) = a_0|\mathcal{E}|^2 \quad \text{C.3b}$$

Where z is the propagation coordinate, $k_0 = 2\pi/\lambda$ is the wavenumber of the central laser wavelength λ and ∇_T^2 is the transverse Laplacian in cylindrical coordinates (for radial coordinate r). The initial beam profile was defined to match the experimental setup of the focused beam at the entrance of the cuvette as

$$\mathcal{E}(r,0) = \sqrt{\frac{2P_{in}}{\pi w_0^2}}\exp\left(-\frac{r^2}{w_0^2} - i\frac{k_0r^2}{2R}\right) \quad \text{C.4}$$

where P_{in} is the input power, w_0 is the initial 1/e^2 beam radius, $R = n_0d - z_R^2/(n_0d)$ is the radius of curvature. We choose $z_R = n_0z_{R,X}$ to be the Rayleigh length, (experimental $z_{R,X}$) and we performed simulations according to the measured values of the beam width along the X axis for simplicity (all simulations can be extended by accounting experimental measurements over Y axis). We examined two cases of d (10 and 15 mm), where phenomenological self-trapping is more pronounced as opposed to $d = 5mm$, for the values of a of each sample shown in Table 7.1. The waist is formed at a position $n_0 \times d$ from the entrance of the cuvette due to the difference in the index of refraction. Since this value is approximately equal to the length of the cuvette for the case $d = 15$ mm, we have solved Equations C.3a-C.3b assuming a 3 cm medium length instead of 2 cm (the latter is the actual length of the cuvette) for convenience in comparing the nonlinear focus

position and beam profile at the output with the ones of $\mathcal{d} = 10$ mm case. The physical picture is not affected since temperature gradients developed for z < 2cm determine self-action for both cases (see for example Figure 7.9). After integration of Equation C.3a, we evaluated the σ^2 beam radius, which is equal to the $1/e^2$ definition for a Gaussian spatial profile, yet more meaningful when the beam profile undergoes thermal lens distortion. A comparison of the experimental fit along X axis and the numerical simulations at very low $P_{in} < 0.1\ mW$ (linear regime) in a medium of refractive index $n_0 = 1.33$ is shown in Figure C.3 for two values of $\mathcal{d}$ (10 and 15 mm). The parameters that were used for the solution of Equations C.3a-C.3b) are shown in Table C.1.

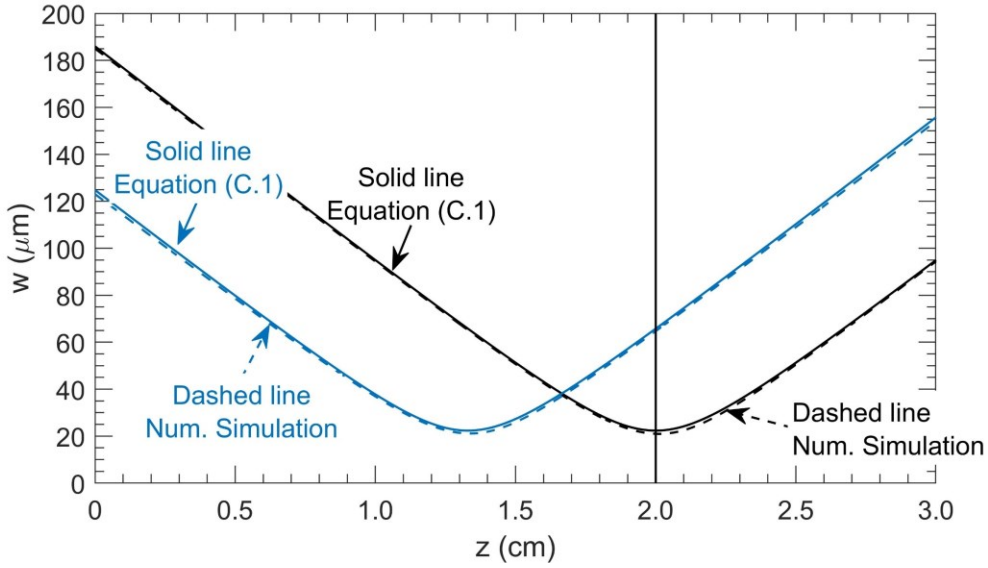

Figure C.3 Comparison of analytical Equation C.1b and the σ^2 beam width determined by solution of Equation C.3a-C.3b. Equation C.1b of the $w_X(z)$ is plotted for $z_{0,X} = n_0 \times \mathcal{d} = 13.3$ mm ($\mathcal{d} = 10$ mm) (solid blue line) and $z_{0,X} = 20.0$ mm ($\mathcal{d} = 15$ mm) (solid black line) for the experimentally determined M_X^2, $w_{f,X}^{ideal}$, $z_{R,X}$ and for $n_0 = 1.33$. The solution of Equation C.3a-C.3b was determined for $n_0 \times \mathcal{d} = 13.3$ mm (dashed blue line) and $n_0 \times \mathcal{d} = 20.0$ mm (dashed black line), for very low powers and for the corresponding parameters shown in Table C.1. The solid vertical line shows the output window of the cuvette.

Table C.1 Parameters used for the solution of Equations C.3a-C.3b, which describes stationary photo-absorption thermal defocusing of a focused beam for the examined colloids and the experimental conditions applied in this study.

Parameter	Symbol – Equation	Value
Central laser wavelength	λ_0	$= 800\ nm$
Linear refractive index of water	n_0	$= 1.33$
Absorption coefficient of S1	a_0	$= 2.10\ cm^{-1}$
Absorption coefficient of S2		$= 0.84\ cm^{-1}$
Absorption coefficient of S3		$= 0.24\ cm^{-1}$
Absorption coefficient of S4		$= 0.06\ cm^{-1}$
Rayleigh length of focused beam	$z_R = n_0 \times z_{R,X}$	$= 1.86\ mm$
Thermo-optic coefficient	dn/dT	$= 3 \times 10^{-5}\ \ 1/^o C$
Thermal conductivity of water	K_T	$= 0.6\ W/(m \cdot K)$
Distance between geometrical focus in air and cuvette entrance $d = 10\ mm$		
Input beam size	w_0	$= 123\ \mu m$
Beam waist distance	$n_0 \times d$	$= 13.3\ mm$
Radius of curvature	$R = n_0 d - z_R^2/(n_0 d)$	$= 13.6\ mm$
Distance between geometrical focus in air and cuvette entrance $d = 15\ mm$		
Input beam size	w_0	$= 185\ \mu m$
Beam waist distance	$n_0 \times d$	$= 20.0\ mm$
Radius of curvature	$R = n_0 d - z_R^2/(n_0 d)$	$= 20.1\ mm$

C.2 Simulation results for the case d = 10 mm and comparison with experiments.

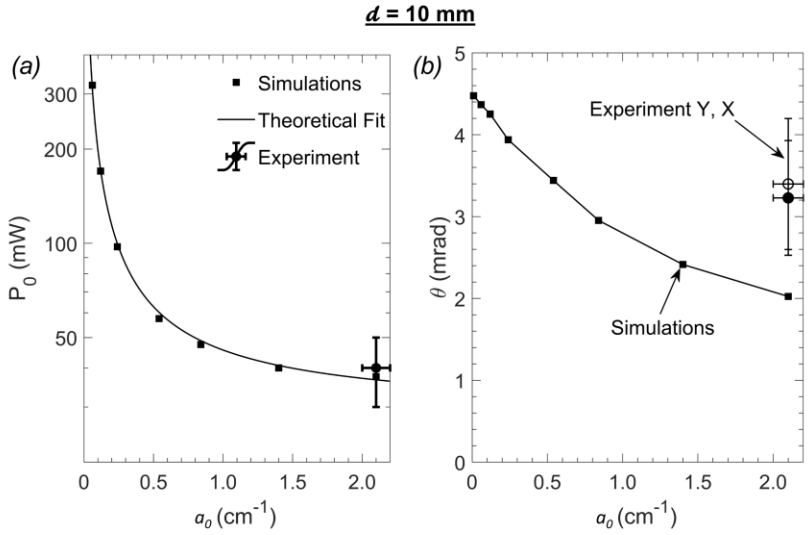

Figure C.4 Results of numerical simulations based on the nonlinear Schrödinger equation with a thermal nonlinearity (Equations C.3a-C.3b) and comparison with experimental observations for d = 10 mm. (a) Comparison of $P_0(a_0)$ by numerical simulation (squares), fitting of analytical expression (2) for m = 1.5 (solid line) and experiments (circles). (b) Comparison of $\theta(a_0)$ between numerical simulations (squares) and experimental measurements (circles).

C.3 Characteristic times of mass diffusion and nonlinear thermal lensing

In most reports on self-trapping in colloidal solutions (plasmonic or not), the experimental setup is rather similar: a cw laser beam is focused on a beam width (FWHM) of ~5-25 μm, typically several millimeters from the entrance of an optical cuvette (2-10 cm long) that contains the samples. Several studies have attributed the effect to phase modulation due to a gradient-force-induced, local concentration change of suspended particles. The supporting theoretical formalism imposes that a steady state is reached, governed by the mass diffusion equation [176]:

$$\frac{\partial \rho}{\partial t} + \nabla \cdot (\rho \vec{v}_d^{\,m} - D_m \nabla \rho) = 0 \qquad \text{C.5}$$

Where ρ denotes the particle concentration, D_m the mass diffusion coefficient and $\vec{v}_d^{\,m}$ the particle convective velocity.

One can perform an order-of-magnitude estimate of the characteristic time of this process, by replacing $\nabla^2 \rightarrow 1/{w_f}^2$ and $\partial\rho/\partial t \rightarrow \rho/t_d^m$, where w_f is a characteristic length (usually the beam spot) and t_d^m is the characteristic time of mass diffusion. Equation C.5 leads accordingly to the approximation (after appropriate treatment of the term $\nabla \cdot \rho \vec{v}_d^{\,m}$ presented in [176]):

$$t_d^m \geq \frac{{w_f}^2}{\left| D_m - D_m \frac{a_R \mathcal{E}\mathcal{E}^*}{4k_B T} \right|} \qquad \text{C.6}$$

Where a_R is the particle polarizability $\mathcal{E}$ is the complex amplitude of the applied electric field, k_B is Boltzmann's constant and T denotes the local temperature. From Equation C.6 we observe that a short value of t_d^m is managed by the polarizability term $D_m \frac{a_R \mathcal{E}\mathcal{E}^*}{4k_B T}$, since the mass diffusion coefficient of nanoparticles of radius ~25-250 nm is relatively small (10-1 $\mu m^2/s$ respectively), if we account for Stokes-Einstein's relation $D_m = k_B T/\left(6\pi\eta r_p\right)$, where η is the dynamic viscosity of the solvent and r_p is the radius of the particle. Thus, for a particle of polarizability $a_R \sim 3V\varepsilon_0$, where V denotes the volume of the particle and ε_0 is the vacuum permittivity, and $\mathcal{E}\mathcal{E}^* \sim 2P_{in}/\left(\pi {w_f}^2 \varepsilon_0 c\right)$, where P_{in} is the optical power and c the speed of light, we find that

$$t_d^m \gtrsim \frac{{w_f}^4}{{r_p}^2}\frac{3\pi\eta c}{P_{in}} \quad \text{C.7}$$

Assuming that P_{in} of 1 W is delivered at a focused spot of 1/e^2 radius w_f of 5 μm (or ~5.9 μm FWHM width), without losses, inside an aqueous solution ($\eta \approx 9 \times 10^{-4} Pa \cdot s$) of 25 nm radius plasmonic particles, we find $t_d^m \gtrsim 2.5\, s$, which significantly exceeds theoretical characteristic times of thermal diffusion. Indeed, if we assume an irradiation volume characterized by two axis, a short axis ~R and a long axis equal to the Rayleigh length $n_0 \pi {w_f}^2/\lambda$ (assume n_0 = 1.33 of water, λ = 800 nm) we can define the thermal diffusion length $L_f = V_f/S_f \sim w_f$, where V_f and S_f are the volume and surface area of the ellipsoid. Then a characteristic thermal diffusion time is defined as [331]

$$t_d^{th} \sim \frac{L_f^2}{4\kappa} \quad \text{C.8}$$

Where κ is the thermal diffusivity of the medium (=1.46×10^{-7} m^2/s for water). Applying w_f of 5 μm, we find that $t_d^{th} \gtrsim 7.9\, \mu s$. Note that the value of t_d^m is increasing dramatically as w_f increases, limited by the characteristic time of Brownian motion. While this problem can potentially be balanced by using larger particles, it comes at the expense of significant increase in absorption and scattering cross-sections for the case of plasmonic particles, which further enhances thermal or radiation pressure effects.

Nonetheless, high repetition fs illumination offers a potential advantage toward the mitigation of thermal effects. If tighter focusing conditions ($w_f \lesssim 2\mu m$, high numerical apertures, limit aberrations) are applied, it is possible that thermal effects are alleviated while maintaining the possibility of mass transport via gradient forces. This is because the time between two pulses δt_p becomes comparable to t_d^{th} so that temperature increase in the medium will be negligible on the next pulse. Contrarily, t_d^m remains much larger than δt_p, ensuring a cumulative effect of exerted optical force. For a smaller repetition rate of ~1 MHz, the time between pulses further approaches t_d^{th} so that such a scenario becomes plausible. Figure C.5 summarizes the conclusions of the foregoing example.

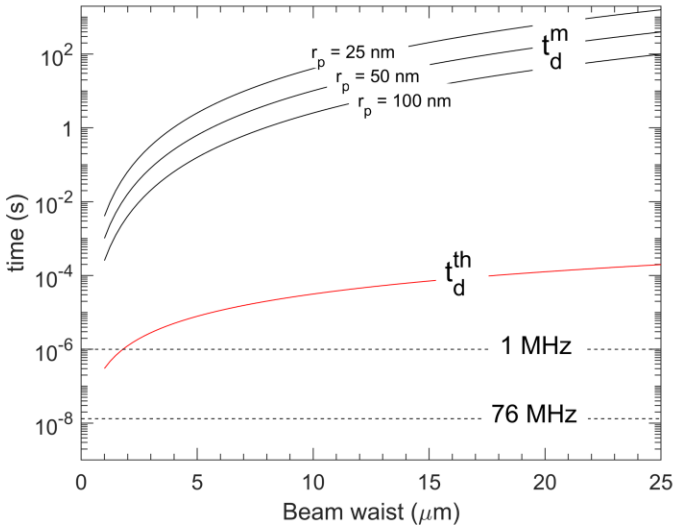

Figure C.5 Characteristic times for heat diffusion (red curve) and mass diffusion (black curves) described by Equations C.7 and C.8 respectively as a function of beam waist radius in the case of aqueous suspension of spherical nanoparticles and an input power of 1 W. The black horizontal dashed lines indicate δt_p for illumination by use of high repetition rate fs pulses at two different repetition rates.

APPENDIX D PUBLICATIONS

D.1 Articles published or submitted to peer-reviewed journals

Agiotis, L., Meunier, M. Nonlinear propagation of laser light in plasmonic nanocomposites. Review article submitted in *Laser & Photonics Reviews* (2022).

Agiotis, L., Meunier, M. Nonlinear thermal lensing of high repetition rate ultrafast laser light in plasmonic nano-colloids. *Nanophotonics*, **11** (2022). https://doi.org/10.1515/nanoph-2021-0775

Agiotis, L., Meunier, M. Femtosecond nearly resonant self-focusing in gold nanorod colloids. *Opt. Express* **29**, 39536-39548 (2021). https://doi.org/10.1364/OE.441117

Agiotis, L., Meunier, M. Optical power limiter in the femtosecond filamentation regime. *Sci Rep* **11,** 14270 (2021). https://doi.org/10.1038/s41598-021-93683-x

Hasanzadeh, M., Agiotis, L., Largillière, I., Patskovsky, S., Meunier, M., Antibody-Functionalized Gold Nanostar-Mediated On-Resonance Picosecond Laser Optoporation for Targeted Delivery of RNA Therapeutics. *Small*, **17**, 2007577 (2021) https://doi.org/10.1002/smll.202007577

Agiotis, L., Theodorakos, I., Samothrakitis, S., Papazoglou, S., Zergioti, I., & Raptis, Y. S. Magnetic manipulation of superparamagnetic nanoparticles in a microfluidic system for drug delivery applications. *Journal of Magnetism and Magnetic Materials*, **401**, 956-964 (2016) https://doi.org/10.1016/j.jmmm.2015.10.111

D.2 Articles published in peer-reviewed Conferences

Zapata, J., Darviot, C., Wang, L., Largillière, I., Agiotis, L., Meunier, M., Virtual training on Biomedical Nanophotonics, in *Education and Training in Optics & Photonics Conference 2021*, A. Danner, A. Poulin-Girard, and N. Wong, eds., OSA Technical Digest (Optica Publishing Group, 2021), paper Th4B.2.

Agiotis, L., Meunier, M. Threshold conditions for resonant Kerr self-focusing in plasmonic nano-colloids, in *OSA Advanced Photonics Congress (AP) 2020 (IPR, NP, NOMA, Networks, PVLED, PSC, SPPCom, SOF)*, L. Caspani, A. Tauke-Pedretti, F. Leo, and B. Yang, eds., OSA Technical Digest (Optica Publishing Group, 2020), paper NpTu2E.6.